



# Kyropoulos Growth and Characterizations of Titanium doped Sapphire

Gourav Sen

## ► To cite this version:

Gourav Sen. Kyropoulos Growth and Characterizations of Titanium doped Sapphire. Applied geology. Université Grenoble Alpes, 2018. English. NNT : 2018GREAI001 . tel-03152448

**HAL Id: tel-03152448**

**<https://theses.hal.science/tel-03152448>**

Submitted on 25 Feb 2021

**HAL** is a multi-disciplinary open access archive for the deposit and dissemination of scientific research documents, whether they are published or not. The documents may come from teaching and research institutions in France or abroad, or from public or private research centers.

L'archive ouverte pluridisciplinaire **HAL**, est destinée au dépôt et à la diffusion de documents scientifiques de niveau recherche, publiés ou non, émanant des établissements d'enseignement et de recherche français ou étrangers, des laboratoires publics ou privés.

## THÈSE

Pour obtenir le grade de

### **DOCTEUR DE LA COMMUNAUTE UNIVERSITE GRENOBLE ALPES**

Spécialité : **Matériaux, Mécanique, Génie Civil, Électrochimie**  
Arrêté ministériel : 25 mai 2016

Présentée par

**Gourav Sen**

Thèse dirigée par **Thierry Duffar**,

préparée au sein du **laboratoire SIMaP-EPM**  
dans l'**École Doctorale I-MEP2, Grenoble-INP**

## **Kyropoulos Growth and Characterisation of Titanium doped Sapphire**

Thèse soutenue publiquement le « **11 Janvier 2018** »,  
devant le jury composé de :

**Mme. Elisabeth, Djurado**

Professeur à Grenoble-INP, Président

**M. Ernesto, Dieguez**

Professeur à Universidad Autónoma de Madrid, Rapporteur

**M. Matias, Velazquez**

Chargé de recherche à l'institut ICMCB, CNRS, Bordeaux, Rapporteur

**Mme. Tamzin, Lafford**

Docteur-Ingénieur à IBEX INNOVATIONS LIMITED, Examineur

**M. Nicolas, Barthalay**

Docteur-Ingénieur à RSA LE RUBIS SA, Examineur

**M. Thierry, Duffar**

Professeur à Grenoble-INP, Directeur de Thèse









## Abstract

There is a huge interest in construction of solid state lasers capable of reaching petawatt (PW) levels and beyond. In order to achieve this level of power,  $\text{Ti:Al}_2\text{O}_3$  amplifiers up to 20 cm in diameter or larger are required and hence there is the need for the growth of large diameter  $\text{Ti:Al}_2\text{O}_3$  crystal boules. The Kyropoulos growth process has been identified by the company RSA le Rubis SA as the most productive technique because it allows massive crystals to be grown under a low temperature gradient and hence they are of good quality.

Growing crystals weighing about 30 kg comes with its share of complications which gravely affect the crystal morphology and hence crystalline quality. To address the issues of morphology, a detailed study of the effects of the growth parameters were carried out by analysing the process of crystals grown in the industrial setup. The factors for the critical issues of a flat plate formation and re-melted zones in the crystal were identified and an ideal set of parameters for the pulling rate and mass growth rate was proposed. These led to marked improvements in the productive volume of the crystal and enabled growth of crystals with predictable morphologies.

To take a step further, a completely autonomous crystal growth system was envisioned which would allow the operator live monitoring of the crystal shape and give control over its radial growth parameters. This is based on the simultaneous *in situ* measurement of crystal weight and remaining liquid level. A mathematical study is presented to explain the relationship between all the weighing forces acting on the growing crystal and to study the feasibility of this control system. It is shown that it could be useful for regulation of the diameter during the Kyropoulos growth process.

Crystals were characterised and checked for defects which would affect their optical properties. One such defect was the presence of a translucent band in the otherwise transparent crystal, called the “milky defect”. The crystalline quality in terms of dislocation density due to induced strain was analysed using X-ray diffraction techniques, along with optical characterisation and chemical analyses. Aided by heat transfer and thermo-mechanical numerical simulations of the growth system, an explanation for the origin of this defect in terms of acting thermal stress and associated crystal growth dynamics is proposed.

Titanium doping in the sapphire crystal is needed for the laser application, but there is segregation of the dopant during growth and this leads to an inhomogeneous distribution in the grown crystals, as shown by optical characterisation of the distribution of titanium in its  $\text{Ti}^{3+}$  and  $\text{Ti}^{4+}$  states. Ideas in order to improve the laser sample homogeneities are proposed.

# Acknowledgements

This research work was carried out at the SIMaP laboratory in the EPM (Electromagnetic Processing of Materials) group within the framework of French national research project FUI TITANSAPHIR with the financial support of the Region Auvergne-Rhone-Alpes, project N° 13 023257 01.

Having spent three years working on this project which culminated in this thesis, I would like to say that it was an extremely rewarding and fulfilling experience. This was thanks to all the people I met and interacted with during these three years, who contributed to my development both personally and professionally.

First of all, I would like to express my sincerest gratitude to my supervisor and guide, Prof. Thierry Duffar. From showing the confidence in me while offering this PhD position, to the tireless work of correcting my manuscript, he has always supported me and was always available to help. Under his guidance, I was allowed to explore the subject and had the freedom to make mistakes, knowing that he would be there to guide and correct me whenever needed. He encouraged me to go beyond the confines of our lab and find collaborators to develop the work and look for solutions and offered whatever support was needed in doing so.

During my work I had the valuable opportunity to work on the industrial crystal growth machines at RSA le Rubis company at Jarrie. I would like to thank Cyril Pezzani for co-ordinating all my trips to the industry and introducing me to the crystal growth process there. I also had support from Jose Pereira and Maud Silvestre for all activities related to crystal growth and sample preparation activities at RSA. Nicolas Barthalay at RSA was responsible for supervising my work at the company and offered valuable insights into the industrial context of this research project whenever needed. Hugues Cabane from Cristallinov was really instrumental in providing me polished samples as required for all the characterisation analysis in this work.

I would like to thank Stephane Coindeau at CMTC, Grenoble INP to whom I rushed numerous times to orient my samples and carry out some rocking curve analysis and he was always available and ready to help me even at a short notice. The TEM analysis presented in this work was carried out by Gilles Renou and Prof. Patricia Donnadieu and Frédéric De Geuser carried out the SAXS analysis for our samples at CMTC, Grenoble INP. A major part of all the characterisation work was carried out at the ESRF in Grenoble at beam line BM-05. Here I had many sessions of beam time to analyse the samples with Thu Nhi Tran Caliste, who was always enthusiastic and open to all my requests. José Baruchel at the ERSF was very instrumental in helping us analyse the data from the experiments and explaining the scientific theory behind those. I am really impressed by his depth of knowledge regarding X-ray diffraction techniques and the opportunities to

have long discussions with him led me to develop a deep interest in this technique and I would love to work more in this field of research.

I would also like to acknowledge the great support I received from unexpected quarters like from Prof. Ievgenii Kryvonosov at the Institute for Single Crystals in Ukraine and from Prof. Vitali Nagirnyi at University of Tartu. The investigation into the mysterious milky defect was greatly aided by their contributions. Prof. Kryvonosov very enthusiastically shared his thoughts and results of the investigations he had regarding this defect and Prof. Nagirnyi carried out thermo-luminescence analysis in his lab on our samples to look for point defects.

This project was really a collaborative one and hence I would like to thank Guillaume Alombert-Goget and Prof. Kheirreddine Lebbou at ILM, Lyon who always welcomed me at their facility and carried out all the optical characterisation for the samples during this work. Carmen Stelian performed thermal simulations for the crystal growth configurations and helped realise the various physical phenomena going on during the growth process. The work of developing the mathematical model for crystal radius determination was possible due to the contributions of Huiyuan Lu, Yoann Malier and Wenqing Jia who devoted their Masters theses to this challenge. We also had the pleasure of inviting Prof. Liliana Braescu from the Université du Québec to guide us in this mathematical work and her efforts were really instrumental in the development of this work.

I am really grateful to all the members of the SIMaP-EPM lab who supported me throughout my journey. I would like to thank Maya Cherif who guided me during my first entry into the lab for my Masters thesis and encouraged me to take up the PhD position. Ahmed Nouri helped me integrate into the lab and was always available to advise me about issues related to life as a PhD student. The secretary of our lab, Khadija Rassouli deserves a special mention for making an extra effort to communicate with my inadequate level of French and addressing all issues related to integration of a foreign student in the lab.

Throughout this journey of three years I had tremendous support from Roberta, who made sure it was an enjoyable one and was ready to give fair criticism whenever I wasn't up to the task and words of encouragement if I was feeling low. Finally, I would like to acknowledge the unwavering support of my parents throughout my life and their tremendous sacrifices which made me the person I am today.

# Nomenclature

$B(r)$	Axisymmetric magnetic field at position $r$	B
$C$	Concentration	at%
$C_{ijkl}$	Components of the elasticity tensor	-
$C_l^*$	Concentration in liquid at the solid/liquid interface	at%
$C_0$	Initial solute concentration	at%
$C_p$	Specific heat	J.K <sup>-1</sup>
$C_s^*$	Concentration in solid at the solid/liquid interface	at%
$E$	Young's modulus	N.m <sup>-2</sup>
$FWHM$	Full width half mean	-
$H$	Distance between the seed and the bottom of the crucible	m
$I$	Nucleation rate	m <sup>-3</sup> .s <sup>-1</sup>
$K_0$	Modified Bessel function of the second kind at order 0	-
$K_1$	Modified Bessel function of the second kind at order 1	-
$N$	Population inversion density	-
$Q_R$	Radiative heat source	J
$R$	Adimensioned radial parameter $r.c^{1/2}$	-
$R_c$	Crucible's radius	m
$R_1$	First radius of curvature of the meniscus	m
$R_2$	Second radius of curvature of the meniscus	m
$R^*$	Adimensioned boundary radial coordinate	-
$T$	Temperature	K
$T_o$	Temperature of objects surrounding the material	K
$T_{ref}$	Reference temperature	K
$T_s$	Surface temperature of the material	K
$V$	Growth velocity	m.s <sup>-1</sup>
$V_{excess}$	Volume of the portion of the meniscus in contact with the crucible located above $h_{meniscus\ 1}$	m <sup>3</sup>
$V_{gas}$	Volume of ambient gas in the crucible located below $h_{meniscus\ 1}$ And trapped between the two menisci	m <sup>3</sup>
$V_{molten}$	Volume occupied by the molten sapphire inside the crucible	m <sup>3</sup>

$V_{submerged}$	Volume occupied by the crystal below $h_{meniscus\ 1}$ Level	$m^3$
$W_{buoyancy}$	Resultant of pressure forces (divided by g) applied by the molten sapphire	kg
$W_{buoyancy1}$	Component of $W_{buoyancy}$ Due to molten sapphire	kg
$W_{buoyancy2}$	Component of $W_{buoyancy}$ Due to gas	kg
$W_{emerged}$	Weight of the crystal's emerged part	kg
$W_{measured}$	Weight measured by the seed holder's sensor	kg
$W_{molten}$	Total weight of the molten sapphire (including menisci weight)	kg
$W_{seed}$	Weight of the sapphire seed	kg
$W_{st}$	Vertical component of surface tension force (divided by g) which applies on the crystal	kg
$W_{submerged}$	Weight of the crystal's submerged part	kg
$W_{total}$	Total weight of $Al_2O_3$ introduced into the crucible	kg
$Z$	Adimensioned vertical parameter $z.c^{1/2}$	-
$Z_0$	Adimensioned difference of pressure between the air and the molten sapphire's surface	-
$Z^*$	Adimensioned boundary vertical coordinate	-
$\tilde{Z}$	Adimensioned parameter $Z+Z_0$	-
$b$	Scattering coefficient	-
$c$	Integration constant	-
$f$	Interface deflection	m
$f_s$	Volume fraction of solid	-
$g$	Gravitational acceleration	$m.s^{-2}$
$h$	Heat transfer coefficient	$W.m^{-2}K^{-1}$
$h_f$	Latent heat of fusion	$J.kg^{-1}$
$h_{measured}$	Level of molten sapphire inside the crucible	m
$h_{meniscus\ 1}$	Height of the meniscus in contact with the growing crystal	m
$k$	Absorption coefficient	$W.m^{-2}K^{-1}$
$k_{eff}$	Effective segregation coefficient	-
$k_s$	Equilibrium distribution coefficient	-
$l$	Characteristic size of the object along the direction of the thermal flow	-
$n$	Index of refraction	-

$\vec{n}$	Normal vector at the interface	-
$p$	Pressure	$\text{N.m}^{-2}$
$p_o$	Gas pressure inside the furnace	$\text{N.m}^{-2}$
$p_v$	Pressure at the surface of molten sapphire	$\text{N.m}^{-2}$
$q$	Heat flux density	$\text{W.m}^{-2}$
$r$	Radial coordinate for the meniscus study	m
$r_c$	Crystal radius	m
$r_{(i)}$	Radius of the crystal at the i-th measurement	m
$r^0$	Critical nucleation radius	m
$\vec{s}$	Tangential vector to the free surface	-
$u_s$	Tangential component of the flow velocity	$\text{m.s}^{-1}$
$u_z$	Unit vector along the direction of the symmetry axis (upwards)	-
$\vec{u}$	Flow velocity vector	$\text{m.s}^{-1}$
$z$	Vertical coordinate for the meniscus study	m
$z_{(i)}$	Distance between the seed and $h_{meniscus\ 1}$ Level at the i-th measurement	m
$\alpha$	Absorption coefficient	$\text{W.m}^{-2}\text{K}^{-1}$
$\beta_T$	Thermal expansion coefficient	$\text{K}^{-1}$
$\gamma_{lv}$	Surface tension at sapphire liquid - gas interface	$\text{N.m}^{-1}$
$\Delta f$	Fluorescence profile (full width at half maximum) of the fluorescence curve	-
$\Delta G$	Total Gibbs free energy	$\text{J.mol}^{-1}$
$\Delta s_f$	Entropy of fusion per unit volume	$\text{J.m}^{-3}\text{K}^{-1}$
$\Delta T_r$	Undercooling due to curvature	K
$\Delta x$	Distance over which heat is transferred	m
$\varepsilon$	Emissivity	$\text{W.m}^{-2}$
$\varepsilon_{kl}$	Strain tensor components	-
$\eta$	Dynamic viscosity	$\text{N.s.m}^{-2}$
$\theta_B$	Bragg angle	-
$\theta_d$	Dynamic contact angle of liquid $\text{Al}_2\text{O}_3$	-
$\theta_l$	Contact angle of liquid $\text{Al}_2\text{O}_3$ on sapphire crystal	-



$\theta_s$	Angle between the vertical and the crystal surface at $h_{meniscus\ 1}$ Level	-
$\lambda$	Wavelength	m
$\lambda_{eff}$	Effective heat conductivity coefficient	W.m <sup>-1</sup> K <sup>-1</sup>
$\lambda_p$	Peak of the fluorescence curve	-
$\lambda_r$	Radiation components of thermal conductivity	W.m <sup>-1</sup> K <sup>-1</sup>
$\lambda_T$	Heat conductivity coefficient	W.m <sup>-1</sup> K <sup>-1</sup>
$\mu$	Magnetic permeability	H.m <sup>-1</sup>
$\nu$	Poisson's ratio	-
$\rho_{gas}$	Density of the ambient gas inside the crucible	Kg.m <sup>-3</sup>
$\rho_l$	Liquid sapphire density	Kg.m <sup>-3</sup>
$\rho_s$	Solid sapphire density	Kg.m <sup>-3</sup>
$\sigma$	Stimulated emission cross section (or gain cross section)	m <sup>2</sup>
$\sigma_{ij}$	Stress tensor components	-
$\sigma_{Mises}$	Von Mises stress	N.m <sup>-2</sup>
$\sigma_r$	Normal stresses in the radial direction	N.m <sup>-2</sup>
$\sigma_{rz}$	Shear stress	N.m <sup>-2</sup>
$\sigma_{sl}$	Solid/liquid interface energy	J.m <sup>-2</sup>
$\sigma_{st}$	Stefan-Boltzmann constant	W.m <sup>-2</sup> K <sup>-4</sup>
$\sigma_z$	Normal stresses in the axial direction	N.m <sup>-2</sup>
$\sigma_\varphi$	Normal stresses in the azimuthal direction	N.m <sup>-2</sup>
$\tau$	Fluorescence lifetime	s
$\tau_c$	Dimensionless interface deflection	-
$\tau_{crss}$	Critical resolved shear stress	N.m <sup>-2</sup>
$\phi_k$	Factor dependent on the optical properties and the systems configuration	-
$\phi(s)$	Angle between meniscus tangent at s and the horizontal	-
$\phi^*$	Angle between meniscus tangent and the horizontal at (R <sup>*</sup> , Z <sup>*</sup> )	-
$\Omega_l$	Liquid sapphire's rotation speed	-
$\omega_h$	Intrinsic width of diffraction	-

# Introduction

The optical properties of lasers have found numerous applications in the fields of medicine, machining or surface treatment. There has been a dramatic rise in peak powers for lasers in recent years which have given impetus to new fields of research in light/matter interactions at extreme intensities. Examples of such research are the new ways of particle and electron acceleration in high energy physics research and potential future applications in the development of compact proton generators for proton cancer therapy.

Today there are around 200 intense lasers facilities in the world; these lasers cost from 5 to 20M € according to the target power. These installations need components capable of creating a fast laser effect and withstanding the power emitted. Among the materials considered for these installations, sapphire crystal doped with titanium ( $\text{Ti:Al}_2\text{O}_3$ ) constitute 65% as shown in figure 1 and are the material favoured by the world's specialists due to their very wide emission spectrum and very good thermal conductivity.

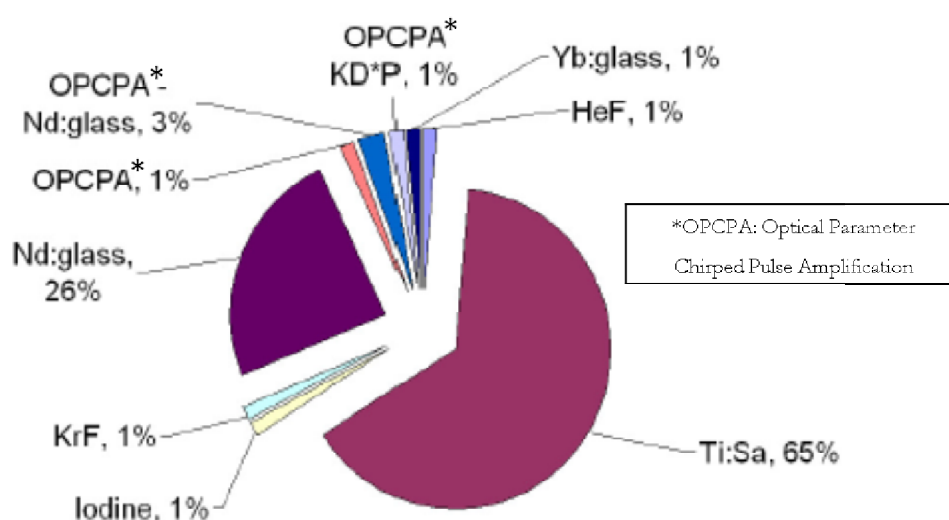


**Figure 1:** Share of different materials used for amplifications in CPA (Chirped Pulsed Amplification) systems as of 2006 [Barthalay, 2013].

The TITANSaphir project has been established in this context to develop titanium-doped sapphire crystal components with high performances and with dimensions greater than 200 mm in diameter which are not available on the market today. To achieve this ambitious goal the project involves the following partners:

- RSA LE RUBIS: Manufacturer for sapphire single crystals.
- CYBERSTAR: Manufacturer of crystallisation furnaces.

- AMPLITUDE TECHNOLOGIES: Manufacturer of high performance laser systems.
- SIMAP-EPM: Research laboratory focussed on processing of materials.
- INSTITUT LUMIERE MATIERE (ILM): Research laboratory focussed on optical materials.

In the context of the TITANSaphir project this PhD thesis work entitled; 'Kyropoulos Growth and Characterisation of Titanium Doped Sapphire' was carried out at the SIMAP-EPM laboratory under the supervision of Prof. Thierry Duffar from September 2014 to September 2017.

The expectations from this PhD thesis were:

- Development of the Kyropoulos growth system at RSA Le Rubis to improve the productivity of the established process.
- Interaction with the engineer responsible for numerical simulation of the growth processes to model the various physical phenomena occurring during the growth.
- Analysis of the growth conditions likely to impact the crystal quality.
- Detailed characterisation of the defects inside the crystals, which influence the optical properties.
- Suggestions of growth process improvements to improve the crystal geometry and reproducibility and to get rid of the optical defects.

The work developed during the thesis is presented in this manuscript divided into four chapters.

The first chapter gives the current state-of-the-art regarding development of sapphire crystals. First, the sapphire crystal structure is described, followed by a review of the application of titanium doped sapphire crystals in laser systems. The various growth techniques available for sapphire single crystals are discussed and the arguments for the choice of the Kyropoulos growth system are validated. A discussion of the possible defects expected in the crystals is also presented.

The second chapter presents the Kyropoulos growth system used at RSA Le Rubis for this project. An analysis of the growth system is presented and improvements in the process have been carried out. The impact of this improved growth process has been observed on the crystal morphology as shown by a crystal with the desired shape in figure 2, which leads to a better productivity of the crystals. The shape of the growing crystal at various stages has been studied by numerical simulation and helps explain the profile of titanium distribution in the crystals.



**Figure 2:** 26 kg crystal with the desired shape obtained after improvements in the growth process.

The third chapter presents a study to check the feasibility of a growth system which would allow the growth of crystals with control over the growing crystal radius, as shown in figure 3. A theoretical analysis of the forces acting on the seed holder during the growth has been carried out. It was demonstrated that, with the possibility of measuring the melt level during the crystal growth with sufficient accuracy, the crystal radius for the major part of the growth can be estimated with good accuracy. Based on this principle, a completely automatic growth system can be further developed.

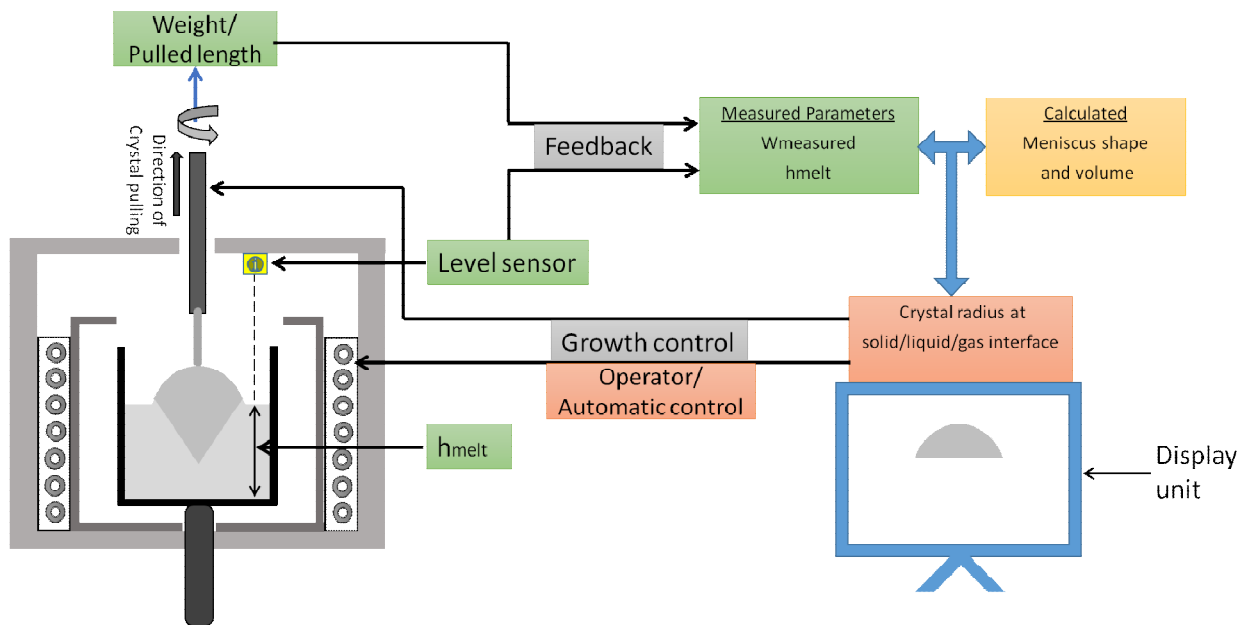


**Figure 3:** Scheme for an automatic crystal growth control and monitoring system.

The fourth chapter describes the investigations into an optical defect found in the crystals, known as the 'milky defect', as shown in figure 4. Various characterisation measurements were carried out for the

defect region, based on which a fair idea about the nature of this defect was established. Aided by numerical simulations for the growth process, a hypothesis for the mechanism of formation for this milky defect is presented.

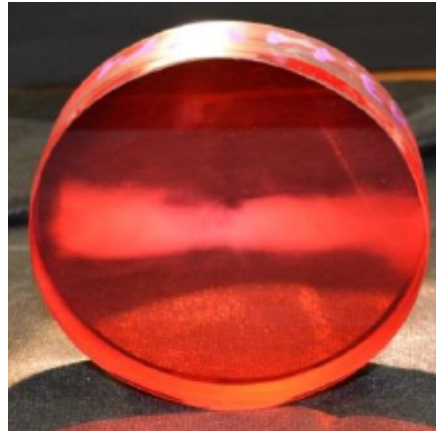


**Figure 4:** Milky defect zone aligned horizontally in a disc cut from the crystal.

Finally, in the conclusion the evolved state of the art for the Kyropoulos system and the new knowledge of possible optical defects in the crystal are summarised. Some suggestions for dealing with the problems of titanium segregation and the milky defect are presented. The possibilities for further improvement and automation of the growth system are discussed.

# Contents

<b>Abstract .....</b>	<b>iii</b>
<b>Acknowledgements.....</b>	<b>iv</b>
<b>Nomenclature .....</b>	<b>vi</b>
<b>Introduction .....</b>	<b>x</b>
<b>1 State of the art .....</b>	<b>1</b>
1.1 History .....	1
1.2 Sapphire Crystal.....	1
1.3 Laser Applications.....	6
1.4 Growth techniques.....	11
1.5 Crystallisation from the Gaseous (Vapour) Phase .....	12
1.6 Crystallisation from Solution .....	13
1.7 Solid-Phase Crystal Growth .....	14
1.8 Melt growth techniques .....	14
1.8.1 Crystal Growth from the Melt Not Using Crucibles.....	14
1.8.2 Methods of Crystal Growth from the Melt in Crucible .....	18
1.9 Choice of Kyropoulos Method.....	29
1.10 Choice of crucible material.....	29
1.11 . Growth process phenomenon of sapphire from the melt .....	30
1.11.1 Processes accompanying melting of $\text{Al}_2\text{O}_3$ .....	31
1.11.2 Processes occurring at the crystallisation front.....	36
1.12 Defects .....	49
1.13 Perspectives.....	50
<b>2 Control over crystal morphology.....</b>	<b>53</b>
2.1 Introduction .....	53
2.2 Kyropoulos Growth set-up.....	53
2.3 Sapphire crystal growth process .....	56
2.3.1 Crucible preparation.....	56
2.3.2 Furnace preparation .....	57
2.3.3 Furnace operation.....	58
2.4 Crystal morphology and quality .....	62
2.4.1 Growth parameters to be studied .....	62

2.4.2	Crystal morphology analysis.....	63
2.4.3	Crystal morphology features.....	75
2.5	Crystal-melt interface shape .....	84
2.6	Titanium distribution.....	86
2.7	Laser performance characteristics.....	87
2.7.1	Figure Of Merit (FOM) .....	87
2.7.2	Slope efficiency .....	90
2.8	Conclusion.....	91
<b>3</b>	<b>Crystal shape prediction.....</b>	<b>93</b>
3.1	Introduction .....	93
3.2	Crystal shape live monitoring system .....	94
3.3	Background .....	95
3.4	Methodology .....	96
3.5	Hypotheses .....	97
3.6	Weighing method applied to Kyropoulos crystal growth.....	97
3.7	Numerical study.....	103
3.7.1	External meniscus .....	103
3.7.2	Internal meniscus.....	108
3.7.3	Capillary bridge .....	109
3.7.4	Crystal Shape .....	112
3.8	Numerical results and discussion .....	113
3.8.1	Menisci's shapes and volumes.....	113
3.8.2	Errors associated to thermal heterogeneousness and pulling .....	118
3.8.3	Generate fictive measurement data.....	120
3.8.4	Finding the imposed shape .....	120
3.8.5	Minimal accuracy required for the melt level measurement.....	123
3.9	Conclusion.....	126
3.10	Perspectives.....	127
<b>4</b>	<b>Investigations into the milky defect .....</b>	<b>129</b>
4.1	Introduction .....	129
4.1.1	Defect Orientation .....	130
4.2	Diffusion of laser in defect zone.....	131

4.2.1	Milky defect (Vertically aligned) .....	131
4.2.2	Milky defect (Horizontally aligned).....	132
4.2.3	Influence of defect alignment .....	133
4.2.4	Observations .....	134
4.3	Sample preparation.....	134
4.4	Characterisation of line defects (dislocations).....	135
4.4.1	X-ray rocking curve analysis .....	135
4.4.2	X-ray diffraction topography.....	136
4.4.3	Rocking curve imaging.....	147
4.5	Stress Analysis .....	159
4.5.1	Temperature gradient .....	159
4.5.2	Thermal stress .....	162
4.6	Characterisation of Point defects (Vacancies).....	172
4.6.1	Thermoluminescence (TSL) .....	172
4.6.2	TEM analysis .....	175
4.6.3	SAXS .....	176
4.6.4	Point defects formation.....	177
4.6.5	Interaction between point defects and dislocations.....	178
4.7	Discussion .....	179
4.7.1	Observations .....	179
4.7.2	Bibliographic references.....	180
4.7.3	Best-fit hypothesis .....	182
4.8	Conclusion.....	183
<b>Conclusion.....</b>		<b>185</b>
<b>Appendix I: Crystal morphology analysis.....</b>		<b>191</b>
<b>Appendix II: Milky defect explained as an optical effect by Carmen Stelian .....</b>		<b>204</b>
<b>Appendix III: Numerical modelling of the Kyropoulos growth process (model by Carmen Stelian).....</b>		<b>213</b>
<b>Appendix IV: Chemical Analysis .....</b>		<b>217</b>
<b>Bibliography.....</b>		<b>220</b>





# 1 State of the art

## 1.1 History

Crystals have always been objects of great interest in the history of mankind because of their visual appeal, shape, colours and the optical effects produced due to their transparency. Ruby and sapphire are such crystals found in nature valued as precious gemstones. They are forms of the mineral known as corundum (chemically:  $\alpha\text{-Al}_2\text{O}_3$ ). White sapphire is the pure  $\text{Al}_2\text{O}_3$  (aluminium oxide) crystal while ruby is the sapphire crystal in which there is the presence of small amounts ( $<0.5\%$ ) of  $\text{Cr}^{3+}$  substituting the Al ions in the lattice giving it an attractive red colour. Similarly, the presence and the combinations of other transition metal ions in the transparent sapphire crystals such as magnesium, copper, titanium and iron leads to green, orange, yellow, pink and blue coloured sapphire crystals [Jayaraman, 2000].

Because of their precious value and limited availability, ruby was the first crystal gemstone for which attempts were made to grow it artificially. The earliest documented efforts are of the French chemist, Marc A. Gaudin who using a torch, fused alumina to prepare small hexagonal pellets of corundum in the period 1837-1840. Similar attempts were made by other scientists but none of them succeeded in obtaining more than microscopic crystals until the end of the century [Harris, 2004]. In the last decade of the 19<sup>th</sup> century, Auguste Verneuil, a professor of applied chemistry at the Museum of Natural History in Paris, started working on a process to develop flame fusion growth of ruby. After a series of improvements the process was finally developed and ready to be able to grow crystals weighing 2-3 grams. These crystals were first presented to the public at the World Fair in Paris in 1900 and subsequently commercial production began using this growth technique which is used to this day and known as the Verneuil growth process. Thus France has been the centre of historical research in the field of synthetic crystal growth and Prof. Verneuil is regarded as “The father of synthetic ruby” [Nassau, 1972].

## 1.2 Sapphire Crystal

Sapphire crystals belongs to the trigonal crystal system but are described using hexagonal crystallographic axes. The crystal structure has been very well explained and visualised in the book entitled ‘Sapphire’ [Pishchik, 2009]. The crystal lattice is composed of  $\text{Al}^{3+}$  and  $\text{O}^{2-}$  ions having ionic radii of 0.57 and 1.40 Å respectively. It takes the form of the closest hexagonal packing of the  $\text{O}^{2-}$  ions with the  $\text{Al}^{3+}$  ions lying in the octahedral sites formed between the closely packed  $\text{O}^{2-}$  ions, filling two-thirds of this site, as shown in figure 1.1. Each octahedral site is surrounded by 6  $\text{O}^{2-}$  ions. The coordination numbers for  $\text{Al}^{3+}$  and  $\text{O}^{2-}$  are 6 and 4, respectively.

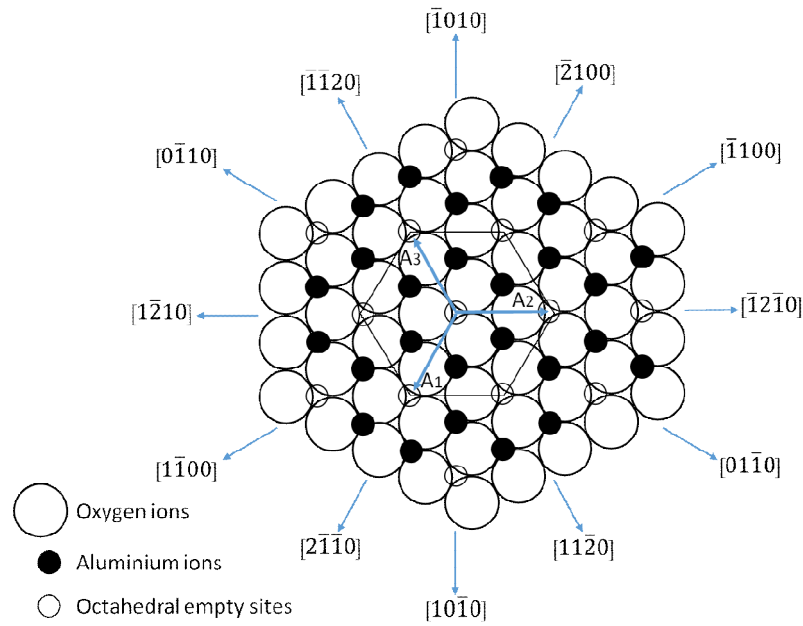


**Figure 1.1:** Schematic arrangement of the  $Al^{3+}$ ,  $O^{2-}$  and octahedral empty sites in the basal plane (C plane).

The three upper  $O^{2-}$  ions in the octahedron are turned by about  $64.3^\circ$  with respect to the three lower  $O^{2-}$  ions and lie in parallel planes at a distance of  $2.164 \text{ \AA}$  from each other. The spatial arrangement of  $O^{2-}$  ions forms the corundum motif in the crystal. The interchanging octahedron positions of  $Al^{3+}$  are replicated in the structure every three layers. The arrangement of the structural units along the C-axis is replicated every  $12.984 \text{ \AA}$ ; i.e the structure is replicated in six  $O^{2-}$  layers and six intermediate  $Al^{3+}$  layers. In the direction of the C-axis, the three Al-O distances are equal to  $1.966 \text{ \AA}$  while the other three are equal to  $1.857 \text{ \AA}$ . The Al-Al and O-O distances are  $2.65$  and  $2.52 \text{ \AA}$ - $2.87 \text{ \AA}$  respectively (figure 1.2).

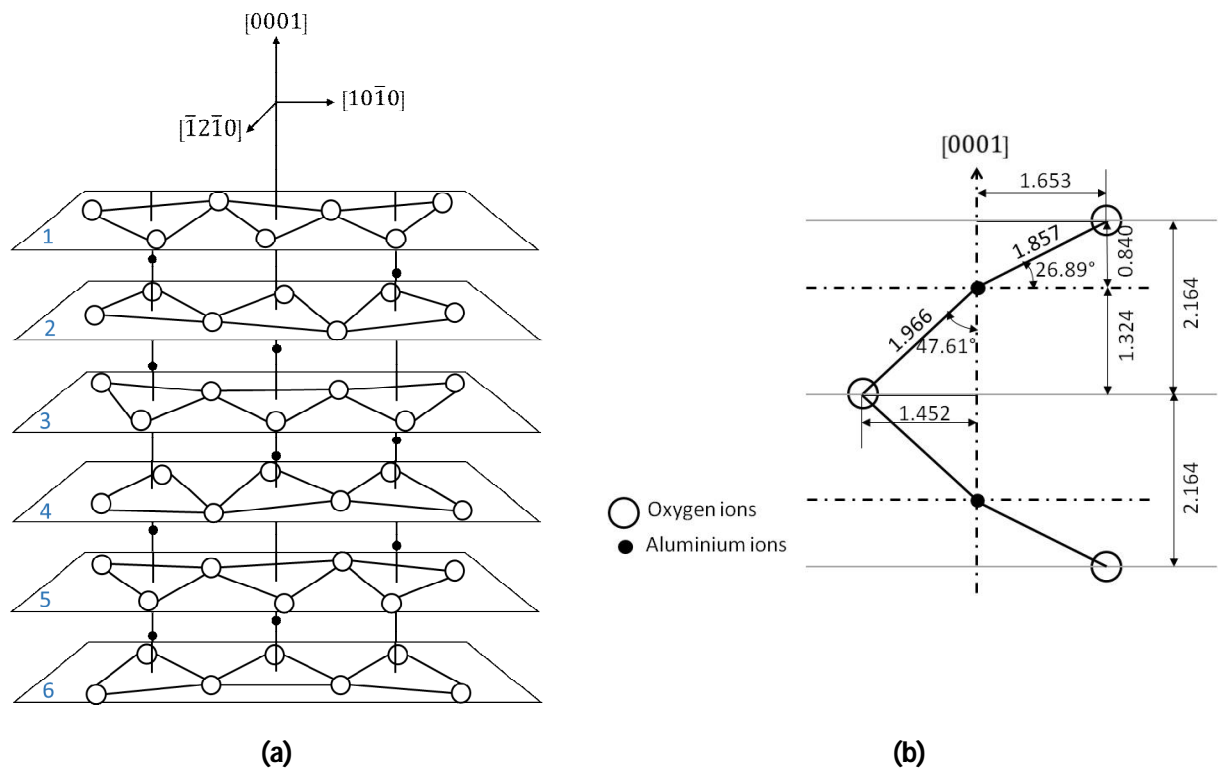


**Figure 1.2:** (a) Schematic arrangement of the  $\text{Al}^{3+}$  ions and  $\text{O}^{2-}$  ions layers along the C-axis. (b) Relative positions of the  $\text{Al}^{3+}$  ions and  $\text{O}^{2-}$  ions.

Sapphire crystals belong to the spatial symmetry group  $R\bar{3}C$  and can be considered to be a slightly distorted close hexagonal packing of oxygen ions. In the crystal lattice of sapphire there are two distinguishable cells – hexagonal (figure 1.3.a) and rhombohedral (figure 1.3.b). The rhombohedral is a primitive unit cell and the hexagonal is a multiple cell with 9 times the volume of the unit rhombohedral cell. The bonding between these two cells is as shown in figure 1.4.

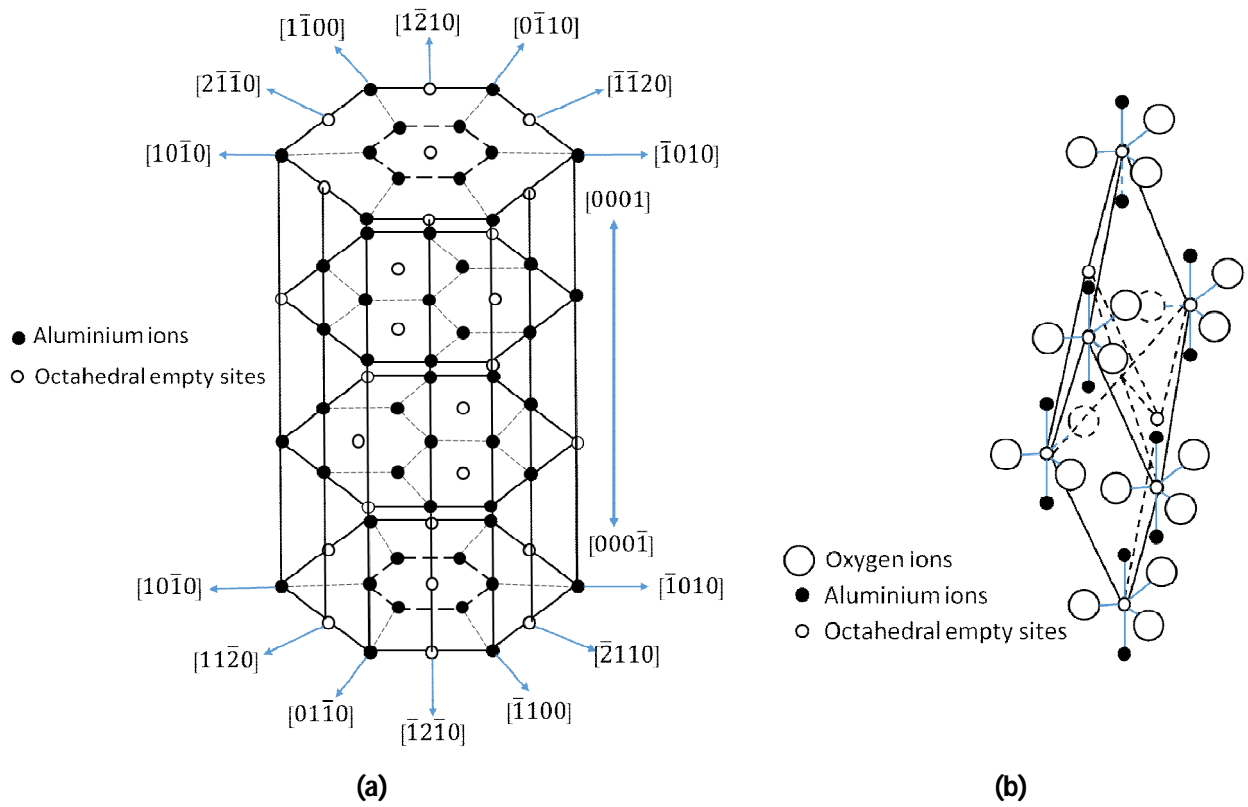


**Figure 1.3: (a) Hexagonal multiple cell. (b) Rhombohedral elementary cell.**

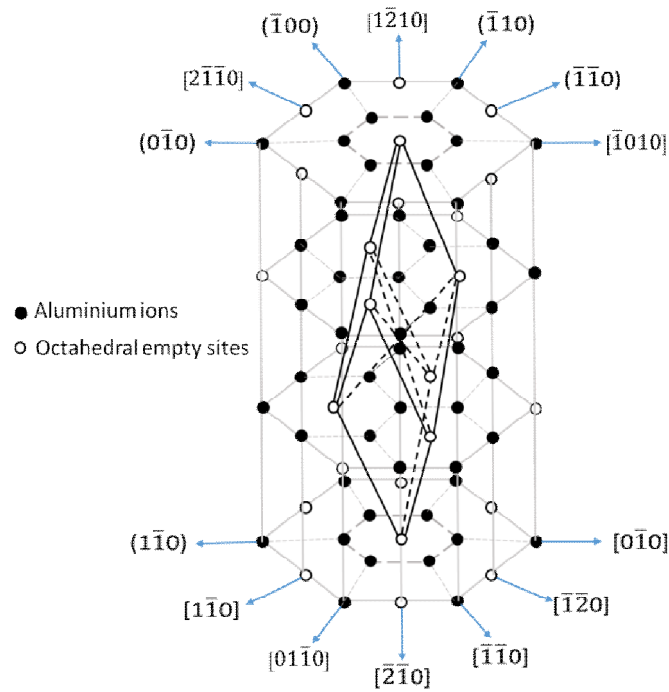


**Figure 1.4: Bonding between the hexagonal and rhombohedral cell.**

The shape of the sapphire crystal is defined by the following facets:  $C\{0001\}$ ,  $A\{11\bar{2}0\}$ ,  $R\{10\bar{1}1\}$ ,  $M\{10\bar{1}0\}$  among others as shown in fig 1.5.

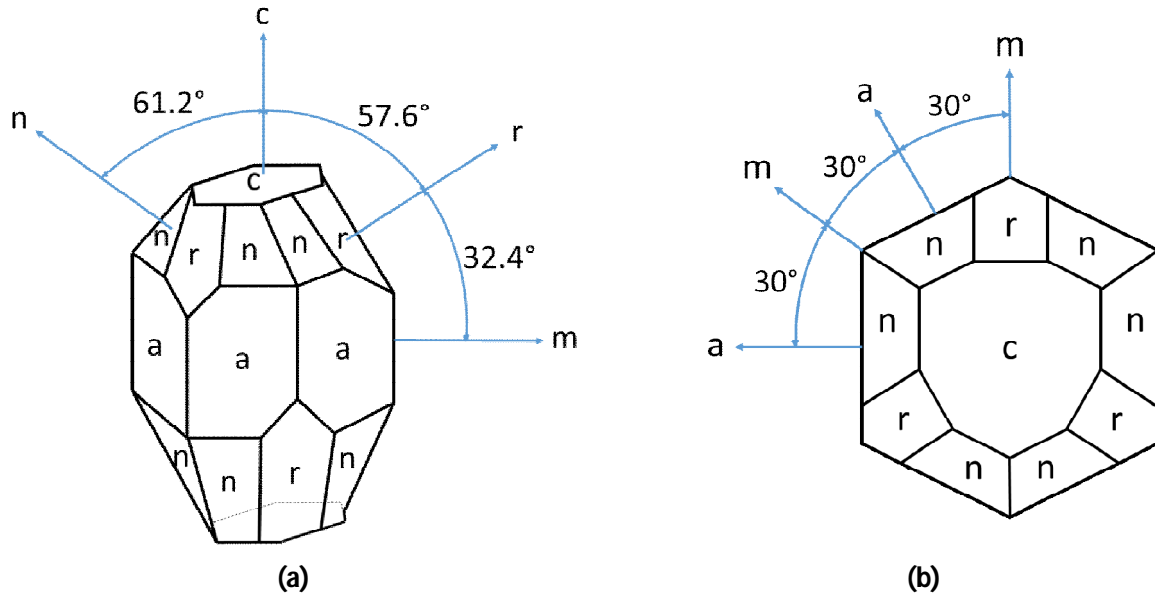


**Figure 1.5:** Crystallographic diagram of Sapphire **(a)** View (slightly shifted) from A-axis and **(b)** view from the C-axis.

The sapphire crystal structure is often described using either the three axis system or the four axis system also known as Miller indices and Miller-Bravais indices respectively. The crystallographic directions and the facets perpendicular to those directions in the C-plane have been described using both indexing system as shown in fig 1.6. The crystallographic directions are denoted using the square brackets and the corresponding planes normal to those directions (facets) are denoted inside rounded brackets. For the four axis systems the crystallographic directions and the corresponding planes normal to those directions have the same denotations. During the course of this work, we will prefer the use of the four axis system.

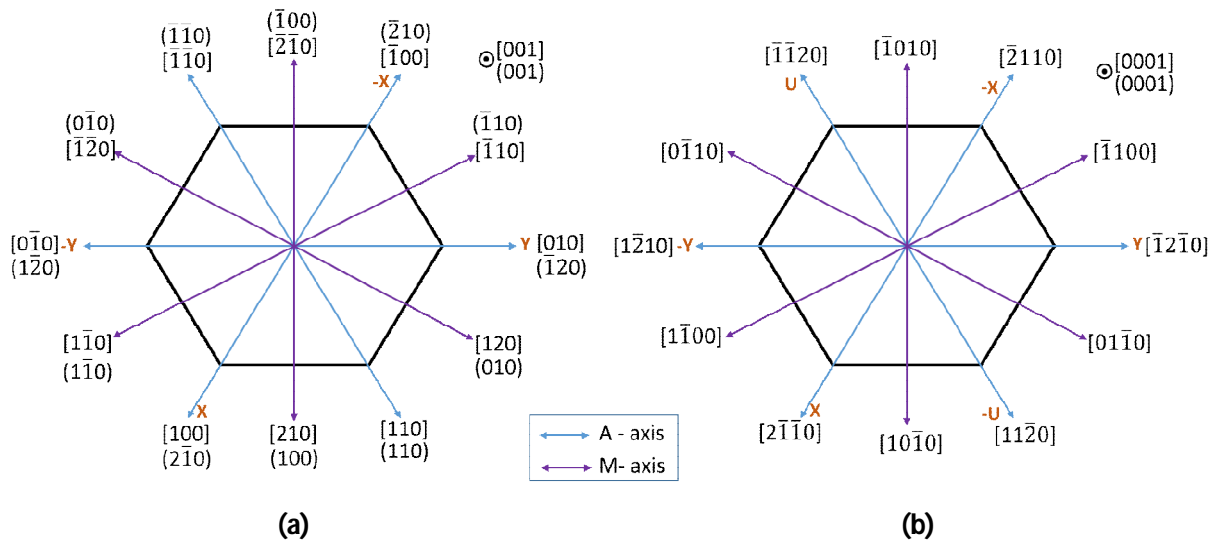


**Figure 1.6:** Indexing in **(a)** three-axis system and **(b)** four axis system.

### 1.3 Laser Applications

The first operation of a laser was demonstrated in 1960 by T.R. Maiman using a crystal of synthetically grown sapphire doped with a small amount of chromium [Maiman, 1960]. Two decades later, in 1982, P.F Moulton demonstrated for the first time a widely tunable laser at the Lincoln Laboratory by incorporating titanium instead of chromium as an impurity into sapphire [P. F. Moulton, 1982] [P. F. Moulton, 1986]. Sapphire is an ideal host crystal in both the  $\text{Cr:Al}_2\text{O}_3$  and the  $\text{Ti:Al}_2\text{O}_3$  lasers, since it is transparent from the ultraviolet to the infrared; also, it is non-hygroscopic and very hard (it has a hardness of 9 on the Mohs scale, compared to 10 for diamond), which is necessary for producing good optical-quality surfaces that are not easily scratched.

In titanium-doped sapphire, the titanium ions substitute for the aluminium ions and (under appropriate growth conditions) exist in only the  $3^+$  charge state. The energy levels of the titanium ions are with a single 3d electron in the outermost shell while the remaining 18 electrons have the filled-shell configuration of a neutral argon atom. When the titanium ions are placed in a host crystal, the electrostatic field of neighbouring atoms, or the crystal field, removes the five-fold angular momentum degeneracy of the single 3d electron. In  $\text{Ti:Al}_2\text{O}_3$  the 3d electron electrostatically interacts with the electronic charges of six surrounding oxygen ions that are positioned at the corners of an octahedron. In three of the five angular momentum states of the 3d electron (designated as the triplet T), the orbitals do not point directly at the neighbouring oxygen atoms; these states have lower energy than the two states in which the orbitals point directly at the oxygen atoms (the doublet designated as E). This difference in energy corresponds to the

energy of a green photon (approximately 500 nm or  $19,000\text{ cm}^{-1}$ ), and absorption of green light causes transitions from the ground state T to the excited state E, as shown in Figure 1.7.

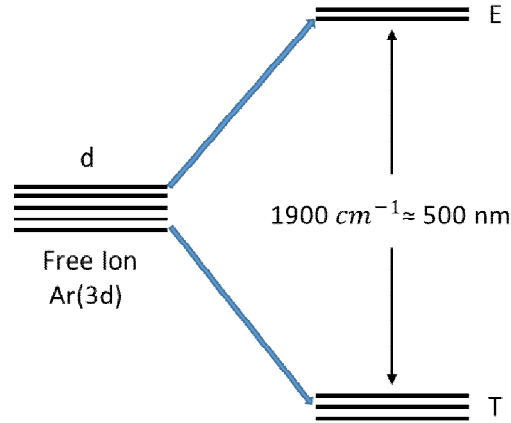


**Figure 1.7:** Simplified energy-level diagram of  $\text{Ti}^{3+}$ . The electronic configuration of the free ion is that of an argon shell plus a single 3d electron. The crystal field of the sapphire lattice removes the fivefold degeneracy of the ground-state level of the free ion to a triplet T ground state and a doublet E excited state [Wall, 1990].

The electronic energy levels of the  $\text{Ti}^{3+}$  ions in  $\text{Ti}:\text{Al}_2\text{O}_3$  are further perturbed by the sapphire host lattice. When the  $\text{Ti}^{3+}$  ion is in the excited state, the overall energy of the system can be lowered if the position of the  $\text{Ti}^{3+}$  ion is displaced with respect to the surrounding oxygen atoms (the Jahn-Teller effect) [Macfarlane, 1968]. This displacement removes the degeneracy of the two excited angular momentum states, which leads to a splitting of the green absorption band. Also, as the  $\text{Ti}^{3+}$  ion moves to its new equilibrium position, it kicks the surrounding lattice and excites vibrations (or phonons); this phenomenon is why the  $\text{Ti}:\text{Al}_2\text{O}_3$  laser is called a vibronic laser.

The coupling of the electronic energy levels of the  $\text{Ti}^{3+}$  ions with the vibrational energy levels of the surrounding sapphire lattice is essential for  $\text{Ti}:\text{Al}_2\text{O}_3$  to operate as a laser. Figure 1.8 shows an energy-level diagram for  $\text{Ti}:\text{Al}_2\text{O}_3$  in which the effects of phonon coupling are included. The abscissa represents the displacement of the  $\text{Ti}^{3+}$  ion. When the  $\text{Ti}^{3+}$  ion either absorbs or emits a photon, the 3d electron rearranges its orbital more quickly than the heavier  $\text{Ti}^{3+}$  nucleus can move. Thus optical transitions are represented as vertical lines in the figure. The Gaussian shaped curves at points A and C in the figure represent the probability of finding the  $\text{Ti}^{3+}$  at a particular position in the lowest vibrational state of the T and E levels, respectively.



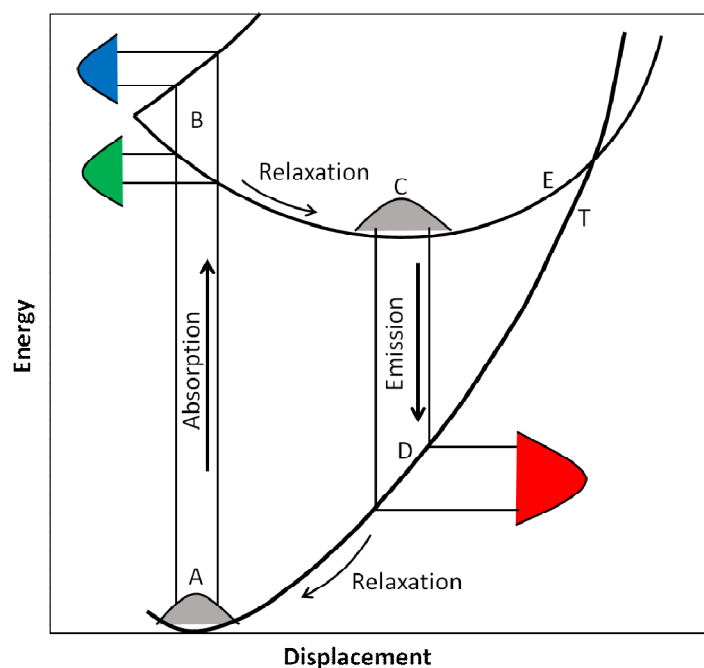


**Figure 1.8:** The  $\text{Ti:Al}_2\text{O}_3$  configurational diagram. The energies of the electronic states are plotted with respect to the displacement of the  $\text{Ti}^{3+}$  ion. Absorption is indicated by the vertical transition from A to B and occurs in the blue and green region of the spectrum as indicated to the left. The emission of light is indicated by the transition from C to D and occurs in the red to infrared region of the spectrum as indicated at the right [Wall, 1990].

Figure 1.8 shows absorption of light as the transition from point A to B. The transition is to either of the Jahn-Teller split upper states, and it results in a broad blue-green absorption, as shown in Figure 1.9. The Jahn-Teller splitting is not totally resolved and is manifested as a main peak with a shoulder. At point B in Figure 1.8 the ion displaces itself and lowers its energy by emitting phonons. The transition from point C to point D shows the emission of light. Again the ion relaxes quickly to the ground state by emitting phonons. Two important results can be noted. First, the emission of light following the absorption of green light is at a longer wavelength (red, or Stokes shifted). A population inversion in the red emission band, necessary for amplification, is more easily achieved because the emission terminates on high vibrational levels of the ground state, which are unpopulated because of the fast vibrational relaxation rate. Second, a large emission bandwidth (and therefore broad tunability), as shown in Figure 1.9, results because the spread in probability of the  $\text{Ti}^{3+}$  ion position at the bottom of the E potential can connect via vertical transitions to a large spread of vibrational levels of the T potential.

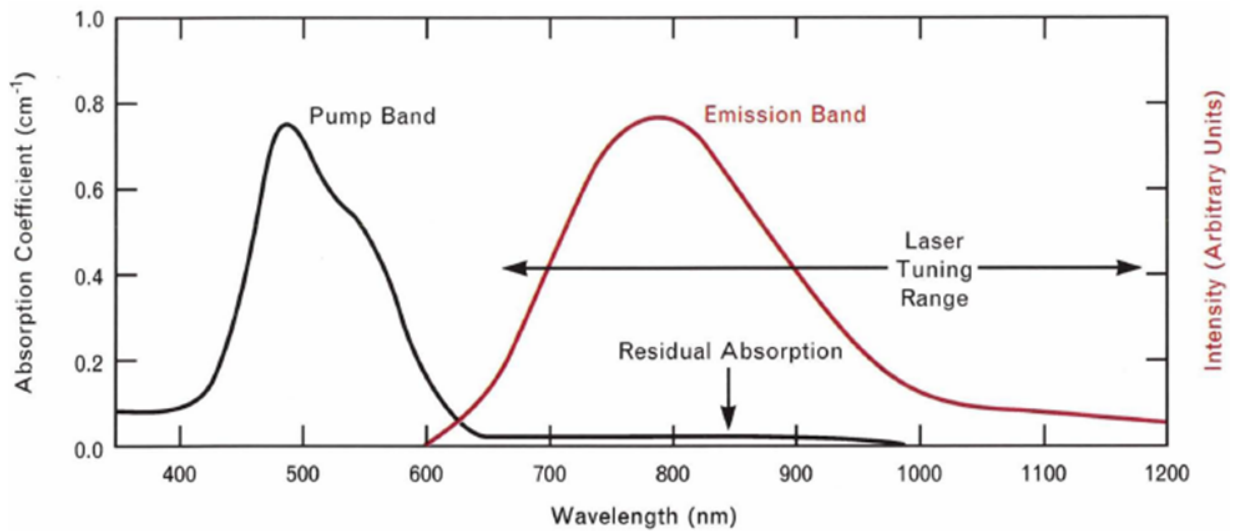


**Figure 1.9:** The emission and absorption bands of  $\text{Ti:Al}_2\text{O}_3$ . The absorption band, which peaks near 490 nm, occurs in the blue-green region of the spectrum and allows  $\text{Ti:Al}_2\text{O}_3$  to be pumped by argon-ion lasers, frequency-doubled Nd:YAG lasers, copper-vapour lasers, or flashlamps. The emission band peaks near 790 nm. A weak absorption band that overlaps the emission band is known as the residual absorption [Wall, 1990].

The width of the emission bandwidth depends on the details of the potential curves. A final desirable feature that the  $\text{Ti}^{3+}$  energy levels exhibit is that further excited levels of the 3d electron lie far above the E levels. The  $\text{Ti}^{3+}$  ion exhibits no excited-state absorption (ESA); higher energy levels are far removed so that green light (pump photons) or red light (laser photons) cannot cause transitions from the E level to higher levels. The situation with other 3d transition metal ion lasers is more complex and ESA is present to some degree.

The various lifetimes of the energy levels of a laser strongly influence laser operation by determining the dynamics of the population inversion. In a four-level laser the lower laser level must quickly relax to the ground state; otherwise a bottleneck occurs and the signal gain disappears. The spontaneous lifetime of the population in the upper laser level (the time in which  $1/e$  of the population in the upper laser level decays to the lower laser level in the absence of a signal) is denoted by  $\tau$ . This quantity determines the available time for the pump to create and store a population inversion. For  $\text{Ti:Al}_2\text{O}_3$  at room temperature  $\tau$  is 3.2  $\mu\text{sec}$ . For comparison,  $\tau$  is 230  $\mu\text{sec}$  for Nd:YAG and 3 msec for ruby.

Another important parameter in the design and operation of a laser is the stimulated emission cross section (or gain cross section). This cross section, denoted as  $\sigma$  and measured in units of area, determines how many transitions from the upper to lower level are caused by a particular flux of photons. The gain per

unit length of an amplifier is given by  $N\sigma$ , where  $N$  is the population inversion density. For a high-gain amplifier and a low-threshold oscillator, a large value of  $\sigma$  is desirable.  $\sigma$  can be estimated for a material before laser-quality crystals are grown by performing spectroscopic measurements of the fluorescence profile  $\Delta f$  and the fluorescence lifetime  $\tau$ . The emission cross section is given by:

$$\sigma = \frac{3}{4\pi^2} \cdot \frac{\lambda^2}{n^2 \tau \Delta f}$$

Where,  $\lambda$  is the peak of the fluorescence curve,  $n$  is the index of refraction, and  $\Delta f$  is the width (full width at half maximum) of the fluorescence curve in frequency. From various-signal gain measurements in a Ti:Al<sub>2</sub>O<sub>3</sub> amplifier, the value of  $\sigma$  has been determined to be  $3.0 \cdot 10^{-19} \text{ cm}^2$  [Peter F. Moulton, 1987].

The broad absorption band of Ti:Al<sub>2</sub>O<sub>3</sub> allows it to be pumped by a variety of methods. Since the peak of the absorption is in the blue-green region of the spectrum, argon-ion lasers (which have strong laser lines at both 515 nm and 488 nm) can be used to pump continuous-wave Ti:Al<sub>2</sub>O<sub>3</sub> lasers. Frequency-doubled Nd:YAG lasers, which emit in the green (532 nm), and copper-vapour lasers, which emit in the green (510 nm) and yellow (578 nm), can be used as efficient pumps for pulsed Ti:Al<sub>2</sub>O<sub>3</sub> lasers. Flashlamp pumping of Ti:Al<sub>2</sub>O<sub>3</sub> and direct diode pumping of Ti:Al<sub>2</sub>O<sub>3</sub> have also been demonstrated and appear promising in the near future.[Wall, 1990]

Thus a Ti:Al<sub>2</sub>O<sub>3</sub> laser has the broadest emission bandwidth of any laser gain material, spanning 680–1100 nm with some component in the visible range. This wide emission bandwidth gives rise to one of the distinguishing features of Ti:Al<sub>2</sub>O<sub>3</sub> lasers: the ability to compress the laser pulses to recently achieved ultrashort length of less than 10 fs ( $10^{-14}$  sec), and thus extremely high peak power. This makes it the prime laser gain medium for ultrafast, ultrahigh powerful laser systems. This dramatic rise in peak powers for lasers in recent years has given rise to renewed interest in light-matter interactions at extreme intensities. Interesting scientific results have been achieved with these lasers in the fields of high order harmonic and short pulse X-ray generations, high density plasmas, relativistic acceleration, relativistic non-linear optics, time resolved X-ray diffraction with unprecedented time resolution and others. Potential future applications include compact generators of protons for proton cancer therapy [Joyce, 2010].

Currently, there are laboratories around the world that are constructing compact, solid state lasers capable of reaching petawatt (PW) levels and beyond. To reach from TW to PW peak power the pulse energies have to be scaled from mJ to J levels. Since Ti:Al<sub>2</sub>O<sub>3</sub> has a saturation fluence of  $\sim 1 \text{ J/cm}^2$ , this scale-up in laser power is directly tied to the scale-up in Ti:Al<sub>2</sub>O<sub>3</sub> amplifier area. As an example, a 1PW laser pulse of 30 fs

duration requires pulse energy of 30 J, necessitating a 30 cm<sup>2</sup> area of gain medium. Taking into account beam clipping considerations, it dictates the need for a Ti:Al<sub>2</sub>O<sub>3</sub> crystal of the order of 100 mm diameter. Thus, large aperture Ti:Al<sub>2</sub>O<sub>3</sub> amplifiers are a key requirement for the new PW class of ultrafast, ultrapowerful lasers.

Petawatt (PW) scale laser operations were first demonstrated in 1996 at Lawrence Livermore National Laboratory (LLNL) using three large Ti:Al<sub>2</sub>O<sub>3</sub> amplifiers of 85 mm to 100 mm diameters. Another system that approached PW scale operation is the JAERI (Japan Atomic Energy Research Institute) system, which achieved a peak power of 0.85 PW in a 33 fs pulse. Later, the Hercules laser system at the University of Michigan reached 0.3 PW peak power operation using a 110 mm diameter Ti:Al<sub>2</sub>O<sub>3</sub> crystal. Another femtosecond petawatt class laser system was developed as a laser driver of the future LASERIX, a new X-ray laser facility of the University of Paris-Sud. The power amplification is based on a 100 mm diameter, 20 mm thick highly doped Ti:Al<sub>2</sub>O<sub>3</sub> crystal and the aim is to achieve peak powers in the range of 0.4 PW [Joyce, 2010].

The success of these near-PW scale lasers has led to an interest in scaling to even higher power laser systems. Next in line is the construction of a single beam line of up to 25 PW constructed by the Institute de la Lumiere Extreme (ILE) and funded through the French State-Region Project Contract (CPER). This system will have three power amplifier stages based on Ti:Al<sub>2</sub>O<sub>3</sub> amplifiers, delivering 600 J of energy. In order to achieve this level of power, Ti:Al<sub>2</sub>O<sub>3</sub> amplifiers 20 cm diameter or larger will be required. The most ambitious system is the proposed 230 PW European Extreme Light Infrastructure, which has the goal of providing the worldwide scientific community a unique laser-based facility allowing investigations in laser-matter interactions at 10<sup>25</sup> W/cm<sup>2</sup> and beyond.

The growth of such large diameter Ti:Al<sub>2</sub>O<sub>3</sub> boules (more than 20 cm diameter) is technically challenging. The first challenge is the design and manufacture of a growth system capable of growing crystals with the required dimensions which is scalable and reproducible. This is to be followed by a detailed characterisation of the defects in the crystals produced and later addressing the growth system again to get rid of these defects.

## 1.4 Growth techniques

Bulk crystal growth, and specifically the growth of single crystals, has been one of the most important modern technologies for the manufacture of many high-tech products for electronics, photonics, communication systems, renewable energy technologies, etc. Sapphire crystals have a unique combination of chemical, mechanical, electrical and optical properties which makes them candidates for a wide range of

product applications. Thus, there has been a particular interest in sapphire crystal growth and commercial production of sapphire is more than a century old [Harris, 2004]. The growth method utilized for sapphire synthesis greatly impacts the quality of crystal produced and hence it is important to make a choice regarding the growth technique based on the required application.

Crystal growth techniques are classified based on the nature of the phase transition involved during the growth process [Pamplin, 1977]. But it is important to remember that a classification by the type of phase transition (from the vapour phase, solution, melt, or solid phase) is somewhat arbitrary, as the process of crystal formation often proceeds through several phases. Sapphire can be grown from the gaseous, liquid, and solid phases and the logic to choose the most suitable method is based on the physical–chemical evolutions of the growth processes, the peculiarities of a particular method, the crystal quality and size required with respect to the applications and the costs involved [Pishchik, 2009].

### **1.5 Crystallisation from the Gaseous (Vapour) Phase**

Crystallisation from the gaseous (vapour) phase can be through physical and chemical transformations.

The physical transformation methods are based on the effect of condensation, and include the sublimation method and the molecular beam method. Crystallisation from vapour is especially suitable for those substances in which a solid–gas transition is not realized via the liquid phase. The sublimation method is used for crystal growth in closed and open systems in vacuum or in a gas medium, with crystallisation often carried out in sealed ampoules. In such cases, the initial material is placed in one part of an ampoule. Both parts of the ampoule are heated to the same temperature, and the pressure of the saturated vapour corresponding to such a temperature is set. Then one part of the ampoule is cooled until crystal nuclei arise. Afterward, the temperature is raised again to prevent the formation of new nuclei, and the process of crystal growth proceeds under constant conditions.

During the growth of crystals by chemical reaction methods (reduction, thermal decomposition, oxidation, etc.), the gaseous phase composition differs from that of the growing crystal. A solid or liquid substance interacts with a gaseous transporter by a reversible reaction and decomposes with subsequent precipitation of a crystalline substance after being transported to another part of the system where equilibrium conditions change. The common feature of these methods is the transport of material from the source to the place of crystallisation, since the concentration of the crystallised material in the medium is low [Schaffer, 1965].

From the gaseous phase, plate-like crystals, whiskers, and epitaxial films can be grown. Crystallisation from the gaseous phase has a number of advantages, such as low process temperatures, inessential supersaturation, easy control of the composition, weak interaction between the container and the crystallized material, and high perfection of the crystals. However, the size of the crystals grown is not large. The largest sapphire crystals reported to be grown from the gaseous phase are with a mass of up to 150 g [Pishchik, 2009].

## 1.6 Crystallisation from Solution

Crystals can be grown from a liquid solution onto a seed, by achieving supersaturation without spontaneous formation of nuclei in the solution. Supersaturation permits growth rates that provide controlled crystallisation onto the seed.

The hydrothermal solution method has been demonstrated to be successful in growing crystals of sapphire and ruby from solutions of  $K_2CO_3$  and  $Na_2CO_3$ . Recently,  $Ti:Al_2O_3$  laser crystals have been grown from a solution of  $TiCl_3$  and HCl using this technique and characterised [B. Wang, 2009]. This method involves establishing conditions that make it possible to dissolve the substance to be crystallised, to provide the required supersaturation of the solution, and then its crystallisation. It is achieved by controlling the parameters of supersaturation in the system by changing the parameters of temperature, pressure, type, and concentration of the mineralizer and the temperature gradient between the zones of dissolution and growth. The temperature gradient method in which the temperature is controlled at the crystal growth zone to create supersaturation has been used to grow rubies and other single crystals.

Another method of crystallisation from solution is the flux method. The crystallisation process takes place in a crucible via gradual cooling of a melt saturated with the components of the growing crystals, under isothermal conditions upon evaporation of the melt, or by the temperature gradient method. The mechanisms of diffusion and convection are responsible for the transport of the material to the crystallisation front. Rubies weighing up to 100 g have been grown from solution in a lithium molybdate melt using this method.

Methods of growth from the solution have a number of significant advantages such as relatively low crystallisation temperatures and the possibility of obtaining crystals unstable at their melting point. Crystals of higher perfection can be grown from the solution by carrying out sequential growth cycles. But the growth rates using these methods are very slow ( $<1\text{mm/day}$ ) and the process itself is complicated. Hence crystallisation techniques from solution have not been implemented for industrial growth of large scale crystals [Pishchik, 2009].

## 1.7 Solid-Phase Crystal Growth

Solid phase crystal growth is the transformation of fine-grained polycrystals into a single crystal. This process is realized when one crystal grain absorbs the others and it grows at the expense of the polycrystalline matrix. The crystal surface captures free atoms and molecules from the adjacent layers of the matrix where all the atoms occupy certain positions and grows owing to the motion of the grain boundaries. The driving force of such a motion is the decrease of free surface energy due to diminution of the surface itself.

Sapphire is grown by this method, by fixing fine-grained  $\text{Al}_2\text{O}_3$  powder around an ingot made of the same material. Then the ingot is sintered or the powder is melted in a gradient furnace where the process is accompanied by the growth of a grain. Sapphire crystals of  $1\text{cm}^3$  size were grown by this method. These crystals have shown a distribution of defects such as pore channels and aggregates of impurities.

Crystals grown by this method have the advantage that it is possible to synthesise crystals at a temperature lower than their melting temperature and the shape of the growing crystal can be preset. But the large concentration of defects and the limited size of crystals obtained have hindered this process from being accepted for industrial growth of large crystals [Pishchik, 2009].

## 1.8 Melt growth techniques

The methods of growing sapphire crystals from the melt are most popular, since they allow the production of large-size crystals at high growth rates. The transition of phase from melt to crystal is the simplest and best controlled process and hence it has been accepted as the basis for modern methods of commercial sapphire production. All methods of high temperature growth from the melt are suitable for sapphire production, but each of these methods has its advantages and disadvantages depending on the application and required finished product form factor. These techniques are broadly classified into growth without a crucible and those using a crucible for the melt.

### 1.8.1 Crystal Growth from the Melt Not Using Crucibles

#### 1.8.1.1 Verneuil Method

The Verneuil method (abbreviated to VT), which is also called as the flame-fusion method is the first industrial crystal growth technology. A scheme of the growth system is represented in figure 1.10 (a).

The crystals are grown in a shaft furnace from finely-dispersed  $\text{Al}_2\text{O}_3$  powder (particle size 2-100  $\mu\text{m}$ ) falling through a bin, that is fed through a flame of hydrogen-oxygen gas onto a ceramic crystal holder inserted at the bottom of the shaft. Flying through the flame, alumina particles melt and hit the face of the crystal

holder upon which a crystal seed is fixed. The top of the forming crystal cone melts and then grows until a preset diameter is obtained. The crystal grows further from the melt film, whose thickness is defined by the crystal diameter and the thermal conditions at the crystallisation front. Since the seed is lowered slowly, the melt film crystallizes at the required rate, being continuously replenished from above by the droplets melted in the flame. If the consumption of the charge and of hydrogen and oxygen is coordinated along with the rate at which the seed is lowered, the film thickness is kept practically constant and its position in the furnace remains unchanged. The standard crystals obtained by this technique have a diameter of 15 – 25 mm and are 50 – 100 mm in length grown at a rate of 10 – 15 mm/hr [Pishchik, 2009] [Tatartchenko, 2005].  $\text{Ti:Al}_2\text{O}_3$  crystals have been grown by this technique at RSA Le Rubis with dimensions of 40mm in diameter and 130 mm in length as shown in figure 1.10 (b) [G. Alombert-Goget, 2016 -a].

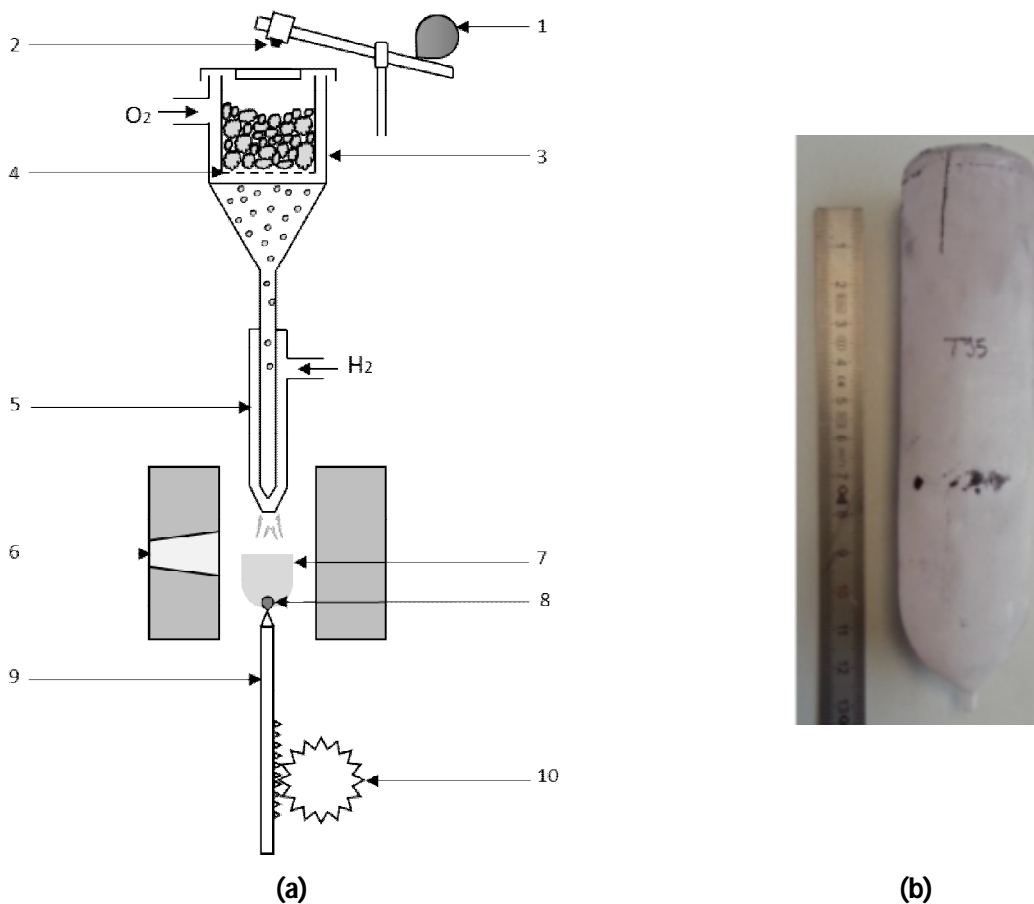


**Figure 1.10:** (a) Scheme for a using this technique Verneuil growth system: (1) shaking mechanism; (2) hammer; (3) bin; (4) vessel with perforated bottom; (5) two nozzle burner; (6) observation window; (7) growing crystal; (8) seed; (9) refractory crystal holder; (10) mechanism for lowering crystal. (b) Ti doped sapphire crystal grown at RSA Le Rubis [G. Alombert-Goget, 2016-a].



The main advantages of this growth technique are:

- Since there is no container, it eliminates problems of physico-chemical interaction between the melt and the container material. Additionally, it also reduces the problems of residual stress resulting from the elastic effect of container walls.
- Crystallisation takes place in an open muffle and hence it is possible to control the oxidation-reduction potential of the crystallisation process by varying the  $H_2/O_2$  ratio in the flame.
- It is possible to grow crystals with controlled doping gradients.
- It is a technically simple process, inexpensive and the growth of crystals can be observed by the controller.

The disadvantages of this technique are:

- A lot of impurities can enter the melt from the working gases, furnace ceramics and the surrounding air.
- High temperature gradients develop in the crystallisation zone (30 – 100 K/mm) which cause high internal stresses in the crystals (10 – 15 kg/mm<sup>2</sup>) and hence lead to high dislocation densities [Chernov, 1984].

Hence, the Verneuil method is very cost effective method to produce sapphire crystals, but the limitations in the diameter of the crystals and the occurrence of various defects due to stress and impurities do not encourage using it for growth of high optical grade crystals. Verneuil sapphire is suitable for production of relatively small diameter articles used in jewellery, wristwatch glasses and precision instruments and as a starting material for other growth processes [Akselrod, 2012].

#### **1.8.1.2 Zone Melting Method**

The zone melting method involves successive fusing of a feedstock ingot. It was a method originally considered for purification of materials. However, zone melting was also adapted for crystal growth since in the process of purification, single crystals are often formed. The two basic configurations for this method are Horizontal zone melting and the Floating zone method, also known as the Vertical zone method represented in the diagram in figure 1.11 (a) and (b) respectively.

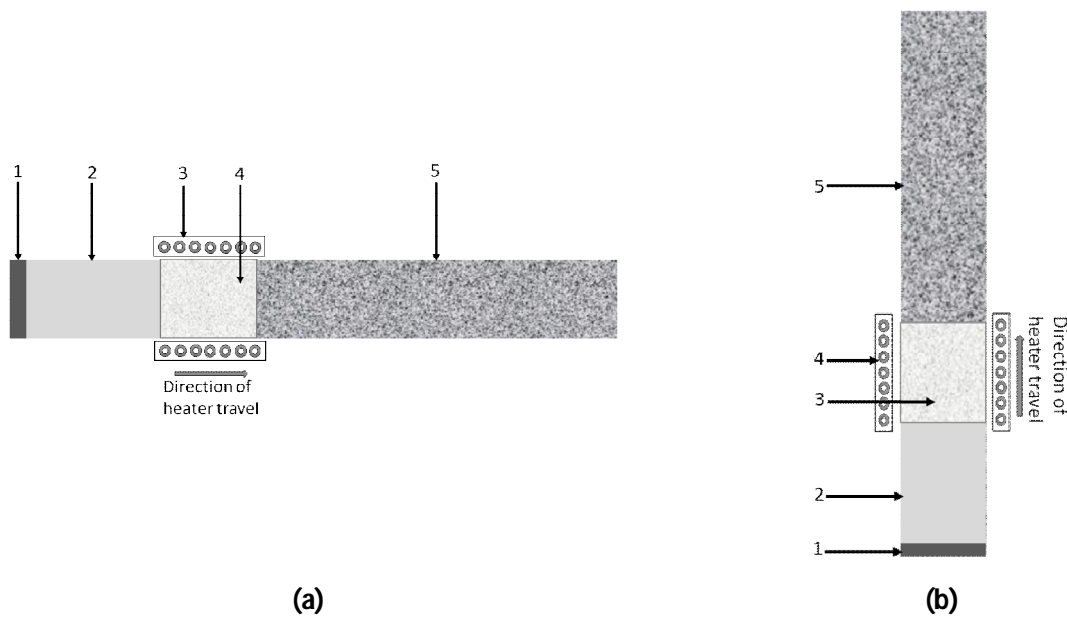


**Figure 1.11:** Diagram of zone melting configurations: **(a)** horizontal and **(b)** floating; (1) seed; (2) crystallized zone; (3) heater; (4) melt zone; (5) raw material feed.

For the horizontal zone melting method, the seed is placed at one end of the polycrystalline ingot aligned horizontally and a melting zone is created at this end. Then this melting zone is shifted towards the other end thus completing the growth of a single crystal. In the floating zone method the melted zone is confined by surface tension in samples placed vertically. This melted zone moves along the rod upward or downward, thus forming a single crystal. Between these two methods, vertical displacement is more convenient in crystallisation without a container because the melt does not spill out from the zone and is self-sustained due to its surface tension. Radio frequency current direct heating is the most common melting technique used but the low electrical conductivity of sapphire even at high temperatures requires very high frequency and preliminary heating to achieve melting. Hence, many unusual heat sources such as plasma heating, electron beam heating, resistance heating and radiation heating have been used [Tatartchenko, 2005] [Pishchik, 2009].

The advantages of zone melting are that the multiple recrystallisation of the specimen allows chemical purification and reduces the disturbance in the stoichiometry by keeping the width of the melt zone to a minimum. Thus it is possible to create precision clean crystallisation using this method, but the complexities related to sapphire growth in particular and its inability to grow crystals of greater diameters do not make it suitable for growth of massive sapphire crystals [Chernov, 1984].

## 1.8.2 Methods of Crystal Growth from the Melt in Crucible

### 1.8.2.1 Shaped crystal growth

Modern engineering applications often require crystals in the form of plates, rods, tubes or other complicated shapes. The shaped crystal growth technique, as the name suggests, allows growth of crystals of specified size and shape with controlled defect and impurity structure that allows them to be used as the final products, with minimal or no additional machining. There are various forms of shaped crystal growth, such as the Stepanov technique, EFG (edge-defined film fed growth), CAST (capillary-action shaping technique), the inverted Stepanov technique,  $\mu$ -PD (micropulling-down) method etc. The main principle in all these techniques is to limit the area and the magnitude of liquid-free surface perturbations, using two possibilities for shaping; either the edges or walls of a shaper [Tatartchenko, 2005].

The schematic diagram for an EFG growth process used to produce sheets of sapphire crystal is represented in figure 1.12(a) and figure 1.12(b) shows sheets produced by the EFG furnace at RSA Le Rubis in Grenoble. In this technique, the raw feed alumina, molten in a crucible, rises through a capillary channel and solidifies at the top of this channel, which gives its outer shape to the pulled crystal. The maximum height of the melt rise in the capillaries above the level of the melt in the crucible is determined by the melt viscosity, the wetting angle of the melt on the die material and the diameter of the capillary. There are only two control parameters in this technique: the pulling rate of the crystal and the upper die temperature which controls the height of liquid meniscus that separates the crystal from the die top [Carroz, 2015] [Akselrod, 2012].

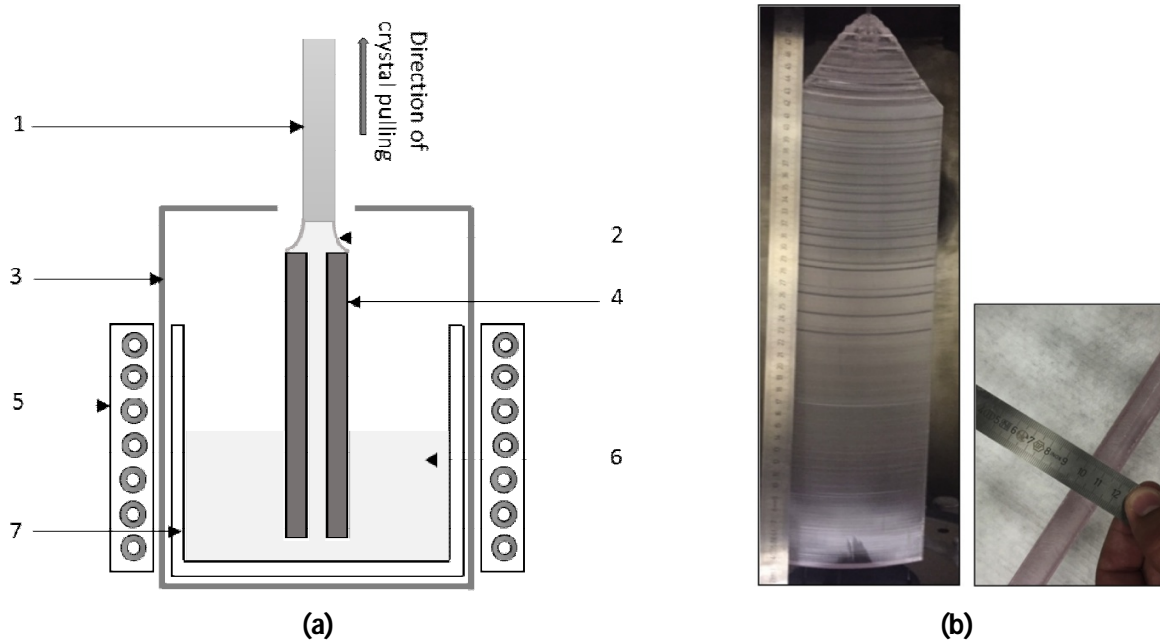


**Figure 1.12: (a)** Schematic diagram for the EFG growth process. (1) Grown crystal, (2) meniscus, (3) thermal insulation, (4) shaping die, (5) heating arrangement, (6) molten liquid, (7) crucible. **(b)** EFG sapphire plates, 1.6 cm thick, 10 cm wide and 48 cm long grown at RSA Le Rubis, Grenoble using an EFG furnace [Stelian, 2017-b].

The  $\mu$ -PD (micropulling-down) method is an important technique for growth of high quality single crystal fibres. The process consists of pulling a crystal under a capillary channel placed at the bottom of a crucible as shown in figure 1.13 (a). The hanging meniscus in this system leads to a very stable capillary due to the combination of die anchoring with a positive gravity effect; and good liquid homogeneity because of strong Marangoni convection. This results in a more uniform distribution of dopants or solutes in the crystal than in the case of methods involving pulling upward, such as the EFG technique. These characteristics have led to the application of these technique to grow  $\text{Ti:Al}_2\text{O}_3$  optical single crystal fibers for laser applications [A Nehari, 2014] [D. Zhou, 2015]. The crystals obtained by this technique have a diameter of 0.5 mm -1 mm and lengths up to 500 mm as shown in figure 1.13 (b).

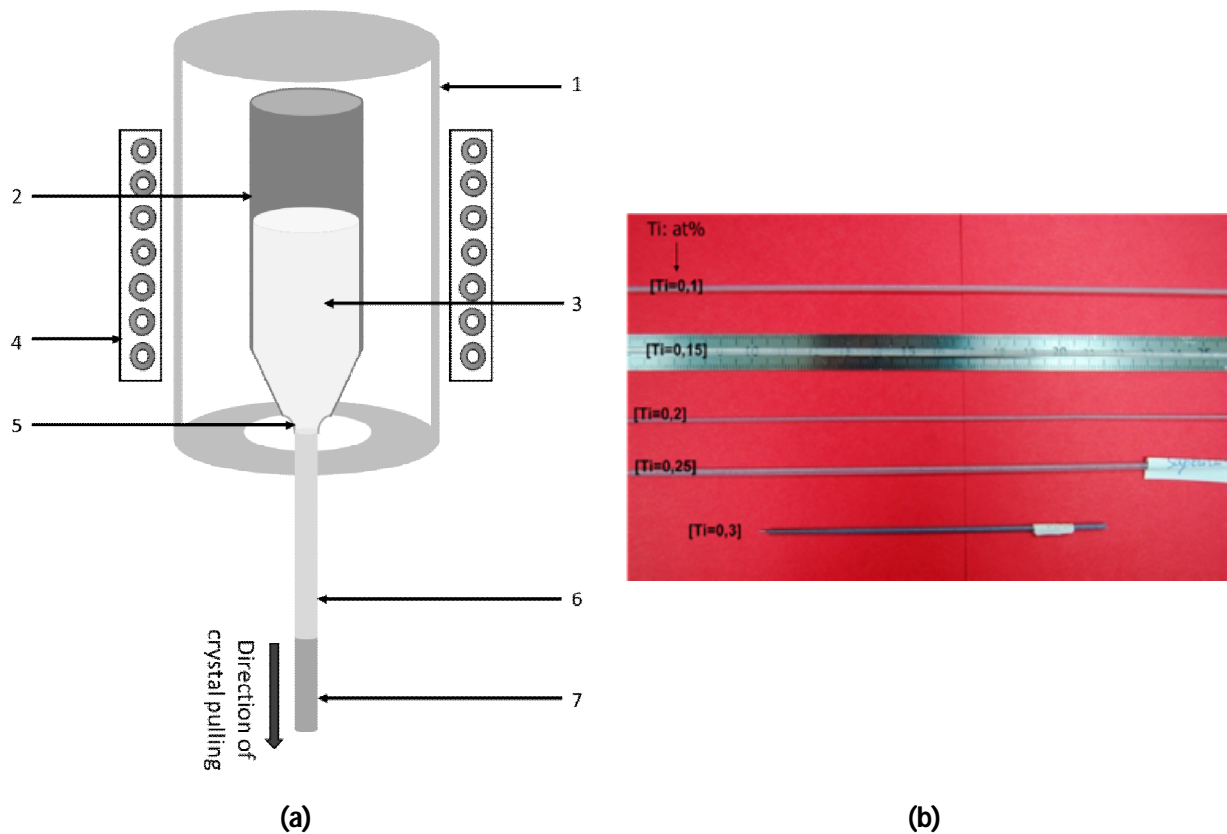


**Figure 1.13: (a)** Schematic diagram for the  $\mu$ -PD growth process. (1) Thermal insulation, (2) crucible, (3) melt, (4) heating arrangement, (5) meniscus, (6) grown crystal, (7) seed. **(b)** Ti:Al<sub>2</sub>O<sub>3</sub> single crystal fibres with varying Ti concentrations [A Nehari, 2014].

Thus, various techniques of shaped crystal growth are applicable for specialized needs of sapphire crystals and using the  $\mu$ -PD (micropulling-down) method, optical grade crystals for laser applications have been grown and they have been characterised. But, it is applicable for only thin diameter, fibre-shaped crystals and not massive crystal dimensions.

#### 1.8.2.2 Directed Crystallisation Methods

The essence of all directed crystallisation methods is that the process of crystallisation takes place in a temperature gradient field, with the entire volume of the melt placed in a container being crystallised. The method is technically simple, and crystals of a preassigned diameter are produced by selecting the appropriate container. Based on this principle, various methods have been developed depending on whether the container is moved through a melting zone or the temperature is reduced gradually at a constant temperature gradient and if the crystallisation takes place in the vertical or horizontal direction [Chernov, 1984].

The Bridgman-Stockbarger technique, also referred to as the Tammann or Obreimov-Shubnikov method based on those responsible for developing it, involves the vertical displacement of the container holding the melt through a temperature gradient in the furnace. When the container is displaced inside the crystallisation chamber, two zones of different temperature are created. This permits combination of the crystal growth process with annealing. A schematic representation of the technique is provided in figure 1.14.

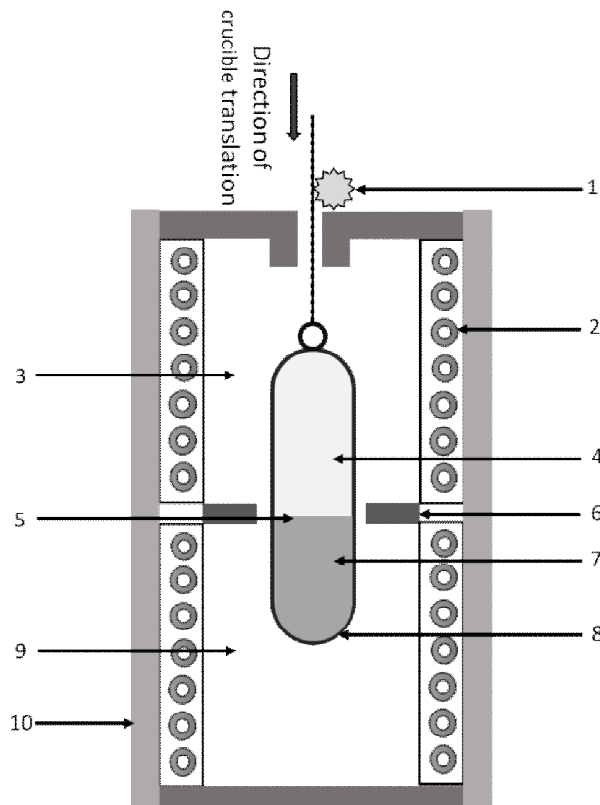


**Figure 1.14:** Schematic diagram for the Bridgman-Stockbarger growth process. (1) Crucible translation mechanism, (2) heating arrangement, (3) hot zone (temperature greater than melting point), (4) melt, (5) crystallisation front, (6) insulation, (7) growing crystal, (8) crucible, (9) cold zone (temperature lower than melting point), (10) thermal insulation.

The horizontal modification of the above method, as represented in figure 1.15 (a), was proposed by Bagdasarov in the 1960's for the growth of sapphire crystals which successfully combines the elements of directed crystallisation with zone melting and hence is known as the Bagdasarov method, horizontal directional crystallisation (HDC) or horizontal Bridgman method. In this technique, the material is melted within the melt zone created between the seed crystal and the polycrystalline aggregate held in a boat-

shaped container. During the process of crystal growth, this zone slowly moves along the container containing the raw material. This method has the advantage that the crystallisation is carried out under conditions facilitating the evaporation of extraneous impurities. The main idea of this technique is to produce single crystal sapphire plates of a large surface area for specialized applications, as shown in figure 1.15 (b) [Tatartchenko, 2005] [Pishchik, 2009].

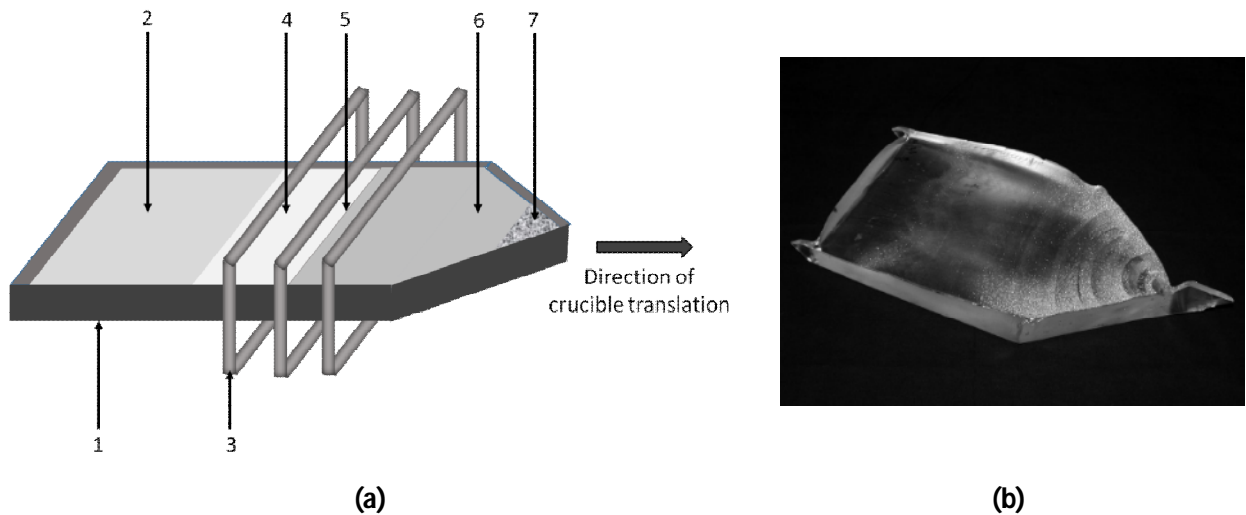


**Figure 1.15: (a)** Schematic diagram for the Bagdasarov growth process. (1) Crucible, (2) polycrystalline material (3) heating arrangement, (4) melt zone, (5) crystallisation front, (6) growing crystal, (7) seed. **(b)** Sapphire plate with dimensions of  $250 \times 170 \times 25 \text{ mm}^3$  grown by the Bagdasarov method [Harris, 2009].

The temperature gradient technique (TGT) is a further modification of the vertical Bridgman technique. As represented by the diagram in figure 1.16 (a), the TGT technique consists of a cylindrical crucible, tapered at the bottom, placed inside a furnace heated by means of resistance heating elements. A vertical temperature gradient is imposed on the crucible by the heating elements and the cylinder is cooled from the bottom by the flow of water, where the crystallisation process starts and progresses towards the top of the crucible.  $\text{Ti:Al}_2\text{O}_3$  crystals weighing 3.5 kg and measuring 140mm in diameter have been grown by this method and characterised for impurities and optical properties as shown in figure 1.16 (b) [Y. Zhou, 1992] [Jianwei, 1998] [G. Zhou, 2006].

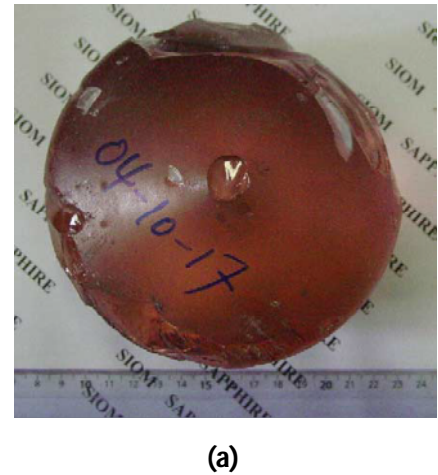
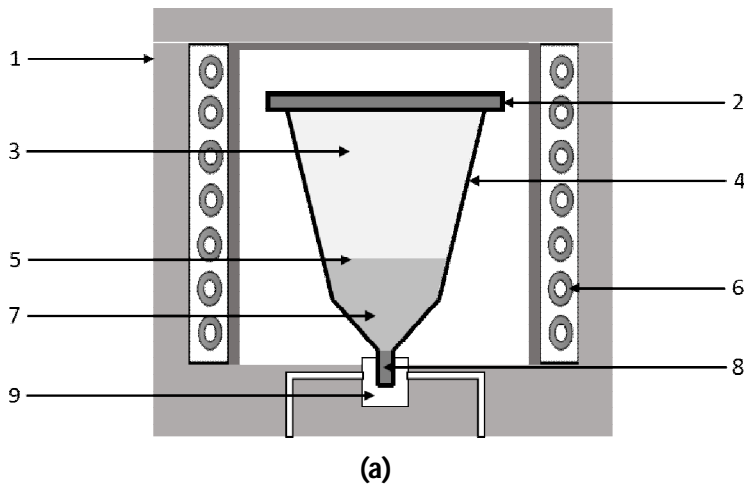


**Figure 1.16: (a)** Schematic diagram for the TGT growth process. (1) Insulation, (2) crucible cover (3) melt, (4) crucible, (5) crystallisation front, (6) heating arrangement, (7) growing crystal, (8) seed, (9) cooling water.

**(b)**  $\text{Ti:Al}_2\text{O}_3$  single crystal with 140 mm diameter grown by the TGT technique [G. Zhou, 2006].

The gradient solidification method (GSM), represented in figure 1.17 (a) is a modification of the vertical Bridgman technique especially suitable for the preparation of sapphire domes. The crystal domes, as shown in figure 1.17 (b), are grown in a double-walled molybdenum crucible inside a vacuum furnace with graphite heating elements. The crucible is first loaded with a seed and the raw feed and a partial melting of the seed is achieved. Thereafter the temperature fields in the furnace are controlled to promote and progress the crystallisation. Crystals with different orientations and shapes with dimensions of up to 150 mm have been achieved by this technique [Horowitz, 1987] [Biderman, 1991] [Horowitz, 1993] [Biderman, 1987].

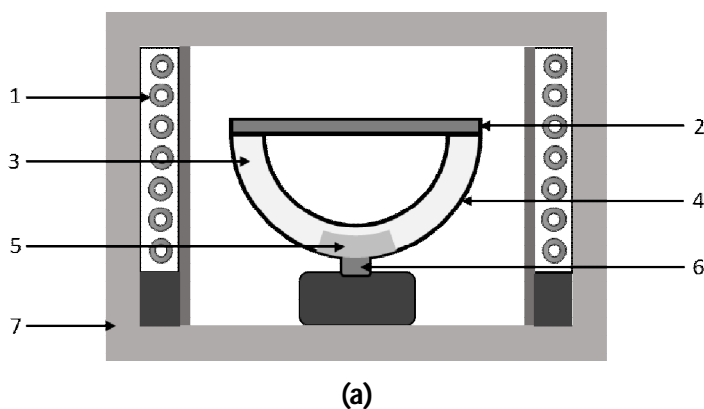


**Figure 1.17: (a)** Schematic diagram for the GSM growth process. (1) Heating arrangement, (2) crucible cover, (3) melt, (4) crucible, (5) growing crystal, (6) seed, (7) insulation. **(b)** Shaped domes of sapphire produced by the GSM method [Horowitz, 1993].



The heat exchanger method (HEM), is a modified directional solidification technique developed in the 1970s by Fred Schmid and Dennis Viechnicki for growth of large sapphire crystals from the melt [Schmid, 1970]. In this growth technique, a sapphire seed crystal is placed at the bottom of a molybdenum crucible which is then loaded with pure alumina crackle. The furnace is evacuated and resistively heated to melt the crackle while keeping the seed just below its melting point by passing helium gas through the heat exchanger beneath the centre of the crucible. Heat and vacuum help purify the alumina by vaporising some impurities. After partial melting of the seed, the helium flow is increased to cool the seed and initiate crystallisation of alumina onto the seed. The furnace is held at constant temperature during growth of the crystal, which proceeds out from the seed in three dimensions. After crystallisation is complete, the furnace temperature and the helium flow are decreased and the boule is slowly annealed. The crystallisation process is controlled by a programmed reduction of heater power and the whole process may take three weeks to complete depending on the crystal size. Figure 1.18 provides a schematic representation of this technique [Harris, 2004].

Growth of very massive sapphire boules weighing 100kg and with dimensions up to 500mm diameter have been grown using this technique [Schmid, 1999]. Recently,  $\text{Ti:Al}_2\text{O}_3$  crystals have been grown by the HEM method weighing 15 kg and being 208 mm in diameter, as shown in figure 1.18 (b) [Joyce, 2010].

One of the advantageous features of this technique is that throughout much of the growth, the solid-liquid interface is protected by the surrounding liquid, and thus mechanical and thermal perturbations to the interface are minimised. Also, since there is no requirement for movement of the crucible or the heat zone it is a fairly simple process. But it is very challenging to establish and control the process, since there are no measurable parameters for automatic control such as crystal diameter or weight. Visual control is also not possible because the growing crystal is submerged in the melt. The fact that the crystal is in contact with the crucible during growth leads to complexities such as cracking due to stress and the crucible has to be broken away to extract the crystal [Akselrod, 2012].

A further modification of the HEM method, the controlled heat extraction system (CHES), was developed by ARC Energy in 2007. It is a variation of the HEM process with a more sophisticated method of controlling the growth rate by allowing motion of certain hot zone parts, crucible and shaft as in the Bridgman method [F.J. Bruni, 2013] [Richard Schwerdtfeger, 2014]. In this process, a reusable crucible is employed, which enables the operating cost to be significantly lowered compared to the traditional HEM technique. It also features a probe system which detects the position of the solid-liquid interface during the melting, seeding and growth steps of the process. This allows correlation of process parameters with the probe data to

achieve optimized crystal growth. The probing step is automated and hence the critical step of seeding can be performed without operator intervention, thus enabling a more automated process and hence higher productivity [Khattak, 2015]. The world's largest ever grown sapphire crystal, weighing 302 kg and with dimensions of 500 mm diameter and 350 mm height, was grown with this newly-developed technique [Khattak, 2016].

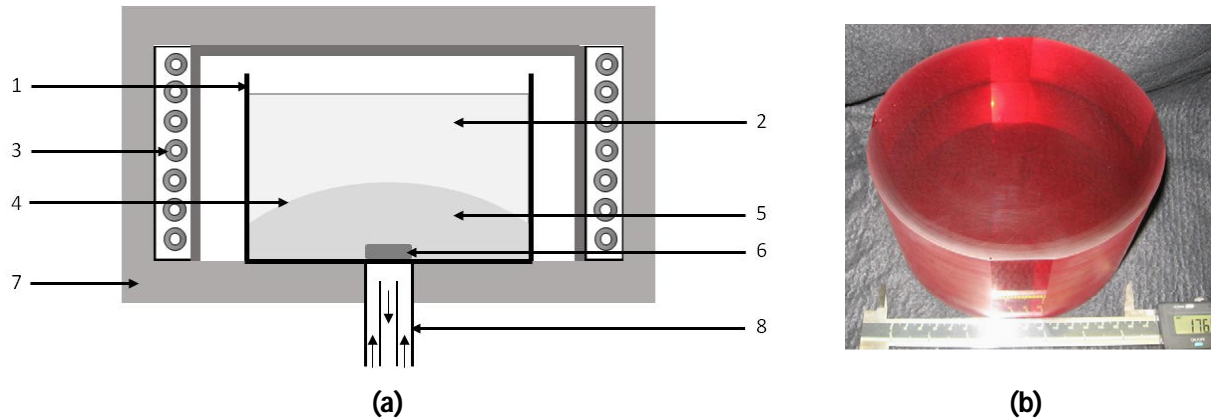


**Figure 1.18:** (a) Schematic diagram for the HEM growth process. (1) Crucible, (2) melt, (3) heating arrangement, (4) crystallisation front, (5) growing crystal, (6) seed, (7) insulation, (8) helium gas flow. (b) A 176.5 mm diameter Ti: Al<sub>2</sub>O<sub>3</sub> crystal produced from a 208 mm diameter boule using the HEM method [Joyce, 2010].

### 1.8.2.3 Czochralski Method

Czochralski (CzT or CZ) is one of the oldest methods of crystal growth accidentally invented by Professor Jan Czochralski in 1916. It has been used for the growth of sapphire crystals since the 1960s [Paladino, 1964]. A diagram of the process is shown in figure 1.19 (a). In this method, the crucible is loaded with the starting material and set in a hot zone with a relatively high temperature gradient. Both induction and resistive heating can be used. In the case of inductive heating, the electromagnetic energy is coupled either directly to the crucible or to a cylindrical graphite susceptor surrounding the crucible. A rotating seed of the desired orientation is touched to the surface of the melt and slowly raised. The expansion profile and the final crystal diameter are controlled by adjusting the heater power based on the weight of the crystal measured by the load cell [Akselrod, 2012].

The Czochralski growth has many advantages which made it suitable for the growth of good quality sapphire crystals. There is no direct contact between the crucible walls and the crystal, which helps in producing unstressed single crystals. The crystals can be extracted from the melt at any stage of the growth, which helps in investigating the growth conditions, and the shape of the crystal can be changed by

varying the melt temperature and the growth rate [Chernov, 1984]. But to achieve the desired melt convection pattern and avoid the rapid drop of melt level, the diameter of the crucible is required to be at least twice the crystal diameter. This imposes restrictions to the scalability of the process for large diameter crystals [Akselrod, 2012]. Hence, using this method, the maximum diameter of product wafers has been limited to 100mm obtained from 150 mm diameter sapphire crystals and with a very low material utilization during the process leading to increased production costs [F.J. Bruni, 2013].

Growth of very good optical quality  $\text{Ti:Al}_2\text{O}_3$  crystals for laser applications weighing up to 400gm and measuring up to 130 mm in length and 35 mm in diameter have been achieved using the Czochralski technique, as shown in figure 1.19 (b) and a study of their optical quality and performance has been carried out in comparison to crystals obtained with other growth techniques [Guillaume Alombert-Goget, 2017] [G. Alombert-Goget, 2016-(a)] [G. Alombert-Goget, 2016-(b)].

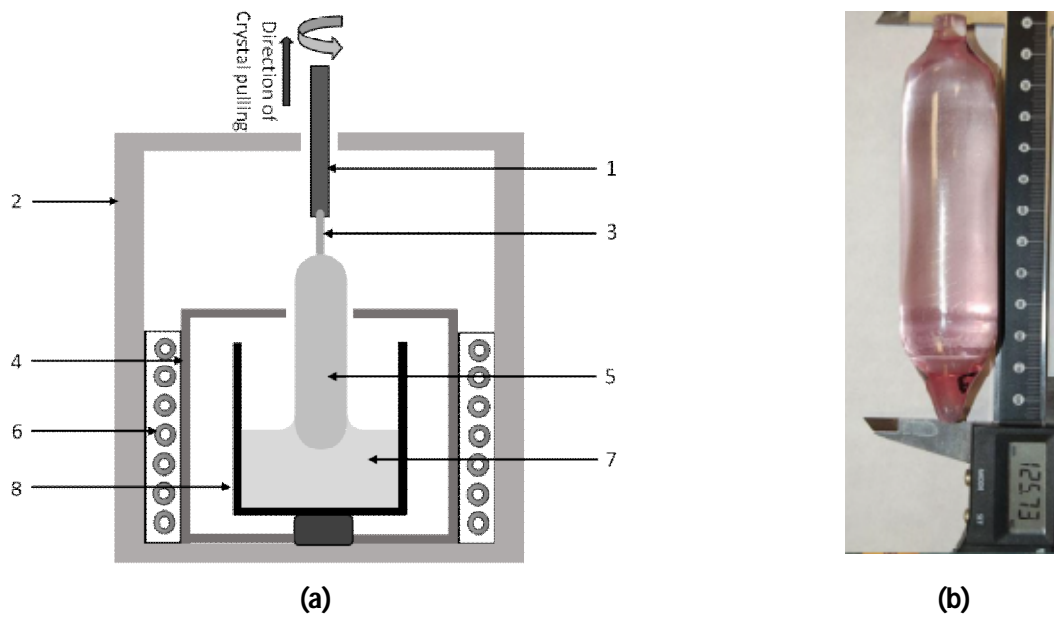


**Figure 1.19:** (a) Schematic diagram for the Czochralski growth process. (1) Seed holder, (2) insulation, (3) seed, (4) graphite susceptor, (5) growing crystal, (6) heating arrangement, (7) melt, (8) crucible. (b)  $\text{Ti:Al}_2\text{O}_3$  crystal grown by the Czochralski method at ILM [G. Alombert-Goget, 2016-(a)].

#### 1.8.2.4 Kyropoulos Method

The Kyropoulos method (KY) was developed by the Greek-German physicist Von Spyro Kyropoulos at Gottingen, Germany in the 1920s for single crystals of alkali halides, with the main goal of avoiding contact between the crystal and the crucible during solidification [Kyropoulos, 1926]. Many decades later in the 1970s, the method was modified and developed at the S. I. Vavilov State Optical Institute (GOI) in Russia by

Mikhail Ivanovich Musatov for the growth of sapphire crystals and it is also known as the GOI method or Musatov method [Musatov, 2009].

A schematic representation of the process is shown in figure 1.20 (a). In this method, a sapphire crystal seed oriented according to the desired growth axis is held on the end of a metal rod and dipped into the surface of high purity molten alumina in a molybdenum crucible. Heat is conducted away from the seed crystal by the metal rod. During seeding, the seed crystal is slowly pulled from the melt in a series of steps to allow the diameter of the growing crystal to increase. After seeding, the crystal grows with very limited motion of the boule. The temperature of the hot zone during the growth process decreases very slowly and is to be very precisely controlled. The key to successful growth of high quality sapphire is to maintain a precise temperature profile with small axial and radial temperature gradients of the order of 1 to 2 K/cm [Harris, 2009]. The relation between the cooling and the pulling rates at different stages of the growth process defines the crystal shape and the quality to a great extent [Perner, 1979].

The first sapphire crystals developed by this technique at the GOI institute in Russia were 40-70 mm in diameter. Since then, the method has been implemented on industrial scales in the country for mass production, most notably by Stavropol (now known as Monocrystal) where crystals weighing 50 kg and 500 mm in diameter were obtained in 1982 [Musatov, 2010] [Musatov, 2009]. Kyropoulos growth for sapphire was later adopted by countries such as the USA, China, Taiwan, Poland, Israel, Ukraine, Uzbekistan, Armenia and France to cater for the ever-growing demand for sapphire wafers as LED substrates. Among recent manufacturers, Kyropoulos systems built by Thermal Technology (now a division of GT Advanced Technologies) have been able to produce sapphire crystal weighing 90 kg [Akselrod, 2012] [F.J. Bruni, 2013] [Frank J. Bruni, 2015]. In the 2000s Rubicon Technology Inc. has made a lot of progress in scaling up the size of the sapphire crystal grown by the Kyropoulos technique and in April 2009 they reported on the growth of a 200 kg boule with a maximum diameter of 420 mm to provide windows and substrates with a diameter greater than 300 mm [Zharikov, 2012] [Harris, 2009].

In 2011, with the Kyropoulos method,  $\text{Ti:Al}_2\text{O}_3$  crystals weighing 5kg and with a diameter of 100 mm for petawatt laser applications were grown in a molybdenum crucible at LPCML in Lyon, France in co-operation with the company RSA, as shown in figure 1.20(b) [Abdeldjelil Nehari, 2011] [Boulon, 2012]. There has been further progress by this group in the collaborative project which will be discussed throughout this manuscript.

Recently, a new technology was developed on the basis of the Kyropoulos and Czochralski methods at the Harbin Institute of Technology in China named as sapphire growth technique with micro-pulling and

shoulder expanding at cooled centre (SAPMAC) [Zharikov, 2012]. As the name suggests, the motive of this technique is to grow large-sized crystals while maintaining crystal orientation by having shoulder expansion at the cooled centre, while micro-pulling reduces the disturbance of the temperature field and hence the temperature tends to be more even. The diameter of the crystal extends to 1-3cm from the crucible, and in the whole process of growing, the crystal is not removed from the crucible. The small temperature gradient inside the crystal helps to reduce stress effectively, prevent crystal cracking, and decrease dislocation density. In the technique, water is the working fluid in the heat exchanger, which allows *insitu* annealing and it is claimed, shortens the growth cycle and hence reduces production costs. Sapphire crystals have been produced by this method with dimensions of 240 mm in diameter and 210 mm in length with a weight of 27.5 kg [Xu, 2007] [Zhang, 2012] [Zhang, 2011-a]. But, up to now, the crystalline qualities of these crystals are not on a par with those achieved by the conventional Kyropoulos method, since they show the appearance of many defects such as dislocations, twins and inclusions [Zhang, 2011-b] [Chenghai, 2007].

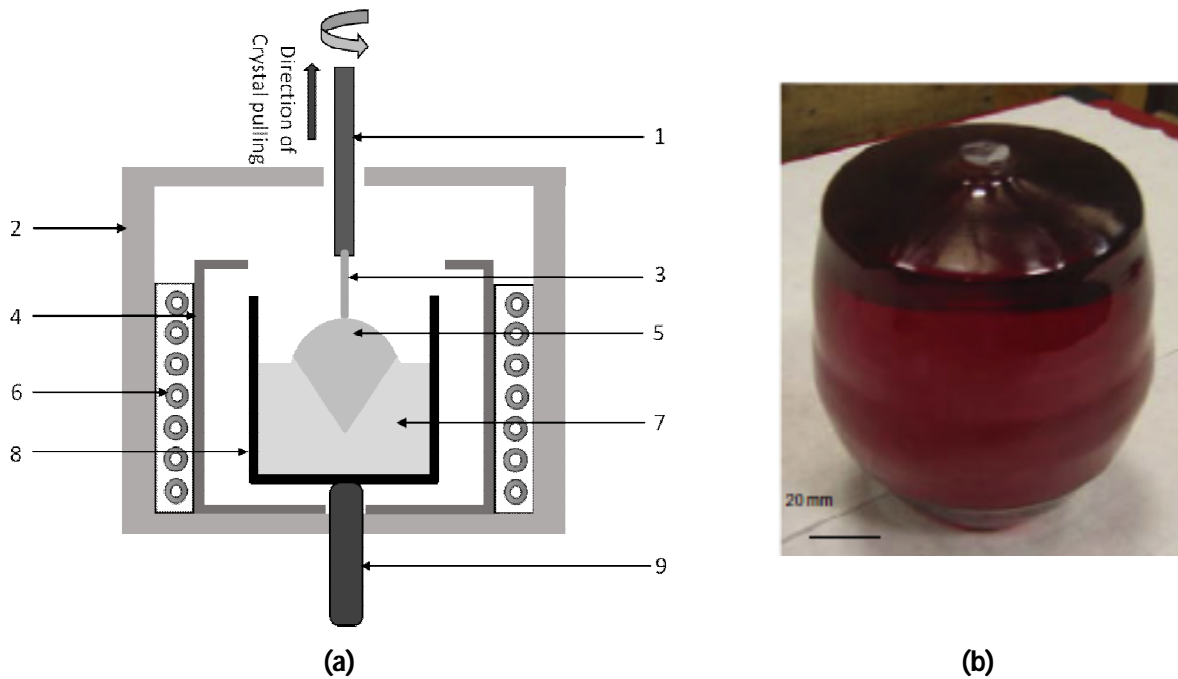


**Figure 1.20: (a)** Schematic diagram for the Kyropoulos growth process. (1) Seed holder, (2) insulation, (3) seed, (4) graphite susceptor, (5) growing crystal, (6) heating arrangement, (7) melt, (8) crucible, (9) crucible support. **(b)** Ti: Al<sub>2</sub>O<sub>3</sub> crystal grown by the Kyropoulos method at LPCML (UCBLyon1) in co-operation with RSA Company for petawatt lasers [Boulon, 2012].

## 1.9 Choice of Kyropoulos Method

Table 1 below summarises the comparison between the various crystal growth technologies for the manufacture of LED substrates [Akselrod, 2012], but they are similarly applicable even for the production of discs. As evident from the table, the Kyropoulos and HEM techniques are the ones capable of producing massive crystal size which is an absolute necessity for obtaining discs with greater diameters. They are also very favourable for large scale commercial production due to high productivity at relatively low cost and low defect density. A comparison in terms of the dislocation density also ranks the Kyropoulos and HEM techniques with dislocation densities in the range of  $10^1 - 10^2 \text{ cm}^{-2}$  much better than the other techniques such as Czochralski with  $10^4 - 10^5 \text{ cm}^{-2}$  and EFG with  $10^6 \text{ cm}^{-2}$  [Harris, 2009].

Method	Crystal size	Temperature gradient	Dislocation density	Productivity	Yield of usable material	Wafer cost advantage
Verneuil	•	•	•	•••	•••	N/A
Czochralski (CZ)	••	••	••	•••	•••	••
Kyropoulos (KY)	••••	••••	••••	•••	••	•••
Heat exchanger method (HEM)	••••	••••	••••	••	••	•••
Stepanov (EFG)	••	•	•	•••	••	••
Bagdasrov (HDC)	•	••••	••••	•••	••	••

**Table 1:** Comparison of major characteristics of sapphire crystal growth methods [Akselrod, 2012].

As explained in the earlier sections, both the HEM and Kyropoulos techniques have their strengths and shortcomings with respect to the process cost and the eventual quality of the crystals obtained. Industries and research institutes have been working on both of these techniques to improve the process and modify them to better suit the demands of productivity and achieve the quality required. The choice between these techniques is based on the know-how available for the technique at the particular organisation. Based on this same logic, the Kyropoulos technique has been explored for this project due to the availability of the state-of-the-art furnace at the company RSA Le Rubis and the availability of technology and scientific partners committed to the technology.

It is to be taken into account that an A-axis oriented sample is more desirable than the C-axis orientation for laser applications and hence we are interested in growth of A-axis oriented crystals. This is because the luminescence yield for  $\text{Ti:Al}_2\text{O}_3$  is at least 50% greater for the A-axis than the C-axis [McCallum, 2002].

## 1.10 Choice of crucible material

The choice of the crucible material is limited by the metals and their alloys which can resist high temperature attack by an  $\text{Al}_2\text{O}_3$  melt. The commonly used crucibles for growth of sapphire crystals are made of iridium, tungsten or molybdenum.

Iridium, with a melting point of 2716 K, interacts less intensely with the than to other materials, but its maximum operational temperature of 2423 K is not significantly higher than that required by the heating elements during the growth process. This is a very constraining feature when it is required to scale the geometry of the crystal and the furnace to larger dimensions. At larger dimensions of diameter, to achieve the temperature gradient at the centre of crucible which can maintain the appropriate solid-liquid interface, the temperature at the crucible walls can often exceed the melting point of iridium which is only 400 K higher than melting point of sapphire [F.J. Bruni, 2013]. Also, iridium is a far more costly metal than the other alternatives and hence affects the economics of the production. Thus, iridium crucibles are very much used in growth of smaller diameter crystals using Czochralski technique but not for the Kyropoulos method.

Molybdenum with a melting point of 2896 K and tungsten with a melting point of 3695 K are much more convenient alternatives in terms of melting issues and metal costs. In the case of a molybdenum crucible, sapphire crystals grown by the Bridgman method have shown the presence of few cracks while crystals grown in tungsten crucible are crack-free which is due to their favourable thermal expansion coefficients [Miyagawa, 2013]. On the other hand, crystals grown in tungsten crucibles have shown the presence of large bubbles while those in molybdenum crucibles do not have a grave issue with bubbles [Suzuki, 2014]. In the Kyropoulos growth technique, the contact between the crucible and the crystal is prevented, hence the formation of cracks during the cooling process in a molybdenum crucible is not an issue. Since a molybdenum crucible helps control the formation of defects in the form of bubbles, it is preferred over a tungsten crucible for the Kyropoulos growth technique. At RSA, there is much experience of using molybdenum crucibles for EFG growth of sapphire and hence it has been qualified for the Kyropoulos growth process, too.

### **1.11 . Growth process phenomenon of sapphire from the melt**

High-temperature crystallisation is characterized by certain peculiarities which make the process complicated. These peculiarities are due to the fact that crystallisation is quasi-equilibrium since the process takes place under critical temperature gradients and in complicated physico-chemical conditions. There are factors of a physical nature (kinetics at the phase boundary and heat and mass exchange) and also physico-chemical processes such as the high-temperature chemical reaction of dissociation and synthesis which influence the chemical composition and real structure of crystals.

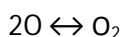
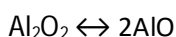
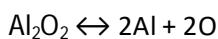
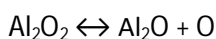
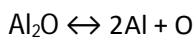
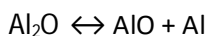
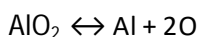
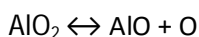
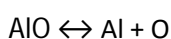
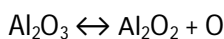
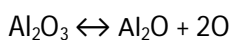
Some of these aspects are discussed in the following sections:

### 1.11.1 Processes accompanying melting of $\text{Al}_2\text{O}_3$

The maintenance of melt composition at high temperature creates a very complex environment wherein a series of processes develops intensively (thermal dissociation, dissociative evaporation, physico-chemical reaction between the melt, container material and crystallisation environment). These processes interact with crystallisation kinetics and influence the resulting crystal structure. Hence these processes are important for determining the conditions of growth and the crystallisation technique.

#### 1.11.1.1 Thermal dissociation

Thermal dissociation in the melt disturbs the stoichiometric composition and thus leads to the formation of defects in the crystal. The intensity of these reactions depends on the thermal and temporal regime which can be established from the phase equilibrium diagrams of the main components of the crystallized compounds, the regions of solid solution stability, phase transitions, possible changes in the composition caused by evaporation, and so forth. Aluminium oxide melting under normal pressure is accompanied by dissociation followed by formation of  $[\text{AlO}]$ ,  $[\text{Al}_2\text{O}]$ ,  $[\text{AlO}_2]$ ,  $[\text{Al}^+]$ ,  $[\text{O}^-]$ , and  $[\text{Al}_2\text{O}_2]$  vapour species governed by the following reactions [Bagdasarov, 1988]:





Due to the relatively high vapour pressure of the thermal dissociation products, the melt is saturated with gaseous inclusions that accumulate at the crystallisation front and influence the growth kinetics and the crystal quality. There have been studies carried out regarding the thermodynamic analyses of these dissociation products, describing their partial pressures as a function of temperature, as presented in figure 1.21 [Bunoiu, 2005]. The thermal dissociation intensity can be lowered by using its dependence on external pressure, temperature, and the time period during which the substance is in the melted state. Since the use of elevated pressures is limited due to technical difficulties, it is preferred to carry out the crystallisation process either under normal pressure or in vacuum. For this purpose, the melt must be overheated only to such an extent that the thermal dissociation intensity is not too significant. The upper overheating limit is defined by the intensity of the substance dissociation and evaporation as well as by its chemical interaction with the container material and the atmosphere. The lower limit depends on the melt viscosity, which if, too low, can impede its convective mixing, since for aluminium oxide at temperatures ranging between 2,320 and 2,220 K, the viscosity value changes by approximately a factor of two [Pishchik, 2009].

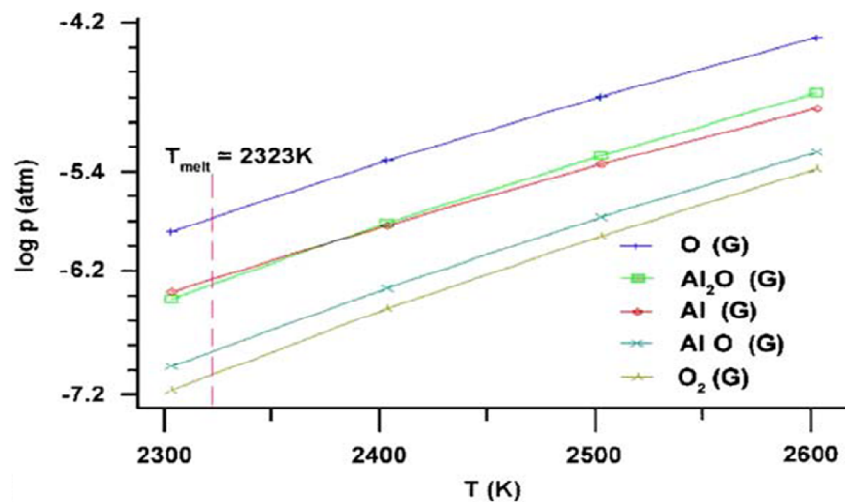


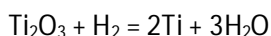
**Figure 1.21:** Partial pressure versus temperature for principal gas species in equilibrium with molten alumina [Bunoiu, 2005].

#### 1.11.1.2 Dissociative evaporation and crystal atmosphere

Thermal dissociation is also one of the main reasons for dissociative evaporation which enhances the violation of composition of the crystallized substance. This process largely depends on the vapour pressure of individual components of the substance, on its temperature and on the nature and pressure of the atmosphere above the melt. Since crystallisation is run both in vacuum and in gaseous atmospheres of different natures (including neutral, reducing and oxidizing) the influence of the atmosphere on the

crystallisation process is very important. In vacuum, the dissociative evaporation of aluminium oxide results in the formation of a chiefly oxidizing atmosphere above the melt, which is evident with the oxidation of crucible material uncovered by the melt. The most active development of oxidation reactions can even cause crucible destruction, which occurs at the contact points of the melt and the crucible wall [Bagdasarov, 1988].

The use of a neutral atmosphere reduces the rate of evaporation very sharply due to the limitation of the melt interface by the gas atmosphere. The chemical interaction between the crystallisation atmosphere and the surface of melt can also be used to solve some particular problems of single crystal synthesis. One of these is the problem of maintaining the valence state of dopants [Guillaume Alombert-Goget, 2017]. In the case of titanium-doped aluminium oxide, for example, titanium ions maintain their trivalent state under oxidizing and inert atmospheres, while under a reducing atmosphere of hydrogen, it is not kept, due to the reaction:



Thus, the crystallisation atmosphere has a great effect upon the rate of high-temperature processes. Vacuum and inert atmosphere are of practical interest since the former helps to enhance evaporation which aids chemical purification of the melt, while to reduce evaporation an inert atmosphere is needed [Bagdasarov, 1988].

#### **1.11.1.3 Interaction of melt with the container material**

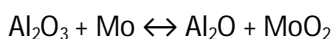
The interaction between the melt and the container material is one of the important factors for the selection of the crystallisation method. The container must avoid mutual solubility and chemical interaction with the substance to be crystallised.

Some of the requirements for the container material are:

- Its chemical binding forces have to differ in nature from those of the crystallizing substance (dielectric crystals are grown in metallic containers, organic crystals are crystallized in containers made of inorganic dielectrics).
- Adequate mechanical strength.
- High machinability of the material.
- Close values of the thermal expansion coefficients of the container material and the crystallizing substance.
- High electric conductivity (in case of high-frequency induction heating).

The interaction between the container and the melt may be caused by the impurities contained in the raw material or by those adsorbed at the container walls, surface of the crystallisation chamber, furnace elements, and so forth. Moreover, it may be induced by some substances (such as oxygen or moisture), which may ingress the melt from the atmosphere [Pishchik, 2009].

Thermal dissociation and dissociative evaporation strongly affect the redox potential of the system which governs the contact interaction of the melt with the container material. The aluminium oxide melt acquires reducing properties due to the predominant loss of oxygen ions. In the case of molybdenum crucibles it leads to the reduction of the molybdenum oxides by the melt of aluminium oxide and thus hinders the chemical interaction of the melt with the container material in the course of the following reaction [Bagdasarov, 1988]:



#### **1.11.1.4 Point defects**

Sapphire is an ionic compound where the point defects typical of those in ionic crystals are formed, namely, anionic and cationic vacancies in various charge states, interstitial ions, ions in cationic and anionic sites, vacancy pairs and aggregates, and vacancy–impurity complexes. Ionic crystals of stoichiometric composition contain equivalent numbers of anionic and cationic vacancies (Schottky defects), i.e., there are three oxygen vacancies per two aluminum ones, or there is one interstitial ion of the same sign for each ionic vacancy (Frenkel defects).

The processes accompanying the melting of  $\text{Al}_2\text{O}_3$  are one of the main contributors to the presence of point defects in the crystals. The growth and annealing atmosphere is a factor of primary importance defining the appearance and disappearance of point defects. The oxygen partial pressure defines the point defect stoichiometry and the atmosphere-oxidizing potential dictates their charges. The trapping of a melt dissociation product into the growing crystal under the absence of the complementary component at the crystallisation front at the instant under consideration gives rise to vacancies in the form of Schottky defects. Under thermodynamic equilibrium conditions, Schottky defect formation is more favourable in energy than Frenkel defect formation among electrically neutral defect families; while it is just the single anionic vacancy that requires the lowest energy of all point defects [Dienes, 1975].

#### **1.11.1.5 Inclusions**

Inclusions are volume defects that exist in sapphire crystals in the form of gaseous pores, inclusions of foreign solid phase, and liquid phase inclusions. Pores are inevitable defects in any growing technique. They

are formed due to imperfect thermodynamic conditions as well as in equilibrium conditions. The pores deteriorate the performance characteristics of pieces and the polish quality, as well as increase the light scattering. The pore size varies from submicron values to 3 to 5 mm. At a high concentration of these defects ( $>10^5 \text{ cm}^{-3}$ ), the material is unsuitable for optical applications.

The pore composition largely depends on the growth atmosphere. The main pore formation factors in sapphire grown from melt are the melt interaction with impurities in the raw blend, container material, and atmosphere as well as the melt dissociation. The general condition favouring the pore formation is the melt supersaturation in dissolved gases. Pore formation in crystals is preceded by the back-driving of the gas dissolved in the melt from the crystallisation front. A bubble of subcritical size is pushed back from the crystallisation front as the liquid is mixed weakly, the concentration densification and the bubble size increase, resulting in its interaction with the crystallisation front and retention due to a complicated interaction of elastic forces, viscosity, heat transfer and surface tension forces. Since the crystal growth above the bubble is hindered, a pore is formed in the solid phase.

When aluminium oxide crystals are grown up to a certain critical growth rate no local heterogeneities like inclusions are formed. But, when the rate goes beyond this critical value these inclusions start to appear. Their size and density depend greatly on the growth rate: the higher the rate, the larger the density and smaller the size. Formation of inclusions is accompanied by their partial coalescence and as a result, hollow channels and individual coarse inclusions can be seen in the crystal. Aluminium oxide itself is the main source of these inclusions since the specific volume of the melt exceeds that of the crystal by 25%, therefore, the melt entrapped by the growing crystal, if any, is crystallised with formation of vacuum cavities. When aluminium oxide is crystallised, thermal dissociation of the substance or gaseous impurities like  $\text{H}_2$ ,  $\text{N}_2$ ,  $\text{CO}$  and  $\text{CO}_2$  are the main processes forming gas inclusions.

These reactions of dissociation are accompanied with the absorption of heat and therefore in sites of their intensive development at the crystallisation front, there are regions which have very large supercooling of the melt. This promotes local increase of the growth rate and hence traps more inclusions. Thus, the critical growth rate is much lower for a melt with a lot of impurities than for a pure one and hence it is important to control the concentration of impurities in the growth environment to achieve a better control over the crystallisation process [Bagdasarov, 1988].

Solid-phase inclusions result from capture of foreign solid particles by the crystallisation front or from the phase segregation under the crystal cooling. In crystals grown from melt by crucible methods, there are inclusions of the metal from which the crucible and other elements of the equipment are made. Such

inclusions can appear in the crystal due to peeling of particles from the crucible, ingress of particles from outside of the heaters or screens, or dissolution of metal oxides from the surface of crucibles, due to their reduction by the products of aluminium oxide dissociation. Another probable contributor to inclusions are due to reduction of the evaporating metal oxides outside the melt by the components of the growth gas atmosphere or gaseous products of aluminium oxide dissociation, which is followed by mechanical ingress of the reduced metal to the melt.

There is pore formation due to vacancies when sapphire is grown at high speeds or in reducing conditions. This is due to deviation from the critical stoichiometry in the  $\text{Al}_2\text{O}_3$  lattice, which leads to second-phase microparticles being precipitated in the crystal. In reducing conditions, the melt becomes depleted of oxygen and the composition of dissociation products becomes shifted toward compounds with excess Al content as compared to stoichiometric  $\text{Al}_2\text{O}_3$ . In crystals with high vacancy density, the pores may arise after its formation, during the cooling. That is, the vacancies along with some impurities still remain in equilibrium during crystallisation and the supersaturation, coagulation, and separation of inclusions occur in the course of cooling. The high-temperature vacuum annealing of such crystals also favours the coagulation of vacancies into faceted pores (negative crystals) as shown in figure 1.22.

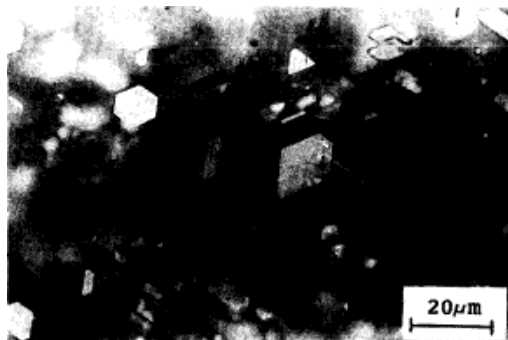


**Figure 1.22:** Photomicrograph of vacancy voids in the (0001) plane of sapphire [Borodin, 1990]

### 1.11.2 Processes occurring at the crystallisation front

Stoichiometric composition and structure of the growing crystals depend a lot on the processes occurring at the growth front. Kinetics and heat and mass transfer are the main factors responsible for the limiting stages of the process. Thus, to understand the nature of crystal composition inhomogeneity and crystal defects, the examination of growth mechanisms and their correlation with real structure is necessary.

#### 1.11.2.1 Growth mechanisms

From a thermodynamic point of view, solidification requires a heat flux from the system to the surroundings which changes its free energy, and therefore the relative thermodynamic stability of the

phases present. Hence, thermodynamically stable phases are more likely to be observed, but the transformation of one phase into another requires rearrangement of the atoms. During the formation of a new crystal structure, it involves a relatively short-range (atomic) rearrangement. Because of these atomic movements, solidification always requires some irreversible departure from equilibrium in order to drive the process.

#### **1.11.2.2 Interface Structure**

After seeding, the crystal grows with the addition of further atoms. During this process, the solid/liquid interface takes on a specific structure at the atomic scale. Its nature depends upon the differences in structure and bonding between liquid and solid. The growth rate of a crystal depends upon the net difference between the rates of attachment and detachment of atoms at the interface. The rate of attachment depends upon the rate of diffusion in the liquid, while the rate of detachment depends on the number of nearest neighbours binding the atom to the interface. The number of nearest neighbours depends upon the crystal face considered, i.e. upon the surface roughness at the atomic scale (number of unsaturated bonds).

An atomically flat interface, as shown in figure 1.23 (a), will maximise the bonding between atoms in the crystal and those at the interface. Thus, such an interface will expose few bonds to atoms arriving via diffusion through the liquid. Such a crystal has a tendency to close up any gap in its solid/liquid interface at the atomic scale. This leads into crystals which are faceted at the microscopic scale and usually exhibit high undercooling.

An atomically rough interface, as shown in figure 1.23 (b) always exposes a lot of favourable sites for the attachment of atoms from the liquid. Such an interface tends to remain rough and leads to smooth crystals which are non-faceted at the microscopic scale and exhibit low kinetic undercooling.

Low index planes with atomically flat, microscopically faceted interface exhibits little tendency to incorporate newly arriving atoms into the crystal. Hence growth is more difficult and requires an additional undercooling. High index crystallographic planes tend to be inherently rough and contain many steps. This leads to a marked anisotropy in growth rates with respect to low index planes and in turn, leads to the disappearance of the higher index planes, due to their more rapid growth, and leads to a characteristic crystal form which is bounded by the slowest growing faces. In the case of sapphire crystals, the C-plane has the lowest growth speed and hence has a tendency to form facets. Thus it is often difficult to grow C-axis oriented crystals using the Kyropoulos technique [Tatartchenko, 2005].

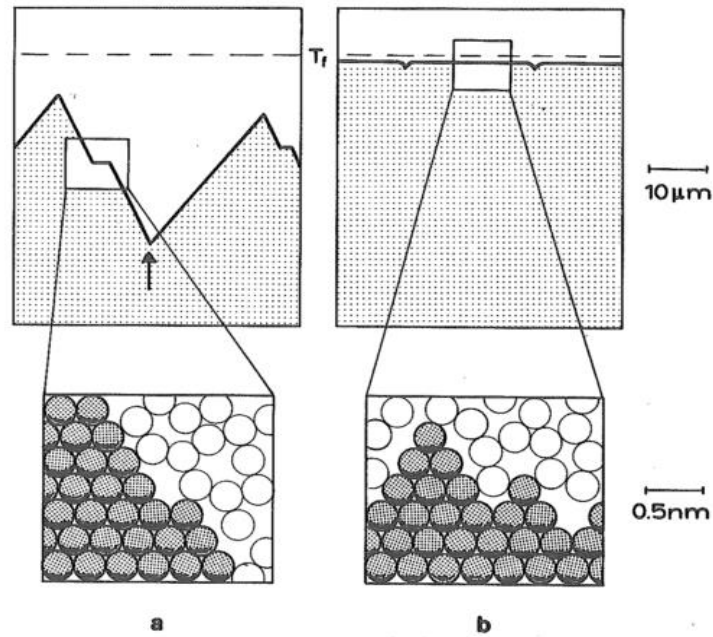


**Figure 1.23:** Form of (a) faceted and (b) non-faceted interfaces [Kurz, 1998].

### 1.11.2.3 Solute redistribution

During the growth of crystals, if local equilibrium is assumed to hold at the solid-liquid interface, then, at the interface, the solid concentration is related to the liquid concentration by the equilibrium distribution coefficient

$$C_s^* = k_s C_l^*$$

This compositional difference always leads to concentration variations in the formed crystal, which is known as segregation and hence the coefficient is also known as the segregation coefficient.

Solute can be transported by diffusion and convection, and the segregation pattern depends upon both the processes involved. Convection leads to the transport of mass over very large distances, compared to those involved in diffusional processes, and may result in macrosegregation, that is, compositional differences over distances equal to the size of the crystal. Microsegregation depends upon solute diffusion in the liquid and the solid.

In order to understand microsegregation, it is essential to understand the initial and final transients of the crystal growth process. The first is required in order to establish the steady-state boundary layer, and the second arises from the interaction of the boundary layer at the solid-liquid interface with the end of the crystal. The diffusion boundary layer in the liquid ahead of a solid-liquid interface can be considered to be a

limited region of the system which transports the solute missing from the initial transients in the solid where the concentration is below  $C_0$ , and maintains constant the overall composition of the system. This moving boundary layer disappears at the end of solidification by 'depositing' its solute content in the final transient. Thus, the mean composition of the solid is always the same as that of the liquid from which it is formed.

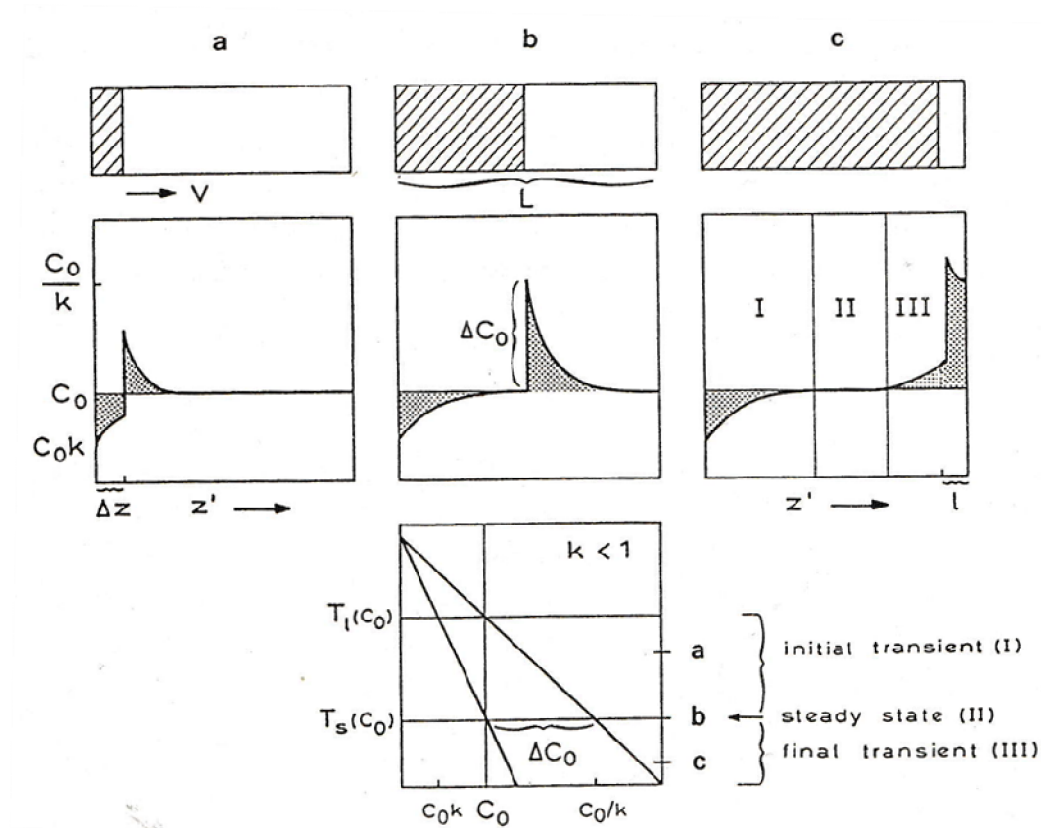


**Figure 1.24:** Initial and terminal transients at the solid-liquid interface in the case of diffusive transport of solute in the melt [Kurz, 1998].

As represented in figure 1.24 during solidification with a solid-liquid interface, the establishment of a steady-state boundary layer requires a distance of growth which corresponds to the length of the initial transient. This distance increases with decreasing growth rate. Within this transient, the concentration of the liquid at the interface increases from  $C_0$  to  $C_0/k_s$ . With respect to the phase diagram, this means that the first solid to freeze has the composition,  $k_s C_0$  and reaches the composition,  $C_0$ , and the interface temperature,  $T_s$ , corresponding to the composition,  $C_0$ , at the steady state. At the steady state, the flux due to the interface advance (which arises from the difference in liquid and solid solubilities) is equal to the diffusional flux due to the concentration gradient at the solid-liquid boundary. In this case, the exponential



decay described in figure 1.29 is the exact solution. Finally, when the boundary layer becomes equal to the length of the remaining liquid region, diffusion into the liquid phase is hindered by the system boundary (the concentration gradient must be zero at the end of the crucible). Thus, the concentration in the liquid at the solid-liquid interface begins to increase to a value which is greater than  $C_0/k_s$ , and the solid concentration therefore becomes greater than  $C_0$  and a terminal transient is created. In order to ensure mass conservation, the surface area of the grey region below  $C_0$  must be equal to the grey region above  $C_0$ . The lengths of the initial and final transients are unequal. These concentration variations lead to the phenomenon known as segregation.

Under the conditions of perfect mixing in the melt due to strong convection and slow growth rate of crystals, the actual concentration profile achieved in the solid depends on details of the melt convection and the freezing rate. The Gulliver–Scheil segregation distribution for perfect mixing in the melt, as a function of the fraction of the molten charge solidified  $f_s$ , is given by

$$\frac{C_s^*}{C_l^*} = k_s(1 - f_s)^{(k_s-1)}.$$

If the growth rate of a crystal is not extremely slow or the convection is not too strong, an effective segregation coefficient is applied, where  $k_{eff}$  becomes a fitting parameter in the Gulliver–Scheil equation, namely,

$$\frac{C_s^*}{C_l^*} = k_{eff}(1 - f_s)^{(k_{eff}-1)}.$$

The effective segregation coefficient can be measured by conducting a normal crystallisation experiment and applying the above equation to the segregation data. The measured  $k_{eff}$  thus includes the complicated influences of melt convection, interface stability, and freezing speed.

In actual crystallisation conditions, the conditions lie between those with no mixing of the solute in the melt and perfect mixing due to convection. Thus the actual segregation profiles controlled by convection fall between those of the two limiting profiles shown in figure 1.25.

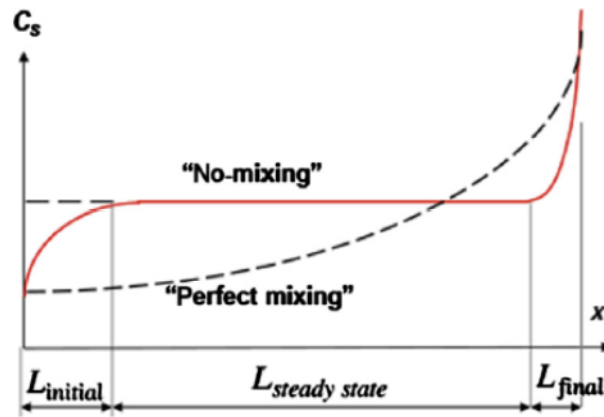


**Figure 1.25:** Solute distribution axial profile with no-mixing and perfect mixing conditions [Ostrogorsky, 2015].

An important case of solute segregation is observed during growth of crystals with a conical interface. Sections of crystal show a radial segregation along with the axial segregation along the length of the crystal. This phenomenon is explained with the help of figure 1.26. The section cut from a growing crystal interface has the centre growing earlier than the periphery and hence it shows a radial variation in the concentration of solutes.

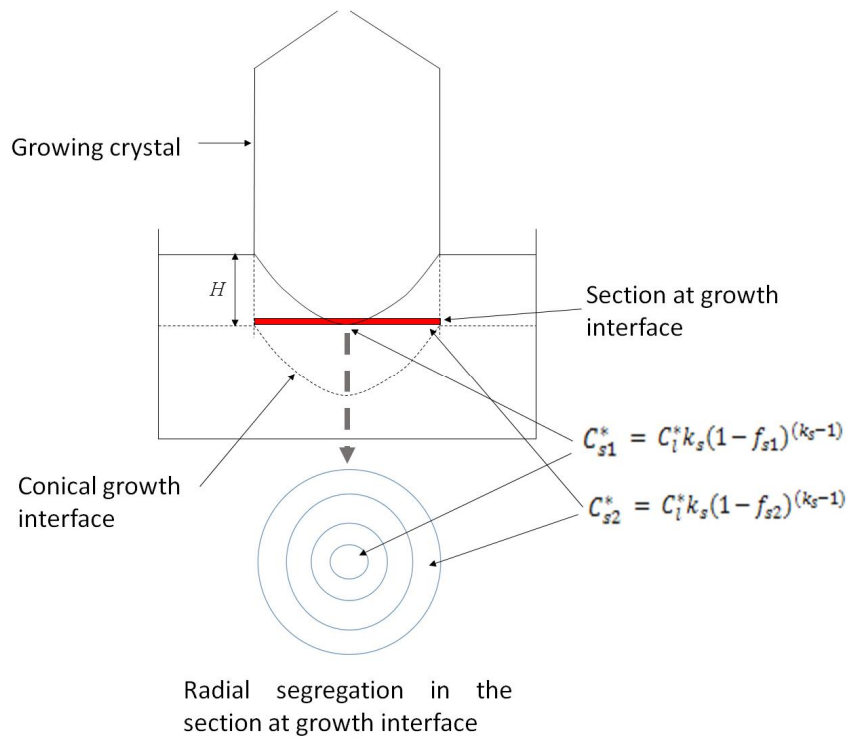


**Figure 1.26:** Radial segregation profile in crystal section with conical growth interface.

#### 1.11.2.4 Interface instability

During growth, any interface is subjected to random disturbances caused by insoluble particles, temperature fluctuations, or grain boundaries. A stable interface is distinguished from an unstable interface by its response to such disturbances. It is imagined that the interface is initially slightly distorted by a spatially regular disturbance. If the distorted interface is unstable, as shown in figure 1.27 (a), the projections may find themselves in a more advantageous situation for growth and therefore increase in prominence. In the case of a stable interface as shown in figure 1.27 (b), the perturbations will be unfavourably situated and tend to disappear.

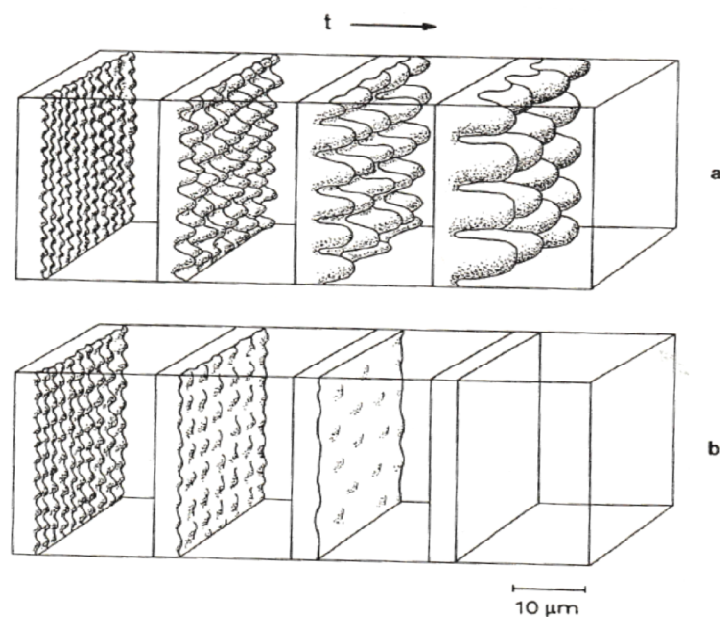


**Figure 1.27:** Initial evolution of an **(a)** unstable and **(b)** stable interface [Kurz, 1998].

During crystal growth, interface stability depends on the direction of heat flow. For a flat interface, as during directional solidification, the liquid temperature always increases ahead of the interface, as shown in figure 1.28. Therefore, the heat flow direction is opposite to that of solidification. When a perturbation, of amplitude  $\epsilon$ , forms at an initially smooth interface, the temperature gradient in the liquid increases while the gradient in the solid decreases (compare full and dotted lines along section, A-A). Since the heat flux is proportional to the gradient, more heat flows into the tip of the perturbation and less flows out of it into the solid. As a result, the perturbation melts back and the planar interface is stabilised.

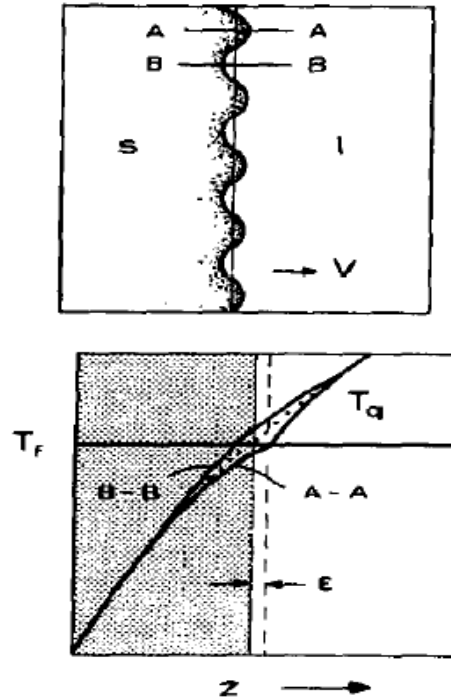


**Figure 1.28:** Mechanism for stabilisation of an interface [Kurz, 1998].

During crystallisation, the conditions for stable/unstable behaviour is more complicated if there is a solute (dopant) present in the melt, since it varies the melting point along the solid/liquid interface. As the interface advances, solute is rejected if the solubility of the solute in the solid is lower than that in the liquid ( $k_s$  less than unity). When the interface has been advancing for some time, the concentration distribution becomes time-independent (steady state). If a planar interface is advancing under steady-state conditions, then the solute concentration in the solid is same as that of the original melt. Under these circumstances, the concentration in the liquid decreases exponentially from the maximum composition,  $C_0/k_s$ , at the interface to the original composition,  $C_0$ , far from the interface. Thus, the rate of rejection of solute at the interface is proportional to the growth rate. The rejected solute must be carried away by diffusion down the interfacial concentration gradient, and this therefore becomes steeper with increasing growth rate.

The steady state diffusion layer is shown in figure 1.29 (upper diagram) for a given growth rate. As the liquid concentration,  $C_l$ , decreases with distance,  $z$ , the liquidus temperature,  $T_l$  (i.e. the melting point), of the melt will increase as indicated by the phase diagram. This means that, for small volumes of liquid at various distances ahead of the solid/liquid interface, the equilibrium freezing points vary with position as described by the curve in figure 1.29 (lower left). However, each volume element finds itself at a

temperature,  $T_q$ , which is imposed by the temperature gradient arising from the heat flow occurring in the melt. Since, at the solid/liquid interface ( $z=0$ ),  $T_q$  must be less than or equal to  $T_s$  in order to drive the atomic addition mechanism, there may exist a volume of liquid which is undercooled when the gradient of  $T_q$  is less than the gradient of  $T_l$ . This region (shaded) is called the zone of constitutional undercooling. There exists a driving force for the development of perturbations in this volume as shown in the cross-hatched region of figure 1.29 (lower left).

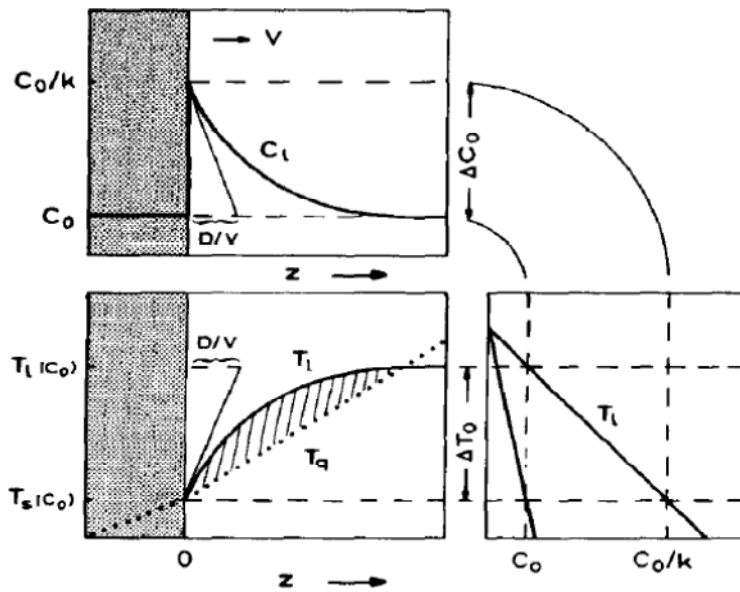


**Figure 1.29:** Undercooling at the boundary layer of solid/liquid interface [Kurz, 1998].

When the temperature gradient due to the heat flux is greater than the liquidus temperature gradient at the solid/liquid interface, the latter is stable as shown in figure 1.30 (a). On the other hand, there is a driving force for interface change whenever the slope of the local melting point curve (liquidus temperature) at the interface is greater than the slope of the actual temperature distribution. This is due to the fact that the undercooling encountered by the tip of the perturbation advancing into the melt increases and therefore the planar interface becomes unstable as shown in figure 1.30 (b)

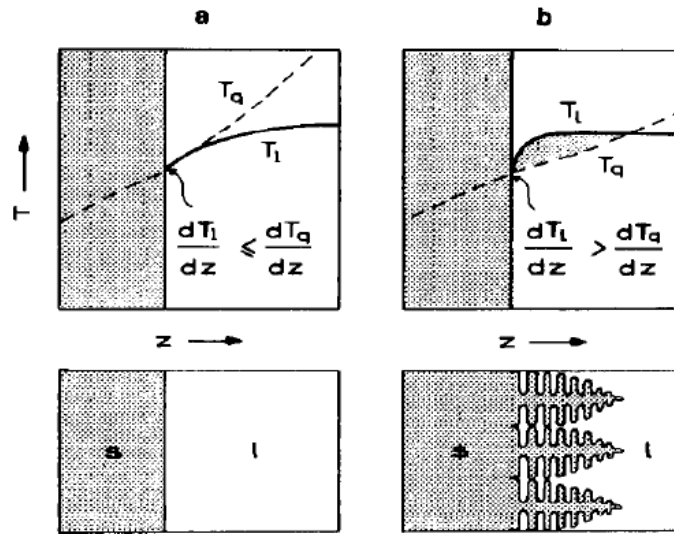


**Figure 1.30:** Solid/liquid interface perturbations due to constitutional undercooling [Kurz, 1998].

#### 1.11.2.5 Heat transfer

For the growth of high-quality single crystals, high stability of the process with strict control of the crystallisation front are required. These conditions are essentially determined by heat transfer processes in the melt and the crystal. To create optimum temperature conditions for growth, the heat transfer processes must be rigorously controlled and it depends a lot on the growing method. Heat exchange in crystallisation can occur by thermal conduction, radiation, and convection in the liquid phase.

The rate of heat transfer due to conduction is governed by Fourier's Law

$$q = \lambda_T (\Delta T / \Delta x) \quad \text{Equation 1.1}$$

where,  $\lambda_T$  is the heat conductivity coefficient.

Thermal conductivity indicates the ease of heat transfer through a material and is a material dependent property. The  $\Delta T$  term is the driving force for heat transfer.

The rate of heat transfer due to convection is described by

$$q = h \Delta T \quad \text{Equation 1.2}$$

In Eqn. 1.2, the heat transfer coefficient replaces the  $(\lambda_T / \Delta x)$  term in Eqn. 1.1. The reason this happens is because convection has a mobile phase, and thickness is no longer an effective way of describing how the heat is transferred. The heat transfer coefficient can be thought of as the inverse of the resistance to heat

transfer. Also, because temperature is a function of distance from a surface, the  $\Delta T$  term is calculated between the surface and the bulk temperature of the mobile phase.

The concept for radiation is that all materials are constantly emitting infrared radiation that is absorbed by other materials, if it is assumed that radiation is emitted directly outward from the surface of objects. While conduction and convection are driven by a temperature gradient, radiation is only based on the temperature of the object emitting radiation.

The rate of heat transfer due to radiation can be described by.

Radiation emitted:  $q_{out} = \epsilon \sigma_{st} (T_s^4)$

Radiation absorbed:  $q_{in} = \alpha \sigma_{st} (T_o^4)$

Taking into account the transparency of the substance and the reflecting power of the container walls, it is possible to establish the conditions for achieving temperature control over the crystal cross section and maintaining its gradient along the crystal axis. With the increase in the substance transparency, the control of the temperature gradients and their constancy becomes more complicated and therefore, convective heat transfer in the melt plays a significant role. Thus, depending on the values of material transparency and reflection ability of the walls, a suitable method of crystallisation for attaining constant temperature along the section of crystal and constant temperature gradient along the crystal axis can be determined [Bagdasarov, 2002] [Bagdasarov, 1988] [Pishchik, 2009].

During high-temperature crystallisation, the formation of the crystal structure is not completed with just the phase transition. Due to high temperature and temperature gradients, several processes continue in various forms at temperatures close to their melting point. Hence, numerical modelling is applied to investigate the factors affecting the shape of the crystal-melt interface during the growth of Ti-doped sapphire crystals by using the Kyropoulos method and also the characteristics of the temperature distributions during the whole cooling process. During the course of this work, the finite element software COMSOL Multiphysics has been used for modelling the heat transfer and melt convection during the Kyropoulos growth of Ti-doped sapphire crystals, as shown in figure 1.31.

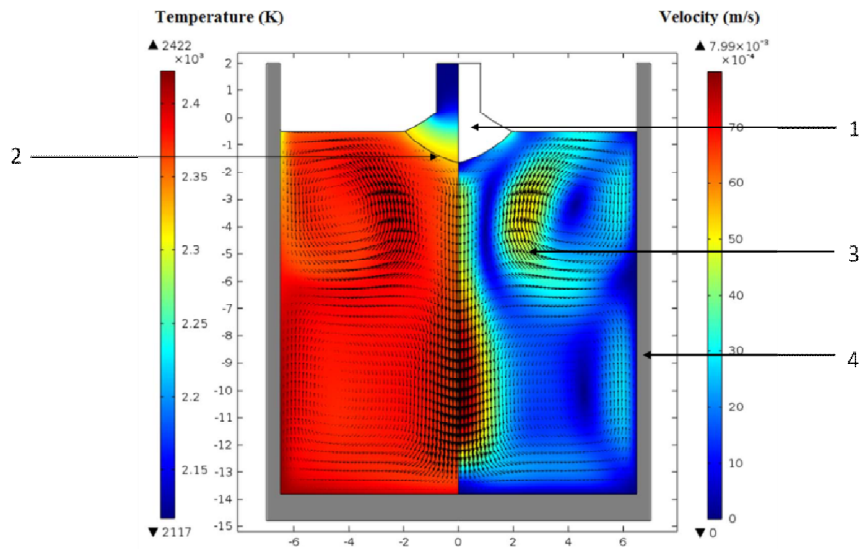


**Figure 1.31:** Flow pattern of the melt during the Kyropoulos crystallization process: (1) growing crystal; (2) solid–liquid interface; (3) melt; (4) crucible. The colour map shows the temperature field (left side) and the velocity field (right side) [Stelian, 2016].

#### 1.11.2.6 Dislocations

Since crystals are grown from melt in the field of temperature gradients, thermoelastic stresses appear. These stresses, when equal to or exceeding the critical stress for dislocation formation, lead to the mechanism of dislocation multiplication due to plastic deformation behind the crystallisation front. There are two kind of residual stresses in the crystal. The first kind is due to temperature field non-linearity. The second kind is due to defects of the real structure, namely, point defect accumulations, dislocations, block boundaries, impurities, and foreign inclusions.

During the crystal growth process, a complex temperature distribution along the crystal causes inhomogeneous thermal expansion of its parts and their elastic interactions, and, as a result, the stresses appear in the crystal even if its outer surface is free. If the action of temperature-induced stresses is considered in an already-formed dislocation-free crystal, where there are no points in the crystal volume where the shear stress exceed the critical one required for dislocation nucleation or the growth of dislocation microloops, then the crystal remains dislocation-free at the macroscale. However the stress value near inclusions may exceed the average values and such stress concentrators are the most probable regions where dislocations may arise, as shown in figure 1.32. If the critical stress is attained somewhere, the nucleated dislocation loops will start to extend, the dislocation multiplication will set in, and the plastic strain will extend over the whole crystal. Only the regions where the stresses are insufficient to move the



dislocation cluster front or even individual dislocations (i.e., where those are lower than the crystal elasticity limit) remain dislocation free.

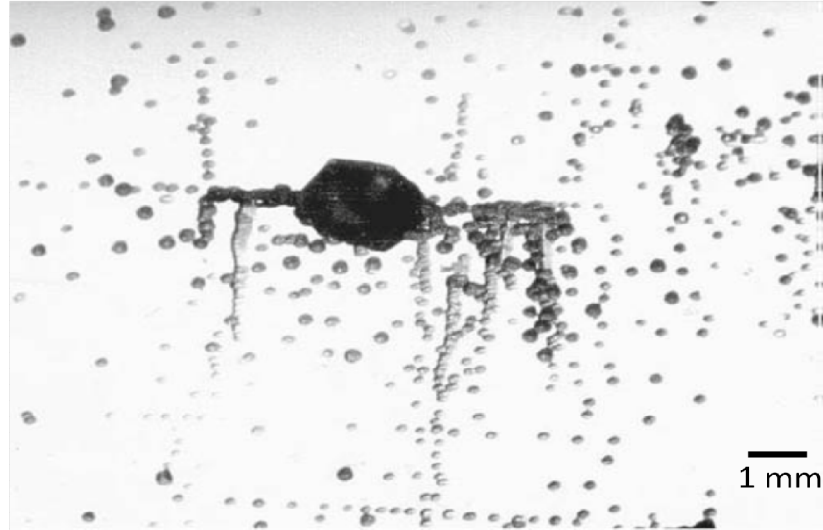


**Figure 1.32:** Dislocations around a faceted pore [Pishchik, 2009].

Plastic flow is associated not only with dislocation sliding but includes also the viscous flow processes with dislocation creep and transfer of vacancies and interstitial atoms. At sub-melting temperatures, plastic straining and diffusion of point defects proceed under much lower stresses. Therefore, the shape and size of the crystal region where the dislocations are nucleated and extended and the point defects are redistributed depend on the thermally induced stresses and temperature in that region. Plastic flow tends to redistribute the crystal material in such a way that the stresses causing the flow will be relaxed and it is over when the total energy of thermoelastic stresses and dislocations attains a minimum.

Now, when the crystal is allowed to cool down to a temperature that is constant over the entire volume and sufficiently low to prevent plastic strain, the regions that were compressed prior to the plastic strain become stretched, and vice versa. The residual internal stresses arising in the crystal in this case are similar in values to the initial thermal ones that caused the plastic strain, but have the opposite sign. The sources of residual internal stresses are the residual strains, i.e., distribution of dislocations and point defects that has been settled as a result of flow.

The formation of dislocations at the growing crystal surface is due to the need to minimize the elastic energy. In this case, the material does not eliminate the stresses but it accumulates in the unstressed state. In the course of this process, the crystal moves with respect to the furnace temperature field. Each element of the surface layer becomes three dimensional and a plastic strain proceeds, thus resulting in relaxation of

stresses that might exist in the corresponding point when it is within the crystal bulk. Finally, the element under consideration attains the temperature zone where there is no plasticity and any straining is impossible. Thus, the grown crystal in each volume element will show a defect structure formed at the moment it leaves the plasticity zone. After cooling down to a constant temperature, the defects chilled in such a manner result in the formation of stresses equal in value and opposite in sign to those that were relaxed by the defects during the growth. If the material is plastic only within a narrow temperature range around the melting point, as is the case for sapphire, the plasticity boundary will go in parallel to the crystallisation front at a small distance therefrom. As a result, the crystal will contain the chilled-in stresses that were at the crystallisation front (with opposite sign). The stresses at the front, in turn, are defined by the temperature field within the crystal bulk.

Thus, the determination of the residual stresses in the crystal is equivalent to determination of thermoelastic stresses in the course of growth and cooling.

### 1.12 Defects

Apart from the point defects, inclusions, segregation and dislocations discussed in the earlier sections there is also the presence of block boundaries as defects. Block boundaries are caused by disorientations in the crystal structure during growth and can lead to inter-crystalline damage. In addition, impurity non uniformities are due to segregation of solutes at the crystallisation front and lead to striations, facets, cellular structures and impurity inclusions in the crystal.

All defects in the crystals are defined by the phenomena occurring during the melting of  $\text{Al}_2\text{O}_3$ , at the crystallisation front and during the cooling process. But these defects are interdependent with respect to their origin and development during the whole process of crystal growth. Thus a summary of these defects and their origins is given below in table 2.

Defects	Origin
<b>Point defects:</b> Vacancies, interstitials, substitution	<ul style="list-style-type: none"> <li>• Trapping of melt dissociation products</li> <li>• Interaction with crystal atmosphere</li> </ul>
<b>Inclusions:</b> Gaseous pores, foreign solid phase, liquid phase	<ul style="list-style-type: none"> <li>• Thermal dissociation products and gas impurities</li> <li>• Interaction with crucible material</li> <li>• Interface instability</li> <li>• Aggregation of point defects (vacancies)</li> </ul>

<b>Line defects (dislocations)</b>	<ul style="list-style-type: none"> <li>• Inheritance of dislocations from seed</li> <li>• Thermoelastic stress during heat transfer</li> <li>• Aggregation of point defects (vacancy)</li> <li>• Aggregation of impurities.</li> </ul>
<b>Blocks (grain structure)</b>	<ul style="list-style-type: none"> <li>• Inheritance of boundaries from seed crystals</li> <li>• Alignment of dislocations</li> <li>• Inclusions of foreign particles</li> <li>• Nucleation on foreign particles</li> </ul>
<b>Impurity non uniformity</b>	<ul style="list-style-type: none"> <li>• Interface instability</li> <li>• Heat transfer</li> <li>• Chemical segregation.</li> </ul>

**Table 2:** Crystal defects and their origins.

### 1.13 Perspectives

- Taking into account the quality requirements for the crystal and the technical considerations of various growth techniques available, the Kyropoulos growth system was selected for the growth of Ti:Al<sub>2</sub>O<sub>3</sub> crystals at the industry RSA Le Rubis.
- There is a need to improve the Kyropoulos growth system from its current state-of-the-art to reach the demands of the crystal dimensions and quality needed for optical applications in PW laser systems.
- A detailed analysis of the current growth process needs to be carried out for possible improvements and to demonstrate the impact of the improved growth process on the crystal productivity.
- The grown crystals have to be characterised for defects which would impact the optical applications. The nature and origin of these defects has to be investigated in order to find solutions to get rid of them.

Based on these perspectives, work was carried out during the course of this thesis and is presented in this manuscript in the following 3 chapters:

**Chapter 2 - Crystal Morphology control:** The current Kyropoulos growth system has been analysed by studying the growth regimes and the shapes of grown crystals. The morphological features detrimental to

the crystal quality have been identified. Finally, a set of growth parameters have been defined which has been demonstrated to improve the crystal morphology.

**Chapter 3 - Crystal shape prediction:** A theoretical study of all the weight forces acting on the crystal during its growth has been studied. Based on this, it has been demonstrated that with a set of measured parameters it is possible to monitor the crystal shape during its growth and hence build up a system that would enable automatic control of the crystal morphology.

**Chapter 4 – Investigation into the milky defect:** A peculiar optical defect in the crystals limits the application of these crystals for laser systems. Characterisation efforts for this defect were carried out along with simulation of the growth system. Finally a hypothesis is presented based on these efforts to reveal the nature and the mechanism of formation for this defect.



## 2 Control over crystal morphology

### 2.1 Introduction

One of the main considerations of the project TitanSaphir is to increase the productivity of the Kyropoulos growth process and the crystals produced. To achieve this goal, the current growth process has to be studied in order to point out possible areas of improvement and then make feasible changes. Finally, discs cut from these crystals have to be checked for their laser performance to validate the growth process for production of crystals for the desired application.

The desired crystal shape for maximum productivity is a cylindrical shape with uniform diameter more than 20 cm which would allow discs to be cut from the length of the cylinder. The crystal should not show the presence of visual defects like bubbles and cracks. The ideal crystal growth process should allow for stable control over the crystal dimensions and be repeatable. The discs cut from these crystals should demonstrate optical homogeneity in terms of titanium concentration, wave transmission, etc.

To this effect, an extensive study of the crystals grown at RSA with respect to their morphology and their growth operation has been carried out. Based on this study, some correlation between regions of defective shape and the growth parameters was noticed. Numerical simulations for the growth configurations at RSA have been carried out by Carmen Stelian. The results of these simulations helped to identify the cause of the defect structures and physical conditions leading to them. To improve the shape of crystals, a set of ideal growth parameters is suggested which, if followed, would lead to growth of crystals with more productive shape and quality. This ideal growth regime has been tested at RSA by Cyril Pezzani under the supervision of Nicolas Barthalay and the validity of the suggested ideal regime in achieving a more productive crystal was demonstrated. To make the growth of crystals with good morphology more reproducible, an automatic growth system has been developed and then implemented by Cyberstar for their growth furnace. Crystal growth experiments have been carried out at RSA to reveal the shape of the submerged crystal-melt interface of the growing crystals which helped explain the profile of the titanium distribution in the crystals. Finally, optical characterisation of the crystal samples was conducted by Guillaume Alombert-Goget at ILM, Lyon, to check for the suitability of the crystals obtained for the laser applications envisioned.

### 2.2 Kyropoulos Growth set-up

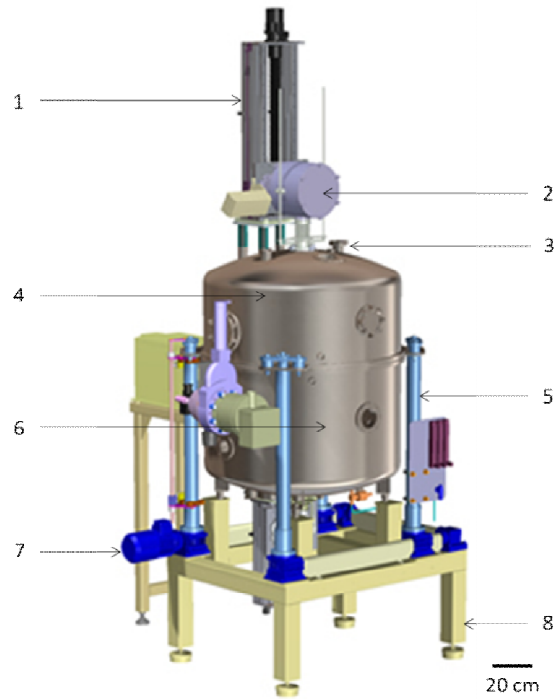
During the course of this project sapphire crystals have been grown using the Kyropoulos technique at RSA Le Rubis using furnaces of three different configurations, all manufactured by Cyberstar. Their

characteristics have been summarised in table 2.1. The method of crucible heating in these machines is through transfer of energy to the graphite susceptor by induction heating coils. The basic configuration is the same in all three furnaces with respect to the parts and the materials used, but they have different capabilities for the crucible which they can hold and hence the size of crystal that can be grown. The three configurations with regards to the size of crystals grown and crucible dimensions are as follows: the biggest machine, (henceforth known as configuration no.7, according to the convention at RSA) is operated with a crucible with dimensions of 275 mm in diameter and 300 mm height and crystals weighing up to 38 kg were obtained with this configuration. The next machine (configuration no.4) is operated with a crucible measuring 220 mm in diameter and 290 mm in height and crystals obtained weighed up to 28 kg. The smallest machine (configuration no.5) had a crucible with dimensions of 140 mm in diameter and 160 mm in height enabling production of crystals weighing up to 7 kg. An interesting feature of the Kyropoulos system at RSA is that it allows remote observation and control of the machine for parameters like seed movement, temperature and heater power.

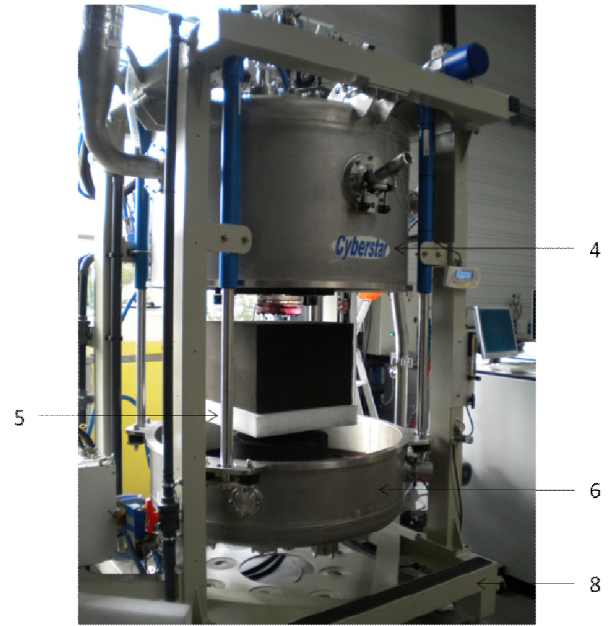
<b>Machine Reference No.</b>	<b>Crucible Dimensions Diameter x Height (mm<sup>3</sup>)</b>	<b>Weight of crystal (Kg)</b>
7	275 x 300	38
4	220 x 290	28
5	140 x 160	7

**Table 2.1:** Kyropoulos growth systems at RSA Le Rubis.

General schemes of the furnace for the biggest configuration, along with the materials used, are shown in figure 2.1 and figure 2.2. The materials used for the other two furnaces are the same but the dimensions are scaled according to the size of furnaces for the three machines. The only noticeable difference in the construction of the big machine compared with the two smaller versions is the method of opening the furnace. For the biggest machine, as shown in figure 2.1, there are two parts – the upper hatch and lower hatch. To load and unload the crucible into the furnace, the lower hatch is unsealed from the upper one and lowered down to split up the furnace and leave a gap big enough for the crucible. For the two smaller machines, the crucible is loaded and unloaded in the furnace through a front opening door.



(a)



(b)

**Figure 2.1:** (a) Schematic diagram for the Kyropoulos growth system showing the components, (b) Kyropoulos installation at RSA Le Rubis. (1) Seed translation mechanism, (2) crystal weight transducer, (3) observation window, (4) furnace vessel (upper hatch), (5) Furnace vessel opening system, (6) furnace vessel (lower hatch), (7) gas pump, (8) furnace support.



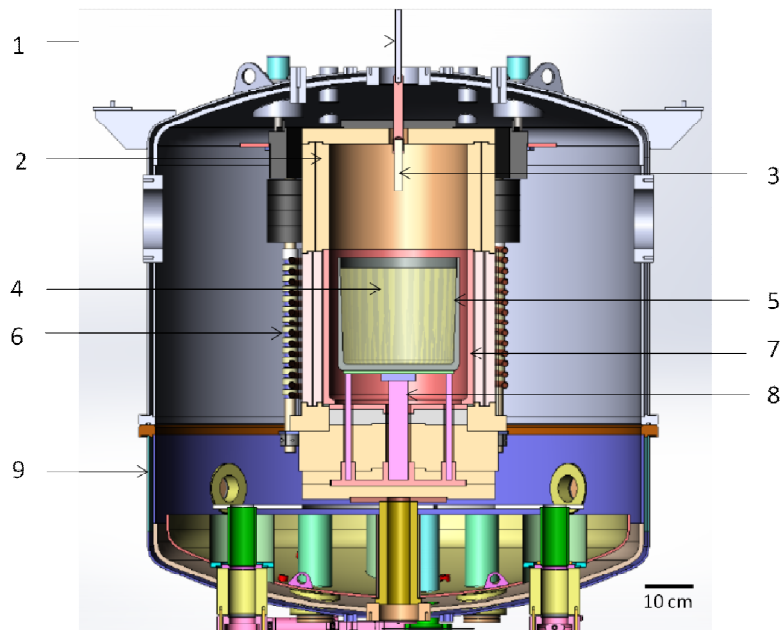


**Figure 2.2:** Schematic cut-away diagram for the Kyropoulos growth furnace showing the components and the materials used. (1) Seed holder - tungsten, (2) insulation - graphite, (3) seed, (4) melt, (5) crucible - molybdenum, (6) induction coils - copper, (7) susceptor - graphite, (8) crucible support - tungsten, (9) outer vessel - steel.

## 2.3 Sapphire crystal growth process

The whole crystal growth process begins from the preparation of the crucible and finishes with the extraction of the crystal from the furnace. For a crystal weighing 38 kg grown in the big machine, it takes up to 30 days from the charging of the crucible with the raw material to the extraction of the crystal. The process is to be controlled under strict quality conditions with well-established manufacturing guidelines to ensure that the crystals produced are of the expected nature and are repeatable.

### 2.3.1 Crucible preparation

The first step in the growth process is the charging of the crucible with raw material. For a crucible which is being reused, there is always some residue left in the form of polycrystalline sapphire at the bottom from the earlier crystal growth process after the extraction of the crystal. The crystal is weighed along with this residue to know exactly the weight of sapphire raw material already present. In the case of  $\text{Ti}:\text{Al}_2\text{O}_3$  crystals the raw materials are  $\alpha\text{-Al}_2\text{O}_3$  in the form of pure alumina crakle (stones), which is a by-product of the Verneuil process and powder along with 1.81 mass% Ti doped  $\text{Al}_2\text{O}_3$  powder. Alumina used is produced by RSA Le Rubis company in good agreement with JSPDS file n° 46-1212. The purity is at least 99.99%. The mass of Ti doped  $\text{Al}_2\text{O}_3$  powder to be introduced is calculated by doing an estimate of the concentration of

titanium in the residue left in the crystal taking into account the segregation of titanium during the former crystal growth. The desired titanium mass concentration in the melt is 0.1%.

The crucible is charged with these raw materials, but it is important to take care that the crucible is not filled up to the brim with the raw materials because the density of liquid sapphire ( $3.03 \text{ kg/cm}^3$ ) is less than that of solid sapphire ( $3.98 \text{ kg/cm}^3$ ) and hence the melt occupies much more volume than the initial charge. It is also important to ensure the purity of the raw materials and to protect the contents of the charged crucible from getting contaminated until the machine is sealed and the heating process begins. A reference for the typical contributions of the components of the raw material for growing a crystal in configuration no.4 of 25 kg is presented in table 2.2.

Constituents	Weight (g)	% weight
Al <sub>2</sub> O <sub>3</sub> craquelé	18000	72
Al <sub>2</sub> O <sub>3</sub> powder	5000	20
Ti doped Al <sub>2</sub> O <sub>3</sub> powder	500	2
Crucible residue	1500	6
<b>Total</b>	25000	100

**Table 2.2:** Crucible charge constituents and their typical contributions.

### 2.3.2 Furnace preparation

It is very important to ensure a clean environment inside the furnace and hence the inside walls of the furnace are cleaned with a vacuum cleaner before charging the crucible with the raw materials. Once the crucible is prepared, it is loaded inside the furnace on the crucible support and covered at the top with a cloth to prevent the contents from getting contaminated. The next step is to install a sapphire seed in the seed holder which promotes nucleation during the crystallisation process. The crystallographic orientation of the seed dictates the orientation of the growing crystal; since we are interested in A-axis crystals, seeds are cored out from earlier A-axis crystals along their length. The seeds used are cylindrical with dimensions of 10 cm in length and 2 cm in diameter. A seed is attached to the seed holder and rotated to check for the proper alignment of the seed with respect to the crucible. The seed is then retracted to a position 15 cm above the crucible top to take it away from the hot zone and hence prevent it from melting during the melting of the contents in the crucible. The cloth covering the crucible is removed and the graphite insulation packages are placed around the crucible before finally closing and sealing the furnace. This marks the end of all manual operations and henceforth the control systems take over.

### 2.3.3 Furnace operation

The Kyropoulos furnace, once sealed with the crucible inside, is completely closed and does not allow visual inspection of the growth process. A small exception is the presence of a glass window at the top of the furnace which allows an observational camera set-up. It has a limited view of the crucible which is permitted by a hole drilled through the insulation layers surrounding the crucible in the axis of its view.

The operation of the Kyropoulos system is carried out by controlling the growth environment and the seed movement based on the feedback of measured parameters.

The feedback parameters which can be measured are:

- Weight: The weight is measured by a weight transducer at the seed pulling mechanism. It measures the weight of the seed and that of the growing crystal attached to the seed with a resolution of 0.1 g.
- Temperature: The temperature is measured using a pyrometer focused on the outer wall of the crucible. It can measure temperatures only above 1000°C.
- Pressure: The pressure sensor reports the gas pressure inside the furnace with a resolution of  $10^{-6}$  mbar.

The parameters which are controlled during the growth process are:

- Seed position: The seed pulling mechanism enables the movement of the seed during the seeding process and the slow extraction during the crystal growth process. It is an extremely sensitive mechanism which allows very small increments of displacement and position measurements in steps of 0.01 mm.
- Seed rotation: It is also possible to rotate the seed around its own axis.
- Power: The temperature inside the furnace for the melting of the raw materials and maintaining the crystallisation conditions is controlled by varying the input power to the induction heating coils.
- Pressure: The gas pressure inside the furnace is controlled by means of a vacuum pump, valves and gas injection pumps which can inject air and argon.

The Kyropoulos growth operation carried out using the control system can be described in the following steps:

### **2.3.3.1 Low pressure sanitisation**

After sealing the machine, the vacuum pump is started which brings down the air pressure inside the furnace from atmospheric pressure,  $1.013 \cdot 10^3$  mbar to  $3.5 \cdot 10^{-4}$  mbar; meanwhile ramping up the heating power to 10%. This process helps to clean the gas atmosphere inside by flushing out all gases and particulate already present in the furnace and brings the crucible temperature up to 1000°C. This process goes on for about 12 hours and also dries up the absorbed moisture from the components of the furnace.

### **2.3.3.2 Crucible pre-heating**

The next step, which goes on for the next 12 hours, is the heating of the crucible up to 1500°C by increasing the power to 17%. During this stage, argon is pumped into the furnace and a continuous flow is maintained by opening a valve which allows the flow of these gases. The pressure inside the furnace from this stage here on is maintained at  $1 \cdot 10^3$  mbar. This gas flow condition is maintained throughout the rest of the growth process and it helps to main a neutral atmosphere in the furnace and flush out gaseous products formed during the process.

### **2.3.3.3 Melting**

This step is the steady ramp up of power from 17% to 37% which raises the temperature inside the crucible to reach slightly more than 2050°C, the melting point of sapphire. The temperature is maintained at these conditions for 12 hours which ensures that the alumina raw material is completely melted and there is no solid chunk left. The state of the melt is investigated using the feed from the camera by checking for a spoke pattern as shown in figure 2.3(a) which indicates a good uniform convective flow. Figure 2.3(b) shows the simulated temperature distribution at the surface of the melt for the spoke pattern. The bright parts in the image are regions of higher temperatures while the dark folds are local areas of lower temperature on the free surface of the melt. When the centre of the spoke pattern is close to the centre of the free surface on the melt, it is the appropriate moment for the start of the seeding process. Such a flow structure ensures that seeding can be started exactly in the point of lowest temperature on the free surface of the melt, providing a stable start to crystal growth and shouldering [Timofeev, 2015].

The reason of the spoke pattern is as follows. Sapphire melt heated from the crucible side wall moves up via buoyancy and flows over the free surface from the periphery to the center, stimulated by the Marangoni effect. To conserve mass of the radial flow to the center within the shrinking flow area, the spokes are formed by downward melt motion. Downward melt motion decreases the total heat flux from the melt to the free surface and, as a consequence, the “spoke” temperature decreases due to radiation from the melt to the surrounding area.

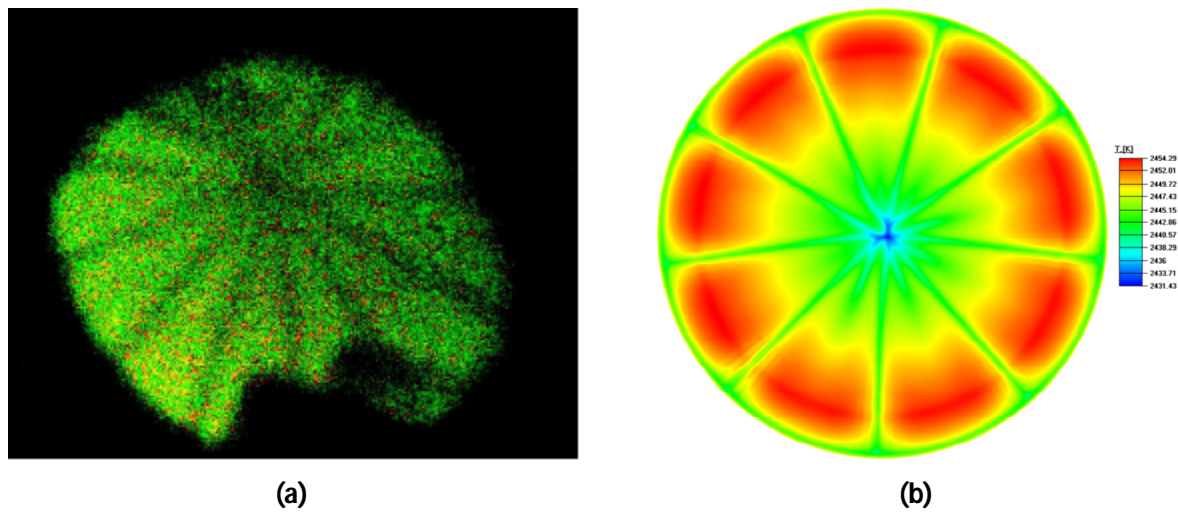


**Figure 2.3:** (a) Free surface of the melt observed by the mounted camera and (b) Computed temperature field of the free surface of the melt [Timofeev, 2015]

#### 2.3.3.4 Seeding

The seeding process is very sensitive since it marks the beginning of the solidification process and hence the start of crystal growth and determines the quality of the growing crystal. It begins with a gradual descent of the seed from its position 150 mm away from the crucible top towards the crucible while also rotating it at a rate of 2-10 rpm. This descent is carried out in slow gradual steps of movement, taking it closer to the hot zone. The main concern is to make sure that the seed does not melt as it gets closer to the melt in the crucible and hence approaches the melting temperature. It is very important to check the weight displayed for indications of the melting of the seed. Thus the approach towards the crucible is done with great caution and if there is any indication of a decrease in weight the seed is moved back far away from the hot zone. Then the heating power is decreased by a very small decrement and the descent of the seed is done again.

This process is repeated many times by the operator until he is convinced that the temperature conditions are perfect and there is no melting of the seed. Once the seed tip reaches the crucible top, i.e. 150 mm from the initial position, the final descent to the free surface of the melt takes place and it is brought in contact with the melt while being visualised in the camera feed. The moment the seed touches the melt, the liquid sticks to it with a meniscus weighing it down and hence there is a sudden increase in the weight by 5-10 g sensed by the seed holder, indicating the moment of contact. From here on, the operator tries to maintain steady state conditions to ensure that the seed and the melt are in equilibrium. The equilibrium conditions here are maintained by regulating the temperature using the heating power. If there is a sudden increase in the weight of the seed, it indicates that there is abrupt solidification at the seed instead of

smooth crystallisation and hence the power is increased to bring up the temperature and shift back to the equilibrium condition. Conversely, if there is a decrease in weight it indicates melting of the seed and hence the power is decreased to bring down the temperature slightly and hence get back to the equilibrium condition.

Thus the process of seeding marks the start of crystal growth and needs expertise on the part of the operator to respond to the feedback signals and control the parameters with sensitivity in order to achieve ideal seeding conditions. The seeding process requires constant operator supervision and cannot be automated as of yet, unlike the other stages, and requires 5-8 hours of constant monitoring.

The evolution of heating power and temperature inside the furnace during the four stages of furnace operation prior to commencement of the crystal growth is shown in figure 2.4.

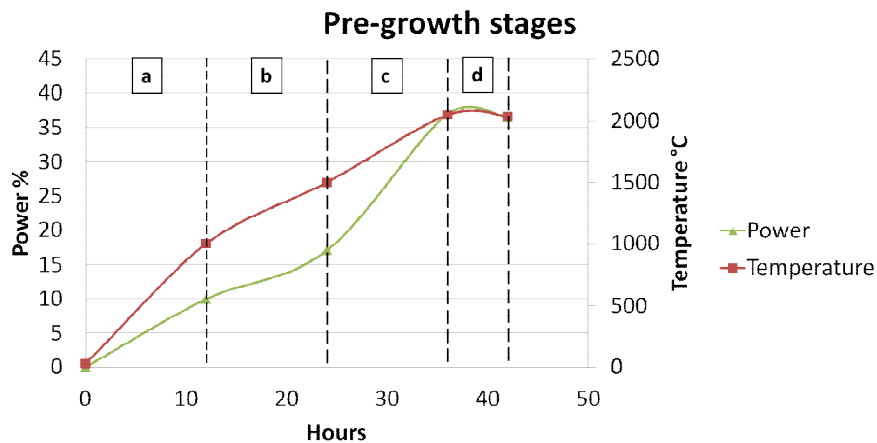


**Figure 2.4:** Power and temperature regulation in the stages prior to crystal growth: (a) Low pressure sanitisation, (b) crucible pre-heating, (c) melting, (d) seeding.

### 2.3.3.5 Crystal growth

The crystal growth process begins after ensuring for 2-3 hours that the seed is in contact with the melt without any change in the weight measured. Henceforth, there is a controlled decrease in power which decreases the melt temperature and promotes crystallisation. The seed onto which the crystal is growing is always rotated at a speed of 2 - 6 rpm and pulled out slowly with a speed of 0.1-0.5 mm/hr. The rotation and pulling of the seed ensure that the crystal does not stick to the crucible walls. At the end of the process, which takes up to 500 hours for a 26 kg crystal in machine configuration 4, the crystal is completely ready, as indicated by its weight, and the furnace temperature is gradually lowered down to room temperature before opening up the furnace for the extraction of the crystal. The cooling-down period

is up to 24 hours. The crystal growth process dictates the morphology and the quality of the crystal and hence will be discussed in detail in the following sections.

## 2.4 Crystal morphology and quality

One of the primary factors affecting the productive volume of the crystals is the crystal morphology. Since the objective is to cut discs from the crystal, it is our objective to produce crystals with uniform diameter and shape. This will enable the cutting and preparation of required diameter discs throughout the length of the crystal. Any deviation in crystal shape from the ideal cylindrical bottle shape decreases the productivity but also is an indication of the occurrence of many macroscopic defects in the crystal. Thus, one of the primary objectives of the project TitanSaphir is to improve the quality of crystals with respect to their shape and to get rid of visible macroscopic defects.

In the following sections, a detailed study of the growth conditions affecting the crystal morphology will be presented and ideal growth evolution parameters for production of crystals with good morphology and repeatability will be presented. For the sake of consistency, only crystals grown in configuration no. 4 will be compared and studied. But the issues of crystal morphology and factors influencing them are very similar in the two other configurations as well.

### 2.4.1 Growth parameters to be studied

As discussed in the earlier sections we have some growth parameters which are monitored throughout the process and based on those we also derive some more parameters which give us a better sense of the growth evolution. The growth system records the parameters every minute during the whole growth process.

The parameters which will be studied are presented in columns from left to right as follows:

Crystal Identity														
time	mass	time diff	Growth rate	z cristal	Seed posi	posn diff	pulling rate	températi	Temp diff	temp rate	puissance	power dif	power rat	temp:pow
hr	gm	hr	gm/hr	mm	mm	mm	mm/hr	°C	°C	°C/hr	%	%	%/hr	°C/power%

**time (h):** time elapsed since seeding.

**mass (g):** weight measured at the seed holder. (It is important to note that the mass measured at the seed holder is only indicative of the growing crystal and not the actual weight of the crystal. This is because of the fact that a portion of the crystal is submerged in the melt and hence there are buoyancy and capillary forces which act on it. A detailed study on the resolution of the components of force acting on the crystal will be carried out in chapter 3).

**time diff (h):** time interval between two consecutive weight readings.

**growth rate (g/h):** mass growth rate between two consecutive weight readings..

**z cristal (mm):** vertical position of seed between two consecutive weight readings.

**seed position (mm):** vertical displacement of seed from initial seeding position.

**position difference (mm):** seed displacement between two consecutive weight readings.

**pulling rate (mm/h):** average pulling rate of the seed between two consecutive weight readings.

**temperature (°C):** temperature measured at crucible outer surface by pyrometer.

**temperature difference (°C):** temperature difference between two consecutive weight readings.

**temperature rate (°C/h):** rate of change of measured temperature between two consecutive weight readings.

**puissance (%):** heating power level.

**power difference (%):** change in power level between two consecutive weight readings.

**power rate (%/h):** rate of change of power level between two consecutive weight readings.

**temp:power (°C/%):** ratio of temperature difference to power level difference between two consecutive weight readings.

**growth:pulling (g/mm):** ratio of mass of crystal grown to distance of pulling between two consecutive weight readings.

**growth:temperature (g/°C):** ratio of mass of crystal grown to temperature change between two consecutive weight readings.

**growth:power (g/%):** ratio of mass of crystal grown to power level difference between two consecutive weight readings.

#### 2.4.2 Crystal morphology analysis

In the following section, an effort to correlate the various growth parameters and the crystal morphology obtained as a result of the growth process has been made. Based on the study of all the crystals grown; an ideal growth regime and its parameters have been decided upon. These ideal growth parameters have



been used to compare with the growth parameters of the crystals and point out the deviations and their effects on the crystal morphology. For each crystal studied, first the crystal morphology is discussed and the distinguishing features are pointed out using the images. The detailed description for four crystals which are representative of the peculiar crystal morphologies have been presented in this section with some further examples in Appendix I.

The various growth parameters and derived parameters during the evolution of crystal growth are presented in the form of a table. Smaller intervals of time of growth and mass of crystal are chosen for the initial stages after seeding and the intervals progressively increase. This is because the initial growth stages are much more sensitive to changes in control parameters and affect the quality of the growing crystal. Some parameters are marked within green or red rectangular boundaries. The ones within green boundaries indicate the parameters that correspond to or follow the trend of ideal values of growth and the red ones significantly deviate from the ideal trend.

The plot of growth evolution in time for the two parameters, growth rate (g/hr) and ratio of growth:pulling (g/mm) is presented for each crystal. A supplementary plot detailing the evolution of these parameters for the initial growth stage (up to 5 kg) is provided to study the sensitive initial growth stage in detail. The markers for the ideal growth parameters are provided in both the plots to help compare the deviation of the growth regime for the crystal from the ideal one. The deviation in the plots for the final part of growth (final time step) is to be neglected, since it is due to abnormal readings during the extraction of the completed crystal.

Finally, a written description of the data analysed is provided for the growth parameters. This description corresponds to the ranges of values marked in the table within the highlighted red and green rectangular boundaries. Each description is then linked to the features of the crystal morphology using the reference numbers in green or red corresponding to the boundaries marked in the table of growth parameters.

The ideal growth parameters are presented first, but it is to be kept in mind that they were developed after studying the growth regimes of all the crystals discussed with non-desirable shapes. The ideal growth parameters have been presented as a reference in all the growth descriptions to point out the deviations in the growth regimes which led to the undesired features in the crystal shape.

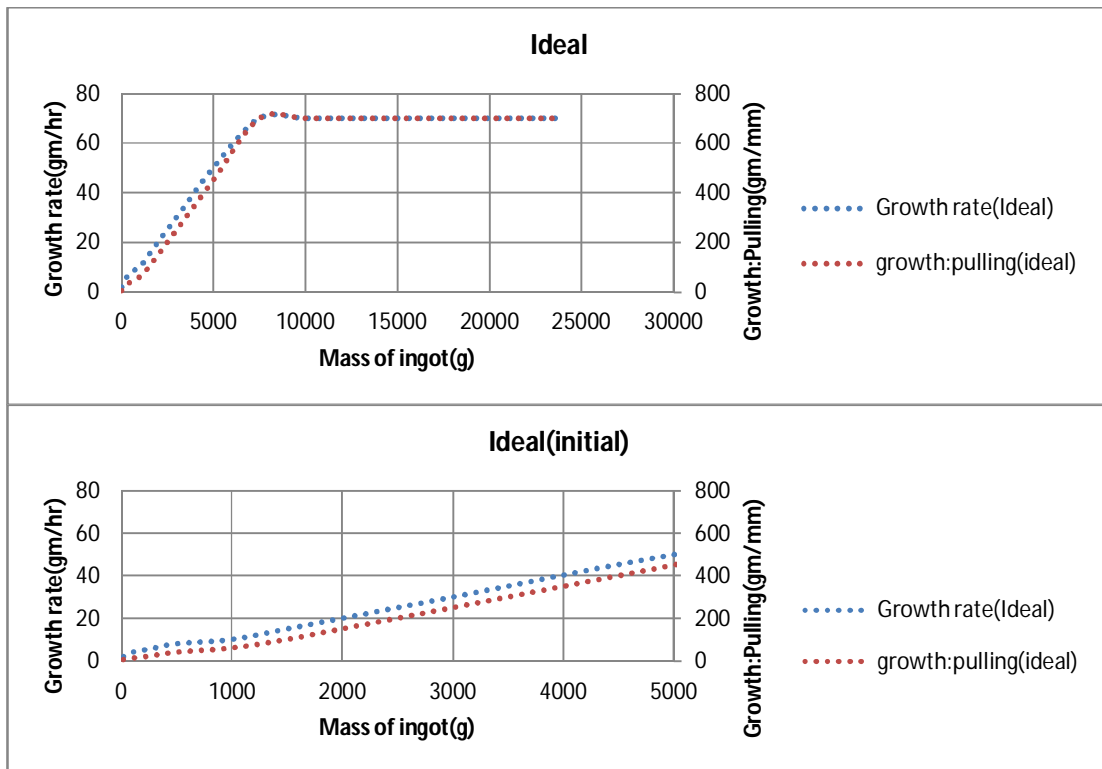
The crystal growth regime is discussed for the following crystals:

- K01-04-14: It is an example of a crystal with a very bad morphology. The crystal shape is not axially symmetrical and there are rapid changes in the radial dimension along the axial length.

- K06-04-14: This crystal has an axisymmetrical shape with some variations in radial dimension during its growth. There is formation of a thick flat plate at the top of the crystal.
- K10-04-14: This crystal has an axisymmetrical shape for most of its axial length except the top portion. There is the presence of a thin plate formation at the top followed by a large cavity below.
- K12-04-14: This is an example of crystal with an acceptable shape. It is axisymmetric throughout its axial length. It has no evidence of plate formation at the top. This crystal was grown by following the ideal growth parameters, which were developed by studying the examples of the three earlier crystals and similar crystals discussed in Appendix I.

### 2.4.2.1 Ideal

Ideal Case 1.2																
time	mass	time diff	Growth rate	raz cristal	(nSeed posi	posn diff	Tirage	températu	Temp diff	temp rate	puissance	power dif	power rat	temp:pow	growth:pu	Growth:Temp
hr	gm	hr	gm/hr	mm	mm	mm	mm/hr	°C	°C	°C/hr	%	%	%/hr	°C/power%	gm/mm	gm/°C
0.00	5.00				0.00											
7.50	20.00	7.50	2.00		3.00	3.00	0.40			#DIV/0!					5.00	
17.50	50.00	10.00	3.00		6.75	3.75	0.38			#DIV/0!					8.00	
30.00	100.00	12.50	4.00		10.92	4.17	0.33			#DIV/0!					12.00	
50.00	200.00	20.00	5.00		16.47	5.56	0.28			#DIV/0!					18.00	
66.67	300.00	16.67	6.00		20.47	4.00	0.24			#DIV/0!					25.00	
91.67	500.00	25.00	8.00		25.47	5.00	0.20			#DIV/0!					40.00	
141.67	1000.00	50.00	10.00		33.81	8.33	0.17			#DIV/0!					60.00	
175.00	1500.00	33.33	15.00		38.81	5.00	0.15			#DIV/0!					100.00	
200.00	2000.00	25.00	20.00		42.14	3.33	0.13			#DIV/0!					150.00	
233.33	3000.00	33.33	30.00		46.14	4.00	0.12			#DIV/0!					250.00	
273.33	5000.00	40.00	50.00		50.58	4.44	0.11			#DIV/0!					450.00	
309.05	7500.00	35.71	70.00		54.15	3.57	0.10			#DIV/0!					700.00	
344.76	10000.00	35.71	70.00		57.73	3.57	0.10			#DIV/0!					700.00	
380.48	12500.00	35.71	70.00		61.30	3.57	0.10			#DIV/0!					700.00	
416.19	15000.00	35.71	70.00		64.87	3.57	0.10			#DIV/0!					700.00	
451.90	17500.00	35.71	70.00		68.44	3.57	0.10			#DIV/0!					700.00	
487.62	20000.00	35.71	70.00		72.01	3.57	0.10			#DIV/0!					700.00	
544.76	24000.00	57.14	70.00		77.73	5.71	0.10			#DIV/0!					700.00	



The ideal crystal growth parameters were developed by studying the growth parameters, pulling rate and growth mass along with the other derived parameters for all the available crystals. The growth parameter regimes responsible for the portions of crystals with acceptable morphology were identified. These series of growth parameters for various acceptable portions from different crystals were stitched together to form the complete set of growth parameters which would define the pulling rate and the growth mass rate from the seeding to the complete growth of crystal.

#### 2.4.2.2 K01-04-14 (irregular shape)

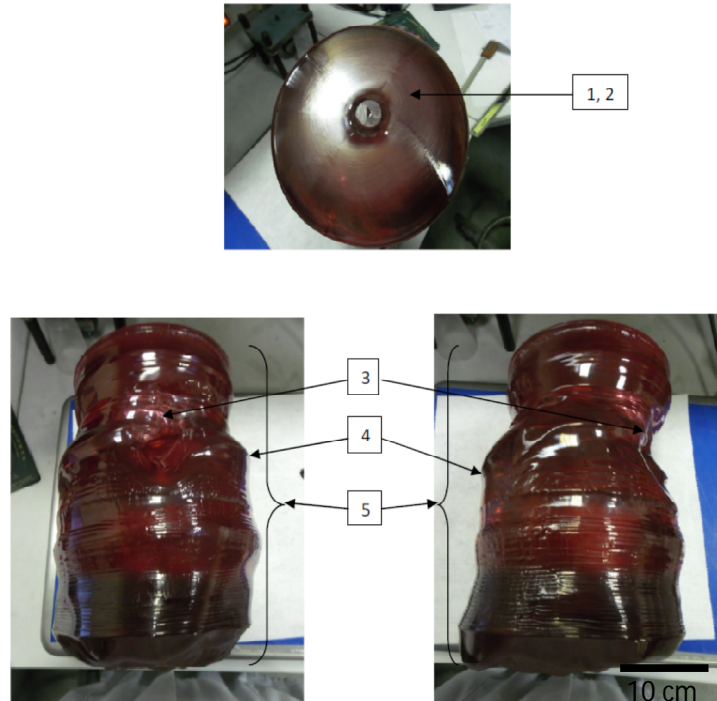
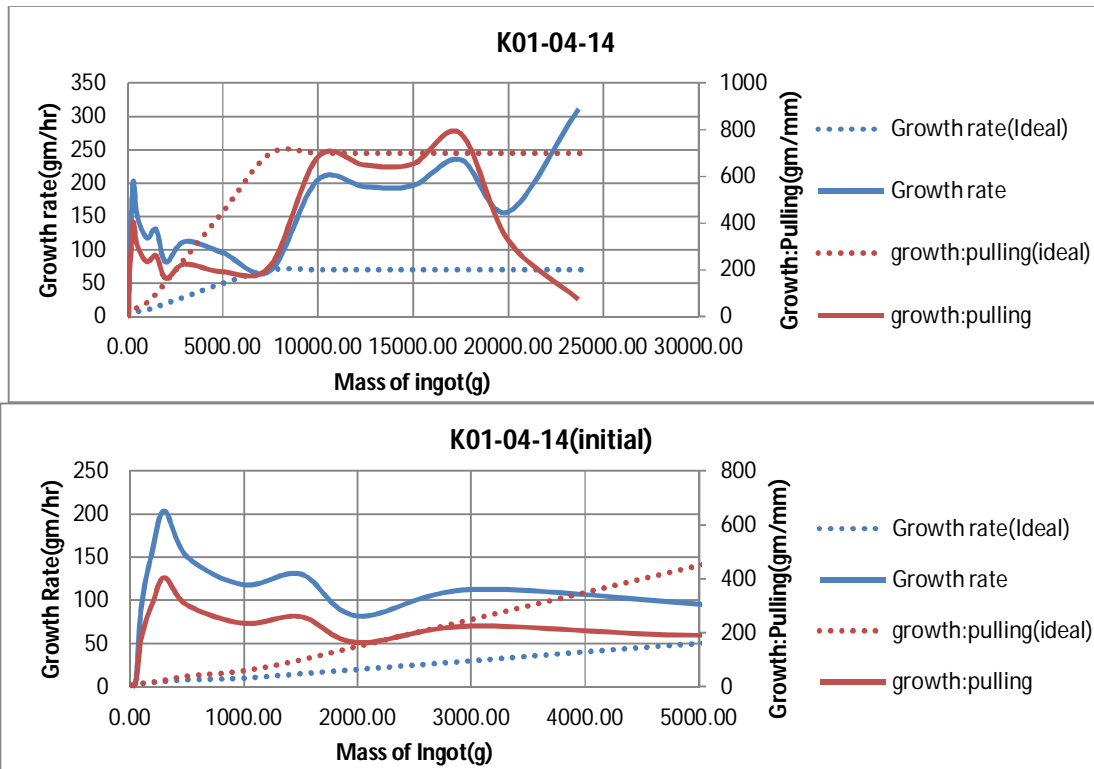


Figure 2.5: Top view and side view of crystal K01-04-14 weighing 23.7 kg.

#### Crystal Morphology features marked in the images above

- 1) Big diameter flat plate. [4] [5]
- 2) Plate with small bubbles layer beneath. [4] [5]
- 3) Constriction of diameter at 50 mm height from seed. [6]
- 4) Increase in diameter at 100 mm height from seed. [1]
- 5) Overall uneven crystal shape with changes in diameter throughout the height. [1] [3]

time	mass	time diff	Growth r	z cristal	Seed posi	posn diff	pulling ra	températi	Temp diff	temp rate	puissance	power dif	power rat	temp:pow	growth:pi	Growth:T	growth:pow
hr	gm	hr	gm/hr	mm	mm	mm	mm/hr	°C	°C	°C/hr	%	%	%/hr	°C/power%	gm/mm	gm/°C	gm/power%
0.02	8.30			-32.85	0.00			2029.00			36.80						
32.86	20.00	32.85	0.36	-22.44	10.41	10.41	0.32	2028.00	1.00	0.03	36.61	0.19	0.0057	5.38	1.12	11.70	62.90
37.16	50.10	4.30	7.01	-20.30	12.55	2.14	0.50	2027.00	1.00	0.23	36.53	0.08	0.0186	12.50	14.07	30.10	376.25
37.69	100.10	0.53	94.19	-20.03	12.82	0.27	0.51	2028.00	-1.00	-1.88	36.53	0.01	0.0151	-125.00	185.19	-50.00	6250.00
38.32	201.60	0.63	161.04	-19.71	13.14	0.32	0.51	2031.00	-3.00	-4.76	36.52	0.01	0.0143	-333.33	317.19	-33.83	11277.78
38.82	302.80	0.50	203.42	-19.46	13.39	0.25	0.50	2033.00	-2.00	-4.02	36.51	0.01	0.0141	-285.71	404.80	-50.60	14457.14
40.13	500.30	1.31	150.70	-18.81	14.04	0.65	0.50	2035.00	-2.00	-1.53	36.50	0.01	0.0099	-153.85	303.85	-98.75	15192.31
44.37	1001.60	4.25	118.05	-16.68	16.17	2.13	0.50	2034.00	1.00	0.24	36.45	0.04	0.0101	23.26	235.35	501.30	11658.14
48.21	1501.60	3.83	130.47	-14.76	18.09	1.92	0.50	2032.00	2.00	0.52	36.40	0.05	0.0133	39.22	260.42	250.00	9803.92
54.30	2000.60	6.09	81.96	-11.72	21.13	3.04	0.50	2031.00	1.00	0.16	36.28	0.12	0.0195	8.40	164.14	499.00	4193.28
63.17	3000.70	8.88	112.68	-7.28	25.57	4.44	0.50	2026.00	5.00	0.56	36.11	0.18	0.0202	27.93	225.25	200.02	5587.15
84.06	5001.60	20.89	95.80	3.17	36.02	10.45	0.50	2019.00	7.00	0.34	35.69	0.42	0.0201	16.71	191.47	285.84	4775.42
120.32	7501.60	36.27	68.93	14.68	47.53	11.51	0.32	2006.00	13.00	0.36	34.94	0.75	0.0206	17.38	217.20	192.31	3342.25
132.50	10000.10	12.18	205.20	18.34	51.19	3.66	0.30	1995.00	11.00	0.90	34.62	0.32	0.0260	34.70	682.65	227.14	7881.70
145.34	12501.50	12.84	194.81	22.20	55.05	3.86	0.30	1983.00	12.00	0.93	34.36	0.26	0.0201	46.51	648.03	208.45	9695.35
158.06	15001.80	12.72	196.51	26.03	58.88	3.83	0.30	1969.00	14.00	1.10	34.09	0.27	0.0211	52.04	652.82	178.59	9294.80
168.68	17502.60	10.62	235.55	29.22	62.07	3.19	0.30	1959.00	10.00	0.94	33.89	0.20	0.0192	49.02	783.95	250.08	12258.82
184.61	20002.30	15.93	156.96	36.83	69.68	7.61	0.48	1954.00	5.00	0.31	33.62	0.27	0.0170	18.52	328.48	499.94	9258.15
196.53	23715.10	11.92	311.48	87.87	120.72	51.04	4.28	1949.00	5.00	0.42	33.35	0.27	0.0231	18.18	72.74	742.56	13501.09



### *Growth Features*

#### **Growth Rate:**

Very high growth rate of crystal mass throughout the growth process. (100 g – 20000 g) [1]

#### **Pulling Rate:**

Initial higher rates of pulling for seed. (0 g – 100 g) [2]

Too high pulling speed for seed. (300 g – 5000 g) [3]

#### **Temp:Power:**

Negative values. (100 g – 500 g) [4]

#### **Growth:Pulling:**

Very High initial values. (100 g – 1500 g) [5]

Sudden decrease and lower values. (5000 g – 7500 g) [6]

### 2.4.2.3 K06-04-14 (Flat top)

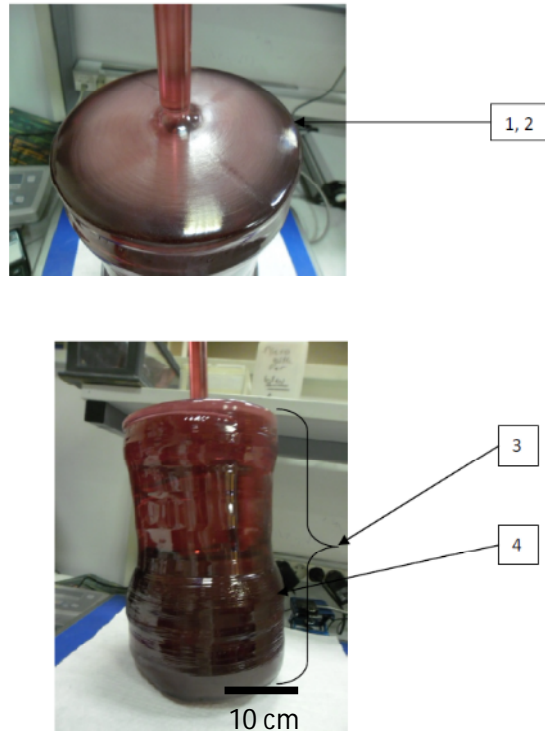
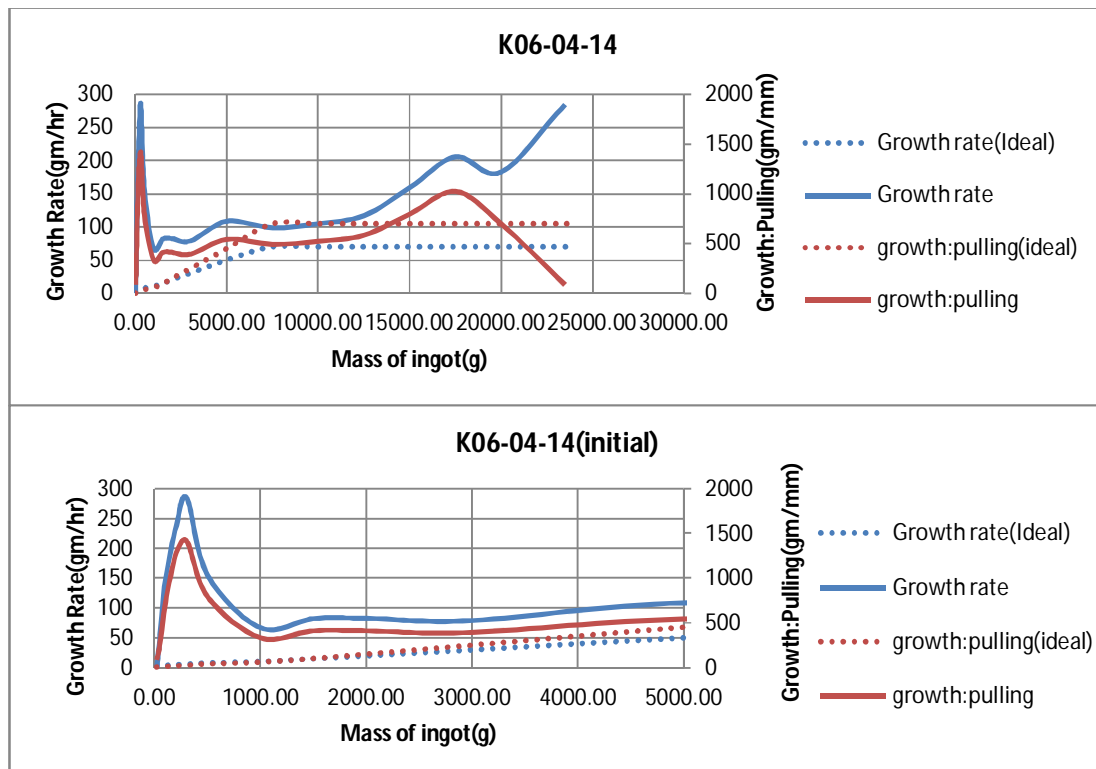


Figure 2.6: Top view and side view of crystal K06-04-14 weighing 23.5 kg.

#### Crystal Morphology features marked in the images above

- 1) Big Diameter flat plate. [1] [3] [4] [5]
- 2) Plate with small bubbles layer beneath. [1] [3] [4] [5]
- 3) Overall even crystal shape with uniform diameter throughout the height. [6]
- 4) Sudden Increase in Diameter. [2] [7]

k06-04-14																			
time	mass	time diff	Growth r	z cristal	(r Seed posi	posn diff	pulling ra	températ	Temp diff	temp rate	puissance	power dif	power rat	temp:pow	growth:pi	Growth:T	growth:pi	growth:pi	growth:pi
hr	gm	hr	gm/hr	mm	mm	mm	mm/hr	°C	°C	°C/hr	%	%	%/hr	C/power	gm/mm	gm/°C	m/power	m/power	m/power
0.02	5.00			-13.94	0.00			2080.00			35.90								
17.70	20.00	17.68	0.85	-13.77	0.17	0.17	0.01	2079.00	1.00	0.06	36.06	-0.16	-0.0090	-6.25	88.24	15.00	-93.75		
18.25	50.20	0.55	55.16	-13.66	0.28	0.11	0.20	2081.00	-2.00	-3.65	36.06	0.00	0.0000	#DIV/0!	274.55	-15.10	#DIV/0!		
18.60	101.60	0.35	147.56	-13.59	0.35	0.07	0.20	2083.00	-2.00	-5.74	36.05	0.01	0.0287	-200.00	734.29	-25.70	5140.00		
19.03	204.40	0.43	238.30	-13.51	0.43	0.08	0.19	2086.00	-3.00	-6.95	36.05	0.00	0.0000	#DIV/0!	1285.00	-34.27	#DIV/0!		
19.38	303.20	0.35	283.64	-13.44	0.50	0.07	0.20	2088.00	-2.00	-5.74	36.05	0.00	0.0000	#DIV/0!	1411.43	-49.40	#DIV/0!		
20.65	500.40	1.28	154.36	-13.19	0.75	0.25	0.20	2091.00	-3.00	-2.35	36.03	0.02	0.0157	-150.00	788.80	-65.73	9860.00		
28.12	1000.60	7.47	67.01	-11.69	2.25	1.50	0.20	2089.00	2.00	0.27	35.96	0.07	0.0094	28.57	333.47	250.10	7145.71		
34.19	1500.10	6.07	82.27	-10.48	3.46	1.21	0.20	2089.00	0.00	0.00	35.86	0.10	0.0165	4	0.00	412.81	#DIV/0!	4995.00	
40.23	2000.10	6.04	82.80	-9.27	4.67	1.21	0.20	2087.00	2.00	0.33	35.77	0.09	0.0149	22.22	413.22	250.00	5555.56		
52.90	3001.60	12.67	79.02	-6.73	7.21	2.54	0.20	2083.00	4.00	0.32	35.58	0.19	0.0150	21.05	394.29	250.38	5271.05		
71.28	5000.70	18.38	108.76	-3.05	10.89	3.68	0.20	2078.00	5.00	0.27	35.21	0.37	0.0201	13.51	543.23	399.82	5402.97		
96.56	7500.80	25.28	98.89	2.01	15.95	5.06	0.20	2066.00	12.00	0.47	34.70	0.51	0.0202	23.53	494.09	208.34	4902.16		
120.37	10001.50	23.80	105.05	6.78	20.72	4.77	0.20	2050.00	16.00	0.67	34.18	0.52	0.0218	30.77	524.26	156.29	4809.04		
141.68	12501.30	21.32	117.27	11.05	24.99	4.27	0.20	2035.00	15.00	0.70	33.71	0.47	0.0220	31.91	585.43	166.65	5318.72		
157.34	15001.70	15.66	159.67	14.19	28.13	3.14	0.20	2014.00	21.00	1.34	33.36	0.35	0.0224	60.00	796.31	119.07	7144.00		
169.49	17501.70	12.14	205.88	16.63	30.57	2.44	0.20	2004.00	10.00	0.82	33.10	0.26	0.0214	38.46	1024.59	250.00	9615.38		
183.16	20001.90	13.67	182.91	20.21	34.15	3.58	0.26	1997.00	7.00	0.51	32.85	0.25	0.0183	28.00	698.38	357.17	10000.80		
195.39	23483.70	12.24	284.51	60.11	74.05	39.90	3.26	1993.00	4.00	0.33	32.64	0.21	0.0172	19.05	87.26	870.45	16580.00		



### *Growth Features*

#### **Growth Rate:**

High growth rate of crystal mass in the growth process. (50 g – 3000 g) [1]

Sudden increase in growth rate. (17500 g) [2]

#### **Pulling Rate:**

Low initial rates of pulling for seed. (0 g – 50 g) [3]

#### **Temp:Power:**

Negative values. (0 g – 500 g) [4]

#### **Growth:Pulling:**

Very High initial values. (0 g – 2000 g) [5]

Good values for later stages of growth process. (5000 g – 15000 g) [6]

Sudden increase in value. (17500 g) [7]



#### 2.4.2.4 K10-04-14 (Flat plate)

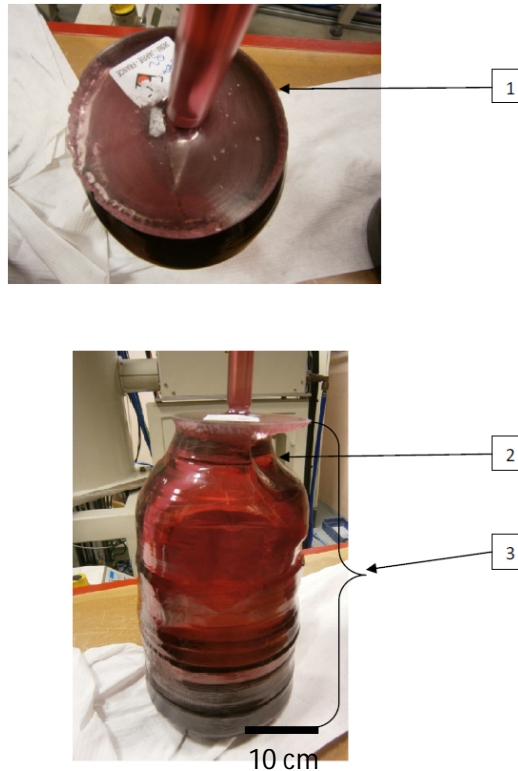


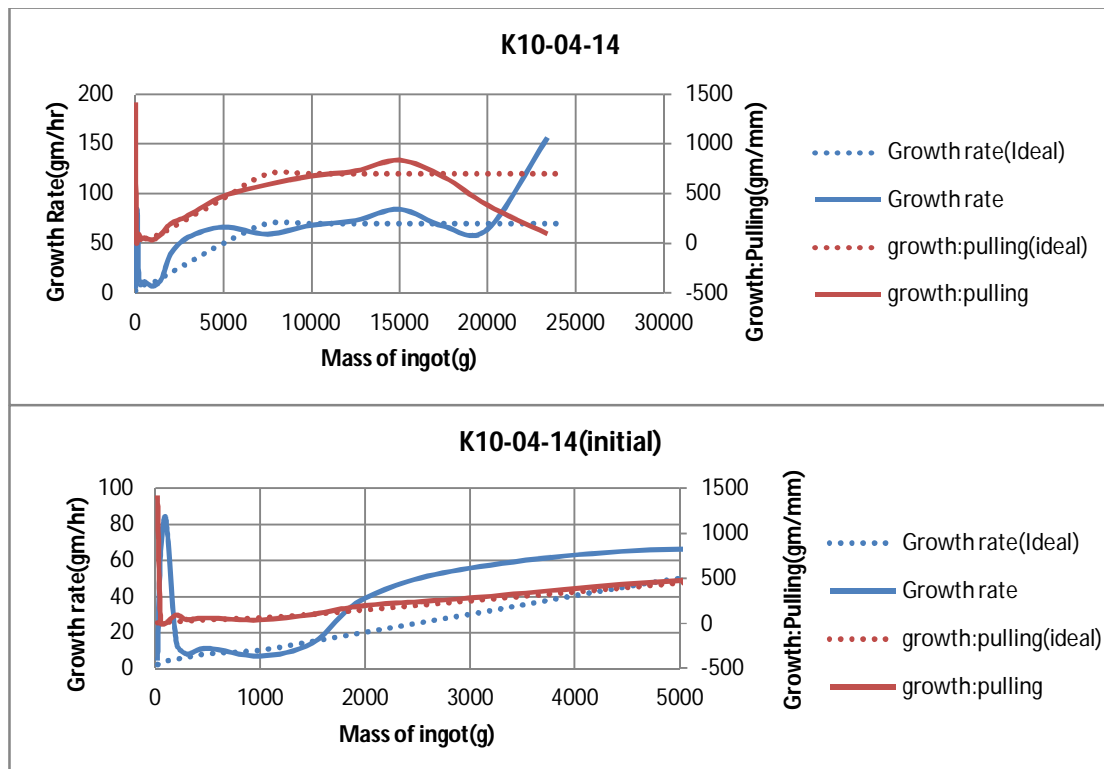
Figure 2.7: Top view and side view of crystal K10-04-14 weighing 23.4 kg.

#### Crystal Morphology features marked in the images above

- 1) Small Diameter flat plate. [1] [4] [6] [7]
- 2) Big Cavity below plate at 20mm from seed. [2] [6] [8]
- 3) Overall even crystal shape with uniform diameter throughout the height. [3] [5] [9]

k10-04-14																			
time(hr)	mass(g)	time diff	Growth r z	crystal (r	Seed posi	posn diff	pulling ra	températ	Temp diff	temp rate	puissance	power dif	power rat	temp;pov	growth;pi	Growth-T	growth;pi		
hr	gm	hr	gm/hr	mm	mm	mm	mm/hr	°C	°C	°C/hr	%	%	%/hr	C/power	g/mm	gm/°C	m/power		
0.02	6.30			-9.82	0.00			2044.00			36.30								
3.25	20.50	3.23	4.39	-9.81	0.01	0.01	4	0.00	2039.00	5.00	1.55	36.40	-0.10	-0.0309	-50.00	1420.00	2.84	-142.00	
3.72	50.90	0.46	1	65.42	-9.81	0.01	0.00	0.00	2041.00	-2.00	-4.30	36.50	-0.10	-0.2152	20.00	#DIV/0!	-15.20	-304.00	
4.31	100.50	0.60	83.09	-9.81	0.01	0.00	0.00	0.00	2045.00	-4.00	-6.70	36.50	0.00	0.0000	#DIV/0!	#DIV/0!	-12.40	#DIV/0!	
11.35	200.50	7.03	2	14.22	-8.69	1.13	1.12	0.16	2047.00	-2.00	-0.28	36.50	0.00	0.0000	#DIV/0!	7	89.29	-50.00	#DIV/0!
23.81	300.00	12.46	7.99	-6.20	3.62	2.49	0.20	2050.00	-3.00	-0.24	36.49	0.01	0.0008	-300.00	39.96	-33.17	9950.00		
41.61	500.00	17.80	11.24	-2.64	7.18	3.56	0.20	2049.00	1.00	0.06	36.46	0.03	0.0017	33.33	56.18	200.00	6666.67		
114.23	1000.10	72.63	6.89	11.89	21.71	14.53	0.20	2041.00	8.00	0.11	35.99	0.47	0.0065	17.02	8	34.42	62.51	1064.04	
149.30	1500.30	35.07	3	14.26	17.05	26.87	5.16	0.15	2036.00	5.00	0.14	35.56	0.43	0.0123	11.63	96.94	100.04	1163.26	
162.14	2000.60	12.84	38.97	19.62	29.44	2.57	0.20	2033.00	3.00	0.23	35.38	0.18	0.0140	16.67	194.67	166.77	2779.44		
180.07	3000.80	17.93	55.78	23.21	33.03	3.59	5	0.20	2028.00	5.00	0.28	35.14	0.24	0.0134	20.83	278.61	200.04	4167.50	
210.28	5000.90	30.21	66.21	27.42	37.24	4.21	0.14	0.14	2021.00	7.00	0.23	34.83	0.31	0.0103	22.58	475.08	285.73	6451.94	
252.60	7500.10	42.32	59.06	31.66	41.48	4.24	0.10	0.10	2011.00	10.00	0.24	34.40	0.43	0.0102	23.26	589.43	249.92	5812.09	
289.36	10000.70	36.76	68.02	35.35	45.17	3.69	0.10	0.10	2000.00	11.00	0.30	34.04	0.36	0.0098	30.56	677.67	227.33	6946.11	
323.75	12500.50	34.39	72.70	38.79	48.61	3.44	0.10	0.10	1989.00	11.00	0.32	33.68	0.36	0.0105	30.56	726.69	227.25	6943.89	
353.52	15000.40	29.77	83.96	41.78	51.60	2.99	0.10	0.10	1975.00	14.00	0.47	33.40	0.28	0.0094	50.00	836.09	178.56	8928.21	
390.86	17500.90	37.34	66.96	45.52	55.34	3.74	0.10	0.10	1959.00	16.00	0.43	33.14	0.26	0.0070	61.54	9	668.58	156.28	9617.31
430.03	20000.30	39.17	63.81	52.07	61.89	6.55	0.17	0.17	1946.00	13.00	0.33	32.70	0.44	0.0112	29.55	381.59	192.26	5680.45	
451.89	23408.00	21.86	155.92	88.18	98.00	36.11	1.65	1.65	1940.00	6.00	0.27	32.37	0.33	0.0151	18.18	94.37	567.95	10326.36	





### Growth Features

#### Growth Rate:

High growth rate of crystal mass in the initial growth process. (50 g – 100 g) [1]

Sudden variations and low growth rate in the later stage of growth process. (200 g – 1000 g) [2]

Good values of growth rate for later stages of growth process. (1500 g – 20000 g) [3]

#### Pulling Rate:

Low initial rates of pulling for seed. (0 g – 200 g) [4]

Good values of pulling speed for later stages. (3000 g – 17500 g) [5]

#### Temp:Power:

Negative values. (100 g – 300 g) [6]

#### Growth:Pulling:

Very High initial values. (0 g – 200 g) [7]

Sudden variations and decrease in values. (300 g – 1000 g) [8]

Good values for later stages of growth process. (1500 g – 17500 g) [9]

#### 2.4.2.5 K12-04-14 (Desired shape)

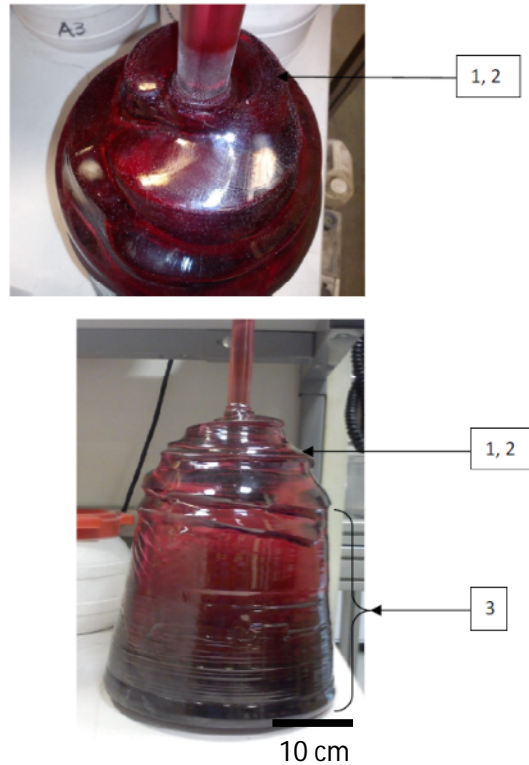
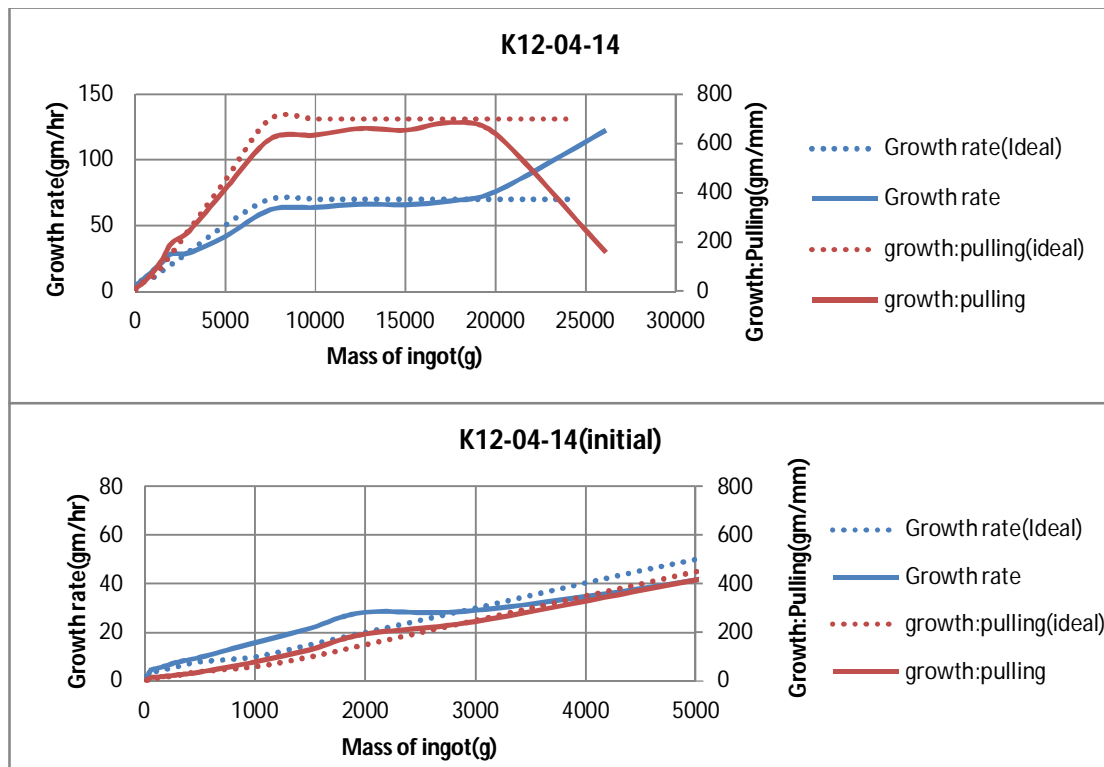


Figure 2.8: Top view and side view of crystal K12-04-14 weighing 26.1 kg.

#### Crystal Morphology features marked in the images above

- 1) Small Diameter head without plate formation. [1] [2] [6]
- 2) Conical head formation without small bubbles layer beneath. [2] [4] [6]
- 3) Overall even crystal shape with increasing diameter from top to bottom. [3] [6] [7]

k12-04-14																		
time	mass	time diff	Growth rate cristal (nSeed)			posn	posn diff	pulling rate	temperati	Temp diff	temp rate	puissance	power diff	power rate	temp:pow	growth:pt	Growth:Ti	growth:pt
hrs	gms	hrs	gm/hr	mm	mm	mm	mm/hr	°C	°C	°C/hr	%	%	%/hr	°C/power%	gm/mm	gm/°C	m/power%	m/power%
0.02	16.70			-30.12	0.00			2028.10				36.32						
28.78	20.00	28.77	1	0.11	-27.55	2.57	2.57	0.09	2024.60	3.50	0.12	36.18	0.14	0.0049	25.00	6	1.28	0.94
35.68	50.00	6.90	4.35	-25.48	4.64	2.07	2	0.30	2027.40	-2.80	-0.41	36.31	-0.13	-0.0188	21.54	14.49	-10.71	-230.77
45.27	100.10	9.59	5.23	-22.60	7.52	2.88	0.30	2027.80	-0.40	-0.04	36.29	0.02	0.0021	20.00	17.40	-125.25	2505.00	
60.65	200.00	15.38	6.50	-17.99	12.13	4.61	0.30	2027.10	0.70	0.05	36.22	0.07	0.0046	10.00	21.67	142.71	1427.14	
73.24	300.00	12.59	7.94	-14.24	15.88	3.75	0.30	2026.90	0.20	0.02	36.13	0.09	0.0071	2.22	26.67	500.00	1111.11	
93.49	500.00	20.26	9.87	-8.95	21.17	5.29	3	0.26	2024.40	2.50	0.12	35.97	0.16	0.0079	15.62	37.81	80.00	1250.00
124.93	1000.10	31.44	15.91	-2.68	27.44	6.27	0.20	2021.70	2.70	0.09	35.69	0.28	0.0089	9.64	79.76	185.22	1786.07	
147.83	1500.00	22.89	21.84	1.16	31.28	3.84	0.17	2018.90	2.80	0.12	35.48	0.21	0.0092	13.33	130.18	178.54	2380.48	
165.48	2000.50	17.65	28.36	3.73	33.85	2.57	0.15	2017.00	1.90	0.11	35.47	0.01	0.0006	190.00	194.75	263.42	50050.00	
199.75	3000.10	34.27	29.17	7.80	37.92	4.07	0.12	2011.20	5.80	0.17	35.14	0.33	0.0096	17.58	245.60	172.34	3029.09	
247.71	5000.70	47.96	41.72	12.61	42.73	4.81	0.10	2004.30	6.90	0.14	34.64	0.50	0.0104	13.80	415.93	289.94	4001.20	
288.05	7500.70	40.34	61.97	16.65	46.77	4.04	0.10	1996.20	8.10	0.20	34.43	0.21	0.0052	38.57	618.81	308.64	11904.76	
327.30	10000.40	39.25	63.69	20.59	50.71	3.94	0.10	1988.80	7.40	0.19	34.14	0.29	0.0074	25.52	634.44	337.80	8619.66	
365.09	12501.20	37.79	66.18	24.37	54.49	3.78	0.10	1978.40	10.40	0.28	33.97	0.17	0.0045	61.18	661.59	240.46	14710.59	
403.15	15000.30	38.06	65.67	28.19	58.31	3.82	0.10	1963.20	15.20	0.40	33.68	0.29	0.0076	52.41	654.21	164.41	8617.59	
439.56	17501.20	36.41	68.68	31.84	61.96	3.65	0.10	1950.30	12.90	0.35	33.42	0.26	0.0071	49.62	685.18	193.87	9618.85	
472.50	20000.50	32.95	75.86	35.75	65.87	3.91	0.12	1939.70	10.60	0.32	33.01	0.41	0.0124	25.85	639.21	235.78	6095.85	
522.60	26133.00	50.10	122.41	74.76	104.88	39.01	0.78	1927.60	12.10	0.24	32.55	0.46	0.0092	26.30	157.20	506.82	13331.52	



### Growth Features

#### Growth Rate:

Good values of growth rate throughout the growth process. (20 g – 20000 g) [1]

#### Pulling Rate:

High initial rate of pulling for seed. (0 g – 300 g) [2]

Low values of pulling rate for later stages of growth process. (500 g – 17500 g) [3]

#### Temp:Power:

Positive values throughout the evolution of the crystal. (200 g – 20000 g) [4]

Slight exceptional negative value. (100 g) [5]

#### Growth:Pulling:

Low initial values. (50 g – 3000 g) [6]

High values for later stages of growth process. (5000 g – 20000 g) [7]

### 2.4.3 Crystal morphology features

#### 2.4.3.1 Crystal-melt interface conditions

One of the main concerns during the growth of crystals was the formation of a flat top or a flat thin plate-like structure. Associated with this structure is always an occurrence of other macroscopic defects like an aggregation of small bubbles forming a white diffused zone just below the flat top as observed in crystal K06-04-14 (figure 2.6) and highlighted in figure 2.9, or in some extreme cases it is associated with big cavities below the plate as observed in crystal K01-04-14 (figure 2.5) and crystal K10-04-14 (figure 2.7). Thus, it is important to get rid of the formation of this flat top to prevent the occurrence of the associated defects.



**Figure 2.9:** Bubble layer beneath a flat plate highlighted by external illumination to reveal the white diffused zone for crystal K06-04-14.

Similar issues with crystal morphology have also been reported by other authors during the Kyropoulos growth of undoped sapphire crystals during the initial stages of growth. These deformations are as shown in figure 2.10 and mentioned as zones of remelting, which are similar to the cavities pointed out in the crystals grown for our project. Numerical simulations have been carried out to simulate heat transfer, melt convection and thermal stress at the different growth stages to understand the mechanism leading to these zones of remelting. These studies have reported the presence of a secondary convective vortex with a flow direction opposite to the primary larger vortex which changes the crystal shape as in the case of crystal shown in figure 2.10(a) [Demina, 2008]; while for the crystal in figure 2.10(b) it is a combination of natural convection and Marangoni convection [Fang, 2013-a].



**Figure 2.10:** Remelting zone in undoped sapphire crystals **(a)** crystal grown by Monocrystal Inc [Demina, 2008]. **(b)** crystal grown by Xida New Energy Inc [Fang, 2013-a].

To study the conditions present in the case of Ti doped sapphire crystals, global and local simulations were carried out for crystals grown in configuration no.7 at RSA company [Stelian, 2016]. A detailed explanation for the simulation model is presented in appendix III. Crystals grown in crucibles of 30 cm in diameter in this configuration have shown the formation of a plateau during the first stage of crystallization as shown in figure 2.11 similar to that of crystal K10-04-14 (figure 2.7).



**Figure 2.11:** Formation of a plateau and temporal concave shape of the crystal observed during the first stage of growth in crucibles of  $d = 30$  cm in diameter for configuration 7 [Stelian, 2016].

The global simulation is first applied to compute the thermal and the flow field in the furnace at the beginning of the crystallization process. The computations are performed in conditions which promote the plateau formation. Fig. 2.12 shows the evolution in time of the velocity field and the solidification isotherm after the seeding stage. The velocity distribution in the melt is computed at temperatures greater than the melting point. Fig. 2.12(a) shows that at the moment of seeding the solidification isotherm is nearly parallel to the free surface of the melt. Since the Marangoni flow is weak at the beginning of the growth process, the flow pattern consists of two cells with the secondary vortex developed near the melt-gas interface. Fig.



2.12(b) shows the results obtained after  $\Delta t = 0.15$  h since seeding. As the power in the heater is decreased, the crystallization occurs very quickly in the radial direction, leading to plateau formation. Small solid zones appearing at the melt-gas interface are remelted by the convection. This generates a very unstable flow at the top surface of the melt, characterized by small opposite vortices as shown in Fig. 2.12(b). It is concluded that a thermal field with isotherms nearly parallel to the free surface of the melt is likely to produce the plateau formation during the first stage of the growth process.

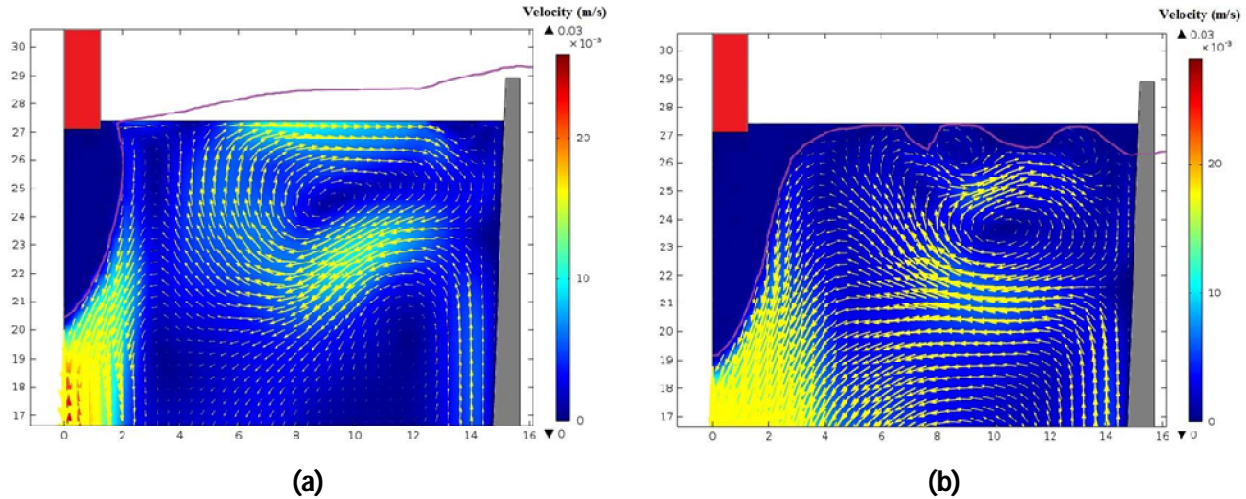


**Figure 2.12:** Evolution in time of the velocity field and solidification isotherm (in red) at the beginning of the growth process: **(a)** after seeding; **(b)** after  $\Delta t = 0.15$  h. Results carried out from global modelling of the Kyropoulos furnace, configuration no.7 with crucible diameter,  $d = 30$  cm [Stelian, 2016].

Local simulation is then applied to study the influence of the Marangoni flow on the crystal shape, after the plateau formation. The deformed mesh technique is used to compute the evolution in time of the crystal shape and the growth interface. The computations are started by considering an initial shape of the crystal, with plateau as indicated by the blue line in Fig. 2.13(a), which corresponds to the final result shown in Fig. 2.12(b). The cases computed with and without Marangoni flow as in Fig. 2.13(a) and (b) respectively, show that the concave shape of the crystal is not influenced by the Marangoni convection ( $Ma = 5400$ ). The flow intensity increases near the triple point due to the Marangoni effect, but the convection is not strong enough to influence the external shape of the crystal. The result plotted in Fig. 2.13(c) is carried out from a computation which neglects the internal radiative effect in the crystal. The curvature of the crystal-melt interface decreases significantly as compared to the simulated cases which account for the internal radiative effect:  $\tau = 6.6 \text{ cm}/7.9 \text{ cm} = 0.84$  (Fig. 2.13(a)) and  $\tau = 2 \text{ cm}/7.7 \text{ cm} = 0.26$  (Fig. 2.13(c)). The transient computation shows a remelting of the plateau in this case. The present results show that the formation of a plateau and the temporal concave shape of the crystal are mainly related to unfavorable heat transfer

conditions in the furnace. The flow can influence the shape of the growth interface, but cannot change significantly the external shape of the crystal.

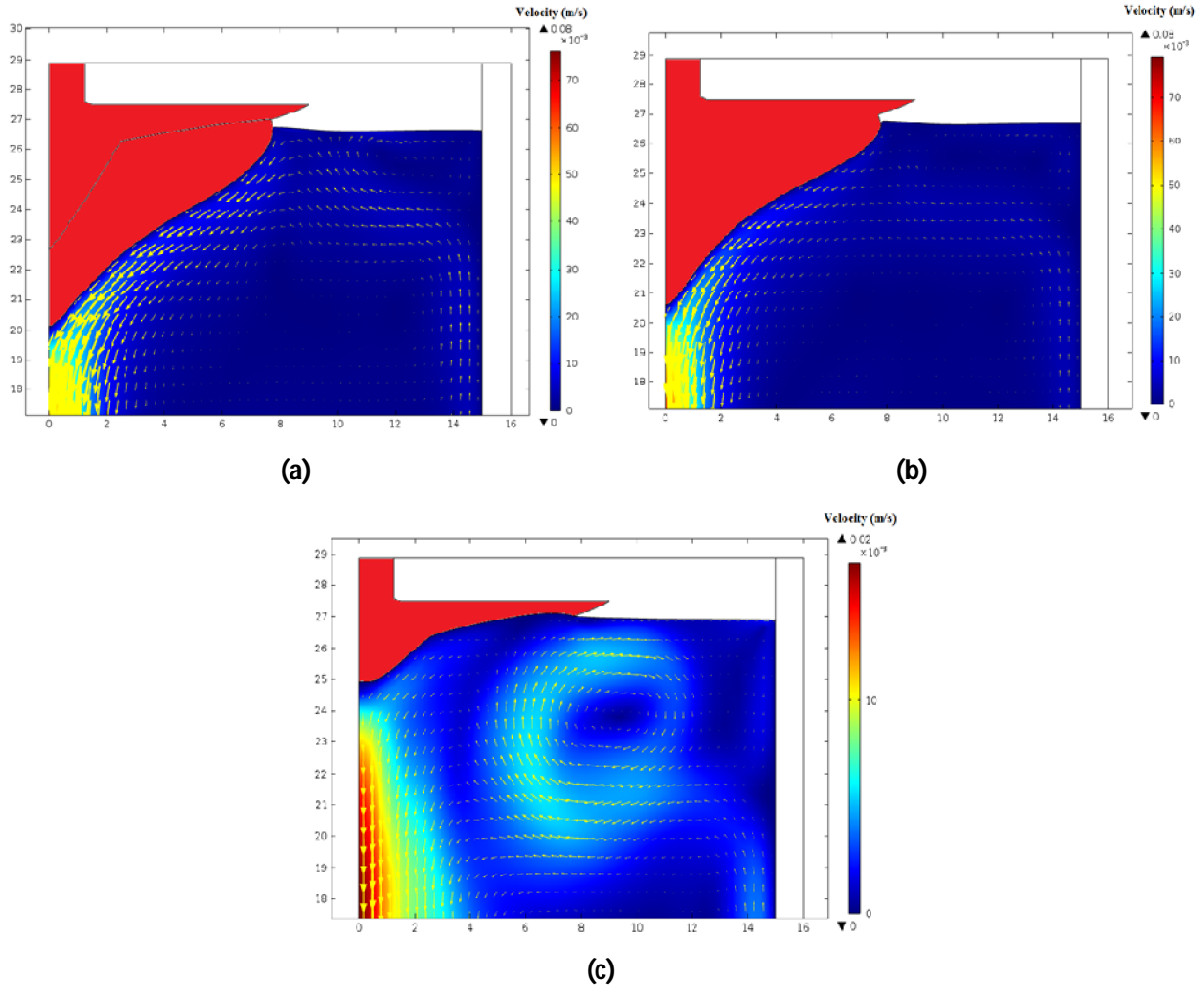


**Figure 2.13:** Evolution of the external shape of the crystal and growth interface in the case; **(a)** with Marangoni convection; **(b)** without Marangoni convection; **(c)** without internal radiative effect in the crystal. Crucible diameter  $d = 30$  cm [Stelian, 2016].

#### 2.4.3.2 Crystal morphology improvement solutions

Once the conditions for the formation of the flat plate structure and the associated temporal concave shape of the crystal are determined to be due to the thermal conditions at the beginning of the growth process; the next step is to make suitable corrections in the growth environment to get rid of this morphological feature.

One of the solutions which was suggested and demonstrated to be effective by using numerical simulations is the modification of the crucible geometry. A cylindrical crucible with an inverted conical shape for the inner wall and a curved bottom has been demonstrated to improve the quality of sapphire crystal [Lee, 2011] [C. Chen, 2014]. It has also been adopted for our project scaled to the size of the three furnace configurations. Another possible solution is the possible rearrangement of the heater configuration and individual control of the heating units in the furnace [C.-H. Chen, 2012] [Liu, 2015]. But, since we are using induction heating coils for our furnace we do not have independent control over sections of our heating arrangement (unlike resistive heating systems) and hence this is not applicable to our growth systems. Also, a rearrangement of the heater configuration is a very time consuming and tedious process since it requires the alignment of all the furnace components and qualifying them for the ideal growth conditions by doing various trials of crystal growth.

Hence, an attempt was made to identify the impact of the controllable growth parameters like power input and pulling speed on the formation of the defect zones and then suggest appropriate corrections by proposing an ideal growth control cycle parameters evolution which would help to consistently avoid the formation of those defects.

#### 2.4.3.2.1 Growth mass rate

As explained by the simulation results in figure 2.12(b) the flat plate at the top is due to very rapid crystallisation in the radial direction. This is evident in the higher than ideal growth mass rate during the initial growth stages for the crystals with the flat top as evident for crystal K01-04-14 (figure 2.5), K06-04-14 (figure 2.6) and crystal K10-04-14 (figure 2.7). The thickness of this flat plate region is reflected in the range of the mass over which this deviation from the ideal growth rate is maintained. Higher than ideal growth mass rate is carried on for a heavier mass range for crystal K01-04-14 (figure 2.5) and K06-04-14 (figure 2.6) hence showing the evidence of a thick flat region; than for crystal K10-04-14 (figure 2.7) with a very thin flat plate. Higher growth mass rate and hence higher crystallisation rate also results into a capture of lot of bubbles which leads to an aggregation of bubbles and hence a diffused zone in the flat top region as in the case of crystal K06-04-14 (figure 2.6).

Any constriction in diameter of the crystal after this plate formation, which is the remelting zone as mentioned in the earlier sections, is reflected with a sudden decrease in the growth mass rate. This is visible in the case of crystal K10-04-14 (figure 2.7), where a lower than ideal growth mass rate is observed immediately after a small range of higher growth rate leading to the occurrence of a big cavity due to remelting just beneath the thin flat plate. After the initial growth mass, a constant growth mass rate is



indicative of extended growth of crystal with uniform diameter. A varying growth mass rate which is more than the ideal indicates an increase in the crystal diameter at that growth stage as evident for the lower third region of the crystal K06-04-14 (figure 2.6).

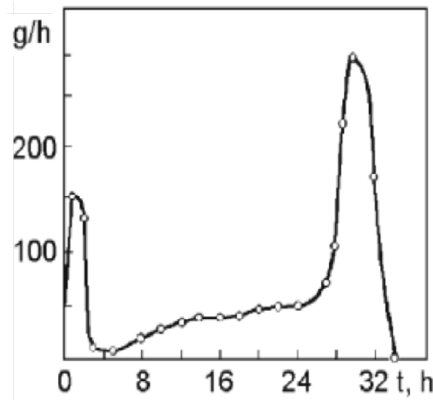


**Figure 2.14:** Plot of growth rate versus crystallisation time for conventional Kyropoulos growth system. [Pishchik, 2009]

The characteristic curve of crystal weight increment per unit time for conventional Kyropoulos system has two maxima as shown in figure 2.14 and this is known to increase the density of macro and microdefects [Pishchik, 2009]. An ideal growth is the one which has a very gradual increase of growth mass rate for the initial growth stages after seeding, until it reaches a stable value. This progressive increase helps the crystal head attain a bottle head shape without the formation of a flat head top or plate and also helps prevent the zones of remelting and bubble aggregations. After forming the head the growth rate is to be maintained for a constant value which will help it achieve a growth with constant diameter. Crystal K12-04-14 (figure 2.8) is an excellent example where the growth rate adheres very closely to the ideal evolution and hence resulting in ideal crystal morphology without any defect zones.

#### 2.4.3.2.2 Pulling rate

There is a need to control the rapid crystallisation in the radial direction and hence the higher growth rates in the moments after the seeding. Since it is very difficult to control precisely the thermal and flow conditions in the melt using the power controls, the growth is managed at this stage by controlling the pulling of the crystal. The idea is to pull the crystal faster during the initial stages to limit the growth in the radial direction by constantly pulling the crystal-melt interface out of the melt before it propagates radially outwards. This is achieved by having a high rate of pulling for the initial growth stages immediately after the seeding, which is lowered progressively as the crystal grows until it reaches a stable lower value. Thus

the crystal achieves a shape for the head which progressively increases in diameter without any abrupt plate formation at the top. After the formation of the head and reaching a stable diameter, the pulling rate is maintained at a low stable value which helps grow a crystal with uniform diameter throughout its height.

In the case of crystal K06-04-14 (figure 2.6) and K10-04-14 (figure 2.7), the pulling rate for the initial stages after seeding was lower than the ideal values suggested and hence there is a flat surface and plate formation in these crystals respectively; while for crystal K01-04-14 (figure 2.5) when a higher than ideal pulling rate is employed there is the evidence of crystal growth with non-uniform diameter for the upper half of the crystal. As evident from the growth of crystal K12-04-14 (figure 2.8), when the ideal pulling regime is followed the flat top formation is avoided along with the defect zones like cavities and aggregation of bubbles related to it and a uniform crystal diameter is achieved for the bulk of the crystal.

It is established that higher pulling rates in the case of sapphire crystals grown using the shaped crystal growth, Czochralski and micro-pulling down techniques leads to an increased density of bubbles; but it is contradictory to what is observed in our growth conditions [Nicoara, 2006] [Ghezal, 2012] [Li, 2013]. This is due to the fact that in our case during the initial stages by increasing the pulling rate we actually decrease the growth rate unlike the other techniques, which helps limit the creation of bubbles. Once we achieve a stable diameter of the growing crystal, we decrease the pulling rate which also limits the growth rate and hence the formation of bubbles.

#### 2.4.3.2.3 Temperature:Power

The ratio of difference in temperature and the power levels between two consecutive stages is a very important indicator for the conditions of remelting or unstable crystal-melt interface. An ideal growth regime should have positive double digit values which indicate that the change in power is reflected proportionally in the temperature variations. A negative value or an undeterminable value for this ratio would indicate an increase or constant temperature respectively in the melt in spite of a decrease in the heating power. This can indicate elevated temperatures in this zone with lower temperatures around and hence giving rise to distortions of the convection isotherms and the crystal-melt interface. But it is important to note that the temperature is measured using a pyrometer pointed at the outer surface of the crucible at a level just below the initial level of the melt, hence it is just an indication of the trend of the changes in the melt temperature inside the crucible and not an accurate value.

From the analysis of the crystal K01-04-14 (figure 2.5), we notice extreme negative values for the initial half of the growing crystal which correspond to the extensive zones of bad morphology and cavities in the upper half of the crystal. Crystal K06-04-14 (figure 2.6) has the evidence of slight negative values linked to

the flat top formation and aggregation of bubbles. For crystal K10-04-14 (figure 2.7), we observe a narrow range of abnormal values very close to the seeding stage which corresponds exactly to the formation of the huge cavity in the crystal. The crystal K12-04-14 (figure 2.8) which follows the ideal growth conditions hardly shows any negative values and hence is evidently devoid of any zones with cavities or related defects.

#### 2.4.3.2.4 Growth rate: Pulling

The ratio of growth mass rate to pulling rate is the most important value because it determines the shape of the crystal by controlling the axial as well as radial growth of the crystal. An ideal growth regime should have low starting values from the seeding stage which increases progressively until it reaches a stable value. Such values are indicative of a crystal head with an increasing radial size which leads to the desired bottle head shape. Once it reaches this stable value it should be maintained throughout the growth which helps the crystal maintain a constant diameter.

This value can be understood as an indicator for the ratio of growth in the radial and axial direction of the crystal. A higher than ideal value for the initial stages of growth indicates the formation of a flat top and the range over which this deviation from the ideal values is carried on determines the thickness of the flat plate. For crystals K01-04-14 (figure 2.5) and K06-04-14 (figure 2.6) we observe a higher than ideal value for most of the initial growth stages and hence there is the occurrence of a thick flat top region; while for crystal K10-04-14 (figure 2.7), it is for just a few initial stages and hence there is a very thin plate formation. This thin plate formation is followed by a big cavity beneath and it is reflected in the values which are much lower than the ideal just after. During the latter stages of growth, any deviation in the values from the ideal is reflected in a slight increase or decrease in diameter of the crystal as evident from the values for crystals K01-04-14 (figure 2.5) and K06-04-14 (figure 2.6). Crystal K12-04-14 (figure 2.8) strictly adheres to the ideal values and hence achieves the desired ideal crystal morphology.

#### 2.4.3.3 Crystal morphology control system

Once the ideal growth parameters for the pulling regime have been established, the next challenge is to be able to maintain them during the process. The only controllable parameters during the growth process are the heating power and the pulling rate of the seed, hence a suitable process has to be designed to be able to control these two parameters based on the feedback of the measurable parameters. As established in the earlier section the ratio of growth:pulling is the factor which is largely responsible for governing the shape of the crystal. The growth rate of the crystal and distance by which it is pulled in the ideal growth

regime is followed by maintaining a fine balance between the power level and the pulling rate based on the feedback parameter which is the weight of crystal.

The ideal values of growth rate:pulling is fed into the computer for the control system of the machine. Here on after seeding, the machine monitors the weight of the growing crystal and pulls the seed accordingly to maintain the ideal ratio. An ideal power ramp down curve is also fed to the control system based on the previous pulling experience. Based on this ideal power evolution data for the growth of crystal the system tries to follow it to balance the growth rate, i.e to increase the growth rate by decreasing the power and vice versa. After seeding, once the automatic growth system takes over, it follows the pulling rate as in the ideal curve and checks for the corresponding mass growth. To compensate for the loss or gain of growth the power levels are automatically adjusted and hence the growth:pulling ratio values are maintained. Although, in theory the evolution of the crystal from the seeding to the complete growth does not need any operator supervision with the automatic system, the growth parameters are regularly monitored and minor adjustments are made by correcting the power evolution and pulling rate data into the control system. Figure 2.15 represents the control system for the Kyropoulos growth machine to follow the ideal growth parameters.

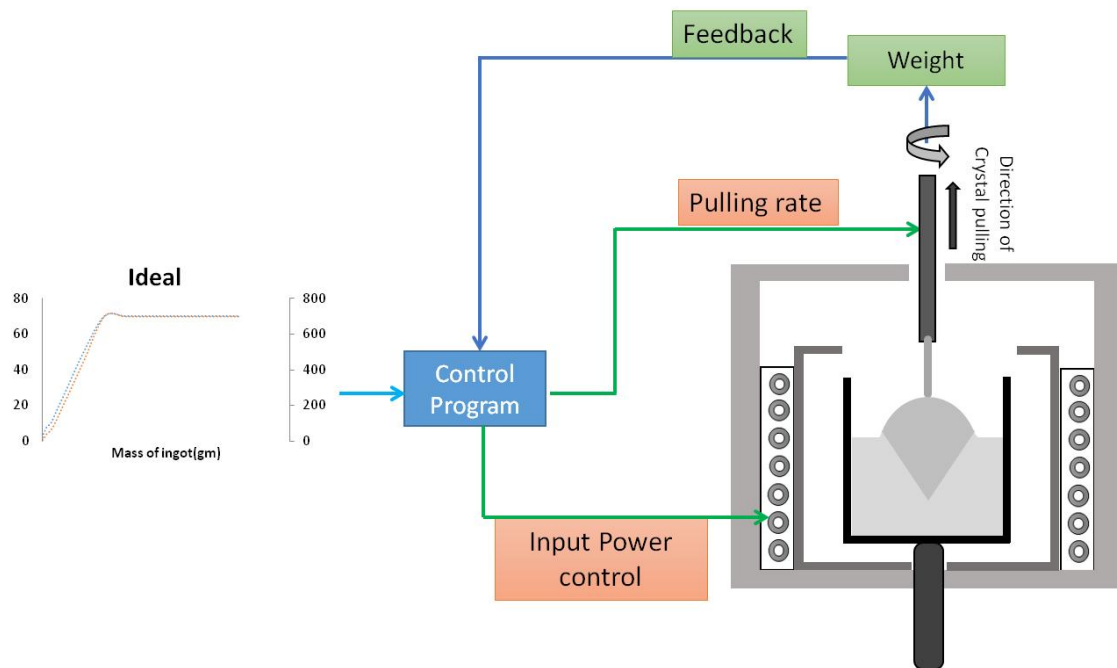


**Figure 2.15:** Scheme for the feedback and automatic control process of Kyropoulos growth machine.

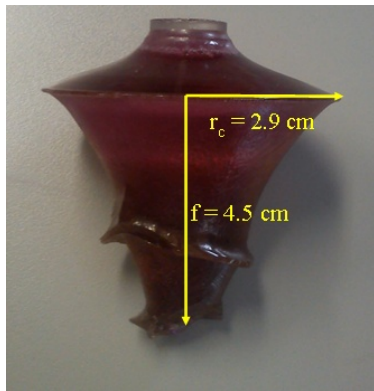
The ideal growth parameters were established on the basis of the study of the growth parameters and its influence on the morphology of the following crystals: K01-04-14 (figure 2.5), K06-04-14 (figure 2.6), K10-

04-14 (figure 2.7), K04-04-14 (appendix I figure I.1), K08-04-14 (appendix I figure I.2), K09-04-14 (appendix I figure I.3) and K11-04-14 (appendix I figure I.4).

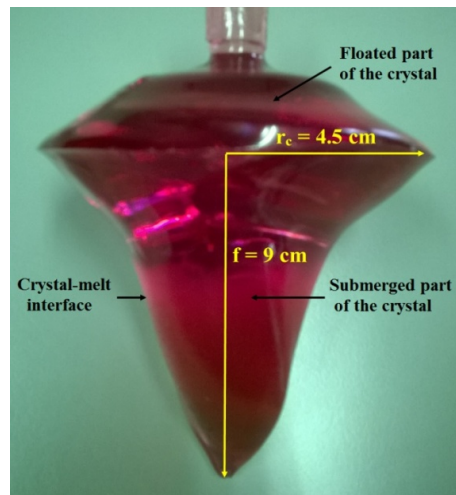
Following our advice, the automatic growth system following the ideal growth parameters have been implemented by Cyberstar company for the furnace. At RSA for the growth of crystals K12-04-14 (figure 2.8), K01-04-15 (appendix I figure I.5) and K02-04-14 (appendix I figure I.6) with this improved ideal growth parameters the improvement in the morphology of these crystals is very evident. The small diameter flat top in the case of K01-04-15 (appendix I figure I.5) and K02-04-14 (appendix I figure I.6) is due to the extended duration of seeding stage. Since, the seeding is a very sensitive process, often it is preferred to have a substantial growth of around 50 g – 100 g without any movement or slower than the ideal recommended making sure the crystal growth process is stable and substantial enough to continue the rest of the growth.

## 2.5 Crystal-melt interface shape

Along with the crystal morphology which describes the outer shape of the final crystal, the progressing crystal-melt interface is an important consideration for the quality of grown crystals. The shape of the crystal-melt interface is an important factor for the radial distribution of titanium in the discs cut from these crystals due to the segregation of the titanium solute at the crystal-melt interface. The curvature of this interface also has an important influence on the formation of facets which in turn influences the formation of crystal defects [Frank J. Bruni, 2015].



(a)



(b)



**Figure 2.16:** Shape of the crystals obtained by interrupting the growth process at various time ( $t$ ) after seeding and with different interface deflection ( $\tau_c$ ) [Stelian, 2017-a] [Stelian, 2016]. The portion of the crystal above the indication for the crystal radius is the emerged part whereas below it is the submerged part under the melt level. **(a)**  $t = 31$  hr,  $\tau_c = 1.55$ ; **(b)**  $t = 67$  hr,  $\tau_c = 2$ ; **(c)**  $t = 67$  hr,  $\tau_c = 2.56$ ; **(d)**  $t = 71$  hr,  $\tau_c = 2.20$ .

Since it is impossible to observe the crystal-melt interface during the growth process, an experiment was devised to pull out the crystals from the melt at various stages of their growth thus interrupting its growth. Upon pulling out the crystal suddenly from the melt, the formed crystal shape bounded by the crystal-gas interface for the part outside the melt and the crystal-melt interface for the submerged part is preserved and can be studied by taking it out of the furnace while the remaining melt just freezes in the crucible. These experiments were carried out in configuration no.5 at RSA within crucible of 15 cm diameter. The crystals in this configuration grow up to a weight of 7 kg and the full crystallisation process takes around 160 hours.

Figure 2.16 shows 4 such crystals obtained in these experiments by pulling out the growing crystal from the melt at various time ( $t$ ) after seeding. The shape of these crystals are defined by the dimensionless interface deflection  $\tau_c = f/r_c$ , where  $f$  is the interface deflection, i.e the maximum depth of the crystal-melt interface from the melt level and  $r_c$  is the crystal radius. The common feature in all these crystals is the convex-concave shape with a large curvature for the crystal-melt interface.

The crystal shown in figure 2.16 (a) weighs 0.15 kg and shows the evidence of thin plates of crystallised solid on the interface unlike the three other crystals. This is because the crystal was obtained as a result of

an accident which involved the emergency extraction of crystal after a power failure. It resulted in rapid solidification of the melt while the crystal was being extracted and hence an interface which is not smooth with solidified melt sticking to it. The crystal depicted in figure 2.16 (b) weighs 0.4 kg and was grown with a very high rotation of the seed (10 rpm) while the crystals in figure 2.16 (c) and (d) weigh 0.7 kg and 1.2 kg respectively and are grown with a 2 rpm rotation of the seed. The high rotational speed of the seed results in a more concave and flat interface shape for the crystal in figure 2.16 (b) unlike the pronounced concave and convex interface for the crystals in figure 2.16 (c) and (d).

## 2.6 Titanium distribution

Non-uniformity in the axial and radial distribution of titanium has been experimentally observed in the discs cut from the grown crystals. Since the absorption coefficient of the crystal is strongly dependent on titanium concentration, the input laser beam is non-uniformly absorbed in the transversal cross-section, giving rise to variations in the intensity of emitted laser beam.

The axial variation of titanium concentration is evident from the increasing darkness of the red colour of the crystal as we go from the top of the crystal axially downwards as evident from figure 2.17. The radial variation in titanium distribution is evidenced by measurements of the absorption coefficient in two slices of 10 cm in diameter, cut from the top and the middle part of the ingot as shown in figure 2.17. Very precise chemical analysis was done to determine the Ti concentration in a disc sample from a similar grown crystal as presented in Appendix IV. The Ti concentration was found to be around 350 ppm. The radial variation is not so evident in this analysis because the samples prepared were very close to the crystal head and hence the effect of solute segregation was not so strong.

This radial variation in the titanium concentration could be explained by segregation of titanium due to the conical growth profile in the submerged part of the growing crystal as marked in the crystal shown in figure 2.17. This was verified experimentally by checking the profile of the growing crystal as explained in the earlier section.



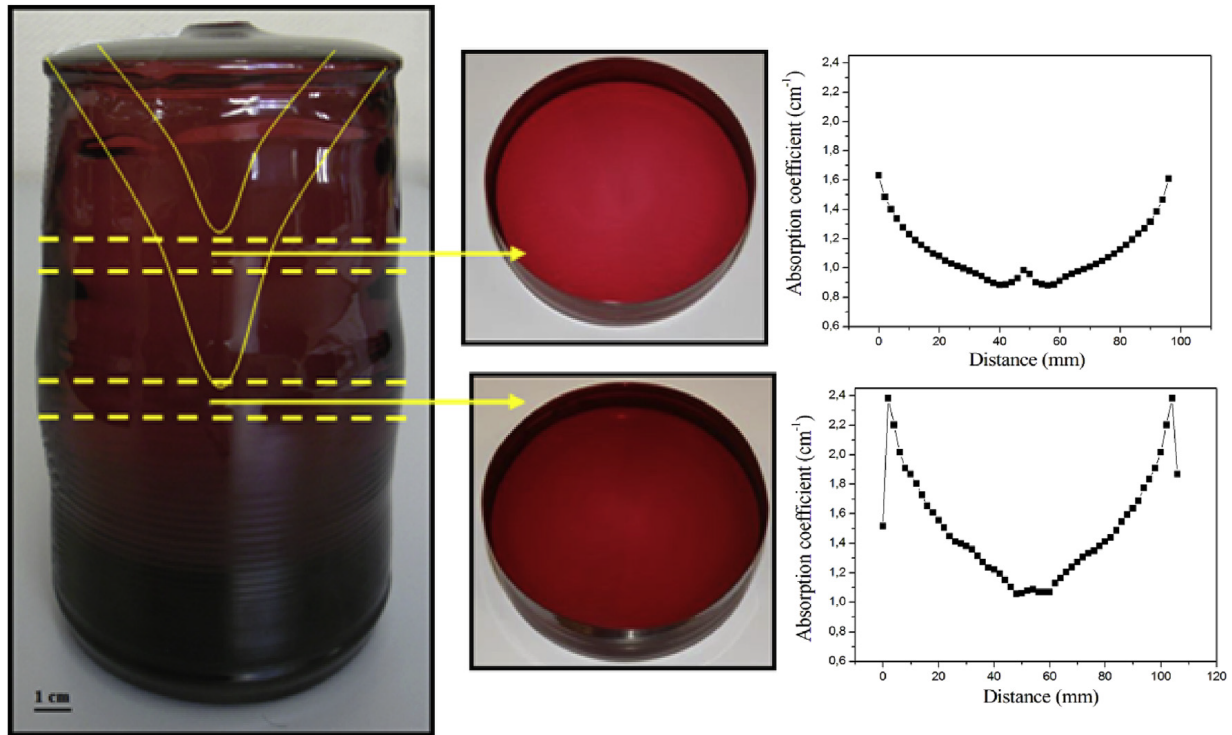


**Figure 2.17:** Radial variation of the absorption coefficient in two slices cut from the top and the middle part of the sapphire ingot. The crystal-melt interface is drawn on the figure (yellow color)[Stelian, 2017-a]

## 2.7 Laser performance characteristics

The first step to prepare the samples for the laser applications is to cut the discs 10 cm in thickness from the crystals. Since sapphire is a very hard material, it is difficult to cut the crystals compared to other materials. Diamond wire saws are used at RSA which can be programmed to cut the discs of required dimensions without fracturing the samples. Once the discs are prepared they are polished at the flat surface using chemico-mechanical polishing to obtain an optical grade finish which finally makes it suitable for the optical applications.

### 2.7.1 Figure Of Merit (FOM)

One of the most common values used to assess the laser potential of titanium doped sapphire is the absorption ratio at laser pump and laser emission wavelength. This ratio is named "Figure Of Merit", FOM. Depending on the final application, different FOM can be evaluated as a function of the wavelength of the laser pump and the titanium emission wavelength. The second harmonic (532 nm) of a Nd: YAG laser is used now as common pump for Ti sapphire laser. The 800 nm wavelength correspond more or less to the center of the emission wavelength range of Ti: sapphire laser. So the FOM is evaluated as the ratio between



absorption coefficients measured at 532 nm and absorption coefficients measured at 800 nm [Guillaume Alombert-Goget, 2016-c].

Eighteen Ti-sapphire samples with 10 cm diameter and 3.2 cm of thickness were produced with a titanium concentration between 0.1 and 0.2 at% from good quality crystals produced in the Kyropoulos configuration no.5 for determination of their FOM. To compare the samples, arbitrarily a similar position was chosen on them for transmittance measurements. All measurements were realized at the half of a radius parallel to the C-axis of the crystal (Figure. 2.18(a)). For each sample, the two points of measurements symmetrical to the centre of the sample presented the same FOM values ( $\pm 3$ ). Here, for each sample the better value of the two is reported. The values of FOM for the eighteen samples with 10 cm diameter and high absorption coefficient at 532 nm are reported on figure. 2.18 (b). The average FOM of these samples is 77. These results show that high quality crystals can be grown, such as the sample number 16 which presents a FOM of 142 and sample 9 which presents a FOM of 102. It is commonly accepted that the sapphires used in a laser cavity must have a FOM greater than 100 [Pishchik, 2009].

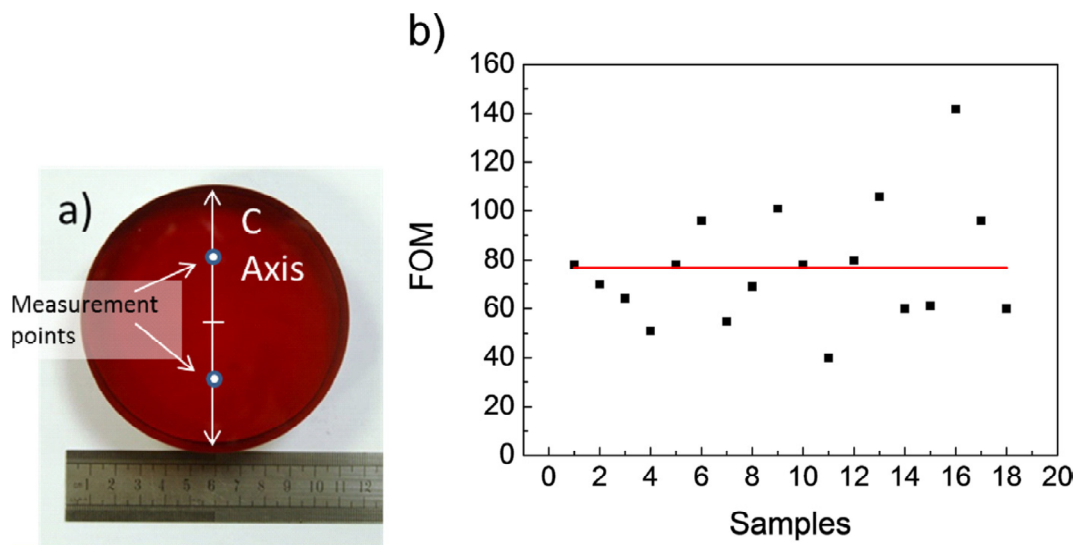


**Figure 2.18:** (a) Diagram presenting the position of transmittance measurements; (b) FOM values evaluated on the different samples [Guillaume Alombert-Goget, 2016-c].

The valence of titanium incorporated into aluminium site in the Ti-sapphire crystals is a fundamental factor for the laser performance. The concentration ratio between the  $Ti^{3+}$  and  $Ti^{4+}$  present in the crystal directly influences the absorption coefficients at 532 nm and 800 nm and therefore the FOM value. The absorption of the Ti-doped sapphire in the green is due to  $Ti^{3+}$  ions and the residual absorption around 800 nm is attributed to  $Ti^{3+}$ - $Ti^{4+}$  pair.

The radial distributions of  $\text{Ti}^{3+}$  and  $\text{Ti}^{4+}$  ions in the Ti-doped sapphire crystal were evaluated by luminescence measurement as shown in figure 2.19. The luminescence intensity of  $\text{Ti}^{3+}$  was evaluated at 730 nm after excitation at 532 nm and the luminescence of  $\text{Ti}^{4+}$  was evaluated at 420 nm after excitation at 256 nm. The luminescence intensities were measured every mm on the crystal diameter. It is assumed that the variation of titanium concentration is linear with the photoluminescence intensity due to a very low concentration quenching effect of the titanium dopant in sapphire.

The  $\text{Ti}^{3+}$  radial distribution profile presents a typical behaviour induced by segregation during crystal growth. The titanium segregation coefficient is evaluated to be 0.2 in Ti-doped sapphire grown by Kyropoulos [Abdeldjelil Nehari, 2011]. So, the  $\text{Ti}^{3+}$  concentration increases at the periphery of the crystal, which is the last grown part. The variation observed in  $\text{Ti}^{4+}$  profile is important in comparison to the low concentration of these ions. The variation of  $\text{Ti}^{4+}$  concentration induces variation of the FOM along the diameter of the sample. In the worst case, the FOM can be locally divided by three. So, a good homogeneity of the  $\text{Ti}^{3+}$  along the crystal diameter is obtained, but the variation of  $\text{Ti}^{4+}$  should be better controlled in order to obtain a high homogeneity of the FOM value in the samples.

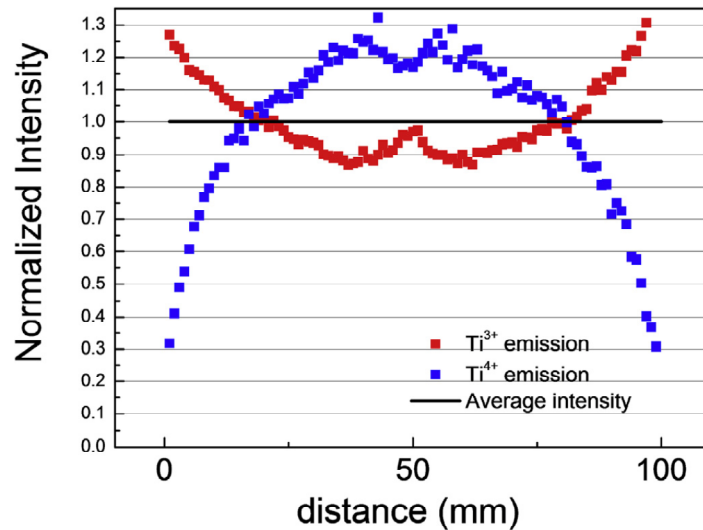


**Figure 2.19:** Profiles of the luminescence intensity of the  $\text{Ti}^{3+}$  and  $\text{Ti}^{4+}$  in Ti-sapphire sample number 16 of that shown in figure 2.18(b). The emission intensities of the  $\text{Ti}^{3+}$  and  $\text{Ti}^{4+}$  are normalized on their respective average emission intensities. The measurements were performed on complete sample diameter [Guillaume Alombert-Goget, 2016-c].

For the potential application of large diameter crystal, the key factor is the homogeneity of the optical characteristic in the sample, although a minimum value of the FOM is requested by the user. Hence, the

possibilities to increase the FOM values of samples with homogenous optical characteristic but with low FOM are very interesting. It is known that after annealing the crystal under reducing atmosphere it is possible to reach high values of FOM (250) on small diameter components (<1 cm). Hence, 1cm<sup>3</sup> samples were taken from a crystal grown in previous growth series presenting a very low FOM (<30), which didn't allow them to be used in laser applications. They were annealed in a reducing atmosphere (argon 95%, hydrogen 5%) for 73 hr at 1300°C. This thermal annealing operation converts the Ti<sup>4+</sup> to Ti<sup>3+</sup>. The values for the FOM of these samples before and after annealing are shown in figure 2.20 which confirms the possibility of using annealing to increase the FOM of Kyropoulos samples.

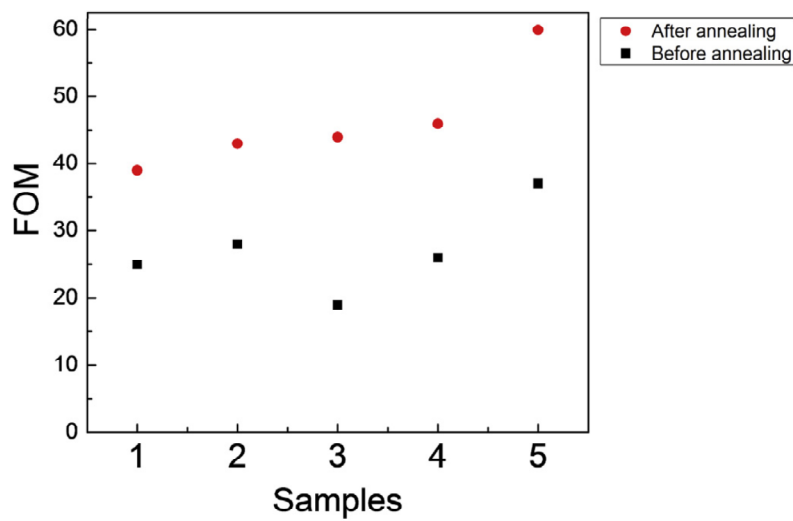


**Figure 2.20:** FOM values before and after annealing treatment of Kyropoulos samples [Guillaume Alombert-Goget, 2016-c].

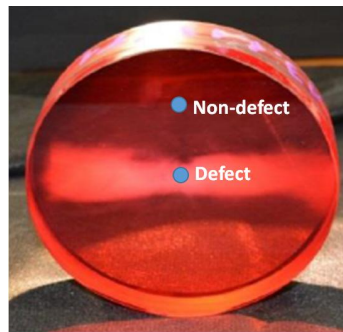
### 2.7.2 Slope efficiency

An important property of an optically pumped laser is its slope efficiency (or differential efficiency), defined as the slope of the curve obtained by plotting the laser output versus the pump power. Above the lasing threshold, the resulting curve is usually close to a straight line. The slope efficiency is the slope of this line. Slope efficiency can be plotted in terms of output laser intensity and input absorbed pump intensity energies.

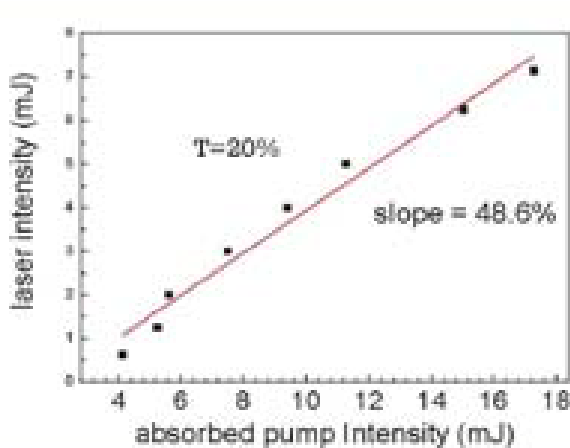
For various disc samples cut from the crystals with very good quality the appearance of a hazy translucent white milky band was found as shown in figure 2.21(a). The slope efficiency was calculated for such a sample in the defect zone and in the non-defect zone to check for the influence of this defect on the laser properties. The slope efficiency for the part in the non-defect zone was found to be 48.6% as shown in figure 2.21(b). But, the slope efficiency for the part in the defect zone is reduced drastically to 38%. Thus,

these measurements have shown that the defect zone reduces the laser efficiency by the order of 10%. A Ti doped sapphire crystal having such a defect cannot be used to make components for laser applications.

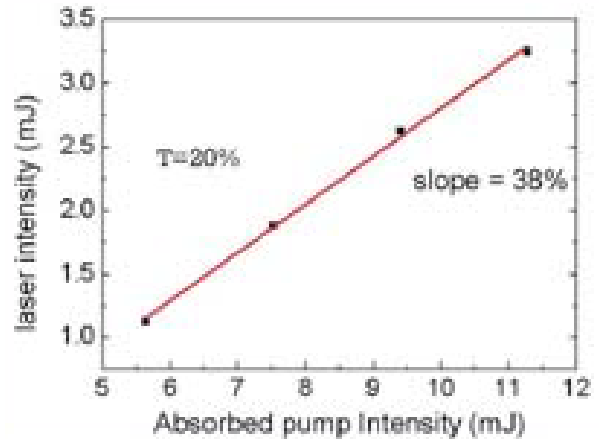
This defect zone is a limiting factor in the exploitation of the crystals for the envisioned laser applications. Hence, it is really important for the TitanSaphir project to understand the nature of the defect and its formation mechanism. A detailed investigation into this defect zone has been carried out and is presented in the fourth chapter.



(a)



(b)



(c)

**Figure 2.21:** (a) Disc cut from a crystal with a horizontal defect zone. Slope efficiency curve for the laser in the (b) non-defect zone and (c) defect zone.

## 2.8 Conclusion

The Kyropoulos growth process has already been demonstrated to be successful in growing large sized Ti doped sapphire boules [Abdeldjelil Nehari, 2011] [G. Alombert-Goget, 2014]. Using industrial Kyropoulos furnace developed by Cyberstar an effort to scale up the size of crystals was carried out at RSA. The scaling

up efforts resulted in crystals with uneven external shape and macroscopic defects which lead to a loss in the productive volume of the crystals and occurrence of defects such as bubbles and haze.

A detailed study of the crystal shape and the growth process helped to establish a relation between them and hence point out the process parameters responsible for the undesirable portions of the crystals. The most pronounced defect feature is a flat top formation and associated zones of remelting have also been demonstrated by numerical simulations. Based on these studies an ideal growth parameter for the growth rate and the ratio of growth:pulling rate was suggested. Crystals pulled by adhering to these growth parameters have demonstrated the possibility of producing crystals of a desired shape as shown in figure 2.8. An automatic growth system which helps maintain these ideal growth parameters has been developed to make the process repeatable and hence assure growth of crystals with good morphology every time.

Growth experiments carried out to reveal the crystal-melt interface have shown the evidence of a conical interface below the melt level. This helps in a better understanding of the growth mechanism which leads to the crystal morphology and fuels further interest in the entire growth mechanism from seeding to the final crystal shape with respect to the progression of the crystal-melt interface. The crystal-melt interface shape is also instrumental in explaining the radial titanium distribution profiles in disc samples prepared from the crystal and the optical phenomenon associated to it.

Finally, the discs obtained from the crystals have been checked for their laser performance characteristics. The FOM values suggest that some of the samples have acceptable Ti doping and optical characteristics for development of laser optic components. The FOM values can be further enhanced by annealing of the samples. But a peculiar defect band observed in the crystal samples reduces the laser efficiency in the zone and hence is the limiting factor in the application of these crystals.

## 3 Crystal shape prediction

### 3.1 Introduction

As demonstrated in the earlier chapter, the crystal shape is of great importance for the industrial growth of bulk crystals. We have managed to understand the effect of crystal growth parameters such as pulling rate and power on the crystal morphology based on experience and used them to create a feedback system to have a predictable crystal shape. But we still cannot predict the exact crystal shape accurately in real time during the growth process. The ultimate ambition for industrial crystal growth is to have complete information of the growing crystal dimension and be able to control it in real time to achieve a growth with complete control over the crystal morphology.

As of now, in industry, the furnace operators only have access to the weight measured, and the length by which the seed in contact with the growing crystal is pulled. The objective of this chapter is to show that it is possible to make a program able to determine the radius of the crystal at the solid-liquid-gas interface for each growth step if the height of the melt is additionally acquired throughout its pulling. This would provide the operators with direct information on the shape of the growing crystal (the radius value at each measurement), and thus help them exercise better control on the growth parameters. Assuming that it is possible to measure with accuracy the level of the molten sapphire inside the crucible, the weighing method could be applied to compute the shape of the crystal which is not possible with the current state of the system. Particular attention is paid to the meniscus effects and to accuracy with which the results are obtained. Finally the precision needed for height measurement data in such a system is discussed to check the feasibility of this idea.

The programming work for the computations has been carried out by Huiyan Lu, Yoann Malier and Wenqing Jia as a part of their Master internship project for 3 months each during 3 consecutive years in the mentioned order. The work started with Huiyuan developing an Excel code for solving a simplified system of forces acting on the crystal growth system. It was followed by Yoann who managed to develop a system of equations to describe the menisci in the system and their interactions and translated them into computational codes for Matlab software to develop a calculation tool which would relate all the forces and their interactions. Finally, Wenqing developed the work further to help determine the radius of crystal at each growth step for a given set of measured data and also determined the range of errors involved for the tolerance with which the data for the measured parameters can be obtained. Professor Liliana Braescu

from Quebec University was invited to help with simplifying the system of non-linear equations and was instrumental in coming up with the mathematical methods to determine the real solutions to the problem.

### 3.2 Crystal shape live monitoring system

The automatic growth system has been described in the earlier chapter and presented in figure 2.14 which allowed for a crystal growth with predetermined shape, but did not have any provisions for the system operator to realise the instantaneous shape of the crystal during the process. Indeed, as will be shown in the following sections, the weight and the pulling distance of the crystal are not enough for computing the crystal radius, and hence one additional parameter must be known. Thus, the first step to enable the determination of instantaneous crystal radius at the solid-liquid-gas interface is to have an additional measured parameter in the form of minimum melt height.

The scheme for such a system is presented in figure 3.1. The melt level sensor, not yet defined, could be for example, a laser-based system which could work on the principle of reflection of light by the liquid surface. The sensor would have to be adapted for the extreme temperature conditions in the furnace and as of now it has not been experimentally studied. The feedback from this level sensor along with the other measured parameters would enable the calculation of radius at the solid-liquid-gas interface at each instant as will be described further. Having the initial value of radius for the seed, the calculated radius at each step along with the pulling data will enable a live construction of the axisymmetric crystal shape and can be visualised on a monitor. Based on the current growth status, the operator can act upon the growth parameters and change the growth parameters and further inspect its effect on the crystal shape as it continues growing. Ultimately this would allow for the system to be completely automatic.

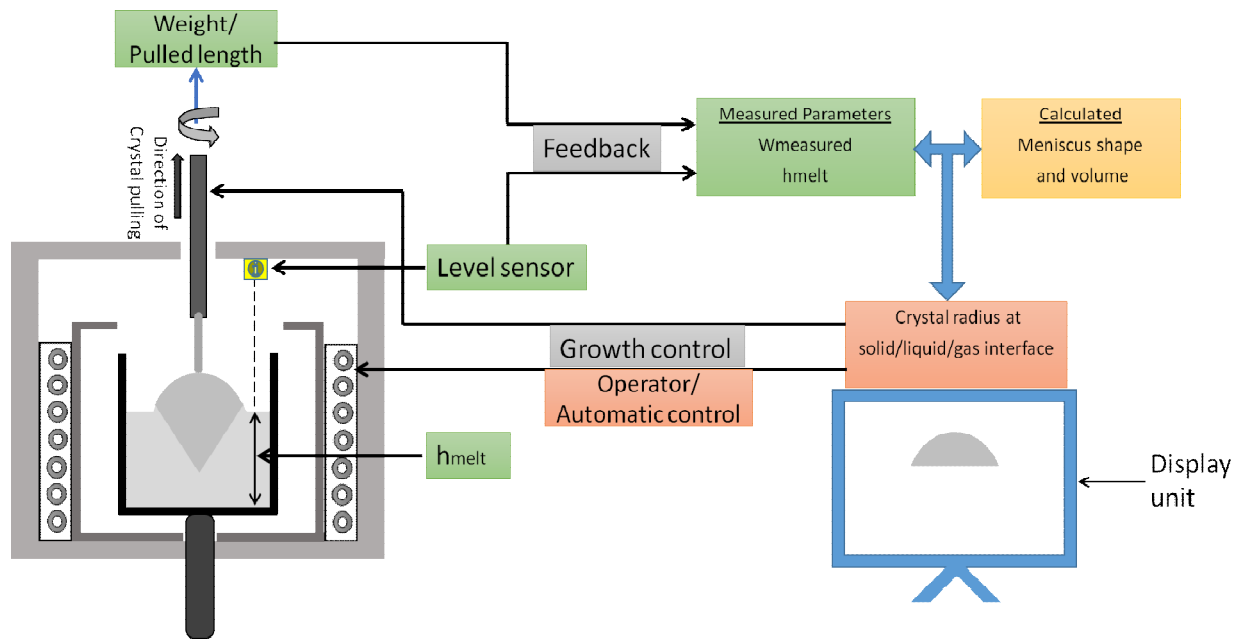


**Figure 3.1:** Scheme for crystal shape monitoring system with melt level sensors.

### 3.3 Background

There have been a few attempts to explore the influencing factors of the shape evolution of a crystal grown by the Kyropoulos technique.

A model of the Kyropoulos method was presented in which the solid-liquid interface is assumed to be spherical or an ellipsoid of rotation to deduce the general shape of the crystal. By using a mass transfer approach, the relationship between the decrease of the melt and the corresponding increase of the crystal size was established [Singh, 1981]. However, in the real case, the shape of solid-liquid interface is much more complicated than what was supposed in the paper and there is no way to get this shape during growth.

A geometric model with a quasi-stationary approximation for crystal growth was proposed to study the effects of the growing process on the evolution of crystal shape. It was revealed that the crystal could grow with a self-stabilized diameter after the shoulder-expanding stage under fixed processing parameters and decreasing the convexity of solid-liquid interface would increase the growth rate of crystal diameter. In this model, the crystal growth is considered as layer-by-layer and to be achieved by two processes alternately: the rising height of the crystal from the melt level and the advancing of crystallization front [Zhang, 2011-a].



Later, the previous model was applied to design the process for growing a shaped crystal by Kyropoulos method through integrating a 1-D model representing the kinetics of the crystallization process. It was stated that reducing pulling rate as well as heater temperature could prevent the decrease of crystal diameter after shoulder expanding [Zhang, 2012]. Even though the diameter undergoes successive changes during the crystal growth in this method, it was assumed that the solid-liquid interface was a cone with a fixed apex angle. In a real crystal growth process in the Kyropoulos furnace, however, it is very hard to get a model relating the crystal diameter changes to the process parameters such as pulling rate, advancing speed of crystallization front and heater temperature without considering the changes of crystal-melt interface [Song, 2015]. Thus a growth control method for Kyropoulos process was proposed by directly calculating the crystal mass and force changes with a simplified conical interface shape-evolution model. In this geometric model, the emerged part above the melt was considered as a piling-up of truncated cones while the submerged part (i.e. the solid-liquid interface) was supposed to keep a conical shape with a constant cone angle, based on some experimental data. The model was applied to analyze data from the industry-scale crystal growth experiment. By obtaining the value of radius of growing crystal at the melt level with examinations of the successfully grown crystal in the test runs, it was possible to obtain the profile of crystal mass built up during one interval, the melt height and cone angle of solid-liquid interface from the crystal pulling force [Song, 2015][I. V. Kryvonosov, 2016][I. V. Kryvonosov, 2017].

But in fact, the shape of the crystal front is much more complicated than just a simplified cone shape and evolves with time. Thus, the measurement of the radius from as-grown crystal is not very accurate and rigorous with these models.

### 3.4 Methodology

In this chapter, the following methodology has been adopted to establish the system of equations to determine the crystal shape using the measured parameters and determine the accuracy associated with these parameters:

1. As a first step, all the physical phenomena related to the mass of the system have been established
2. The mass and volume balance of the Kyropoulos growth system have been established. This allowed the establishment of a system of equations with the measured parameters and the geometry of the crystal.
3. Mathematical representation of the internal and external menisci was established based on their physical description.

4. The interaction of both these menisci (capillary bridge) is considered and is described mathematically.
5. A set of non-linear equations allowing the computation of the crystal radius at the solid-liquid-gas interface from the measured parameters was developed.
6. Since these equations are non-linear, a computational code was developed to solve these equations numerically.
7. To check for the validity of the idea, a perfectly cylindrical crystal shape was considered.
8. Since we don't have physical values for the measured parameters, capillary bridge calculations were carried out for this crystal shape to obtain the geometry of the menisci and derive the measurable parameters, most importantly the liquid melt level (simulated data).
9. Based on these available measurable parameters (simulated data) from the earlier step, the system of differential equations from step 5 was solved using the computational code to check it was possible to reconstruct the crystal shape and hence validate the computational system.
10. Finally, to be able to suggest an accuracy needed for the measured parameters, an analysis for the impact of tolerance of measured parameters on the determined crystal shape was carried out by adding error in the measured parameters. This helped to determine the accuracy needed for a prospective tool to measure liquid level.

### 3.5 Hypotheses

To apply the methodology described previously, some hypotheses which help us simplify the problem are considered as follows:

- The growing crystal is assumed to be axisymmetric and its axis corresponds to the crucible axis.
- It is considered that the melt height values are always obtained at its minimum height.
- The total initial weight of the sapphire ( $W_{total}$ ) introduced in the system is accurately known.
- The emerging crystal shape can be approximated by conical layers with a straight segment joining the crystal radius known at the earlier step to the current crystal radius.
- The physical properties for the solid and liquid sapphire are assumed to be constant irrespective of temperature variations.

### 3.6 Weighing method applied to Kyropoulos crystal growth

The weighing method, which proved to be particularly useful for Czochralski and floating zone crystal shape control, consists in balancing the different forces that contribute to the weight measured by the seed

holder's sensor [Duffar, 2010]. To adapt this method to Kyropoulos technique, the axisymmetric system presented in the Figure 3.2 is studied.

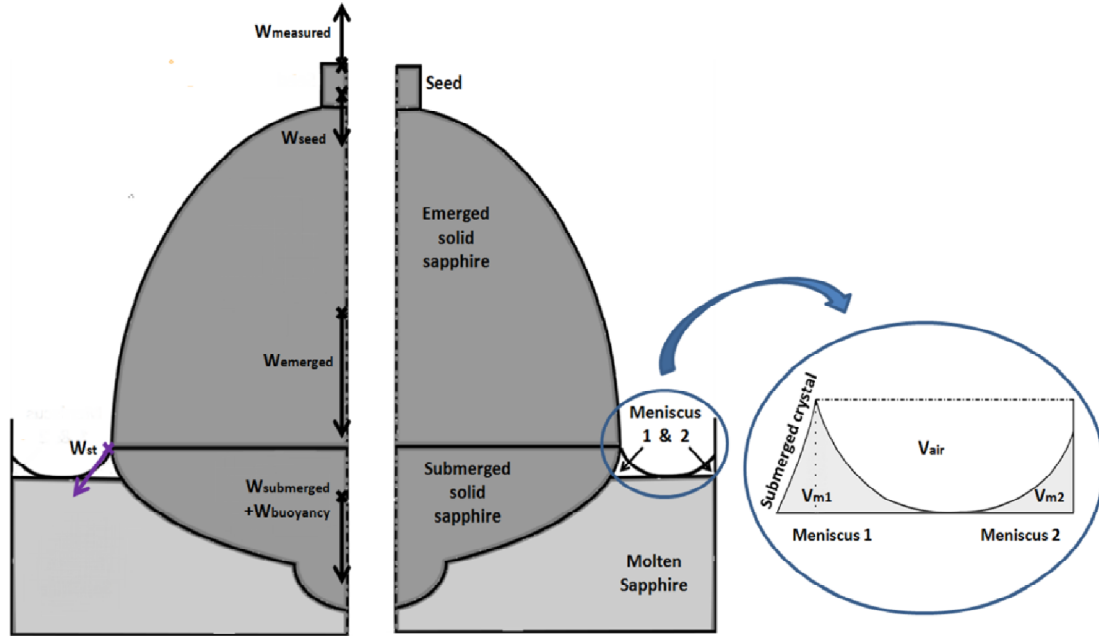


**Figure 3.2:** Scheme for the crystal growth with the balance of forces.

In existing works on control logics, the sapphire geometry was simplified. But it is notable to mention that in this work, no hypothesis is performed on the crystal shape, since the shape of the submerged crystal cannot be determined. Consequently, in the forces balance written below,  $W_{submerged}$  is unknown.

$$W_{measured} = W_{seed} + W_{emerged} + W_{submerged} + W_{st} + W_{buoyancy} \quad \text{Equation 3.1}$$

where,  $W_{st}$  is the weight component due to the force exerted by the meniscus surface tension.

In order to remove indetermination, other equations are needed. A mass balance gives the relationship below.

$$W_{total} = W_{seed} + W_{emerged} + W_{submerged} + W_{molten} \quad \text{Equation 3.2}$$

Moreover, it is possible to obtain a geometrical relationship between the volumes of the molten and the submerged part as shown in figure 3.3.

$$\pi R_c^2 (h_{measured} + h_{meniscus\ 1}) = V_{gas} + V_{submerged} + V_{molten} - V_{excess} \quad \text{Equation 3.3}$$

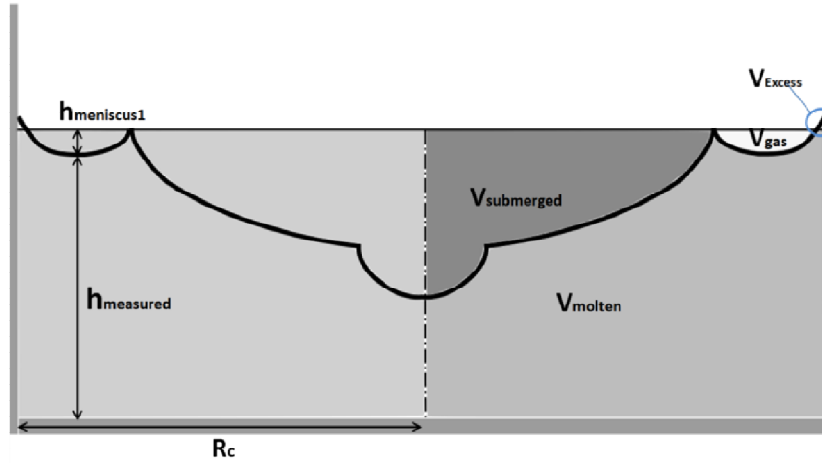


**Figure 3.3:** Geometrical parameters for the crystal growth scheme.

After manipulating and simplifying these three relationships to eliminate  $W_{molten}$  and  $W_{submerged}$  from one of them, the equation below is obtained [Johansen, 1987]

$$W_{measured} - W_{total} = -\rho_l \pi R_c^2 (h_{measured} + h_{meniscus\ 1}) + W_{st} + \rho_l (V_{gas} - V_{excess}) + \pi r_{(i)}^2 \left( \frac{p_o - p_v}{g} + \rho_l h_{meniscus\ 1} \right) - \rho_{gas} (V_{emerged} - V_{seed}) \quad \text{Equation 3.4}$$

To obtain this equality,  $W_{buoyancy}$  has been replaced by its exact expression in the equation 3.1. A submerged body inside a fluid is, according to Archimedes' principle, submitted to the force ( $\mathbf{u}_z$  pointing up, all the terms in bold being vectors):

$$F = \rho_l g V_{submerged} \mathbf{u}_z \quad \text{Equation 3.5}$$

But this expression applies only if the body is entirely submerged, which is not the case here. Then, the buoyancy force must be adapted adequately, as it has been done for Czochralski process [Furlong, 1979]. On the Figure 3.4, it appears that the fluid pressure does not apply on the section S as it would on an entirely submerged body.

Hence, the force exerted by the molten sapphire on the crystal is the following

$$F_1 = \iint_{A-S} P(M) d\mathbf{S} \mathbf{n} = \oint_S P(M) d\mathbf{S} \mathbf{n} + \pi r_{(i)}^2 (p_v - \rho_l g h_{meniscus\ 1}) \mathbf{u}_z = \iiint_V \nabla P(M) dV + \pi r_{(i)}^2 (p_v - \rho_l g h_{meniscus\ 1}) \mathbf{u}_z \quad \text{Equation 3.6}$$

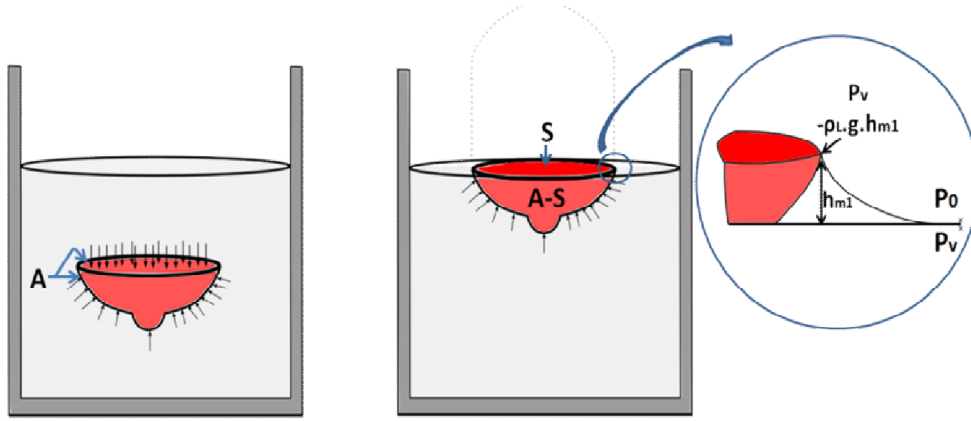


**Figure 3.4:** Diagram of pressure forces applying to the crystal's submerged part

Finally:

$$W_{buoyancy1} = \frac{1}{g} F_1(-\mathbf{u}_z) = -\rho_l V_{submerged} - \pi \frac{r_{(i)}^2}{g} (p_v - \rho_l g h_{meniscus1}). \quad \text{Equation 3.7}$$

The gas also applies forces of pressure on the external surface of the emerged part of the crystal. It is possible, as previously, to demonstrate that the overall gas pressure contribution is:

$$W_{buoyancy2} = \rho_{gas} (V_{emerged} + V_{seed}) + \pi \frac{r_{(i)}^2}{g} p_o, \quad \text{Equation 3.8}$$

$$W_{buoyancy} = W_{buoyancy1} + W_{buoyancy2}.$$

In equation 3.4,  $W_{st}$ , due to surface tension can be evaluated. Indeed, from the Figure 3.5, it is possible to deduce that:

$$W_{st} = \frac{2\pi}{g} r_{(i)} \gamma_{lv} \cos(\theta_s + \theta_l), \quad \text{Equation 3.9}$$

Considering the hypothesis that the crystal shape can be represented by small consecutive conical layers, it can be written:

$$\tan(\theta_s) = \frac{r_{(i)} - r_{(i-1)}}{z_{(i)} - z_{(i-1)}}. \quad \text{Equation 3.10}$$

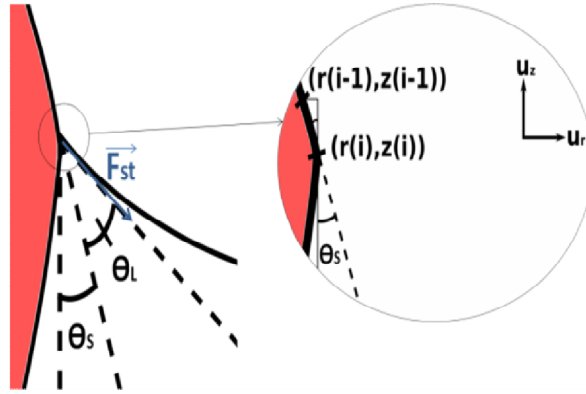


**Figure 3.5:** Angle of projection on the vertical axis of the force associated to surface tension.  $\theta_s$  being the angle between the tangent to the crystal surface and the vertical direction and  $\theta_l$  the static contact angle between liquid  $\text{Al}_2\text{O}_3$  and sapphire (whose value is  $17^\circ$ ).

And, at any iteration  $i$ ,  $z_{(i)} = H_{(i)} - h_{\text{measured}(i)} - h_{\text{meniscus1}(i)}$ .

By injecting these expressions in 3.4, the final weighing method's equation 3.11 is obtained.

$$W_{\text{measured}} = \rho_l(V_{\text{gas}} - V_{\text{excess}}) + \frac{2\pi}{g}r_{(i)}\gamma_{lv}\cos\left(\theta_l + \text{atan}\left(\frac{r_{(i)} - r_{(i-1)}}{z_{(i)} - z_{(i-1)}}\right)\right) - \rho_l\pi R_c^2(h_{\text{measured}} + h_{\text{meniscus1}}) - \rho_{\text{gas}}(V_{\text{emerged}} + V_{\text{seed}}) + \pi r_{(i)}^2\left(\frac{p_o - p_v}{g} + \rho_l h_{\text{meniscus1}}\right) + W_{\text{total}} \quad \text{Equation 3.11}$$

From these equations,  $r_{(i)}$  can be computed, provided that all the terms related to the geometry of the menisci ( $V_{\text{gas}}$ ,  $V_{\text{excess}}$ ,  $h_{\text{meniscus1}}$ ,  $\theta_l$ ) can be determined. It is worth noting that the shape of the submerged crystal need not be known to solve the problem. It is possible because of the additional measured parameter in the form of the melt height level ( $h_{\text{measured}}$ ).

In the demonstration above, the menisci are assumed to be upwardly concave-shaped. But, in some extreme cases, it could not be the case. As shown in Figure 3.6, when the crystal surface angle relative to the vertical is too high (i.e. if growth rate is very high) or lower than  $-17^\circ$  (i.e. if remelting phenomenon is occurring), the shape of the meniscus 1 is strongly affected.

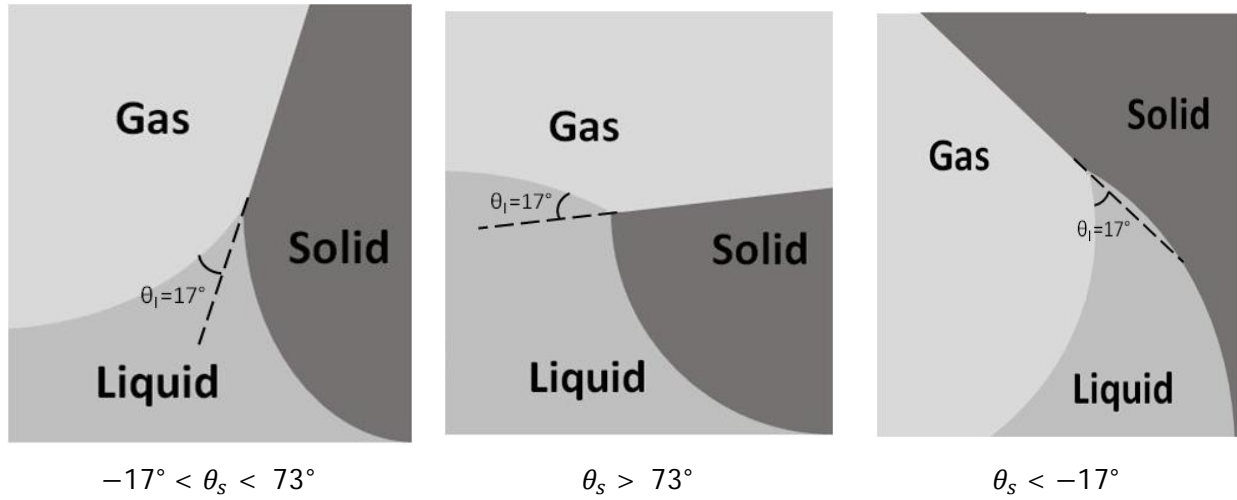


**Figure 3.6:** Different possible shapes for the meniscus1 depending on the value of  $\theta_s$

The equations 3.1 and 3.2 remain unmodified by this change; but the equation 3.3 and the buoyancy force, thus equation 3.11, are impacted if the crystal tangent angle value is higher than  $73^\circ$ . In this case, it becomes as shown in figure 3.7:

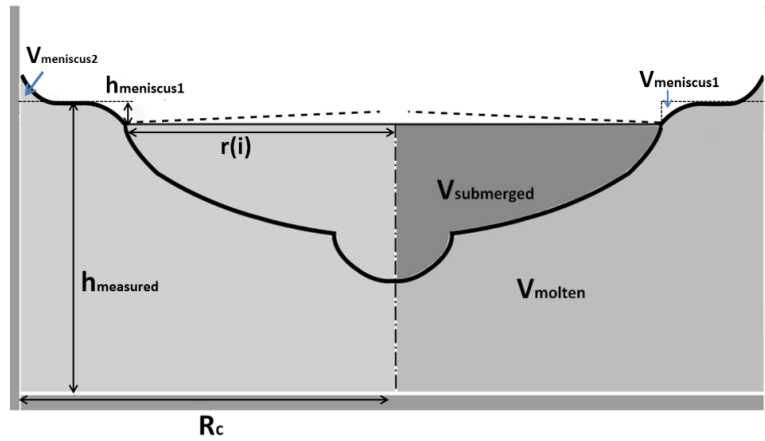


**Figure 3.7:** Geometrical parameters for the crystal growth scheme for  $\theta_s > 73^\circ$

$$V_{submerged} + V_{molten} = \pi R_c^2 h_{measured} - \pi r_{(i)}^2 h_{meniscus1} - V_{meniscus1} + V_{meniscus2} \quad \text{Equation 3.12}$$

Hence,

$$W_{measured} = W_{total} + \rho_l (V_{meniscus1} - V_{meniscus2}) - \rho_{gas} (V_{emerged} + V_{seed}) + \frac{2\pi}{g} r_{(i)} \gamma_{lv} \cos \left( \theta_l + \text{atan} \left( \frac{r_{(i)} - r_{(i-1)}}{z_{(i)} - z_{(i-1)}} \right) \right) - \rho_l \pi R_c^2 h_{measured} + \pi r_{(i)}^2 \left( \frac{p_o - p_v}{g} \right) \quad \text{Equation 3.13}$$

However, when the crystal tangent angle value is negative, the equations 3.3 and 3.11 remain unchanged as shown in. figure 3.8.

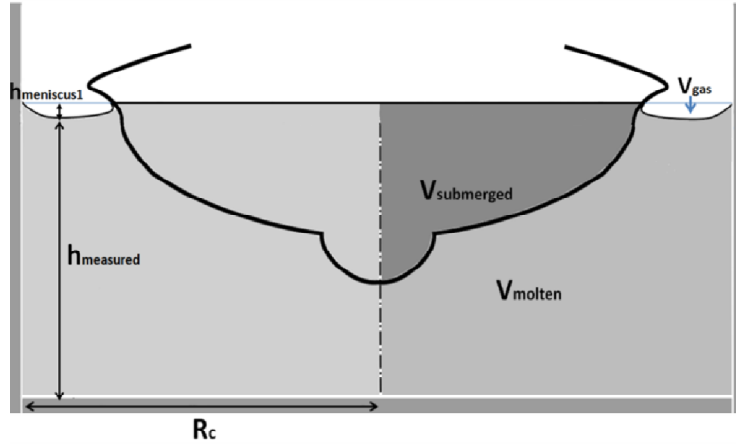


**Figure 3.8:** Geometrical parameters for the crystal growth scheme for  $\theta_s < -17^\circ$

At each instant, to solve the equation 3.11 or 3.13 (i.e. to determine  $r_{(i)}$  value knowing the height of the melt  $h_{measured}$ ), the values of  $V_{gas}$  and  $V_{excess}$  and  $h_{meniscus\ 1}$  must be calculated. Indeed,  $h_{measured}$ ,  $H$  (directly linked to the pulling rate) and  $W_{measured}$  would be acquired throughout the crystal growth and the other terms depend on physical characteristics of the system. The volume of the emerged part of the crystal is determined by integrating the radius values calculated at previous instants. The following section is dedicated to the determinations of the menisci shapes and their volumes

### 3.7 Numerical study

As a first step, mathematical representation for the meniscus at the crystal (external meniscus) and crucible (internal meniscus) is represented without considering their interaction. Later on, the interaction between the two menisci is considered and the geometry of the interacting menisci (capillary bridge) is described.

#### 3.7.1 External meniscus

In order to determine the equation characterizing the shape of the external meniscus (i.e. the meniscus in contact with the crystal), one has to consider its parametric representation as described in figure 3.9.



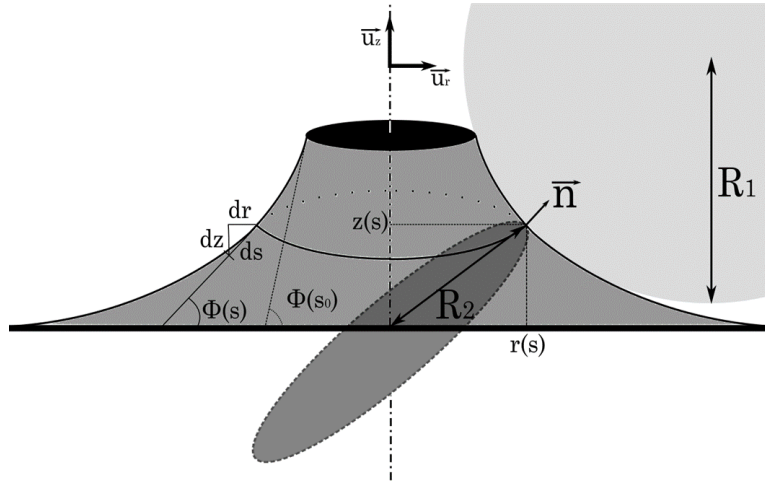


**Figure 3.9:** Parametric representation of an external meniscus

It can be followed using the above scheme:

$$\frac{dr}{ds} = \cos(\phi(s))$$

$$\frac{dz}{ds} = \sin(\phi(s))$$

$$\frac{d\phi(s)}{ds} = \frac{1}{R_1}$$

$$\frac{\sin(\phi(s))}{r} = -\frac{1}{R_2}$$

The Young - Laplace equation is obtained from the last two equations as follows:

$$\frac{d\phi(s)}{ds} - \frac{\sin(\phi(s))}{r} = \frac{1}{R_1} + \frac{1}{R_2} \quad \text{Equation 3.14}$$

To be solved, this equation must contain only two parameters. Using the chain rule, one obtains:

$$\frac{dz}{dr} = \frac{dz}{ds} \frac{1}{\frac{dr}{ds}} = \frac{\sin(\phi)}{\cos(\phi)} = \tan(\phi)$$

$$\frac{d\phi}{ds} = \frac{d\phi}{dr} \frac{dr}{ds} = \frac{d\phi}{dr} \cos(\phi) = \frac{d\phi}{dr} \frac{1}{\frac{( \cos^2(\phi) + \sin^2(\phi) )^{\frac{1}{2}}}{\cos(\phi)}} = \frac{d\phi}{dr} \frac{1}{(1 + \tan^2(\phi))^{\frac{1}{2}}} = \frac{d\phi}{dr} \frac{1}{(1 + (\frac{dz}{dr})^2)^{\frac{1}{2}}}$$

$$\sin(\phi) = \tan(\phi) \cos(\phi) = \frac{\tan(\phi)}{\frac{( \cos^2(\phi) + \sin^2(\phi) )^{\frac{1}{2}}}{\cos(\phi)}} = \frac{\frac{dz}{dr}}{(1 + (\frac{dz}{dr})^2)^{\frac{1}{2}}}$$

$$\frac{d^2 z}{dr^2} = \frac{d}{dr} \left( \frac{dz}{dr} \right) = \frac{d}{dr} (\tan(\phi)) = \frac{d\phi}{dr} \frac{1}{\cos^2(\phi)} = \frac{d\phi}{dr} \left( 1 + \left( \frac{dz}{dr} \right)^2 \right)$$

So the equation 3.14 can be written as:

$$\frac{\frac{d^2 z}{dr^2}}{\left( 1 + \left( \frac{dz}{dr} \right)^2 \right)^{\frac{3}{2}}} - \frac{1}{r} \frac{\frac{dz}{dr}}{\left( 1 + \left( \frac{dz}{dr} \right)^2 \right)^{\frac{1}{2}}} = \frac{1}{R_1} + \frac{1}{R_2} \quad \text{Equation 3.15}$$

As such, the equation doesn't contain any physical parameter related to the crystal growth configuration. To address this, a modified Young-Laplace law is applied. This model was tried and tested for Czochralski growth technique and presented in the book [Duffar, 2010].

$$\frac{1}{R_1} + \frac{1}{R_2} = \frac{-p_v + p_o + \rho_l g z - \frac{1}{2} \Omega_1^2 r^2}{\gamma_{lv}} \quad \text{Equation 3.16}$$

The pressure due to rotation in Kyropoulos system is only a few Pascals and is commonly neglected in this equation as it is done for the Czochralski system. In Kyropoulos, it is even smaller since the seed's rotation speed and temperature gradient are lowered compared to Czochralski. Moreover, z must be 0 when r tends to infinity. Indeed in a huge container, the meniscus doesn't affect the level of liquid in its center. So the internal pressure applied on the liquid  $p_o$  is the same with the pressure of the external gas on the melt  $p_v$ , i.e  $p_v = p_o$ . Hence the equation 3.16 becomes:

$$\frac{\frac{d^2 z}{dr^2}}{\left( 1 + \left( \frac{dz}{dr} \right)^2 \right)^{\frac{3}{2}}} - \frac{1}{r} \frac{\frac{dz}{dr}}{\left( 1 + \left( \frac{dz}{dr} \right)^2 \right)^{\frac{1}{2}}} = \frac{\rho_l g z}{\gamma_{lv}} \quad \text{Equation 3.17}$$

Since it is second order differential equation, it can split into two first order differential equations. Hence, in the system written below the following dimensionless coordinates have been introduced:

$$Z = \sqrt{\frac{\rho_l g}{\gamma_{lv}}} z \text{ and } R = \sqrt{\frac{\rho_l g}{\gamma_{lv}}} r$$

$$\frac{d\left(\frac{dZ}{dR}\right)}{dR} = \pm \frac{\left(1 + \left(\frac{dZ}{dR}\right)^2\right)}{R} \frac{dZ}{dR} + Z \left(1 + \left(\frac{dZ}{dR}\right)^2\right)^{\frac{3}{2}} : f_1\left(\frac{dZ}{dR}, Z, R\right)$$

$$\frac{dZ}{dR} = \frac{dZ}{dR} : f_2\left(\frac{dZ}{dR}\right)$$

This system of non-linear first order differential equations, combined with boundary conditions make possible the computation of the shape of any external meniscus using numerical methods (the equation being non linear it has no exact analytical solution). Throughout this work, RK4 (i.e, Runge-Kutta method at order 4) and RKF45 (i.e, Runge-Kutta-Fehlberg method, which is similar to the RK4 one, but with an

adaptive step size) codes are developed for solving initial value problem of the meniscus. If RK4 requires less iterations, hence less computational time, the error is not mastered by this technique. The main advantage of RKF45 method is the control over the error made at each step, thanks to modifications of the step size.

As explained above, to solve the equation 3.17, boundary conditions are needed. More precisely, to apply RK4 or RKF45 methods, both the position of one boundary and the slope at this point must be known. This condition is only fulfilled at infinite  $r$ , where  $z$  and the slope are zero. Since it is impossible to start from infinite, approximations are made on this boundary. Tsivinskii's assumptions are commonly used to determine an approximate meniscus height with a simplified equation and thus to create fixed boundary conditions [Duffar, 2010]. In this work, to verify the equation and the RK4 code validity, the model of Stanley Hartland and Richard W. Hartley is applied instead [Hartland, 1976]. In their study, they started that far from the contact interface, where the meniscus effect and the angle  $\phi$  are small ( $\phi = 10^{-4}$ ). Under these conditions, the equation 3.16 simplifies into

$$\frac{d^2 Z}{dR^2} - \frac{1}{R} \frac{dZ}{dR} = Z$$

Indeed,  $\frac{dZ}{dR}(R^*, Z^*) = \tan(\phi^*) \approx 10^{-4} \ll 1$ . This is a Bessel differential equation (the  $-ve$  sign is converted into  $+ve$  due to the used co-ordinate system), and it has an analytical solution:

$$K_1(R^*) = \frac{\tan(\phi^*)}{c}$$

$$Z^* = \frac{K_0(R^*)}{K_1(R^*)} \tan(\phi^*)$$

Using these two relationships, for a given  $c$  value (constant of integration which depends on the physical properties of the system), it is possible to determine the boundary conditions. As shown in the Figure 3.10, from this starting point, the developed Matlab program computes the meniscus shape until the slope reaches the value of  $\tan(\Phi(s_0))$  and then stops (with an accuracy of  $10^{-9}$ ). By varying  $c$  between  $1.66139 \cdot 10^{-4}$  and  $169980$  (as it is the case in Hartland & Hartley's book), it is possible for each contact angle  $\Phi(s_0)$  to obtain the value of the meniscus height and length along with its shape [Hartland, 1976].

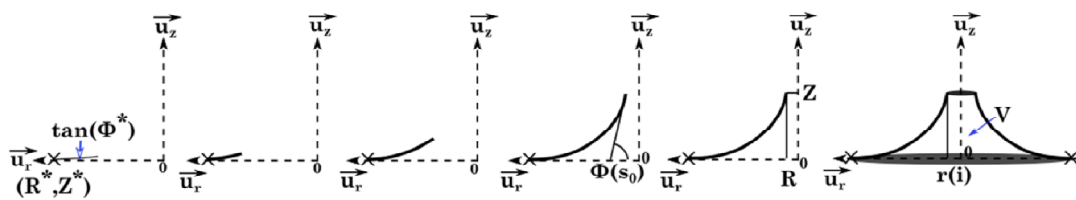


**Figure 3.10:** Schematic of meniscus creation by the code. The output of the program being  $R$ ,  $Z$  and the volume  $V$

To compute the meniscus volume, trapezoidal integration is used and the volume below  $Z^*$  is added, along with the analytic volume comprised between infinity and  $R^*$  as shown in figure 3.11.

As such, the code is able to create any external meniscus shape. In practice, at the  $i$ -th measurement, the meniscus must reach  $(\phi(s_0)) = 90^\circ - \theta_l - \theta_s$  for  $r=r_{(i)}$ . For this work, the crucible radius is considered to be sufficiently higher than  $r_{(i)}$  to consider that the Bessel analytic solution is valid at  $r = R_c$  (this assumption will be discussed in section 6). Then, it is possible to use

$$R^* = \sqrt{\frac{\rho_l g}{\gamma_{lv}}} R_c, \text{ and}$$

$$Z^* = Z(R = R^*) = \frac{K_0(R^*)}{K_1(R^*)} \tan(\phi^*)$$

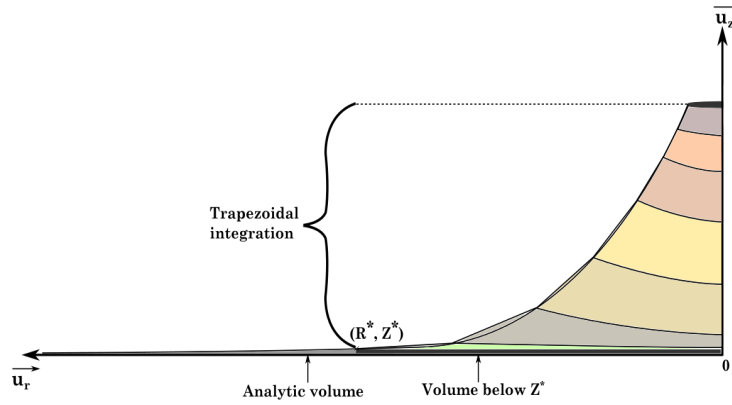


**Figure 3.11:** Principle of volume calculation used to compare our values to literature's ones. The errors visible in the schematic are amplified, since the code creates trapezoids between each successive point.

The adequate  $Z^*$  is determined using a dichotomy technique on  $\phi^*$ . If  $\phi^* \in [0, 2\pi]$  is too high (resp. too small), the meniscus length will be smaller (resp. larger) than  $R_c - r_{(i)}$ . Moreover, in the weighing method equation,  $V_{meniscus\ 1}$  corresponds to the volume computed through trapezoidal integration minus  $\pi r_{(i)}^2 \frac{\rho_l g}{\gamma_{lv}}$ . The volume below  $Z^*$  and the analytic must not be added. At this stage it is also possible to compute  $V_{gas} + V_{meniscus\ 2} + V_{excess}$  as shown on the figure 3.12.

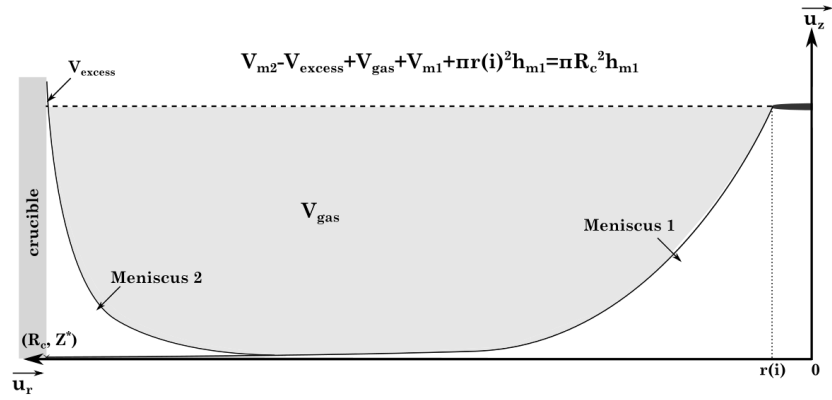


**Figure 3.12:** Illustration of the relationship linking the volume of the meniscus 1 to  $V_{gas}$

But, to obtain the values of  $V_{gas}$  and  $V_{meniscus\ 2}$ , the code should also compute the shape of the meniscus in contact with the crucible.

### 3.7.2 Internal meniscus

This internal meniscus (i.e. the meniscus in contact with the crucible) as shown in figure 3.13 is present on the walls of a large container (in this study  $R_c=11\text{cm}$ , but it could be even larger). So, the capillary rise at the center of the crucible is neglected.

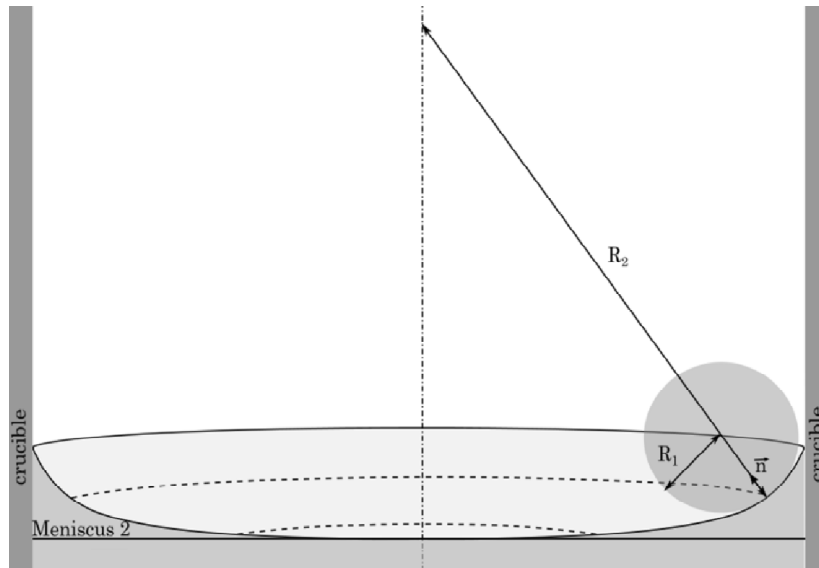


**Figure 3.13:** Radii of curvature of the internal meniscus.

The parametric representation is similar to the one used for the external menisci and the equations remain almost identical, with a “sign” difference (i.e. positive radius of curvature) due to the different coordinate system. Indeed, the origin has to be taken in the center to maintain the following equation valid.

$$\frac{\sin(\phi(s))}{r} = \frac{1}{R_2}.$$

The principle remains the same. At the center,  $Z^*$  value is determined by dichotomy. The value for which the meniscus size matches the radius of the crucible is unique, knowing that the slope and the radial coordinate at this boundary are zero. On the crucible wall, the contact angle for alumina on molybdenum is known to be  $48.2^\circ$  [Tandjaoui, 2016].

The volume of this meniscus is indirectly calculated using a trapezoidal integration as shown in Figure 3.14.

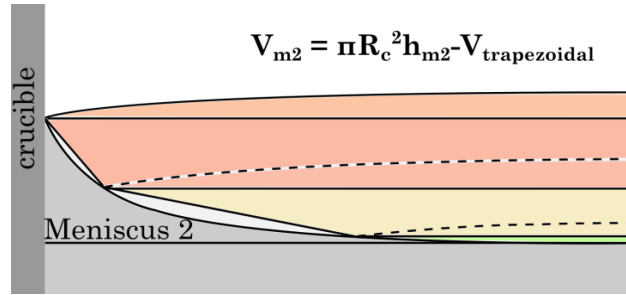


**Figure 3.14:** Volume calculations associated to the internal meniscus. The errors visible in the schematic are amplified, since the code creates trapezoids between each successive point.

The volume of the meniscus 2 remains constant, so it is calculated only once for a given  $R_c$ . Knowing  $h_{meniscus\ 1}$ , to obtain  $V_{excess}$  an extra trapezoidal integration is done for the points located above  $h_{meniscus\ 1}$ . Using the relationship presented on the figure 3.12  $V_{gas}$  value is then calculated.

Rigorously, the meniscus located at the molybdenum crucible's wall, and the one placed at the growing crystal surface are interacting. Indeed, the combination of the two forces both meniscus shape to reach a minimum with a horizontal tangent between the crystal and the crucible wall. And this shape must fit the angle  $\theta_s + \theta_L$  and the contact angle ( $48.2^\circ$  for a molybdenum crucible) at its boundary conditions [Tandjaoui, 2016]. However, the fluid elevation associated to meniscus formation becomes negligible in front of meniscus height at several capillary lengths from the interface (which represent approximately 5mm for sapphire) [Duffar, 2010]. The way this interaction can be taken into account to construct the exact capillary bridge is detailed in the next section.

### 3.7.3 Capillary bridge

When the two menisci interact, it creates a capillary bridge between the crystal and the crucible. At its minimum point the first radius of curvature is smaller than previously considered as shown in figure 3.15. According to Young-Laplace law, that means that the pressure at the melt's surface is decreased, so  $p_v < p_0$ . Hence, the equation 3.16 becomes:

$$\frac{\frac{d^2 z}{dr^2}}{(1+(\frac{dz}{dr})^2)^{\frac{3}{2}}} + \frac{\frac{dz}{dr}}{(1+(\frac{dz}{dr})^2)^{\frac{1}{2}}} = \frac{-p_v + p_o + \rho_l g z}{\gamma_{lv}} \quad \text{Equation 3.18}$$

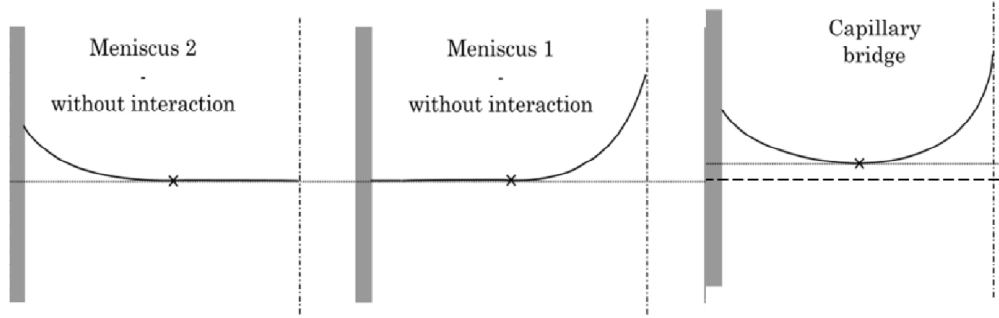


**Figure 3.15:** Minimum point and shape of capillary bridge.

Introducing,  $\check{z} = z + \frac{p_o - p_v}{\rho_L g}$ , and then  $\check{Z} = \check{z} \sqrt{\frac{\rho_L g}{\gamma_{lv}}}$ , the equation 3.19 is obtained

$$\frac{\frac{d^2 \check{z}}{dr^2}}{(1+(\frac{d\check{z}}{dr})^2)^{\frac{3}{2}}} + \frac{1}{R} \frac{\frac{d\check{z}}{dr}}{(1+(\frac{d\check{z}}{dr})^2)^{\frac{1}{2}}} = \check{Z} \quad \text{Equation 3.19}$$

To have this equation fulfilled all along the capillary bridge, the origin of the coordinate system must be taken on the axis of symmetry at  $\check{Z} = 0$  (and the scale adimensioned). But the physical model is more complex than the previous one. Thus, for the computation of the bridge, we use respectively two different ways as will be described in the following sections; for generating the fictive data ( $W_{measured}$ ,  $H$ ,  $h_{measured}$ ) and for finding the unknown shape ( $r_{(i)}$ ,  $z_{(i)}$ ).

### 3.7.3.1 Capillary bridge calculation for generating fictive data

In order to test the method we need to generate a set of fictive data for the growth of an a priori known crystal shape.

In this process, knowing ( $r_{(i)}$ ,  $z_{(i)}$ ).for the considered crystal shape, we can solve separately equations for meniscus1 and for meniscus2.

Indeed, starting the calculations from  $R^* = R_c \sqrt{\frac{\rho_L g}{\gamma_{lv}}}$  or from  $R^* = r_{(i)} \sqrt{\frac{\rho_L g}{\gamma_{lv}}}$  is not convenient, since there will be problem in the middle point, where one meniscus joins another. One way to solve this problem would be to start from the joining point ( $R_0$ ,  $Z_0$ ), but both  $z$  and  $r$  coordinates of this point are unknown. So, firstly, we carry out a dichotomy on  $\check{Z}(R_0)$ , where we have boundary condition for each meniscus.

$$\frac{dz}{dr} = 0$$

and we use RK4 to compute along the menisci until other boundary conditions are satisfied:

$$\frac{dz}{dr} = \tan(90 - (\theta_L + \theta_s)) \quad \text{for meniscus 1}$$

$$\frac{dz}{dr} = \tan(90 - \theta_L) = \tan(90 - 48.2) \quad \text{for meniscus 2}$$

Physically, this method consists in testing several differences of pressure  $p_0 - p_v$ . If this depression is overestimated (resp. underestimated), the radius of curvature at each point will also be overestimated (resp. underestimated). As a result, the capillary bridge will be too short (resp. too long) to connect the crucible wall and the crystal as shown in the Figure 3.16.  $\tilde{Z}$  being an adimensionned parameter depending both on the height and the value of  $p_0 - p_v$  (assumed to be constant along the capillary bridge), the bridge should be placed in the real space system using  $h_{measured}$ .

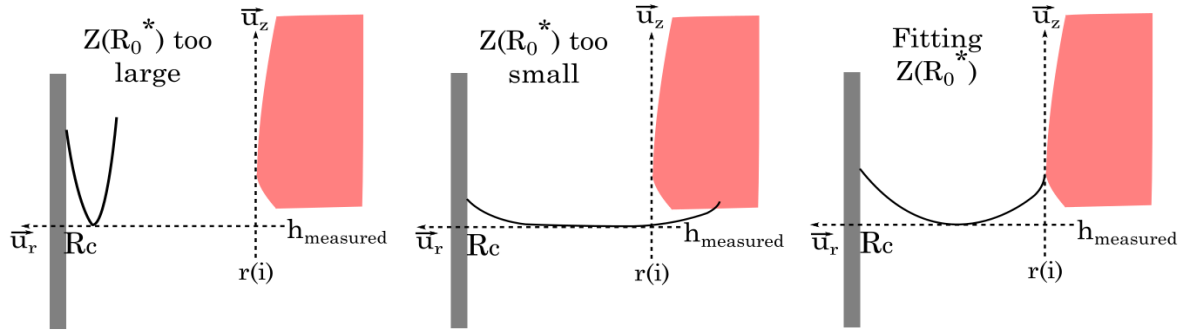


**Figure 3.16:** Influence of  $\tilde{Z}(R_0)$  value on the shape of the capillary bridge.

Moreover, the shape's equations being slightly different for the two menisci, the code must be adapted to converge properly.

Using these calculations once the capillary bridge shape is established, every parameter required to generate the fictive triplet ( $W_{measured}$ ,  $H$ ,  $h_{measured}$ ) can be computed all along the simulated growth process.

### 3.7.3.2 Capillary bridge calculation for finding the unknown shape

In this case, we use the same method as before, however, now we know the triplet ( $W_{measured}$ ,  $H$ ,  $h_{measured}$ ) instead of the radius of crystal  $r_{(i)}$  and the angle  $\theta_s$ . So, firstly, we compute meniscus2 by starting from  $(R_0, Z_0)$ , where  $Z_0$  is obtained by dichotomy. Mathematically, these different  $Z_0$  determine the curvature of meniscus2 and meniscus1 and the point where they join together. And physically, this method also consists in testing several differences of pressure  $p_0 - p_v$ .



As for meniscus1, we start also from  $(R_0, Z_0)$  to guarantee the continuity of the capillary bridge. Knowing previous point  $(r_{(i-1)}, z_{(i-1)})$ , we can do the calculation until finding the  $(r_i, z_i)$ . In fact, as shown in figure 3.17, physically, there is always a unique  $(r_i, z_i)$ , which corresponds to  $(r_{(i-1)}, z_{(i-1)})$ . At each point on meniscus1, there is a corresponding angle  $\theta_i$ , and there could be only one point who satisfies  $\theta_i = 17^\circ$ . And that is the next radius we are looking for.

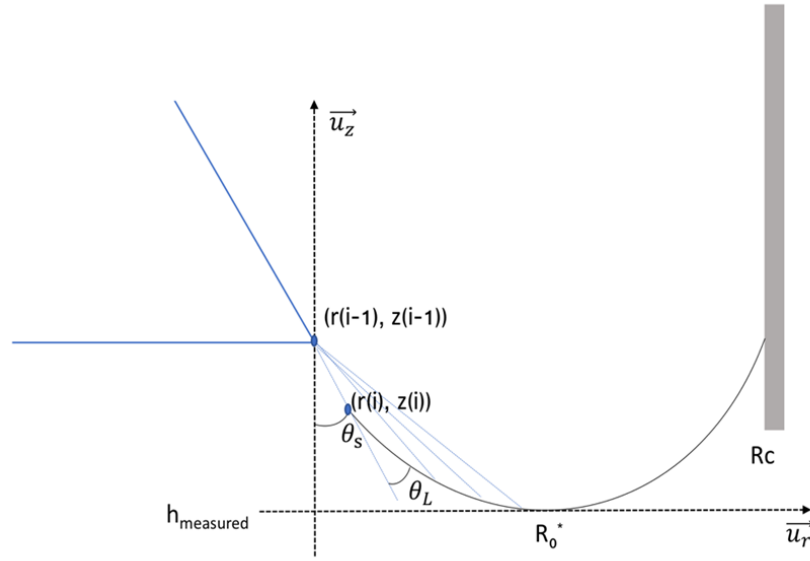


**Figure 3.17:** Process of finding  $(r_i, z_i)$  from  $R_0$

On one hand, for every  $R_0$ , we can find an unique  $(r_i, z_i)$ , and calculate the corresponding weight  $W_{measured'}$ , so that we can adjust the position of  $R_0$  by comparing  $W_{measured'}$  and  $W_{measured}$ . On the other hand, each  $R_0$  can determine a unique  $(r_i, z_i)$ . Finally, knowing  $W_{measured}$ , we can find a  $(r_i, z_i)$  and if the accuracy could be high enough, this  $(r_i, z_i)$  should be the next point, determining the crystal surface.

In both cases, we start the calculation from center  $(R_0, Z_0)$ . But we use different methods for the computation of the capillary bridge because of different starting conditions.

### 3.7.4 Crystal Shape

To test the equations and the technique we use for solving the problem, a theoretical crystal shape should be created. At first, we impose a simple cylindrical shape shown in the Figure 3.18, in order to avoid the sudden change of radius and to generate only once the capillary bridge as precisely as possible when we generate the fictive experimental data  $(W_{measured}, H, h_{measured})$ .

By applying the equations 3.1, 3.2 and 3.3, fictive experimental data ( $W_{measured}$ ,  $H$ ,  $h_{measured}$ ) are created. In reality, the operators will have access only to these experimental measurements. So, the code should be able, using only these data, to converge towards the shape initially imposed. Since the submerged volume is required to create  $W_{measured}$ , an elliptic submerged volume was created. The weighing equation being independent of this volume, it is possible to take any arbitrary shape.

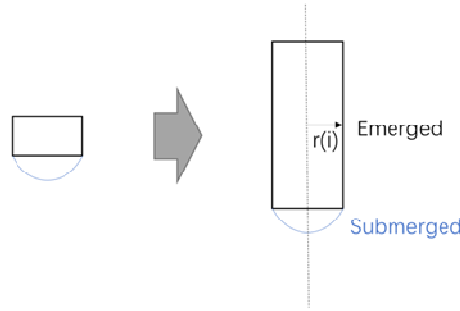


**Figure 3.18:** Shape tested for growing crystal created in the code

Knowing  $r_{(i-1)}$ , by applying the technique for the computation of capillary bridge, it is possible to calculate the unknown parameters in equation 3.11 and find  $r_{(i)}$ .

The results obtained using the models described above, and their limitations, are detailed in the next section

## 3.8 Numerical results and discussion

### 3.8.1 Menisci's shapes and volumes

The equation 3.17 has been tested, and the results checked towards Hartland and Hartley's results [Hartland, 1976]. The values compare well, since the relative error is lower than  $10^{-5}$ , except for  $90^\circ$  contact angle. Indeed, for such an angle, the slope is infinite, so when the  $R$  value is increased by  $\Delta R$  the  $Z$  value should also be infinite. That is why the values can be computed for up to an angle of  $89.9^\circ$ . The smaller the step size, the better the accuracy. Hence, the RKF45 (adaptive step size) is more accurate, at this angle value, than RK4 (constant step size). The code is limited to angles below  $90^\circ$ .

Then, external meniscus corresponding to the physical system is obtained using the code in Matlab, but could not create the shape of the meniscus if  $\theta_s < -17^\circ$ . This may happen if there is an important remelting phenomenon. Nevertheless, the code is adapted to the two other possible meniscus shapes

presented in figure 3.7 and figure 3.8. The relative error between Runge-Kutta calculation at order 4 and at order 5 is around  $10^{-5}$ , so the code proved to be accurate.

The curves and values obtained for several  $(r_{(i)}, \theta_s)$  couples are shown below.

### 3.8.1.1 External meniscus

#### 3.8.1.1.1 $\theta_s < 73^\circ$

The meniscus shape profile for 3 different crystal radius and growth angle combinations:  $(r_{(i)} \rightarrow 0.5\text{cm}, \theta_s \rightarrow 0^\circ)$ ,  $(r_{(i)} \rightarrow 3\text{cm}, \theta_s \rightarrow 45^\circ)$ ,  $(r_{(i)} \rightarrow 6\text{cm}, \theta_s \rightarrow 0^\circ)$  have been plotted using Matlab as shown in figure 3.19. The meniscus profile corresponds to the scheme presented in figure 3.3.

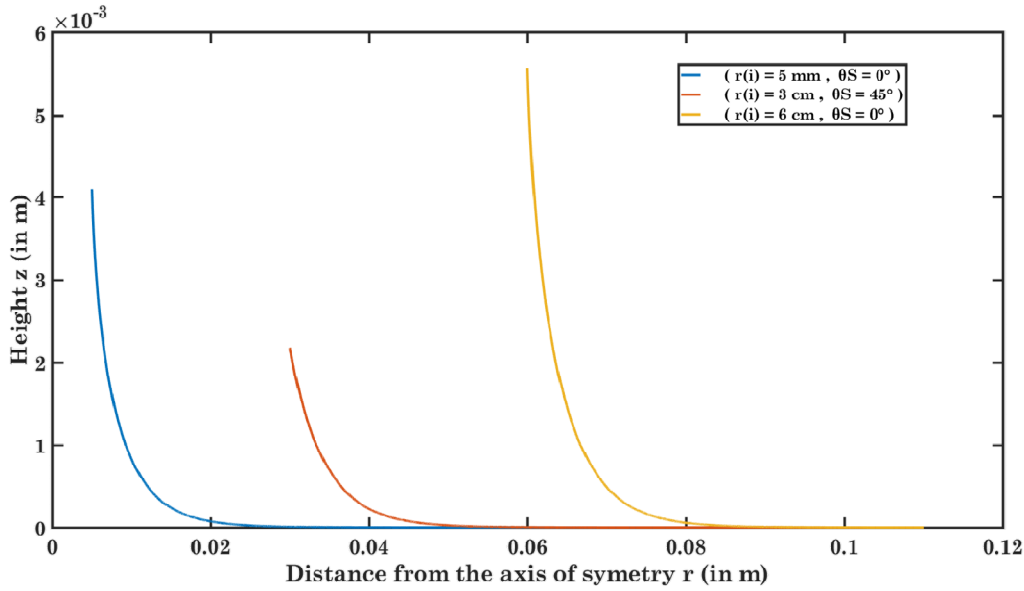


**Figure 3.19:** External meniscus shapes for different crystal radius and growth angle lower than  $73^\circ$

#### 3.8.1.1.2 $\theta_s > 73^\circ$

The meniscus shape profile for 3 different crystal radius and growth angle combinations:  $(r_{(i)} \rightarrow 0.5\text{cm}, \theta_s \rightarrow 85^\circ)$ ,  $(r_{(i)} \rightarrow 1.5\text{cm}, \theta_s \rightarrow 85^\circ)$ ,  $(r_{(i)} \rightarrow 2.5\text{cm}, \theta_s \rightarrow 85^\circ)$  have been plotted using Matlab as shown in figure 3.20. The meniscus profile corresponds to the scheme presented in figure 3.7.

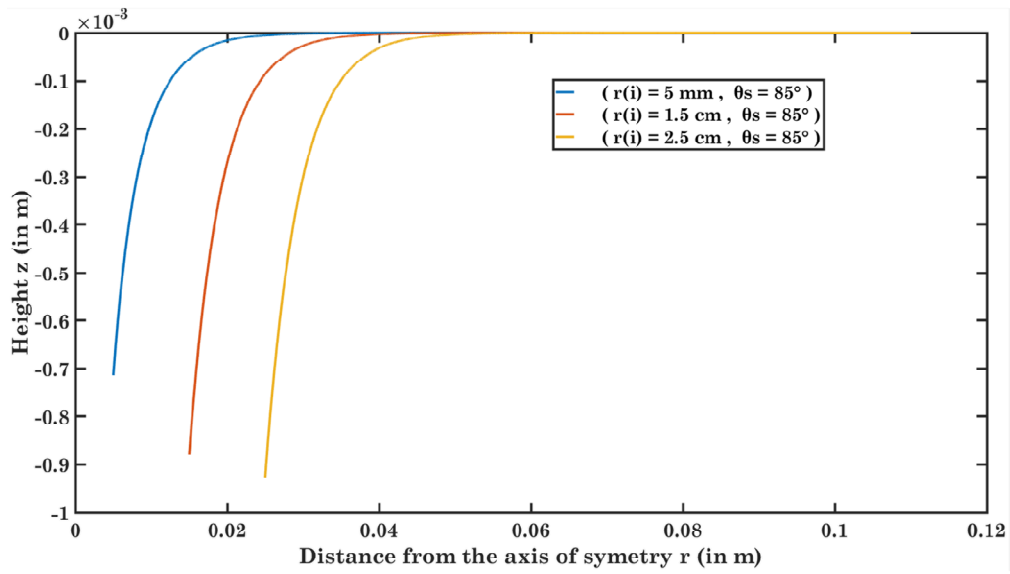


**Figure 3.20:** External meniscus shapes for different crystal radius and growth angle larger than  $73^\circ$

### 3.8.1.2 Internal meniscus

The meniscus shape profile for crucible radius of  $R_c = 11\text{ cm}$  has been plotted using Matlab as shown in figure 3.21. The meniscus profile with a contact angle of  $48.2^\circ$  to the crucible corresponds to the scheme presented in figure 3.13.

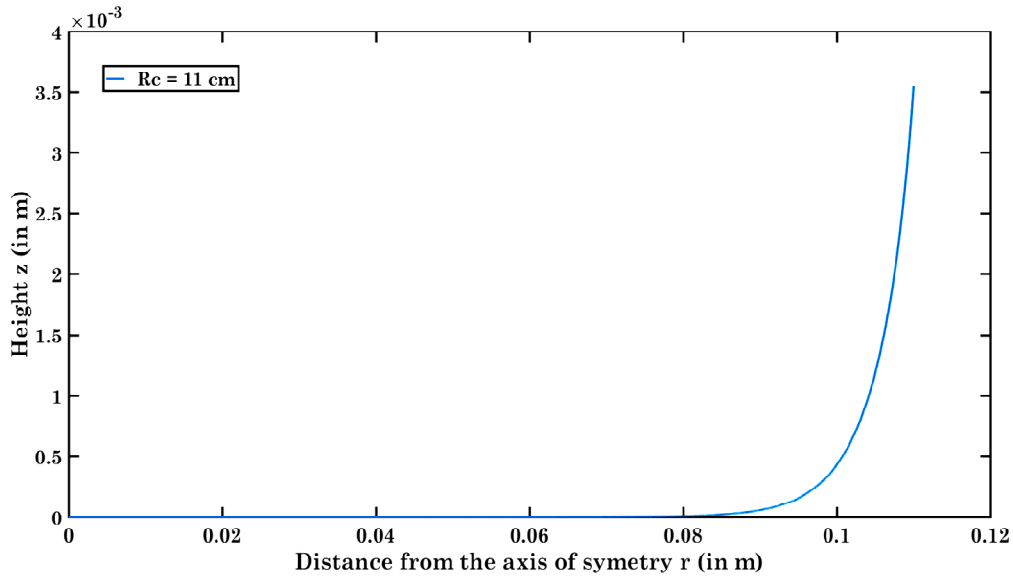


**Figure 3.21:** Internal meniscus shape for  $R_c = 11\text{ cm}$

The meniscus shape profile for crucible radius of  $R_c = 20\text{ cm}$ ,  $11\text{ cm}$ ,  $5\text{ cm}$  and  $2\text{ cm}$  have been plotted using Matlab as shown in figure 3.22.

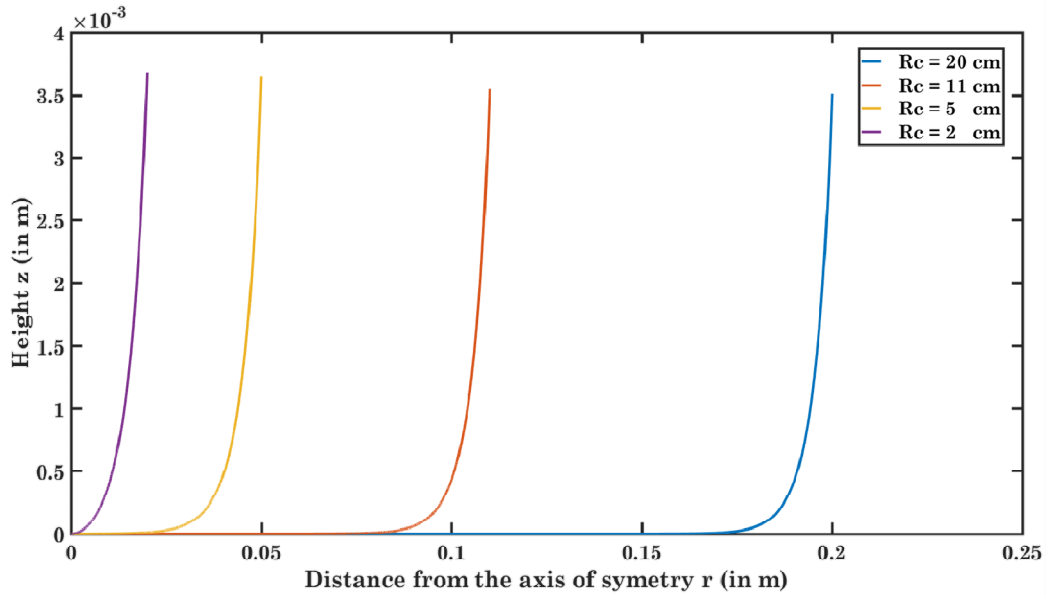


**Figure 3.22:** Internal meniscus shape for various crucible radius  $R_c$  values.

In this representation, it can be seen that the meniscus length matches the crucible radius. The crucible radius is assumed to be constant in this study, if the interactions between the two menisci could be neglected, its shape would remain the same throughout the crystal growth, thus, the coordinates of each computed point could be stored in a file and could be reused at any time of the pulling without making all the calculations again. Moreover, the technique applied works for any crucible size as shown in Figure 3.22.

### 3.8.1.3 Meniscus interaction

However, if the crucible size is too small or the simulation demands a high accuracy, the hypothesis of no interaction between the two menisci would be incorrect. It is particularly clear on the curve obtained for  $R_c = 2$  cm as shown in figure 3.21, for which  $Z^* = 5.9$ . It shows that the crucible size forces the surface of the liquid to be depressed of  $p_0 - p_v = Z^* \sqrt{\gamma_{lv} \cdot g \cdot \rho_L} = 8.4$  Pa. Each meniscus height becomes negligible in front of its total height ( $10^{-3}$  ratio) at 2 cm to 3 cm from the crucible or crystal interface. Thus, the assumption becomes incorrect when the distance between the crystal radius and the crucible reaches 5 cm or less. To avoid such inaccuracy, the shape of the capillary bridge should be directly calculated.

To demonstrate this phenomenon two cases have been studied and demonstrated. Figures 3.23 and 3.24 reveal the profile of the menisci with and without considering menisci's interaction (for  $R_c = 11$  cm,  $r_{(i)} = 9$  cm and  $R_c = 11$  cm,  $r_{(i)} = 6$  cm respectively).

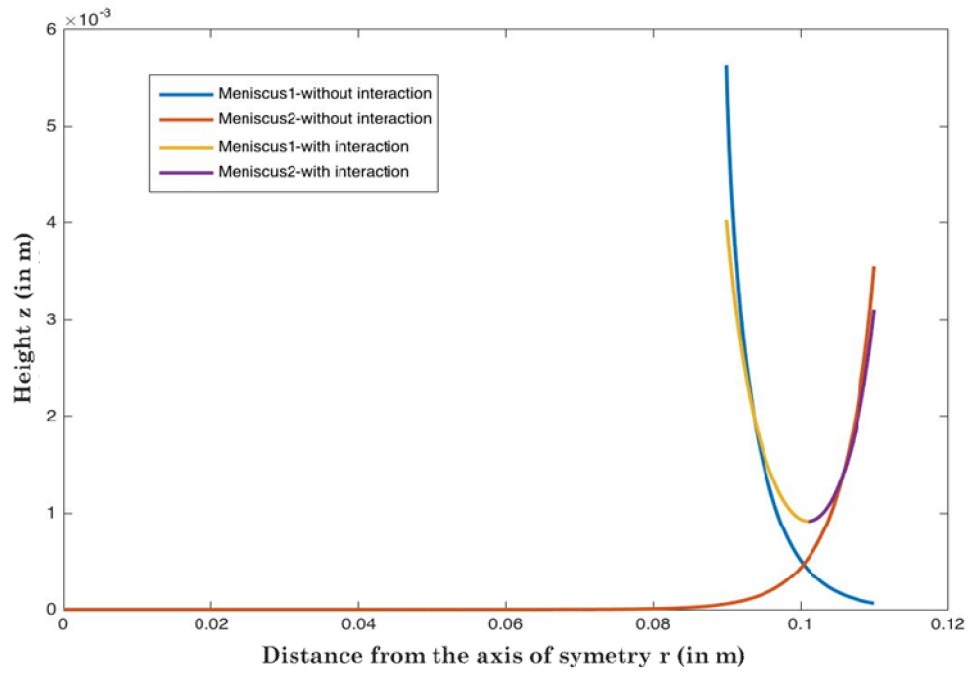


**Figure 3.23:** Comparison between menisci shapes obtained without considering any interaction and capillary bridge's one for  $r_{(i)} = 9$  cm and  $R_c = 11$  cm.

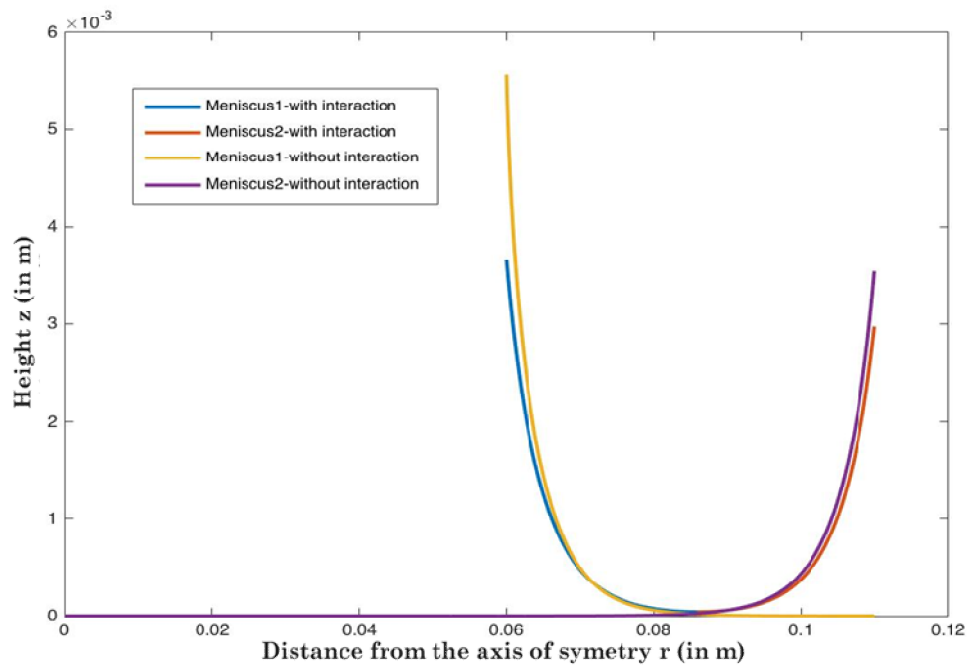


**Figure 3.24:** Comparison between menisci shapes obtained without considering any interaction and capillary bridge's one  $r_{(i)} = 6$  cm and  $R_c = 11$  cm

From figure 3.23 it can be observed that when the meniscus length is just 2 cm there is considerable interaction between the two individual menisci and there is a vertical displacement of about 1 mm. But when the meniscus length is 5 cm, the vertical displacement is negligible as shown in figure 3.24.

### 3.8.2 Errors associated to thermal heterogeneousness and pulling

In the weighing method equations 3.11 and 3.13, other assumptions are indirectly introduced. Indeed, so far  $\rho_L$ ,  $\rho_s$ ,  $\theta_L$  and  $\Upsilon_{lv}$  has been considered constant. But, due to temperature heterogeneousness, it is not rigorously the case. The resulting errors are discussed in the next paragraph.

Inside the melt and the crystal, even though the temperature gradient is small its effects on physical parameters such as the density should be considered, since they may not be negligible. To quantify the impact of this heterogeneousness, a combination of modeling results and analytical equations have been used.

The molten sapphire density dependence over temperature is described by the relationship.

$$\sigma_L = 5543.16 - 1.08T \text{ [Timofeev, 2015]}$$

On Figure 3.25, the temperature repartition inside the melt at some moment during the crystal growth after seeding is represented [Stelian, 2016]. Molten sapphire is submitted to temperatures between 2300 K and 2400 K. Hence, its density could fluctuate in between  $3059 \text{ kg.m}^{-3}$  and  $2951 \text{ kg.m}^{-3}$ , approximately  $3000 \text{ kg.m}^{-3} \pm 2\%$ . However, the mean temperature of the melt does not change very much along the duration of the growth process. Hence, the variation of the liquid density is much lower than its absolute value.

Solid sapphire temperature interval goes from 2117 K to 2300 K. Since the sapphire's thermal expansion coefficient is  $3.56 \cdot 10^{-4}$  and the relative error on the density is given by:

$$\frac{\Delta \rho_s}{\rho_s} = \alpha \Delta T$$

The relative error made by taking an average value is around 3%.

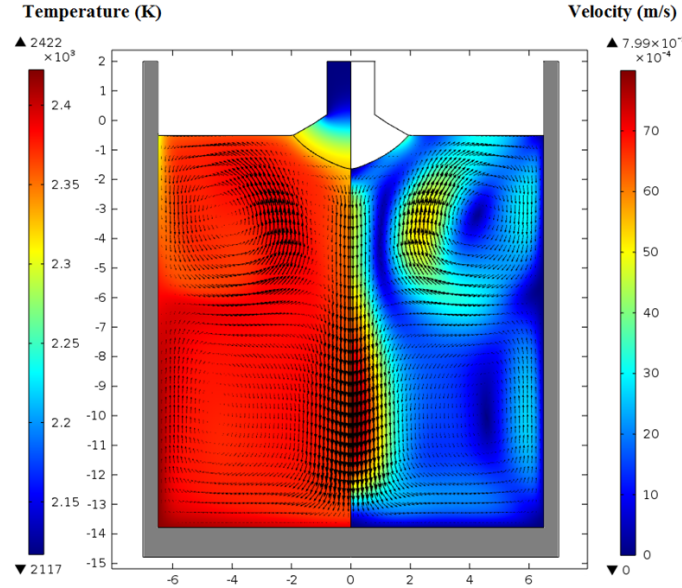


**Figure 3.25:** Temperature and liquid velocity repartition during sapphire growth.

Surface tension is also impacted by temperature gradients. Using Eötvös rule, it is possible to calculate a relative error of 1 to 2 % (the exact temperature gradient at the surface of molten sapphire is not very accurate when read in the Figure 3.25).

Another approximation is used to develop the model explained so far. Both contact angles on the crucible wall and the crystal surface are assumed to be constant and equal to the static value. Rigorously, the dynamic angle value should be used:

$$\frac{\eta \cdot \text{PullingRate}}{\gamma_{lv}} = \theta_d(\theta_d^2 - \theta_L^2)$$

Where  $\theta_d$  is the dynamic contact angle and  $\eta$  the dynamic viscosity. For sapphire, considering a pulling rate of 1 mm/hr and a dynamic viscosity of 0.6 Poise, one obtain  $\theta_d = 17.0001^\circ$  for  $\theta_L = 17.0000^\circ$  [Pishchik, 2009]. Thus, they can be considered equal.

Even though neglected in this work, whose aim was to develop a model able to determine the shape of any crystal pulled using the height measurement in addition to the usual experimental data, these uncertainties must be considered to maximize the precision of shape measurement. Nevertheless, to build an experimental set up to verify this model, specification on the height measurement device accuracy is required.



### 3.8.3 Generate fictive measurement data

In practice, presently there is no way to get the measurement data from the experiment. In fact, we have  $W_{measured}$  and  $H$ , but the exact crystal shape corresponding to it is not known and we do not have the system to measure  $h_{measured}$  yet. So, the only way is to generate numerically the fictive measurement data ( $W_{measured}$ ,  $H$ ,  $h_{measured}$ ).

Based on the fictive shape imposed (figure 3.18), we can do a calculation of the capillary bridge at each point, as well as every parameter in equation 3.11. Finally, we can get a set of measurement data. However, these data are not the exact value, their accuracy depend on the (error\_Bridge), which describes the error in the calculation of the capillary bridge. (error\_Bridge) is the relative error defined as follows:

$$\text{error\_Bridge} = \frac{\text{Length of capillary bridge calculated}}{R_c - r_{(i)}}$$

Thus, by controlling the parameter error\_Bridge, we can control the error of fictive measurement data ( $W_{measured}$ ,  $H$ ,  $h_{measured}$ ). For each step, we have a set of these data, and a corresponding accuracy associated with it. The maximum working accuracy of error\_Bridge taking into consideration the computation time has been determined to be  $1 \cdot (10^{-7})$ .

Supposing that there is no error when error\_Bridge =  $1 \cdot (10^{-7})$ , the propagated error in the measured set of data ( $W_{measured}$ ,  $H$ ,  $h_{measured}$ ) was studied by increasing the error\_Bridge to  $1 \cdot (10^{-6})$ ,  $1 \cdot (10^{-5})$  and  $1 \cdot (10^{-4})$  and comparing it to error\_Bridge =  $1 \cdot (10^{-7})$ . The results are as depicted in Table 3.1.

error_Bridge	$1 \cdot (10^{-4})$	$1 \cdot (10^{-5})$	$1 \cdot (10^{-6})$	$1 \cdot (10^{-7})$
$W_{measured}$ (kg)	$2.7 \cdot (10^{-6})$	$1.9 \cdot (10^{-6})$	0	0
H (m)	$8 \cdot (10^{-6})$	0	0	0
$h_{measured}$ (m)	$2.5 \cdot (10^{-8})$	$3 \cdot (10^{-9})$	0	0

**Table 3.1:** Error in  $W_{measured}$ ,  $H$  and  $h_{measured}$  with error\_Bridge.

From this table, it is clear that as error\_Bridge increase, the error of data ( $W_{measured}$ ,  $H$ ,  $h_{measured}$ ) also increase. It has been checked that the error remains invariant as  $z$  changes for the crystal shape in consideration.

### 3.8.4 Finding the imposed shape

To determine the minimal accuracy required for this measurement, our first step is to figure out how to find the shape imposed by the fictive measurement data ( $W_{measured}$ ,  $H$ ,  $h_{measured}$ ) and prove numerically that this idea can work.

To find the shape, i.e crystal radius  $r_{(i)}$  and height  $z_{(i)}$  at each step, it is needed to solve equation 3.11 and equation 3.13. However, in these two equations, almost every parameter is related to  $r_{(i)}$  and  $z_{(i)}$ , which are unknown. Thus, we can neither treat these two equations like equation with constant coefficient, nor plot the relation of  $r_{(i)}$ ,  $z_{(i)}$  and  $W_{measured}$  because  $r_{(i-1)}$  and  $z_{(i-1)}$  also affect the result.

Based on the technique introduced in section 5.3.1, knowing the last point  $(r_{(i-1)}, z_{(i-1)})$ , a capillary bridge can be generated starting from the point  $(R_0, Z_0)$ , where the meniscus is horizontal and a unique  $(r_{(i)}, z_{(i)})$  can be found for each  $R_0$ , as well as every parameter in equations. For the simple shape imposed, it is just needed to solve equation 3.11 and as of now not consider the remelting phenomenon.

As an example, we take

$$\begin{cases} r(i) = r(i-1) = 0.5\text{cm} = 0.005\text{m} \\ \Delta z = z(i) - z(i-1) = 1\text{cm} = 0.01\text{m} \end{cases} \text{ for } i \in [1,10]$$

On one hand, for every  $R_0^*$ , we can find a  $(r_{(i)}, z_{(i)})$ , and calculate the corresponding weight  $W_{measured}'$ , so that we can adjust the position of  $R_0$  by comparing  $W_{measured}'$  and  $W_{measured}$ . On the other hand, each  $R_0$  can determine a unique  $(r_{(i)}, z_{(i)})$ . Finally, knowing  $W_{measured}'$ , we can find a  $(r_{(i)}, z_{(i)})$  and if the accuracy could be high enough, this  $(r_{(i)}, z_{(i)})$  should be the next point of the crystal.

By doing the simulation, we find that the middle point of radius of crystal  $r_{(i)}$  and crucible  $R_c$ , is always very close to the minimum point of the capillary bridge. Thus it is important to study how the system evolves close to this point. By doing the calculation, we find that  $R_0^*$  is around 12.05 when  $r_{(i)}=0.005\text{m}$  and  $R_c=0.11\text{m}$ .

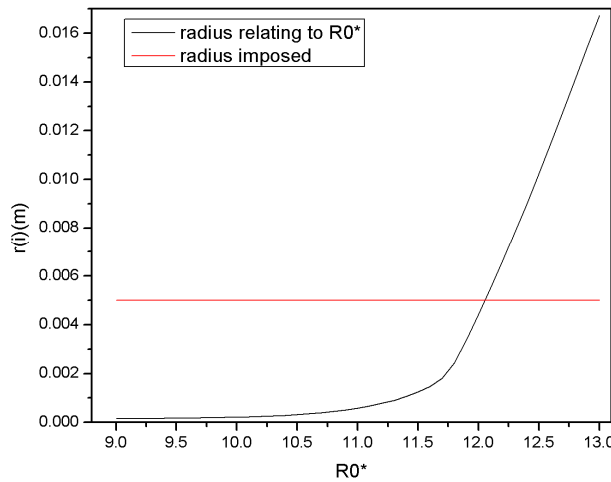


**Figure 3.26:** Plot of  $r_{(i)}$  and  $(R_0^*)$

Plotting the function  $r_{(i)}$  and  $(R_0^*)$  in Figure 3.26, we find that at the neighbourhood of  $R_0^*=12.05$ ,  $r_{(i)}$  changes rapidly with a slight variation of  $R_0^*$ , which means we need a high accuracy of  $R_0^*$  to have an acceptable  $r_{(i)}$ .

To determine the position of  $R_0$  by comparing  $W_{measured}'$  and  $W_{measured}$ , it is necessary to know the relation of  $R_0$  and  $W_{measured}'$ . If function  $W_{measured}'(R_0^*)$  is monotonous at the neighbourhood of this point, then we can carry out a dichotomy.

Fixing  $h_{measured}$  and  $H$ , we plot the function  $W_{measured}'(R_0^*)$ . Results are shown as below:

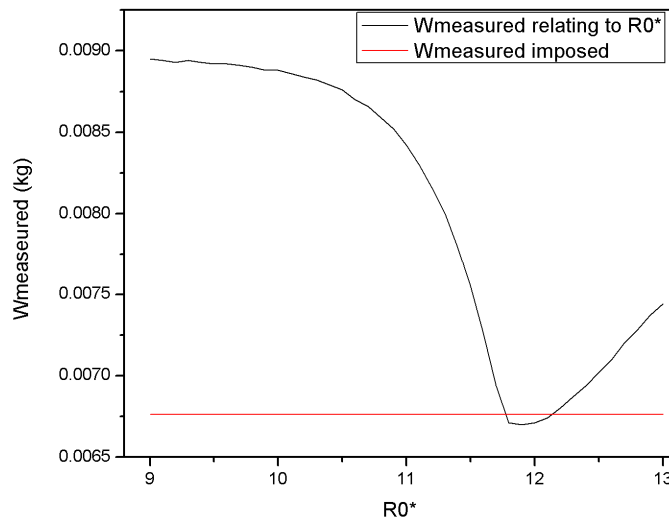


**Figure 3.27:** Plot of  $W_{measured}'$  and  $(R_0^*)$

From Figure 3.27, it can be seen that  $W_{measured}'(R_0^*)$  is not always monotonous. But if figure 3.26 and figure 3.27 are observed together, it can be seen that  $W_{measured}'$  is monotonically increasing when  $r_{(i)} \geq r_{(i-1)}$ , which is the case during crystal growth without remelting. In fact, it is monotonous at the neighborhood of  $R_0^*=12.05$ .

As  $W_{measured}'$  changes slightly with  $R_0^*$ , it is needed to have a very accurate  $W_{measured}$  to determine  $R_0^*$ .

Numerically, the error of  $W_{measured}$  equal to  $10^{-5}$  was considered as the criterion. To be specific, in every step to find  $(r_{(i)}, z_{(i)})$ , iterations have been carried on until  $W_{measured}' - W_{measured} \leq 10^{-5}$ .

Different error\_Bridge are taken as criterion to generate  $(W_{measured}, H, h_{measured})$  with different accuracy. By using these data, the imposed shape can be found out with the varying accuracies as demonstrated in figure 3.28.

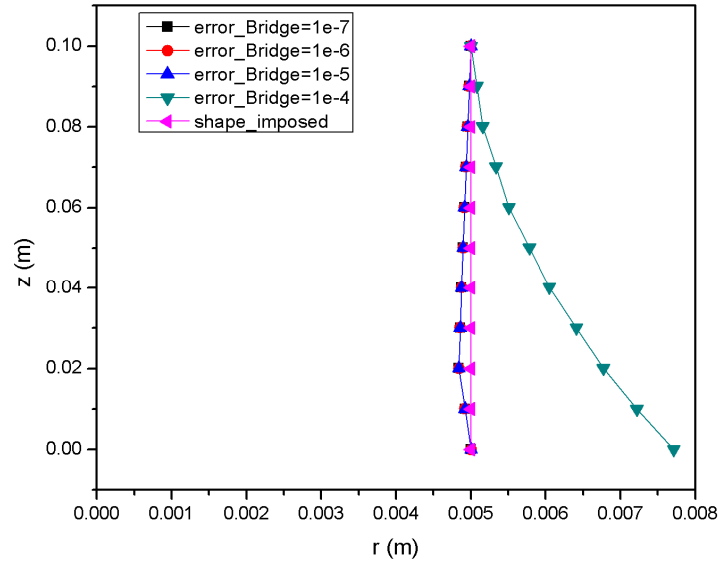


**Figure 3.28:** Error in  $h_{measured}$  with  $error\_Bridge$

From this figure, it can be seen that for  $error\_Bridge < 10^{-4}$ , the calculation is stable and the imposed shape can be traced back within 10 points (0.1m). The maximum relative error of radius is less than 4%, which is still acceptable. However, when  $error\_Bridge > 10^{-4}$ , the error propagates rapidly and there is considerable error in finding the imposed shape. From table 3.1 it can be deduced that the initial shape can be found, when

$$\begin{cases} error\_W_{measured} \leq 2.7 \times 10^{-6} kg \\ error\_H \leq 8 \times 10^{-6} m \\ error\_h_{measured} \leq 2.5 \times 10^{-8} m \end{cases}$$

### 3.8.5 Minimal accuracy required for the melt level measurement

The aim of the whole exercise was to demonstrate that with a viable system to measure the melt level  $h_{measured}$  it is possible to trace the shape of the growing crystal. Hence, it is important to determine the accuracy of  $h_{measured}$  needed to be able to determine  $r_{(i)}$  and the impact of error in  $h_{measured}$  on determination of  $r_{(i)}$  at each step.

To determine the minimal accuracy required for this measurement, different error values are added to  $h_{measured}$  calculated value. As a result, the computed menisci parameters, and finally  $r_{(i)}$ , are modified. When using the most accurate  $W_{measured}$  and H values, by adding an error on  $h_{measured}$ , the effect of accuracy needed for  $h_{measured}$  can be studied. The error is added by an arbitrary number. For example,  $error\_h=10^{-7}m$  means that the error added to  $h_{measured}$  is smaller than  $10^{-6}m$  and may be up to several  $10^{-7}m$ .

First we considered a case where;  $R_c = 0.14 \text{ m}$  and  $r_{(i)} = 0.005 \text{ m}$  as shown in figure 3.32. This would correspond to the early stages after seeding since the crystal radius considered corresponds to that of the seed and the meniscus bridge length is very long (0.135 m) where there is negligible interaction between the two menisci.

From the figure 3.29 it can be seen that an error of measurement upto several  $10^{-8} \text{ m}$  in  $h_{measured}$  would be acceptable and would not affect the value of  $r_{(i)}$  being determined and hence would be accurate.

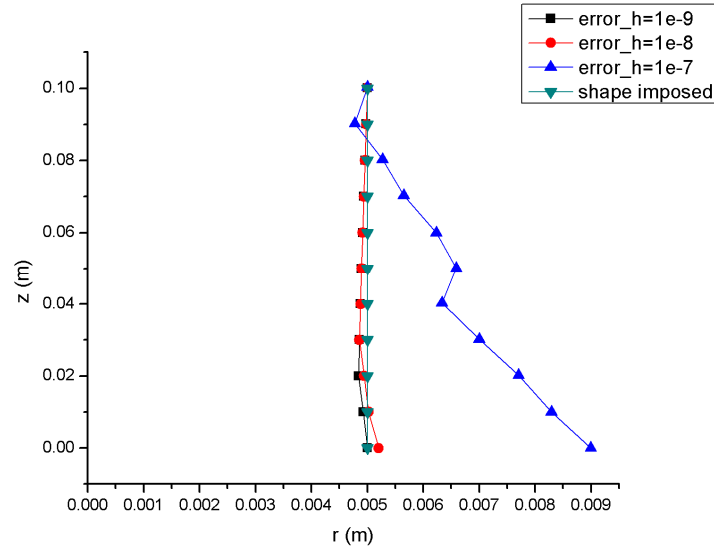


**Figure 3.29:** Error in  $r_{(i)}$  with  $h_{measured}$  for  $R_c = 0.14 \text{ m}$  and  $r_{(i)} = 0.005 \text{ m}$

Then we considered a case where;  $R_c = 0.14 \text{ m}$  and  $r_{(i)} = 0.10 \text{ m}$  as shown in figure 3.30. This would correspond to the crystal growth stage after shouldering where it grows with a constant radius. The meniscus bridge length (0.04 m) is just about the value where the interaction of individual meniscus would start playing a role.

From the figure 3.30 it can be seen that an error of measurement upto several  $10^{-6} \text{ m}$  in  $h_{measured}$  would be acceptable and would not affect the value of  $r_{(i)}$  being determined and hence would be accurate.

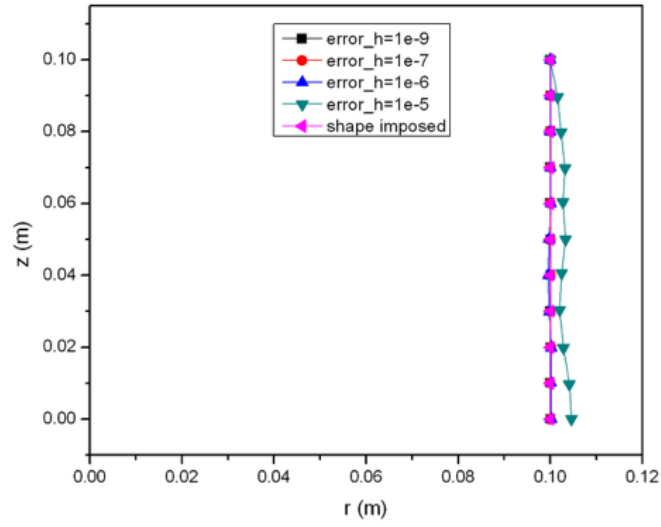


**Figure 3.30:** Error in  $r_{(i)}$  with  $h_{measured}$  for  $R_c = 0.14\text{ m}$  and  $r_{(i)} = 0.10\text{ m}$

Finally we considered a case where,  $R_c = 0.14\text{ m}$  and  $r_{(i)} = 0.13\text{ m}$  as shown in figure 3.31. This would correspond to the crystal growth stage after shouldering where it grows with a constant radius and very close to the crucible. The meniscus bridge length (0.01 m) is the value where there would be definite interaction of the two individual menisci.

From the figure 3.31, we can see that an error of measurement upto several  $10^{-5}\text{ m}$  in  $h_{measured}$  would be acceptable and would not affect the value of  $r_{(i)}$  being determined and hence would be accurate. In figure 3.32 we magnify the x-axis to display the range of error which is around 0.002 m for the crystal radius with an error of measurement up to several  $10^{-5}\text{ m}$  in  $h_{measured}$ .

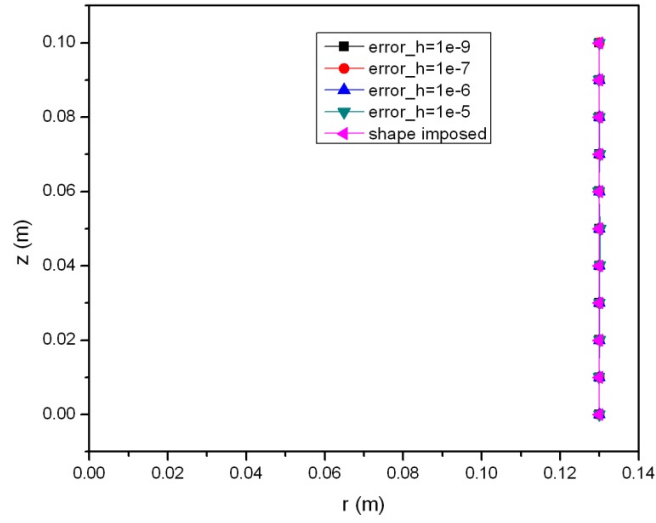


**Figure 3.31:** Error in  $r_{(i)}$  with  $h_{measured}$  for  $R_c = 0.14$  m and  $r_{(i)} = 0.13$  m

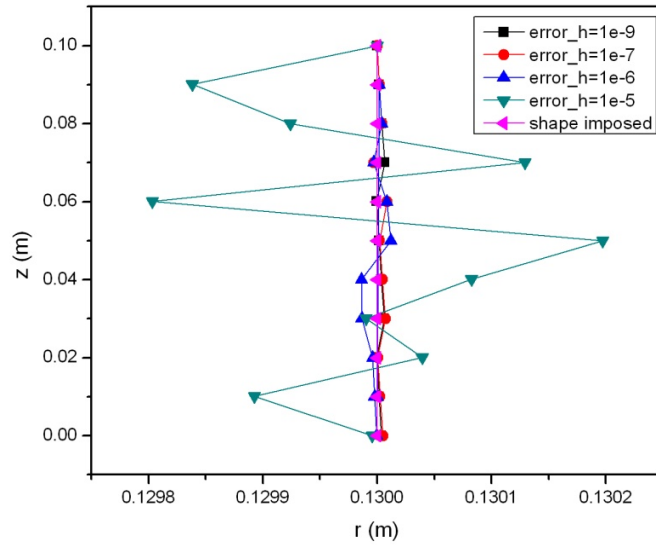


**Figure 3.32:** Error in  $r_{(i)}$  with  $h_{measured}$  for  $R_c = 0.14$  m and  $r_{(i)} = 0.13$  m with the x-axis zoomed in.

Hence, we can see a trend that as the distance between the growing crystal and crucible decreases from 0.135 m to 0.01 m, the accuracy needed for  $h_{measured}$  also decreases from several  $10^{-8}$  m to several  $10^{-5}$  m.

### 3.9 Conclusion

In this chapter a new technique for crystal radius reconstruction and hence the crystal shape reconstruction in Kyropoulos growth system has been introduced and studied. It is based on the simultaneous measurement of the crystal weight and the remaining melt level.

An important result is that taking into account force balance, weight conservation and volume transformation, the unknown shape of the submerged part of the crystal can be removed from the equations. This allowed computing the crystal radius at any moment, through computation of the menisci shapes.

This method has been tested for fictive data considering a cylindrical crystal shape. It was shown that the accuracy needed when the crystal radius is very small compared to the crucible radius is beyond the capabilities of conventional measurement tools. However, when after the initial growth stages the crystal attains a constant growth diameter and the distance between the crucible and the crystal is bridged by a small capillary bridge, the accuracy needed for the melt height measurement is lower and a system can be implemented to monitor this regime of growth.

In the Kyropoulos growth technique, the crystal diameter is generally closer to the crucible diameter than in Czochralski technique. Therefore, the proposed technique is well fitted to the Kyropoulos growth system to control the crystal radius variations during the steady state growth but not during the initial stages of growth after seeding when the distance between the crucible and crystal is much larger.

### 3.10 Perspectives

At the current stage of the work developed in the context of crystal shape control, it is very prospective and a lot more remains to be developed to have it ready for adoption in a crystal growth system.

It is needed to check mathematically the stability of the system. The response of a periodic change in the crystal radius has to be checked. The particular cases and the conditions fulfilling those in which it is possible to have a unique solution for the value of crystal radius have to be studied.

The accuracy is also limited by the increasing computational time required with increasing accuracy. Hence, an optimized solution between the computational time required and the maximum accuracy possible has to be determined.

From this study it follows that the liquid level measurement system must be able to determine the minimum point of the melt (meniscus bridge) where it is horizontal. It must also be able to determine the liquid level at this point with accuracy better than 100  $\mu\text{m}$ . In addition this system has to be adapted for service at a very high temperature environment and hence an instrument which can be at a distance from the melt should be preferred.



Apparently, a laser based distance measurement tool could be adapted to fulfil these requirements. It would also need a powerful filtering system to damp out the fluctuations at the liquid surface and give a corrected value for the liquid level which would be reliable with desired accuracy.

## 4 Investigations into the milky defect

### 4.1 Introduction

Based on the long experience and research initiatives in improving the Kyropoulos growth technique for  $\text{Ti:Al}_2\text{O}_3$ , we have achieved a good control over the process which has resulted in growth of crystals with a good morphology and devoid of any macroscopic defects. But owing to the envisioned application of these crystals in laser technology, the optical quality and characteristics of the discs cut from the crystal are under utmost consideration.

In this context, there is one defect in particular which has been observed in the disc samples cut from the crystals and has been investigated during the course of this project. This defect is observed as a slightly translucent band of around 1cm in width in the otherwise transparent matrix, passing through the centre of the disc along the diameter reaching the surface at opposite ends. It is observed much better in thick disc samples (1 cm thickness) than in thin samples (1 mm thickness) and the apparent contrast of this region depends on the direction of the incoming light. These disc samples show the evidence of these defects when they are cut from the vertical mid-section of the crystal, i.e excluding the top shoulder region of the crystal where often there is the presence of small bubbles and the bottom quarter of the crystal. Henceforth, this region or defect will be referred to as the milky zone since it is translucent and white in contrast to the sample. Some images of the mentioned defect are shown in figure 4.1.

It has been already mentioned in Chapter 2, that this defect is detrimental to the laser efficiency. Understanding the nature of this milky defect and its formation mechanism is of utmost importance because it is the most evident defect that can be seen by the naked eye in the otherwise defect free discs cut from the crystals. The visual evidence of this defect makes it difficult for such samples to be sold to prospective customers. To characterise this milky defect in the crystals a series of analysis were undertaken on various samples throughout the course of the project with the hope that the results from all these analyses, when put together, will reveal the nature of the defect and provide some clues into its possible formation mechanism.

The first intuition regarding this defect was the presence of smaller aggregation of bubbles than those seen in the top shoulder region of the crystal as shown in figure 2.9, but samples from this milky defect region were analysed with optical microscope and scanning electron microscope and showed no evidence of such macro and micro bubbles. Hence, as a first step the defect zone was characterised for its crystalline quality

by using X-ray topography and Rocking curve imaging analysis at BM-05 of ESRF, Grenoble. It was done in order to check the hypothesis that the milky defect zone could be linked to dislocations and stresses. The experiments were carried out with the help of Thu Nhi Tran Caliste and Jose Baruchel assisting in qualitative and quantitative analysis of the results. Thermal simulations of the Kyropoulos system carried out by Carmen Stelian helped establish a relation between the growth process and the milky defect zone regions in the crystals. Thermally stimulated luminescence spectra were obtained for our samples at the University of Tartu by Vitali Nagirnyi who helped to determine the nature of the defect. Optical characterisation carried out by Guillaume Alombert-Goget at ILM, Lyon along with Small Angle X-ray Scattering analysis carried out at Grenoble INP-CMTC by Frédéric De Geuser revealed the physical scale and nature of the constituents in this defect zone. Finally TEM microscopy analyses were carried out by Gilles Renou and Patricia Donnadiou at CMTC, Grenoble to make an attempt to visualise the constituents of this defect zone.

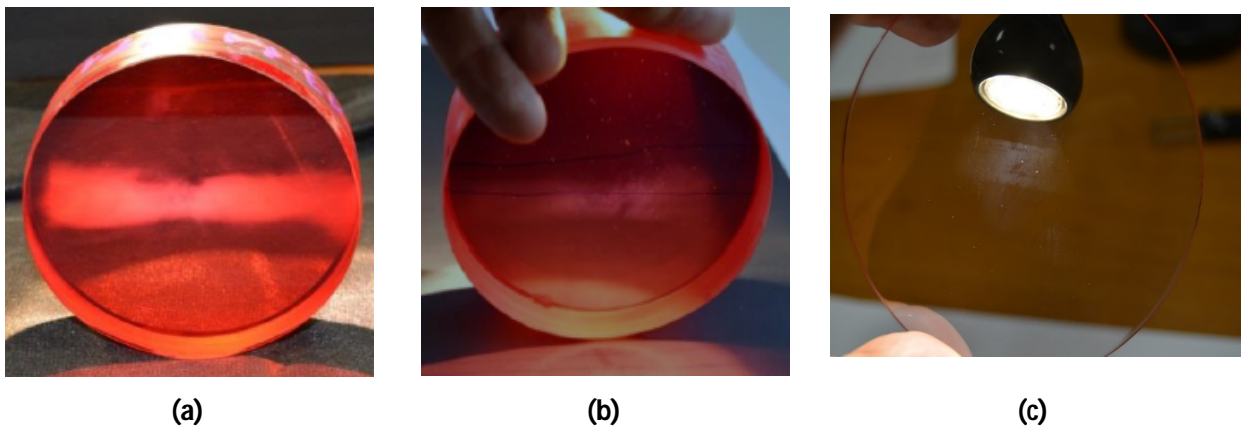


**Figure 4.1:** (a) Thick disc(10 mm) with milky region (b) the milky region observed with a different direction of incoming light (c) thin disc(1 mm) with the milky region.

#### 4.1.1 Defect Orientation

The interesting aspect of this milky zone is that it is a very sharp and bounded zone exactly passing through the centre in all the samples observed in different crystals pulled along the A-axis direction, but never observed in crystals pulled along the C-axis. This leads to the idea of there being a correlation of this zone with the crystallographic directions of the sapphire crystal. Hence investigations were carried out to determine the direction of the milky zone and it was always found to be coincident with the C-plane(0001) (perpendicular to the C-axis). A representation of the milky defect zone with respect to the crystallographic orientations is presented in figure 4.2.

Thus, it is clear that there is an influence of crystallographic orientations on the existence of the defect but it poses more questions than it answers. Why is the defect only present as a narrow band along the diameter, while the C-planes are oriented parallel to it on either side throughout the surface? Also, since the growth process ensures a quasi-perfect axis-symmetric condition it is difficult to explain any effect of perturbations during the growth since this region is not axisymmetric. Thus, there are further investigations needed to explain this milky zone formation.

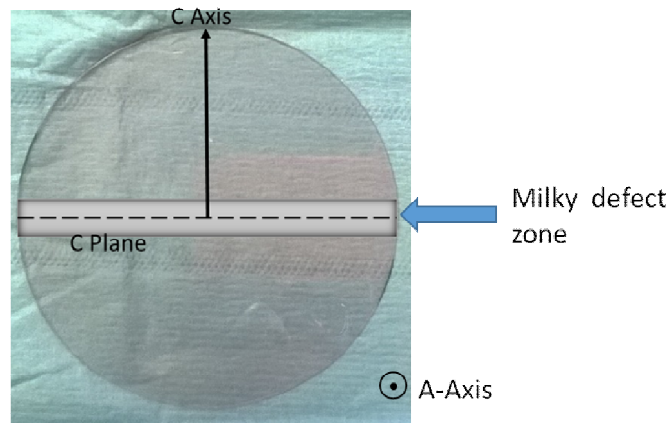


**Figure 4.2:** Orientation of the milky defect zone along the C-plane passing through the centre.

## 4.2 Diffusion of laser in defect zone

This defect zone has also been observed to diffuse laser light and an analysis of the behaviour of laser light in this region has been performed.

The laser light is green in colour in air, but turns red in colour inside the titanium doped sapphire crystal due to its interaction with the titanium ions. Hence, red colour of the laser in the crystal media indicates desired laser propagation but green colour inside the crystal indicates the diffusion of the laser light.

### 4.2.1 Milky defect (Vertically aligned)

As shown in figure 4.3(a), the disc was positioned so as to have the milky defect zone aligned vertically. The incoming laser passed through the sample and the disc was moved from right to left, so as to have the laser passing outside the defect, then progressing to the vertical defect zone and then again outside it. We observe that there is a very sharp diffusion of the laser light inside the defect zone as indicated by the bright green colour in figure 4.3(d) and 4.3(e). Outside the defect the beam is red in colour as shown in figure 4.3(b), 4.3(c) and 4.3(f), indicating there is no diffusion at all.

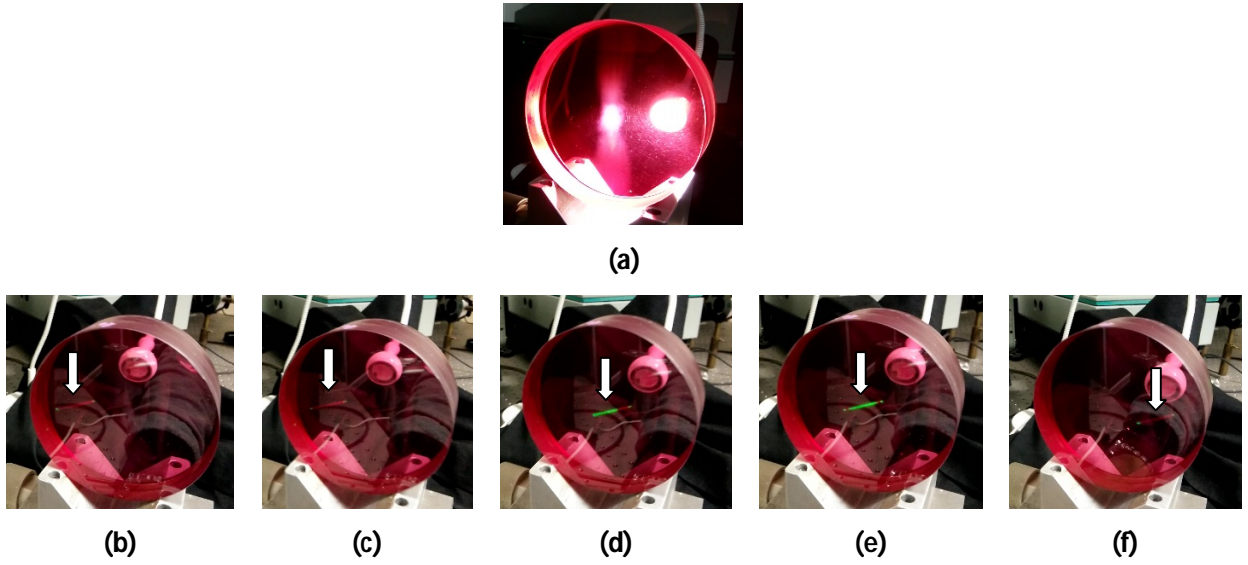


**Figure 4.3:** Diffusion of a thin laser beam by the milky defect. **(a)** Milky defect vertically aligned. **(b) -> (f)** Displacement of the laser beam (shown by the white arrow) from the left to the right of the defect passing through it in the centre.

#### 4.2.2 Milky defect (Horizontally aligned)

As shown in figure 4.4(a), the disc was positioned so as to have the milky defect zone aligned horizontally. The incoming laser passed through the sample and the disc was moved from right to left, so as to have the laser passing through the defect, from its one end to the other end, but throughout passing in the defect zone. We observe that there is a diffusion of the laser light as indicated by the bright green colour in figure 4.4(d) at the centre of the horizontal defect band. But, as we move towards the either edge of this defect, we observe that the intensity of the green light slowly decreases and becomes red towards the extreme edge.

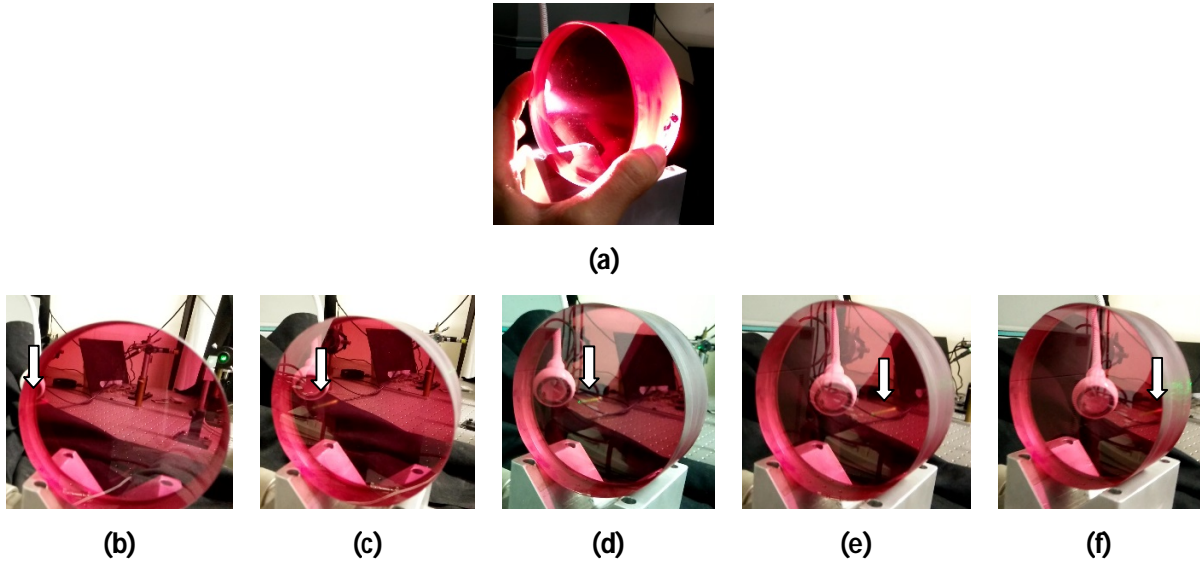


**Figure 4.4:** Diffusion of thin laser beam in the milky defect. **(a)** Milky defect horizontally aligned. **(b) → (f)** Displacement of the laser beam (shown by the white arrow) from the left to the right of the defect passing through it throughout.

#### 4.2.3 Influence of defect alignment

Shown in figure 4.5 is the effect of the orientation of the defect zone on the diffusion of the laser light. In figure 4.5(a) and 4.5(b) the defect zone was aligned horizontally and the laser light passing through the centre of the defect. While in figure 4.5(c) and 4.5(d) the defect zone was aligned vertically and the laser light passing through the centre of the defect. We can observe from these images that the diffused green light is much brighter when the defect is oriented vertically than when oriented horizontally. The difference in the intensity of diffused light is highlighted by comparing figure 4.5(a) and 4.5(c), where in spite of external illumination we can see the diffused green light very clearly in figure 4.5(c).

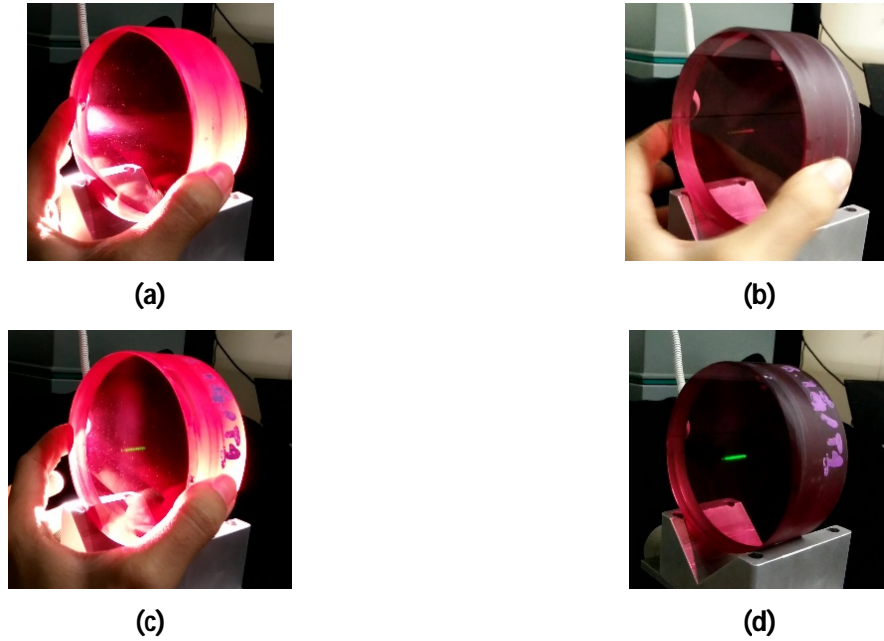


**Figure 4.5:** Diffusion of thin laser beam in the milky defect. **(a),(b)** Milky defect horizontally aligned. **(c),(d)** Milky defect vertically aligned. **(a),(c)** The light source revealing the milky defect is ON. **(b),(d)** The external light source is switched OFF.

#### 4.2.4 Observations

Thus, from the phenomenon observed in figure 4.3, it can be deduced that the milky defect zone is very well bound between its lateral edges and there is a sharp transition from the defect zone to the non-defect zone as expressed by the sharp change in the colour of the laser light when passing through the transition between the defect and the non-defect zone.

From the phenomenon observed in figure 4.4, it is realised that the defect band has the strongest influence in its central region and the influence on the diffusion of laser beam decreases as it moves towards the crystal edge passing through the defect zone.

Finally, from the analysis presented in figure 4.5, we realise that the laser light is diffused much more strongly in the C-axis direction perpendicular to the defect band, than in the direction of the C-plane parallel to the defect band.

### 4.3 Sample preparation

To facilitate all characterisation efforts for analysing the defect it is very important to have a sample which is a representation of the good quality of the crystals and also has the evidence of the milky zone which we are interested in. Hence, a crystal grown along the A-axis, weighing around 6 kg with an average diameter



of 11 cm and devoid of any visual macro and microscopic defects like bubbles or inclusions was selected as shown in figure 4.6(a). Three pieces were cut in the form of two circular discs and a rectangular plate from the upper half of the crystal. The circular disc had its face perpendicular to the A-axis. The rectangular plate had its longer edge perpendicular to the A-axis. The circular discs were with a diameter of 100mm and a thickness of 0.5mm while the rectangular plate had a dimension of 100mm and 30mm for its edges with also a thickness of 0.5 mm. All samples used for the analysis discussed in the work were chemo-mechanically polished.

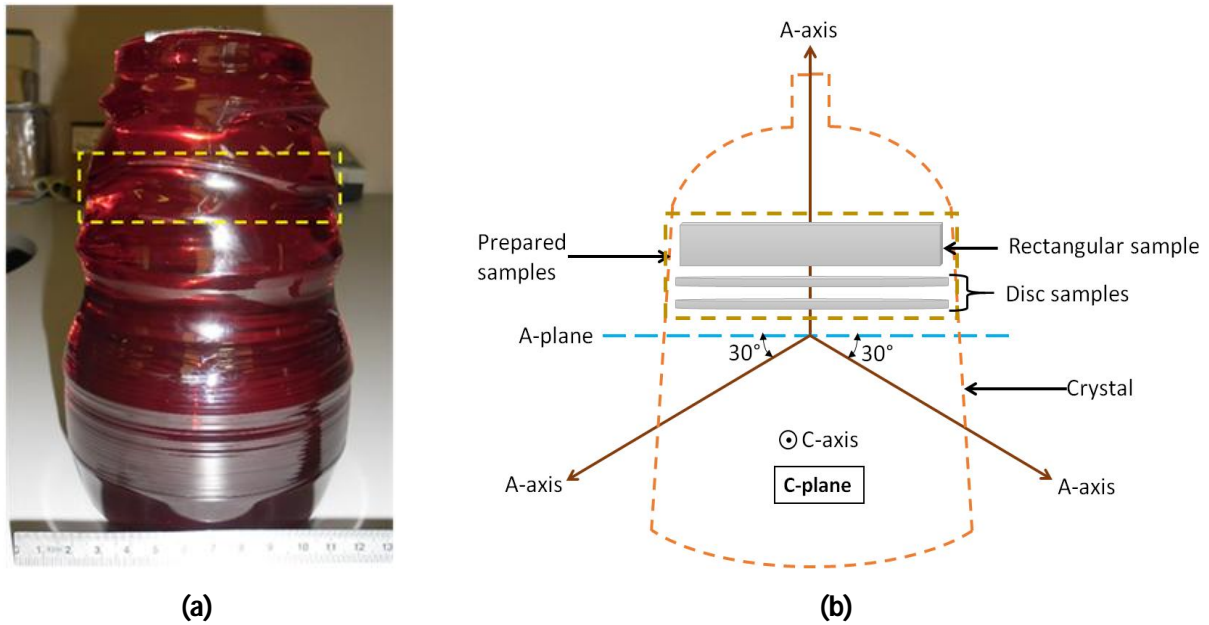


**Figure 4.6:** (a) Ti doped sapphire crystal grown along the a-axis. Dotted lines indicate the region of the crystal from where the samples were prepared, (b) Scheme of the prepared samples.

## 4.4 Characterisation of line defects (dislocations)

### 4.4.1 X-ray rocking curve analysis

The rocking curve method is an important crystal quality analysis tool since it reflects any variation in the crystalline structure and quality on the X-ray diffraction profile. For a perfect crystal, the profile is with a sharp diffraction peak, resulting from the convolution of the 'intrinsic width of diffraction' [Authier, 2003] with the instrumental broadening. On the other hand, structural variations in the form of plastic strain is reflected on the profile as an increase in the width of the diffraction peak quantified by measuring the full width at half maximum (FWHM) [G. G. Wang, 2010].



Rocking curve analysis was performed at CMTC, Grenoble for  $(11\bar{2}0)$  reflection of the circular sample and  $(000\ 12)$  reflection of the rectangular sample, at different locations as described in figure 4.9(b) and 4.10(b) to check if there was a difference in the FWHM values depending on the location on the sample. The idea was to look for variation in the crystal quality, if any, between the centres of the samples and the periphery and peculiarities within the milky defect region. The results are presented in Table 4.1. The analysed regions in the milky defect zone are denoted by MD and in the non-defect zone as ND and followed by their radial distance from the centre in mm. From the values of FWHM it can be inferred that, within the precision of these measurements, the crystal quality is mostly consistent along all the locations on the sample and the values justify the good crystalline quality of the sample [G. G. Wang, 2010] [W. Chen, 2014]. In order to detect possible small departures from the ideal “perfect crystal”, it is needed to utilise a technique more sensitive than the used X-ray generator based rocking curve setup. Synchrotron X-ray Bragg diffraction imaging was therefore used.

A more comprehensive study using Rocking curve imaging was later carried out at ESRF and will be discussed later.

Circular Sample $(11\bar{2}0)$ reflection			Rectangular Sample $(00012)$ reflection		
Reference No.	Position	FWHM(arcseconds)	Reference No.	Position	FWHM(arcseconds)
4	C-MD-0	$14.04 \pm 2.0$	15	R-MD-0	$31.97 \pm 2.0$
8	C-ND-10	$16.92 \pm 2.0$	20	R-MD-0	$30.24 \pm 2.0$
10	C-ND-30	$14.40 \pm 2.0$	16	R-ND-10	$29.52 \pm 2.0$
3	C-MD-10	$13.10 \pm 2.0$	18	R-ND-30	$31.18 \pm 2.0$
1	C-MD-30	$13.46 \pm 2.0$			
5	C-MD-10	$18.43 \pm 2.0$			
7	C-MD-30	$13.39 \pm 2.0$			

**Table 4.1:** FWHM values for X-ray rocking curve analysis

#### 4.4.2 X-ray diffraction topography

##### 4.4.2.1 Diffraction Technique

X-ray Bragg diffraction imaging techniques (historically “X-ray topography”) mainly apply to single crystals and basically consist of mapping the intensity and direction of the locally Bragg diffracted beams. These

techniques are non-destructive and sensitive to a large range of distortions (typically in the  $10^{-3}$ – $10^{-8}$  range). They reveal defects in the bulk of single crystals through the distortion fields associated with the defects, and the way these distortion fields modify the diffraction behaviour of the underlying perfect crystal (described by the dynamical theory of diffraction) [Authier, 2003].

Fig. 4.7(a) schematically represents the main idea of all the diffraction imaging methods. The single crystal sample is set to diffract a fraction of the incoming beam, according to Bragg's law. The diffracted beam is recorded on a position sensitive detector (usually X-ray films, or, increasingly, CCD cameras equipped with a high resolution scintillator). If a small volume  $V$  within the crystal behaves differently from the matrix, intensity variations ("contrast") can be produced on an area  $S$  of the two-dimensional image of the diffracted beam. The features that can be visualized using X-ray diffraction topography include defects like dislocations, twins, domain walls, inclusions, impurity distribution, and macroscopic deformations, like bending or acoustic waves, present within the single crystal sample.

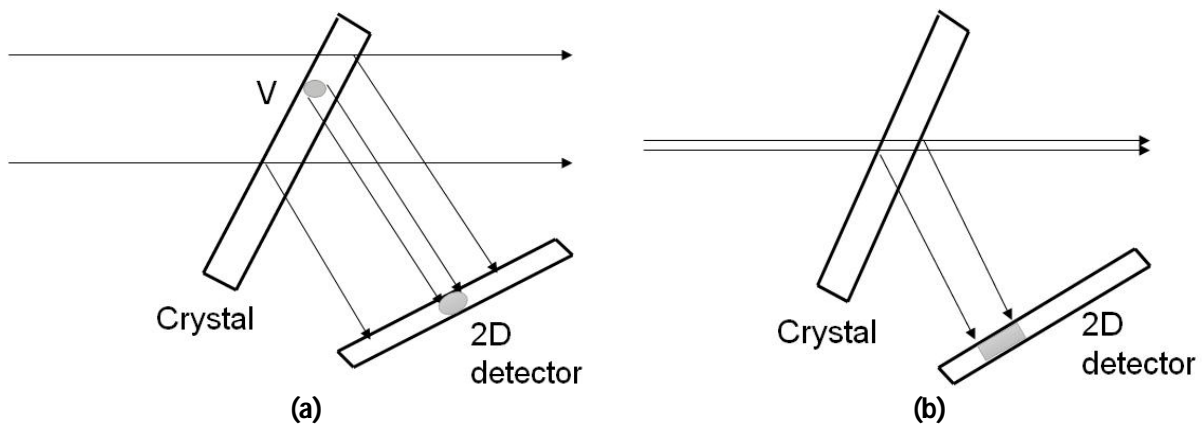


**Figure 4.7:** Basic principle of the Bragg diffraction imaging methods (a) "projection" (b) "section"

In the low absorption case the predominant contrast mechanism is the so-called direct image process. Let us consider the actual experimental case, carried out at the beamline BM05 of the European Synchrotron Research Facility (ESRF) in Grenoble. A polychromatic (6–100 keV), extended beam impinges on the crystal, which produces a "Laue pattern" where multiple Bragg diffraction spots are generated as shown in figure 4.8. Each of the diffracted spots can exhibit contrast that reveals the defects. This is because the incident beam has a very low divergence, the angular width of the beam reaching a given point of the sample being in the  $\mu$  radians range. Let us now come back to the schematic drawing of Fig. 4.7(a): the small crystal volume  $V$  can be such that it contains a defect (inclusion, dislocation,...) associated with a distortion field, which decreases with growing distance from the defect core. The dynamical theory of diffraction predicts that a wavelength range  $\Delta\lambda/\lambda$ , with typical values in the order of  $\sim 10^{-4}$  range, participates to the diffraction

by the “perfect” crystal matrix. The dynamical theory provides a simple expression for  $\Delta\lambda/\lambda = \omega_h / (\tan \vartheta_B)$ , where  $\omega_h$  is the “intrinsic width of diffraction” [Authier, 2003]. The incident beam being polychromatic, regions around the defect are at the Bragg position for components of the incoming beam which is outside this spectral range. The defect thus leads to additional diffracted intensity on the detector.

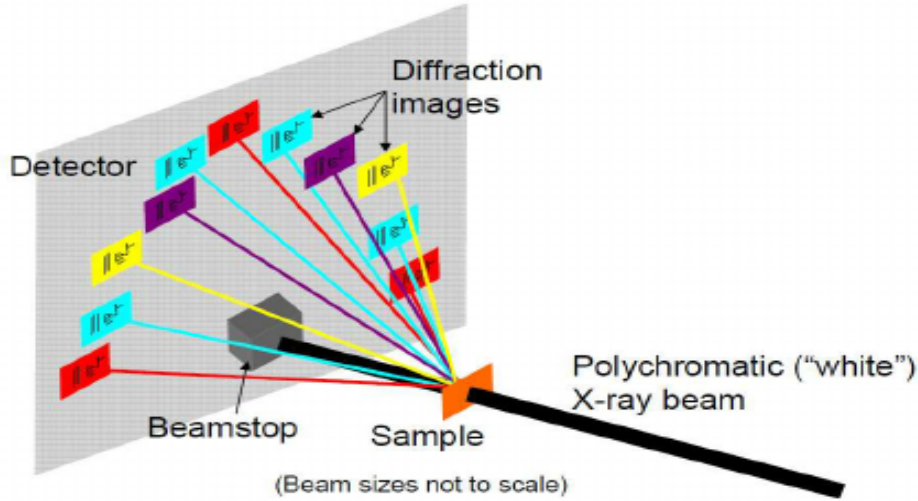


**Figure 4.8:** Diagram of white-beam topography [Tran Thi, 2017]

The regions that produce the direct image of a given defect are some distance away from the core of the defect. This distance depends not only on the nature of the defect, but also on the diffraction process itself, leading to an image width of a dislocation ranging in the 1– 100  $\mu\text{m}$  scale [Authier, 2003]. In addition a dislocation will be visible if it distorts the lattice planes used to produce the Bragg diffraction. This image is usually not observed when  $\mathbf{h} \cdot \mathbf{b}_r = 0$ , where  $\mathbf{h}$  is the diffraction vector and  $\mathbf{b}_r$  is the Burgers vector of the dislocation.

The recorded diffraction images have a lateral spatial resolution of a few  $\mu\text{m}$ , but a poor depth resolution: indeed the images of defects present in the 3D volume of the sample can overlap on a given point of the detector. A way to overcome this limitation (at the cost of dramatically reducing the investigated volume) is “section topography”, where, as shown on Fig. 4.7(b), the incident beam is limited by a slit (50  $\mu\text{m}$  aperture, in our case), in such a way that a “virtual slice” of the sample is, as a first approximation, projected on the detector. Fig. 4.7(b) also shows that section topography is such that one side of the image corresponds to the entrance surface of the X-rays, the other side corresponding to the exit surface.

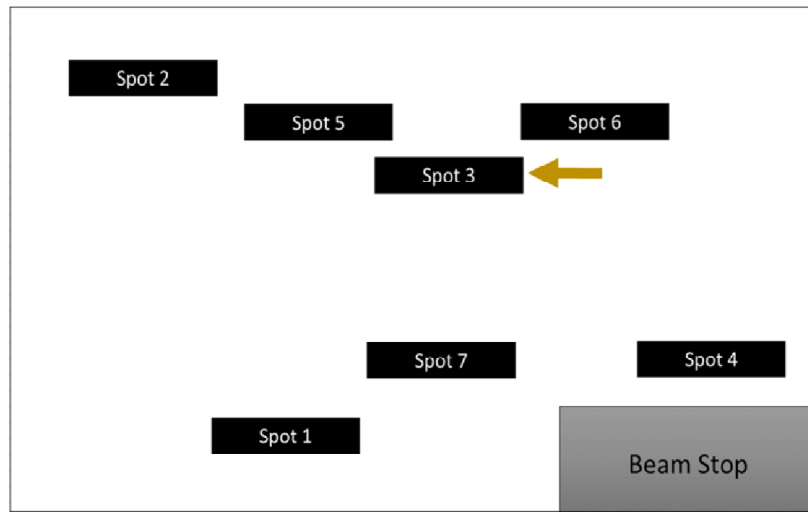
We therefore used both projection and section diffraction topography to obtain results with a higher sensitivity to small lattice distortions than the ones produced by the above-described rocking curve

analysis, and more in particular to look for differences in the features observed at the centre of the samples and the periphery, which also correspond to the central and outer region of the crystal.

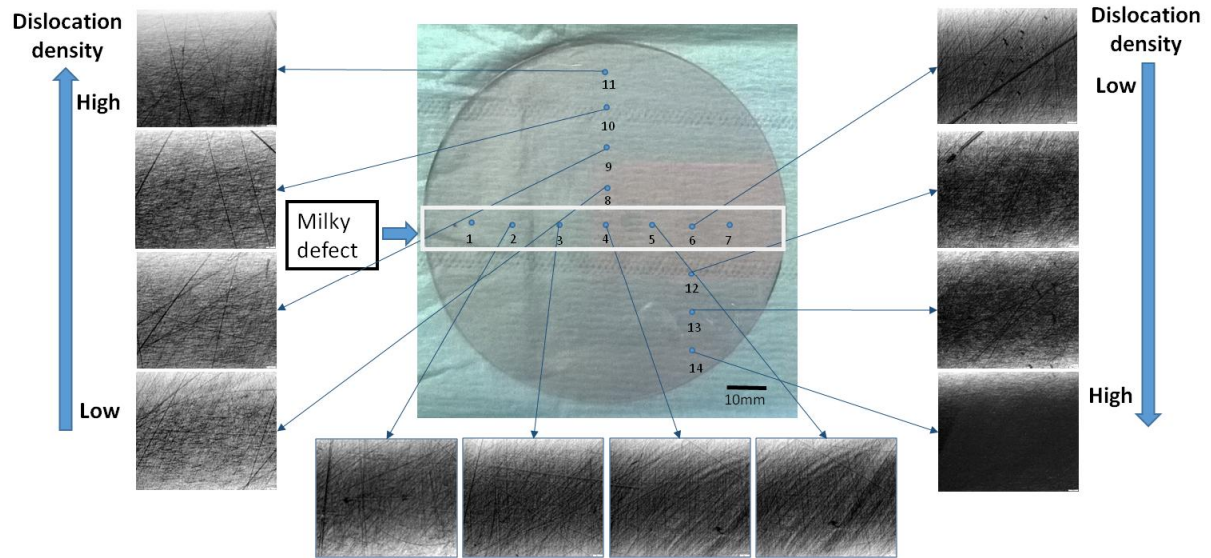
#### **4.4.2.2 Topography analysis**

Figs. 4.9(b) and 4.10(b) show the projection X-Ray diffraction topographical images in transmission obtained for a particular lattice plane reflection from the Bragg diffraction spots marked on Figs. 4.9(a) and 4.10(a) for various regions of the circular and rectangular sample, respectively. Projection X-ray diffraction topography, in the transmission mode, provides information integrated throughout the sample thickness, where the spatial resolution is much reduced along the depth direction as shown in Fig. 4.7(a). The prominent features seen in the images are the cluster of threading dislocations, each of them signifying an individual dislocation. Straight lines are also observed with a bright contrast as an effect of superficial scratches on the samples during polishing which is shown as artefact 'b' in Fig. 4.11(a). A small spot showing the presence of precipitates within the samples is shown as artefact 'c' in Fig. 4.11(a), but this is observed just in one instance and hence can be considered to be very rare.

The most striking aspect is the variation of the dislocation attributed features based on the imaged region of the sample. For the circular sample, an increase in the darkness of the image (which corresponds, with the usual photographic convention, to more illuminated regions) is observed as moving from the central part of the sample to the periphery, as observed in Fig. 4.9(b). In the low absorption scenario, as is the case with our samples, "more illuminated/more diffracting" corresponds to "more distorted", suggesting an increased density of dislocations. This is confirmed by the images of the rectangular sample, where it is possible to clearly see the progressive increase in the number of dislocations on moving from centre (point 15, R-MD-0) to the edge of the sample (point 18, R-ND-30). This is obvious from Fig. 4.10(b). These qualitative observations lead to a reasonable conclusion that the dislocation density depends on the position inside the crystal and the number of dislocations increase as we move from the centre to the radial edge of the crystal.



(a)



(b)

**Figure 4.9:** (a) Laue diffraction pattern and the selected lattice plane diffraction marked with an arrow for the circular disc sample, (b) with the points of analysis and the projection X-Ray diffraction topographical images in the transmission mode.

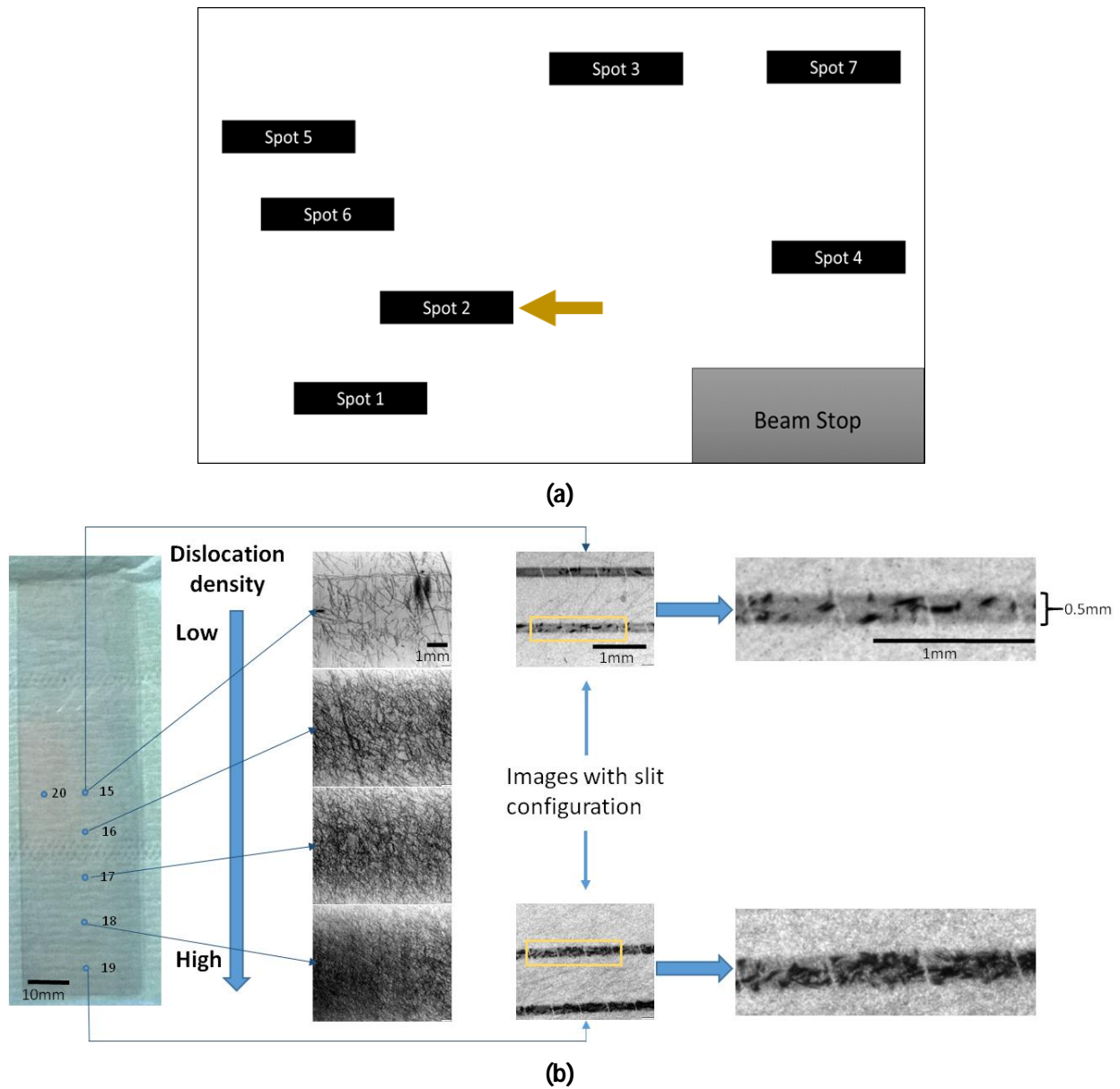


**Figure 4.10:** (a) Laue diffraction pattern and the selected lattice plane diffraction marked with an arrow for the rectangular sample, (b) with the points of analysis and the projection X-Ray diffraction topographical images in the transmission mode (points: 15 R-MD-0, 16 R-ND-10, 17 R-ND-20 and 18 R-ND-30) along with section topography images (images with slit, points 15 R-MD-0 and 19 R-ND-40).



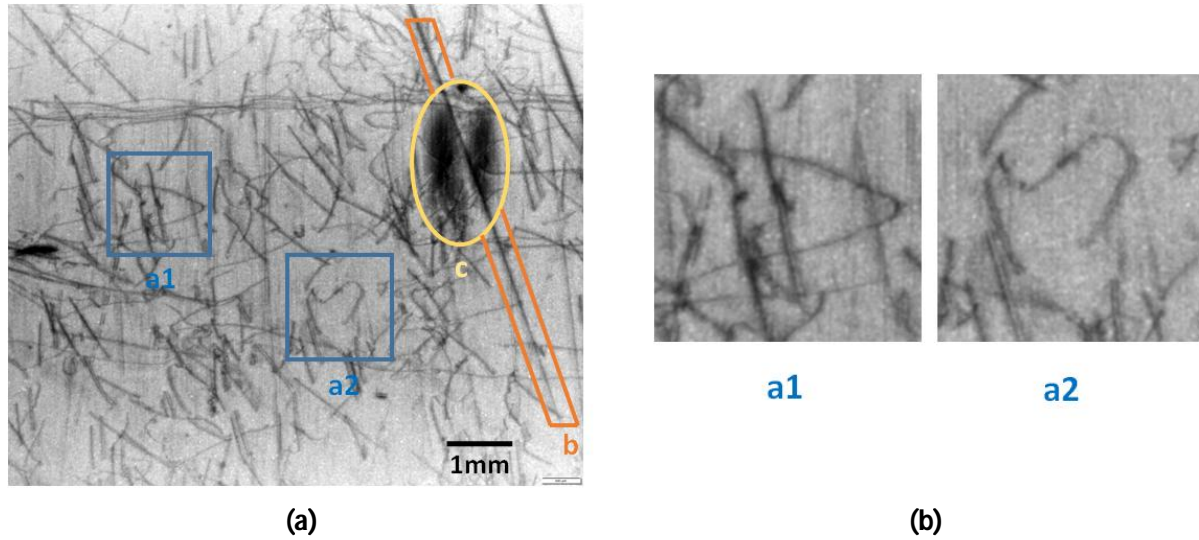


**Figure 4.11: (a)** X-Ray diffraction topography image (15 R-MD-0) with observed features: a1 and a2 – dislocations, b – scratch marks, c – precipitate. **(b)** Enlarged snapshots from topography image and visualization of dislocations.

#### 4.4.2.3 Quantitative analysis

Fig. 4.10(b) also shows section topographical images obtained for a particular lattice plane reflection on two different regions of the rectangular sample (point 15 R-MD-0 and point 19 R-ND-40), using the special slit configuration at the beam source as shown in Fig. 4.7(b). In this experiment, very thin 50  $\mu\text{m}$  incident beams are incident to the sample. These beams get reflected from the lattice planes to reveal the features within the depth of the sample. Section topography allows the resolution in depth to be recovered and the origin of the defect images to be located within the sample “nearly -2D” virtual volume, defined by the intersection of the 50  $\mu\text{m}$  wide beam with the crystal. As seen from the magnified snapshots of Fig. 4.10(b), the dislocations are easily identified with high contrast in the horizontal bands. There is also the presence of some white vertical bands at regular intervals in the illuminated horizontal bands due to the shadows of the gold wires holding the slits together. These gold wires are at a distance of 0.05 cm, while the depth of the sample is 0.05 cm too; hence considering each grid composed within the 2 horizontal bands it signifies a surface area of  $0.05 \times 0.05 = 0.0025 \text{ cm}^2$ . By counting the total number of dislocations in the image and calculating the number of grids captured it is possible to obtain the average dislocation density per unit  $\text{cm}^2$  at these two locations, namely  $1100 \text{ cm}^{-2}$  for point 15 R-MD-0 and  $6000 \text{ cm}^{-2}$  for point 19 R-ND-40.

#### 4.4.2.4 Quantitative estimation of dislocation density variation

As observed from Fig. 4.11(a), it is difficult to count the total number of dislocations in the whole image, so 2 small grid snapshots have been selected from each image and the number of dislocations has been

counted and averaged to provide a representation for the whole image. Two different approaches have been implemented to count the individual dislocations in the grid. In the first approach, the total number of dislocations observed in the grid has been counted while, for the second approach, only the dislocations completely enclosed within the grid have been counted. This leads to the exclusion of dislocations passing out of the selected grid and hence a lower count than the first approach. For the point 15 R-MD-0, the dislocation density per unit  $\text{cm}^2$  using the slit image is available, as explained before, and hence a conversion factor is calculated by dividing the dislocation density by the number of dislocations as counted by the two different approaches. This conversion factor is then used to calculate the dislocation density by multiplying it into the number of dislocations observed by each of the two approaches for the points 16 R-ND-10, 17 R-ND-20 and 18 R-ND-30. The dislocation density is plotted along the sample radius in figure. 4.12.

There are very few dislocations in the centre of the crystal, less than  $10^3 \text{ cm}^{-2}$ , and their density increases almost linearly with the radius of the crystal. However the maximal value, 2 to  $4 \cdot 10^4 \text{ cm}^{-2}$  remains low enough for optical application as verified by optical analysis of the samples. The values obtained for the dislocation density at points 16 R-ND-10, 17 R-ND-20 and 18 R-ND-30 measured by the method of counting completely enclosed dislocations are greater than those of total number of dislocations. This is due to the fact that the conversion factor obtained is higher for the former method at point 15 R-MD-0 and hence when multiplied by the enclosed dislocations observed at the following locations it gives a greater value for the dislocation density than the latter. There is some disparity between the dislocation density values obtained by section topography for point 19 R-ND-40 and those calculated by measuring the number of dislocations. This could be due to the fact that in the section topographical image for point 19 R-ND-40 with a high dislocation density there could be a lot of dislocations that overlap each other in the image and hence the value of dislocations counted for are much less than those actually present.



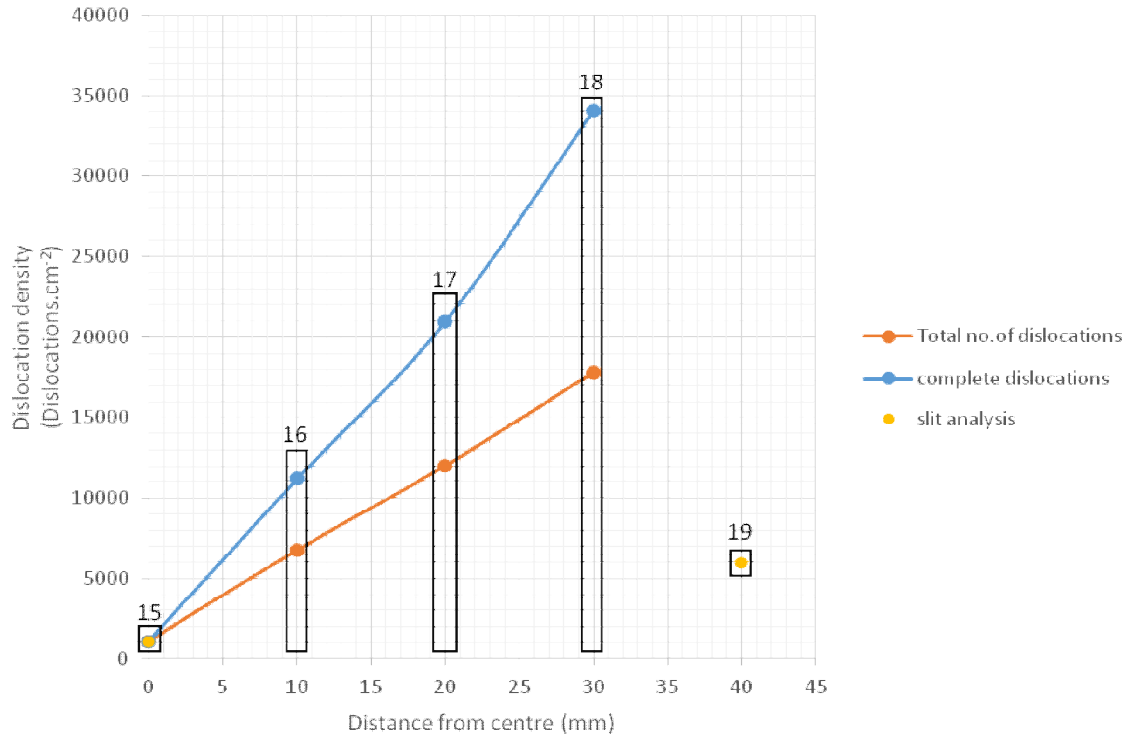


**Figure 4.12:** Plot of dislocation density at various positions calculated by different approaches compared to the distance from the centre of the crystal.

#### 4.4.2.5 Radial distribution of dislocation density

The topography images reveal that dislocations are the predominant kind of crystal defect that is present in the samples except some rare precipitates as found in 15 R-MD-0. Topographs in Fig. 4.10(b) reveal that there is the presence of dislocations in the form of clustered knots and tangles for the points 16 R-ND-10, 17 R-ND-20 and 18 R-ND-30 which indicates the influence of strong thermal stresses acting at these regions. On the contrary, for the centre of the sample at point 15 R-MD-0 the dislocations are individually resolved and we see very few of curved dislocations but a lot of straight ones due to stress relaxation at the centre of the crystal as shown in Fig. 4.11(a) [Asadchikov, 2016].

Thus, X-ray topography investigations carried out on Kyropoulos grown sapphire crystals using synchrotron radiation helped us identify the defect structures. Dislocations were found to be the main type of defect in the samples and the average dislocation density was in the range of  $(<10^3) - (\leq 10^5 \text{ cm}^{-2})$ . This value of the dislocation density shows a crystal of good quality which is suitable for optical applications. The dislocation density increased from the centre of the crystal to the outside. The possible factors responsible for this radial increase in the dislocation density will be discussed in the following sections.

#### 4.4.2.6 Dislocations in milky defect zone

Although, these studies brought forth the radial variation of the dislocation density, it does little to explain the occurrence of the milky defect. Hence, we look for the other diffracted planes and we see a very interesting pattern for the (0001) lattice plane reflection from the Bragg diffraction spots marked on figure 4.13(a). We know that the particular diffraction spot is due to the (0001) lattice plane reflection because the sample was placed with the C-plane oriented horizontally and the diffracted spot is perpendicular to it, suggesting a diffraction of the horizontal C-plane. The projection X-Ray diffraction topographical images in transmission obtained for various regions of the circular sample are presented in figure 4.13(b). From this image it is clear there is a distinction in the dislocation behaviour in the milky zone region (points: 2 C-MD-20, 3 C-MD-10, 4 C-MD-0, 5 C-MD-10 and 6 C-MD-20) and the non-defect region (points 8 C-ND-10, 9 C-ND-20, 10 C-ND-30, 11 C-ND-40, 12 C-ND-25, 13 C-ND-30 and 14 C-ND-40).

For the milky region we observe the dislocations to be very distinct, parallel to each other and oriented along the C-plane. In this region we also observe the dislocation density gradually increasing from the centre of the sample to radially outwards. It will be shown in section 4.3.6 that they correspond to the basal slip system, where there are only three dislocation directions. So that, at a maximum, only one third of dislocations could not be seen in the figure 4.13(b) in case their Burgers vector would be perpendicular to the diffraction vector. In conclusion, the dislocation density remains remarkably small in the Milky Defect zone.

Outside the milky zone reaction, there is a sharp increase in the dislocation density and the dislocations are entangled and not clearly oriented as in the milky zone, but once again they increase radially outwards and they are much higher than those in the milky defect region.

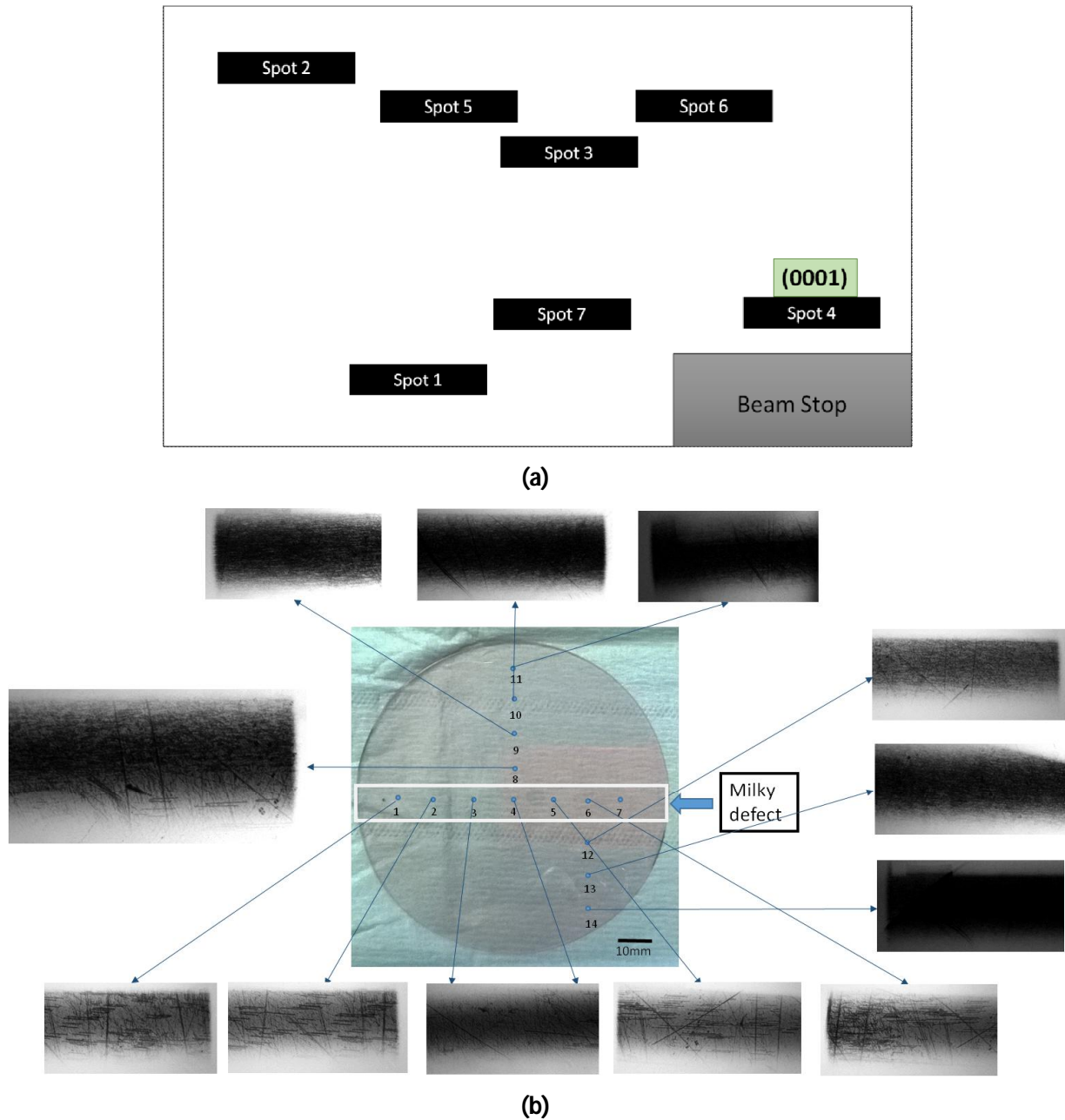


**Figure 4.13:** (a) Laue diffraction pattern and the  $(0001)$  lattice plane diffraction, (b) the points of analysis and the projection X-Ray diffraction topographical images in the transmission mode.

The most interesting dislocation pattern is observed for point 8 C-ND-10 as shown in figure 4.13(b) and magnified in figure 4.14. The point 8 C-ND-10 is very close to the milky zone defect region and hence the dislocation pattern here shows two distinct behaviours. The lower part which is closer to the milky zone shows the presence of oriented dislocations parallel to the C-plane, while the upper part shows a mesh of

entangled dislocations as in the rest of the crystal. This suggests there is a sharp demarcation of this milky defect region with respect to dislocations in accordance to the sharp boundary seen optically.

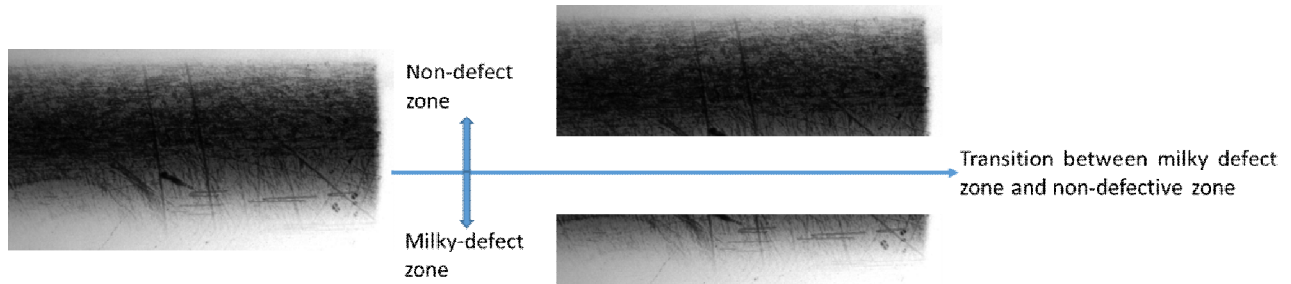


**Figure 4.14:** Transition of dislocation behaviour between milky zone and non-defective zone observed for point 8 C-ND-10 as shown in figure 4.13(b).

#### 4.4.3 Rocking curve imaging

##### 4.4.3.1 Technique

Rocking curve imaging (RCI) is the quantitative counterpart of monochromatic Bragg diffraction imaging. RCI enables the local determination of both the effective misorientation, which results from lattice parameter variation and the local lattice tilt, and the local Bragg position. Maps derived from these parameters are used to measure the magnitude of the distortions. By using digital cameras together with sophisticated analysis software, RCI enables the measurement of the spatial distribution of local lattice distortions. The RCI technique can be used in both reflection (Bragg) and transmission (Laue) geometries. Developments have been reported using the Laue geometry carried out in both projection [D Lübbert, 2000] [Daniel Lübbert, 2005] [Hoszowska, 2001] [Calamiotou, 2007] as shown in figure 4.15(a) and section [Kluender, 2011] [Pernot, 2010] modes as shown in figure 4.15(b). Information is extracted on a pixel-by-pixel basis from a series of typically several hundred X-ray diffraction images recorded at small angular steps of the crystal rotation or rocking angle  $\theta$  from one side to the other of a Bragg diffraction peak. Maps of the integrated intensity, the FWHM and the peak position angle of the diffracted intensity are then calculated from the ensemble of these rocking curve images, using rocking curve imaging analysis (RCIA) software which produces two-dimensional maps on a pixel-by-pixel basis as shown in figure 4.15(c). These maps provide quantitative values related to the local distortion of the crystal lattice. [Tran Thi, 2017].

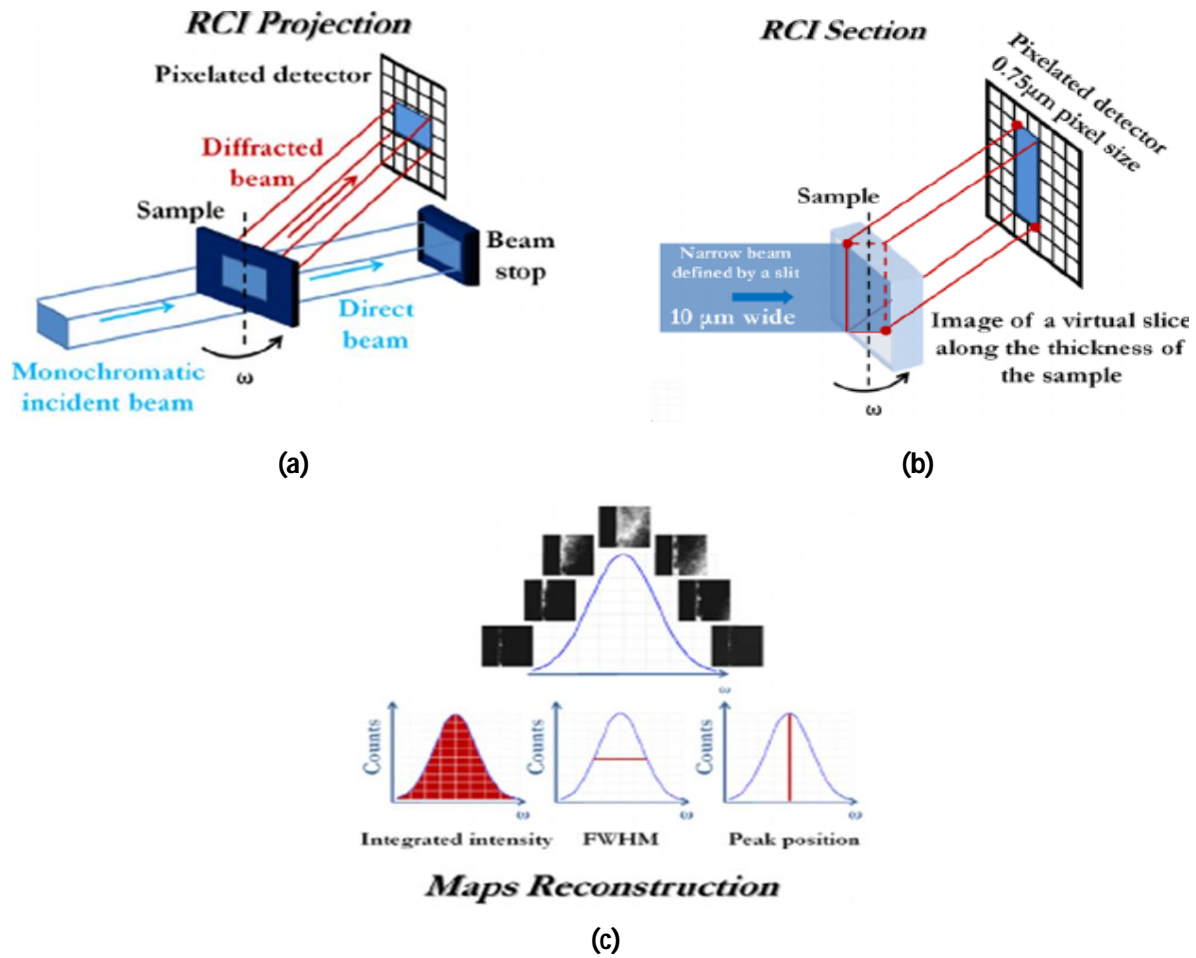


**Figure 4.15:** Rocking curve imaging technique in (a) projection and (b) section modes. (c) Acquisition of an image series with calculation of integrated intensity, FWHM and diffraction peak position, extracted on a pixel-by-pixel basis from the local rocking curves.[Tsoutsouva, 2015]

#### 4.4.3.2 Sample

The rocking curve imaging analysis was carried out at the beamline BM05 of the European Synchrotron Research Facility (ESRF) in Grenoble. The motive of this analysis was to confirm the peculiarities and transition of the dislocation behaviour in the milky zone and the non-defect zone as observed during the X-ray diffraction topography. Hence, it was important to prepare samples which would be representative of both the regions and also have the exact transition point in between milky zone and non-milky zone within it.

Initially a thin disc sample was prepared from the crystal region shown in figure 4.6, similar to the one used for the earlier analysis with X-ray topography so that the results from the X-ray diffraction topography can be compared to the RCI results. Three rectangular samples with dimensions of 30 mm in length and 10 mm

in width denoted as sample 3, 4 and 5 along with two square samples with dimensions of 10 mm in length and 10 mm in width denoted as sample 1 and 2 were cut from this disc as shown in figure 4.16(a). The three rectangular samples were used for the RCI analysis. The locations of these samples with respect to the disc are represented in figure 4.16(b). The three samples are selected such that the milky zone passes through the centre of sample 4 and 5 and the edge of sample 3 as shown in figure 4.16(b).

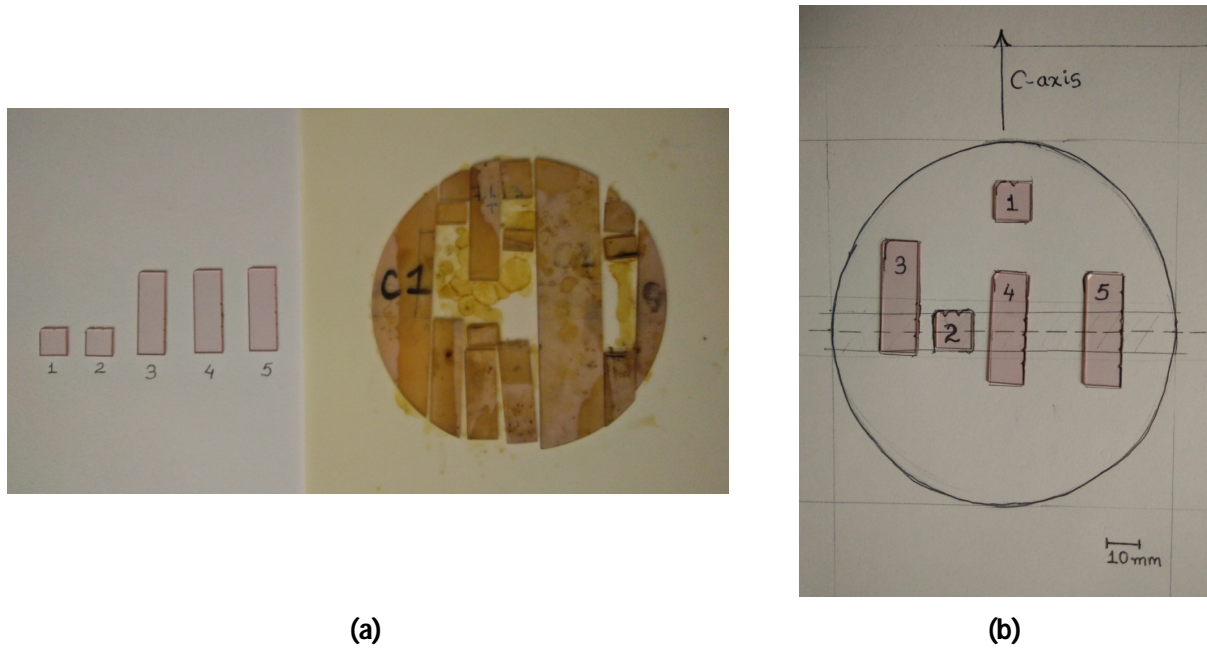


**Figure 4.16:** Sample preparation for Rocking curve imaging (RCI) at ESRF. **(a)** Thin disc sample (1 mm) prepared from the region of crystal shown in figure 4.6, used to prepare 5 samples. **(b)** The location of the samples from the disc and the milky defect zone passing through them.

#### 4.4.3.3 Experimental set-up

Bragg diffraction images were acquired on a detector system comprising a scintillator screen equipped with microscope folded-relay optics to the ESRF-developed 2048 x 2048 pixel FReLoN CCD camera. The optical demagnification of the CCD sensor pixels in this system resulted in an effective square pixel size of 0.7 mm at the scintillator screen, so the recorded images had a corresponding field of view of 1.4 x 1.4 mm<sup>2</sup>. X-ray topographs of the C-plane (0006) and A-plane (11 $\bar{2}$ 0) reflection were recorded using the RCI technique, i.e. multiple images were acquired while rotating the sample with respect to the beam axis, in this case with angular steps of (10<sup>-4</sup>)° through the Bragg diffraction angle. The diffraction plane for (0006) was horizontal while for (11 $\bar{2}$ 0) it was vertical, and the distance between the sample and the detector scintillator screen was 50 mm. Given the very low divergence of the synchrotron beam, and the short sample-to-detector distances, it can be considered as a sensible first approximation, at least for section images, that there is a



one-to-one spatial correspondence between one pixel of the camera and a particular 'voxel' in the crystal. This voxel corresponds to the intersection between the sample volume illuminated by the beam and a geometrical tube obtained by back tracing the pixel of the detector along the diffracted direction.

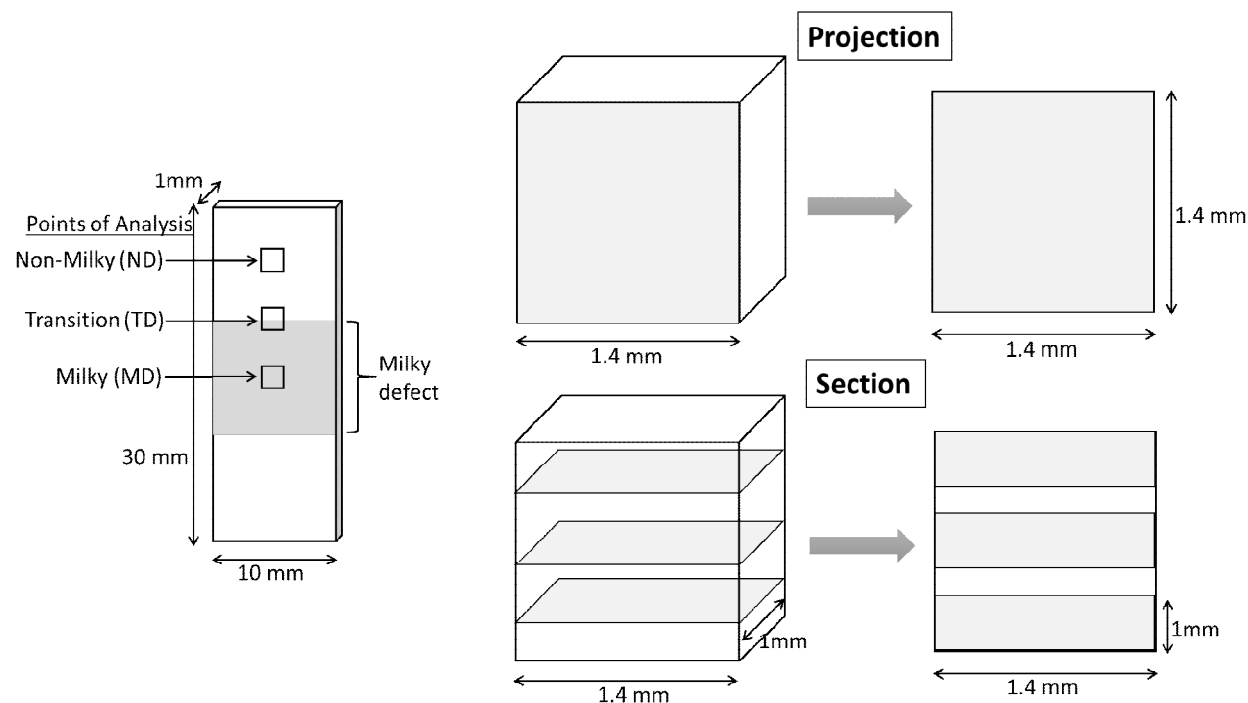
#### ***4.4.3.4 Integrated intensity, full width at half-maximum and peak position maps***

The three maps (Integrated Intensity - INT, Full width at half mean - FWHM and Peak position - PPOS) were extracted routinely from the RCI data (i.e. the intensities recorded in the various pixels of the detector as a function of the sample angular position) and they provide complementary information. The integrated intensity map gives features very similar to those obtained by synchrotron radiation white beam topography techniques. The FWHM map is a quantitative measurement of the local distortion and the general evolution of its variations over the sample. Under low-absorption conditions, which correspond to our case, the FWHM map should produce results qualitatively very similar to those of the integrated intensity map, and thus higher intensity and FWHM values correspond to an increased gradient of distortion of the diffracting volume. The peak position map provides information on the local departure from the nominal Bragg angle. This departure includes contributions mainly from lattice rotations (tilts) but also from lattice plane spacing variations (strain). By combining the INT, FWHM and PPOS maps, we obtain extra information with respect to that provided by classical topography techniques, especially in the case of distorted crystals.

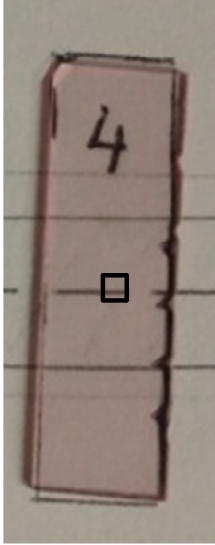
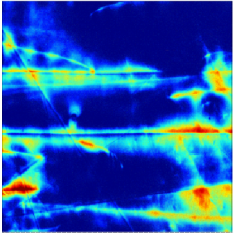
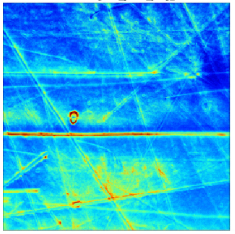
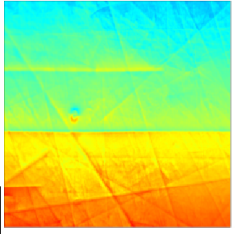
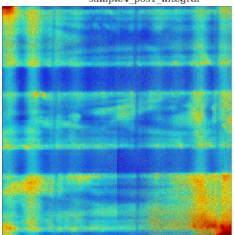
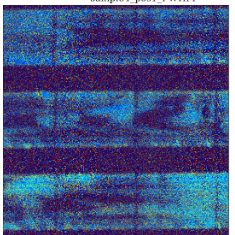
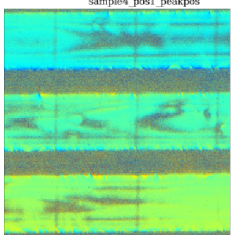
RCI analysis was carried out for sample 4 and 5, but was not possible for sample 3 due to beam time constraints. Maps were recorded in both projection and section modes for the C-plane (0006) reflection of samples 4 and 5. Maps were also recorded for the A-plane ( $11\bar{2}0$ ) reflection of sample 4 in projection mode. The incident X-ray beam position is marked on the samples with the black square and its dimension is 1.4 mm x 1.4 mm. Three regions of analysis have been selected which are 5 mm apart, starting from the centre progressing towards the end of the sample. The selected regions are such that the central analysis point would be definitely in the milky zone and the outermost in the non-milky zone. The analysed point in between these two could possibly lie right at the sharp junction between the milky and non-milky zone. The projection RCI images in the 2D frame overlap the images in the depth of the sample, while with the section RCI images we have images on the depth of the sample for three sections in the sample volume. The scheme of the sample, along with the points of analysis and the transformation of the analysed 3D volume into the 2D images is explained in the scheme presented in figure 4.17.

In the following section from table 4.2 to table 4.10 we present the images of RCI. Here in, the images have been presented after adjusting the range of values in the colour maps so that the features in the samples

are clearly visible. This leads to having different ranges of values for the colour maps and hence the intensity cannot be directly compared with the representation of the colours.

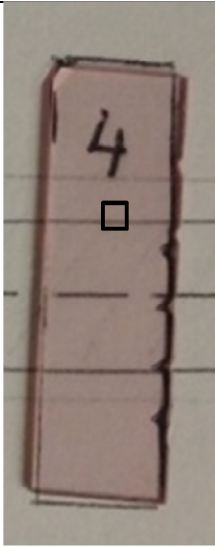
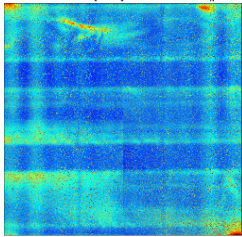
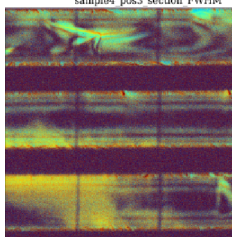
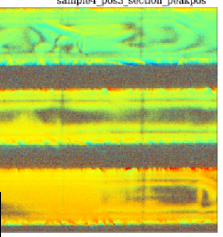


**Figure 4.17:** Scheme of the points of analysis on the samples and the RCI imaging scheme in projection and section method.

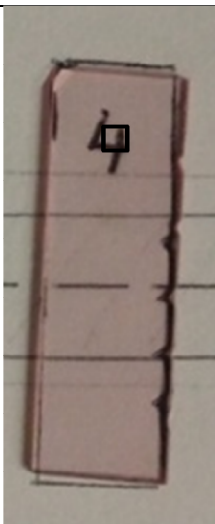
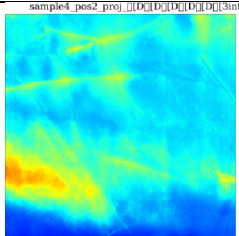
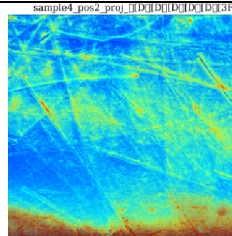
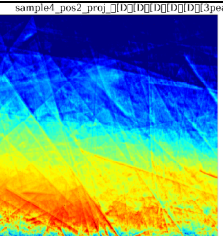
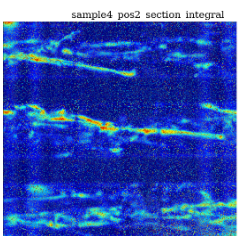
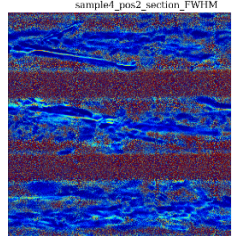
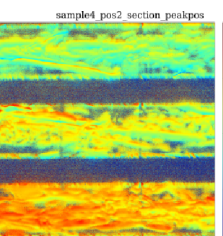
Sample		Integrated Intensity	FWHM	Peak position
	Projection	 <div> <div>sample4_post1_proj_integral</div> <div>9.5 e+3</div> <div>8.95e+03</div> <div>(a.u)</div> <div>7.5 e+3</div> </div>	 <div> <div>sample4_post1_proj_FWHM</div> <div>1.00 e-3</div> <div>3.46e-04</div> <div>(°)</div> <div>8.00 e-4</div> </div>	 <div> <div>sample4_post1_proj_peakpos</div> <div>1.04 e+1</div> <div>1.04e+01</div> <div>(°)</div> <div>1.04 e+1</div> </div>
	Section	 <div> <div>sample4_post1_integral</div> <div>2.95 e+3</div> <div>2.83e+03</div> <div>(a.u)</div> <div>2.56 e+3</div> </div>	 <div> <div>sample4_post1_FWHM</div> <div>1.50 e-3</div> <div>1.19e-03</div> <div>(°)</div> <div>6.00 e-4</div> </div>	 <div> <div>sample4_post1_peakpos</div> <div>1.04 e+1</div> <div>1.04e+01</div> <div>(°)</div> <div>1.04 e+1</div> </div>

**Table 4.2:** C-plane (0006) reflection in the milky zone for sample 4. (point 4-MD)

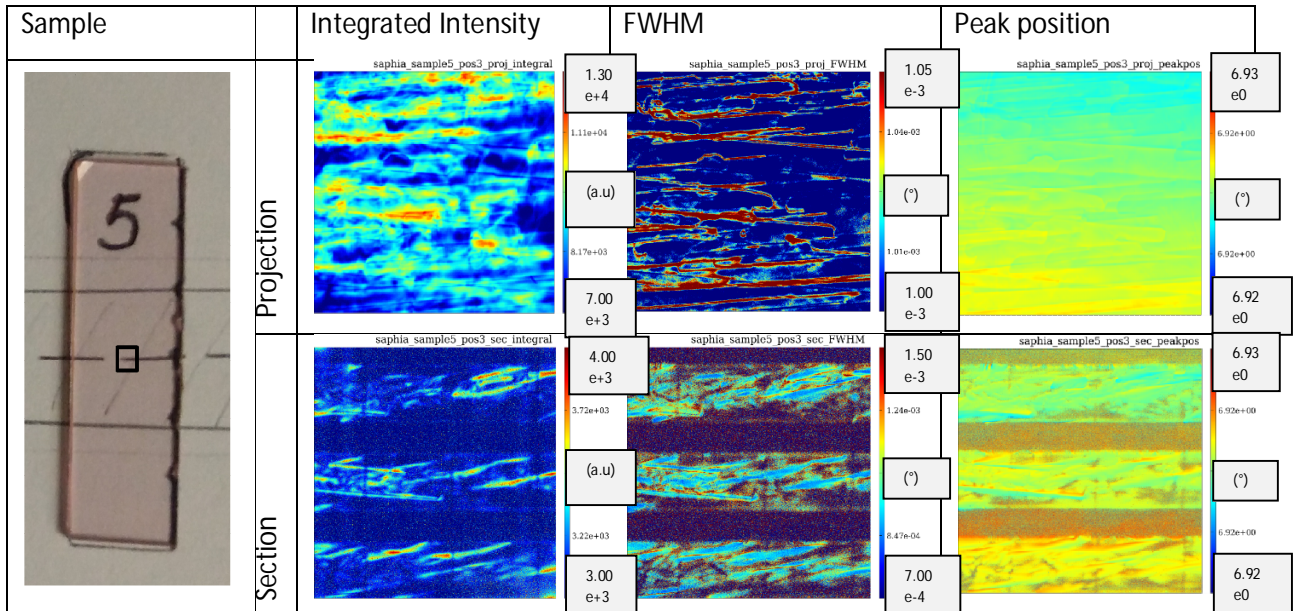


Sample		Integrated Intensity	FWHM	Peak position
	Section	 <div> <div>3.80 e+3</div> <div>3.58e+03</div> <div>(a.u)</div> <div>3.18e+03</div> <div>3.00 e+3</div> </div>	 <div> <div>1.00 e-3</div> <div>8.41e-04</div> <div>(°)</div> <div>5.95e-04</div> <div>5.00 e-4</div> </div>	 <div> <div>1.04 e+1</div> <div>1.03e+01</div> <div>(°)</div> <div>1.03e+01</div> <div>1.03 e+1</div> </div>

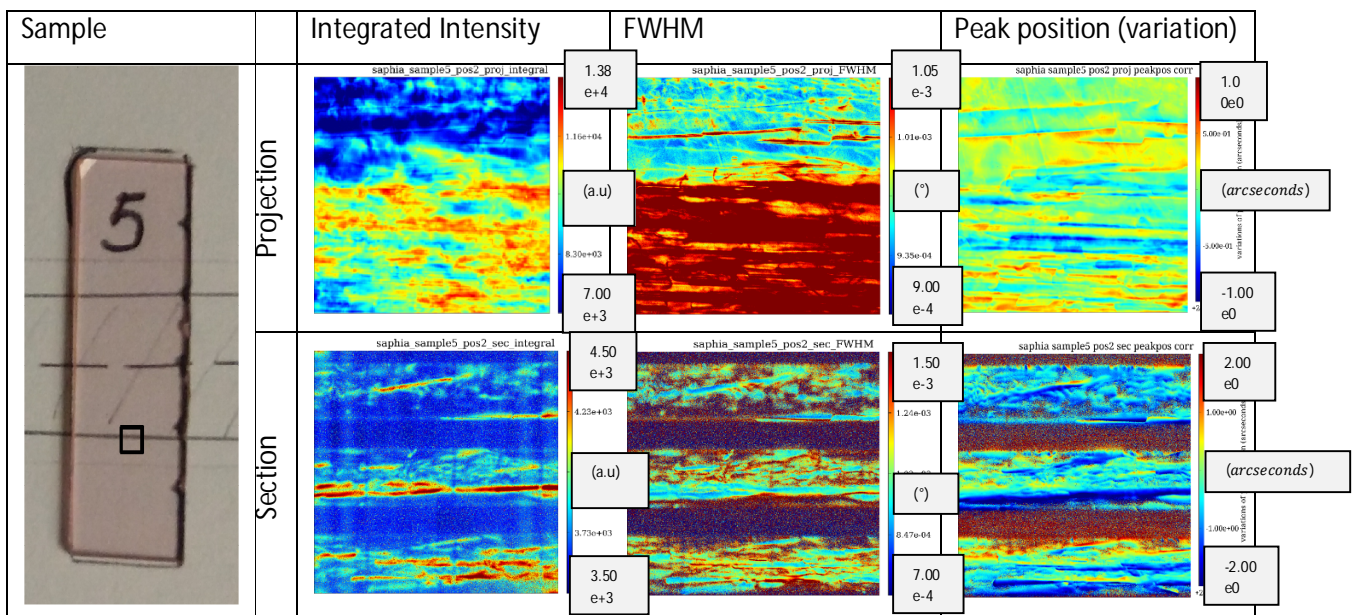
**Table 4.3:** C-plane (0006) reflection in the transition zone for sample 4. (point 4-TD) (No analysis for projection mode was carries out due to time constraints)

Sample		Integrated Intensity	FWHM	Peak position
	Projection	 <div> <div>8.0 e+3</div> <div>6.15e+03</div> <div>(a.u)</div> <div>3.64e+03</div> <div>2.80 e+3</div> </div>	 <div> <div>9.50 e-4</div> <div>8.95e-04</div> <div>(°)</div> <div>7.96e-04</div> <div>7.50 e-4</div> </div>	 <div> <div>1.04 e+1</div> <div>1.04e+01</div> <div>(°)</div> <div>1.04e+01</div> <div>1.03 e+1</div> </div>
	Section	 <div> <div>5.00 e+3</div> <div>4.79e+03</div> <div>(a.u)</div> <div>4.39e+03</div> <div>4.20 e+3</div> </div>	 <div> <div>1.70 e-3</div> <div>1.36e-03</div> <div>(°)</div> <div>8.74e-04</div> <div>7.00 e-4</div> </div>	 <div> <div>1.04 e+1</div> <div>1.04e+01</div> <div>(°)</div> <div>1.04e+01</div> <div>1.03 e+1</div> </div>

**Table 4.4:** C-plane (0006) reflection in the non-milky zone for sample 4 (point 4-ND)

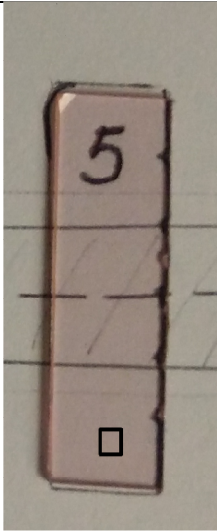
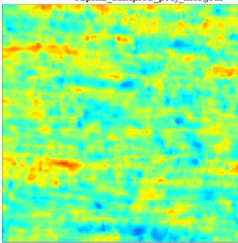
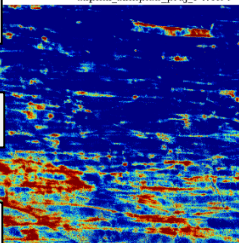
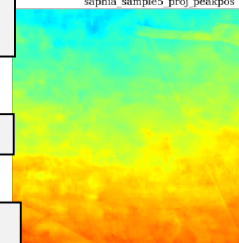
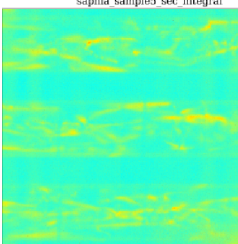
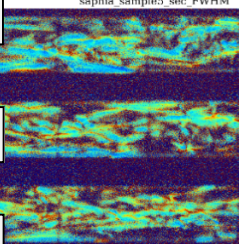
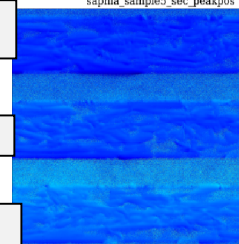


**Table 4.5:** C-plane (0006) reflection in the milky zone for sample 5 (point 5-MD)

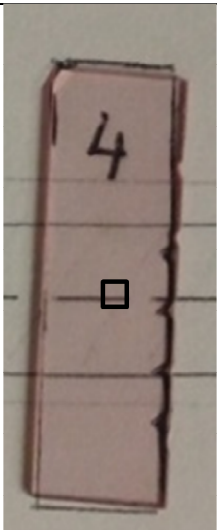
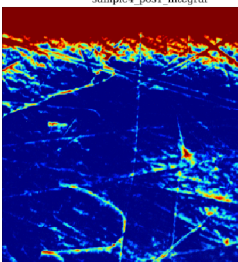
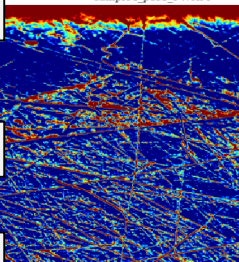
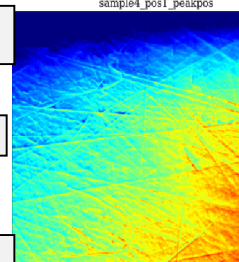


**Table 4.6:** C-plane (0006) reflection in the transition zone for sample 5 (point 4-TD)



Sample		Integrated Intensity	FWHM	Peak position
	Projection	 <div> <div>1.20 e+4</div> <div>9.12e+03</div> <div>(a.u)</div> <div>5.26e+03</div> <div>4.00 e+3</div> </div>	 <div> <div>1.05 e-3</div> <div>1.04e-03</div> <div>(°)</div> <div>1.01e-03</div> <div>1.00 e-3</div> </div>	 <div> <div>6.93 e0</div> <div>6.93e+00</div> <div>(°)</div> <div>6.92e+00</div> <div>6.92 e0</div> </div>
	Section	 <div> <div>5.00 e+3</div> <div>3.98e+03</div> <div>(a.u)</div> <div>2.51e+03</div> <div>2.00 e+3</div> </div>	 <div> <div>1.50 e-3</div> <div>1.24e-03</div> <div>(°)</div> <div>8.47e-04</div> <div>7.00 e-4</div> </div>	 <div> <div>6.93 e0</div> <div>6.93e+00</div> <div>(°)</div> <div>6.92e+00</div> <div>6.92 e0</div> </div>

**Table 4.7:** C-plane (0006) reflection in the non-milky zone for sample 5 (point 5-ND)

Sample		Integrated Intensity	FWHM	Peak position
	Projection	 <div> <div>2.00 e+4</div> <div>1.87e+04</div> <div>(a.u)</div> <div>1.67e+04</div> <div>1.60 e+4</div> </div>	 <div> <div>1.90 e-3</div> <div>1.79e-03</div> <div>(°)</div> <div>1.59e-03</div> <div>1.50 e-3</div> </div>	 <div> <div>3.88 e1</div> <div>3.88e+01</div> <div>(°)</div> <div>3.88e+01</div> <div>3.88 e1</div> </div>

**Table 4.8:** A-plane (11 $\bar{2}$ 0) reflection in the milky zone for sample 4 (point 4-MD)

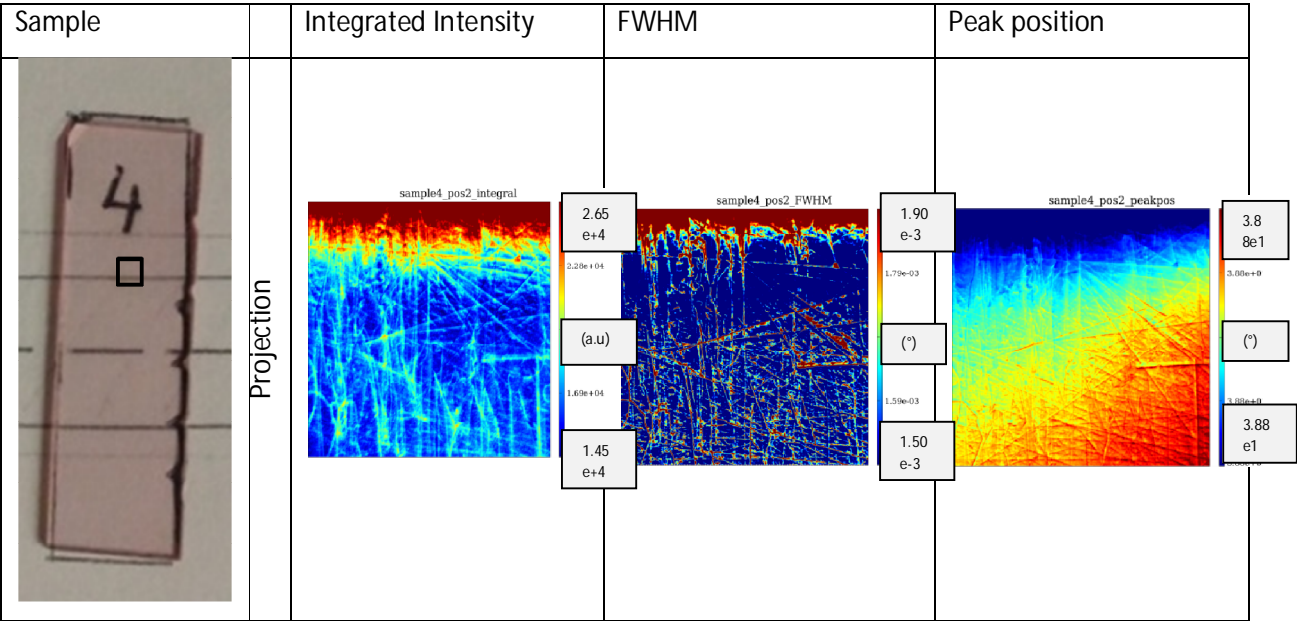


Table 4.9: A-plane (1120) reflection in the transition zone for sample 4 (point 4-TD)

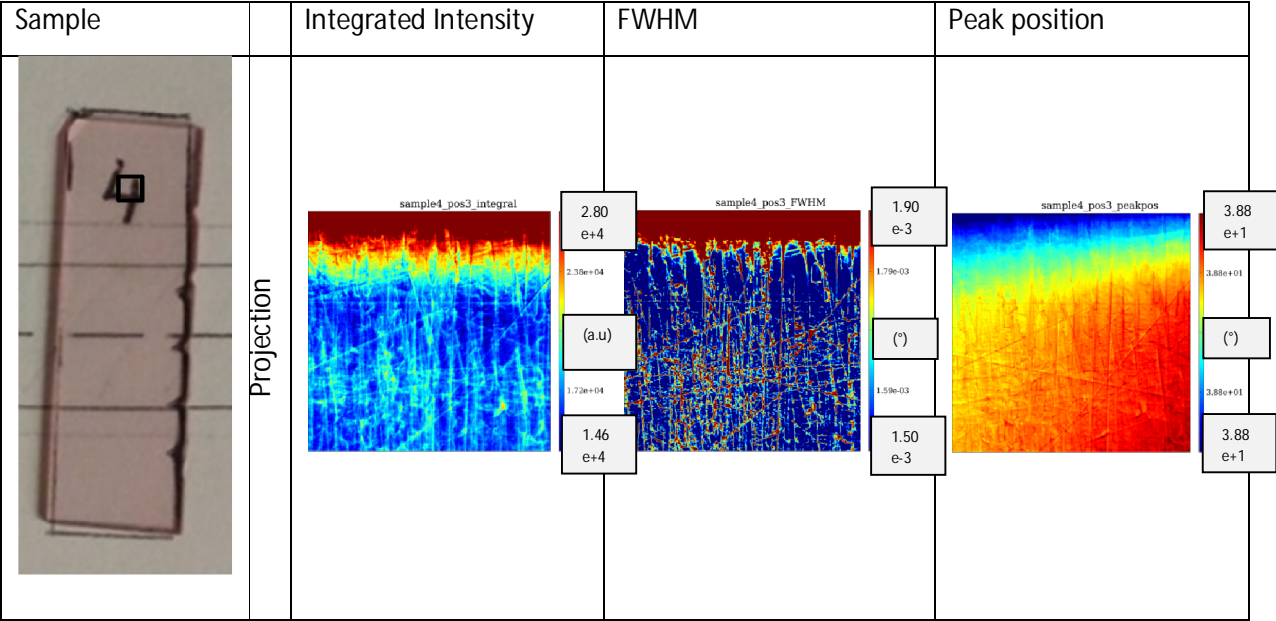


Table 4.10: A-plane (1120) reflection in the non-milky zone for sample 4 (point 4-ND)

#### 4.4.3.5 Variation of dislocation density

The most distinguishable feature in all the maps are the dislocations as evident from the integrated intensity and FWHM maps and it is in accordance with the features observed from the X-ray diffraction images. Thus below we discuss the dislocation behaviour by analysing the integrated intensity and FWHM maps.

##### 4.4.3.5.1 C-plane (0006) reflection

From table 4.2, 4.3 and 4.4 for sample 4, the integrated intensity and FWHM maps show that there is a progressive increase in the number of dislocations as we move from the centre of the sample to outside. At the centre of the milky defect zone as shown in table 4.2 (point 4-MD) we do not see any dislocation in the section images. The section maps in table 4.3 (point 4-TD) are particularly interesting because in the centre we do not observe any dislocations for the milky zone and a single dislocation in the upper region of the transition zone. But there is a sharp increase in the observed dislocations as soon as we progress into the non-milky zone as shown in the maps in table 4.4 (point 4-ND). For the section images in table 4.2 (point 4-MD) and table 4.3 (point 4-TD) we observe a ripple effect in the images. This is due to the extremely high crystalline quality at these positions which does not distort the incoming beam and eventually leads to the interference of the beam which gives rise to the Pendellosung fringes [Tsoutsouva, 2015].

From table 4.5, 4.6 and 4.7 for sample 5, we immediately observe more dislocations than for the corresponding regions of sample 4. This can be attributed to the fact that the sample 5 is farther away from the centre than sample 4 as evident from figure 4.16 and hence there is a radial increase in the dislocation density. We also observe an increase in the dislocation as we progress from the milky zone to the non-milky zone similar to sample 4. But the most striking feature is observed in the projection images for the transition zone in table 4.6, where we observe a sharp increase in the dislocation density. This suggests the presence of a very sharp demarcation between the milky and non-milky zone which leads to the sudden change in the dislocation density. This phenomenon is in good accordance with that observed during the X-ray diffraction analysis as observed from figure 4.14.

##### 4.4.3.5.2 A-plane (11 $\bar{2}$ 0) reflection

From table 4.8 (point 4-MD), 4.9 (point 4-TD) and 4.10 (point 4-ND) for sample 4, we see a sharp change in the direction of the dislocations along with the increase in the number of dislocations as we move from the milky zone to the non-milky zone. There are very few dislocations in the milky zone and they are horizontal. But as we move to the transition zone and to the non-milky zone we see a sharp increase in the number of dislocations and there is change in direction of dislocations from horizontal to a mixture of dislocations in

all directions forming a mesh with predominantly vertical direction. There is the presence of a distorted region in the upper end of all the images, but it can be neglected since it can be due to noise occurring during the recording of the images.

Thus, from the RCI analysis we realise that there is a sharp transition from the milky defect zone to the non-defect zone which is accompanied by a sharp increase in the dislocation density.

#### 4.4.3.6 Burgers vector

The variation of Bragg angle when going from one side of the dislocation to the other side is given by:

$$\partial\theta_B = \frac{b_r}{\pi r_d} \text{ [Tsoutsouva, 2015]} \quad \text{Equation 4.1}$$

Hence, to calculate the magnitude of the Burgers vector we can use the value of dislocation width and variation of the Bragg angle from the peak position maps. The peak position map for projection of sample 5 from table 4.6 (point 5-TD) was selected and the calculations were carried out for the dislocation marked in figure 4.18. Knowing the dimensions of the image as marked and using the colour scale for the angle variation we can determine the value of  $r_d$  and  $\theta_B$  to be 0.02 mm and 1.5 arc sec respectively. Thus using equation 4.1 the Burgers vector for the marked dislocation was determined to be 4.57 Å. This value of Burgers vector is very close to the lattice parameter,  $a=4.76$  Å, suggesting that the dislocations are due to slip of the C-planes in the A-axis direction. Considering that the dislocation analysed belongs in the milky defect zone, we can consider that the milky zone mainly consists of dislocations formed by the basal slip.

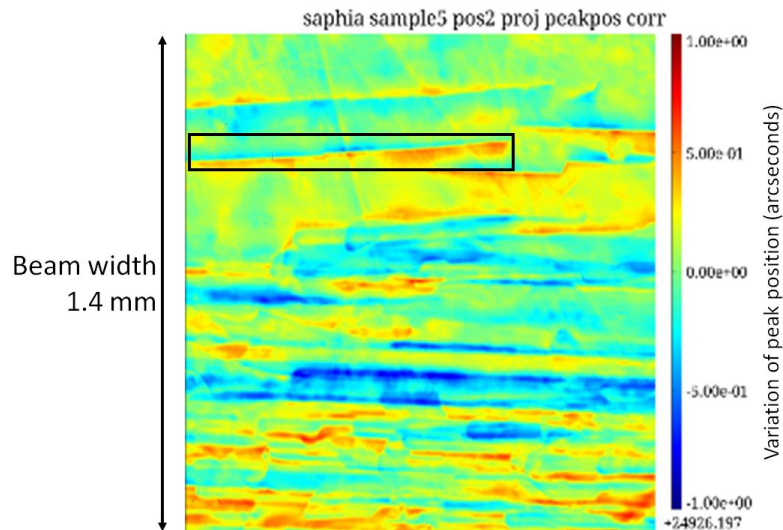


**Figure 4.18:** Peak position map from table 4.6 with a selected dislocation marked to calculate the Burgers vector.

#### 4.4.3.7 Dislocation density estimate

From the X-ray diffraction topography as seen in figure 4.14 and in the Rocking curve images as seen in table 4.6, a sharp transition in the dislocation density is observed at the interface between the milky defect zone and the non-defect zone. It is interesting to quantify the increase in dislocation density at this transition zone as we move from the milky defect zone to the non-defect zone.

The Hirsch formula allows a relation to be established between the FWHM values and the dislocation density at those regions given by:

$$\rho_d = \frac{(FWHM)^2}{9b_r^2} [\text{Gay, 1953}] \quad \text{Equation 4.2}$$

But the FWHM signal contribution from a region of the crystal is not just due to the defect ( $FWHM_d$ ) in the form of dislocations but is also due to any possible sample curvature ( $FWHM_r$ ) and the intrinsic value of the crystal including the convolutions due to the instrumentation ( $FWHM_i$ ). If each term causes a gaussian broadening in the rocking curve, then the resultant FWHM is given by:

$$FWHM = \sqrt{(FWHM_i)^2 + (FWHM_r)^2 + (FWHM_d)^2} [\text{Wie, 1994}] \quad \text{Equation 4.3}$$

An attempt was made to quantify the dislocation density using the above relations for the FWHM values marked on the colour scale at either side of the transition zone in sample 5 (point 5-TD) as shown in figure 4.19(b). To determine the ( $FWHM_d$ ) for figure 4.19(b) it is necessary to determine the contribution due to ( $FWHM_i$ ) and ( $FWHM_r$ ). The FWHM map for sample 4 from table 4.2 (point 4-MD) where no dislocations were observed was selected as shown in figure 4.19(a). The FWHM value for figure 4.19(a).marked in the colour scale corresponds to the value of  $\sqrt{(FWHM_i)^2 + (FWHM_r)^2} = 8 \cdot 10^{-4}^\circ$ . Using this value we can find the value of ( $FWHM_d$ ) for the two regions of figure 4.19(b) using equation 4.3.

Finally, substituting the value of ( $FWHM_d$ ) for both the regions in equation 4.2 and using the value of  $b_r = 4.57 \text{ \AA}$  as obtained from the earlier section we obtain values of  $\rho_d = 6800 \pm 200 \text{ cm}^{-2}$  for the region outside the milky zone and  $\rho_d = 4600 \pm 200 \text{ cm}^{-2}$  for the region in the milky zone. Thus there is a sharp increase in the dislocation density by 50% as we cross the transition point from milky to the non-milky zone. Also these values of dislocation density fit the plot for the quantitative estimate of dislocation density provided in figure 4.12.



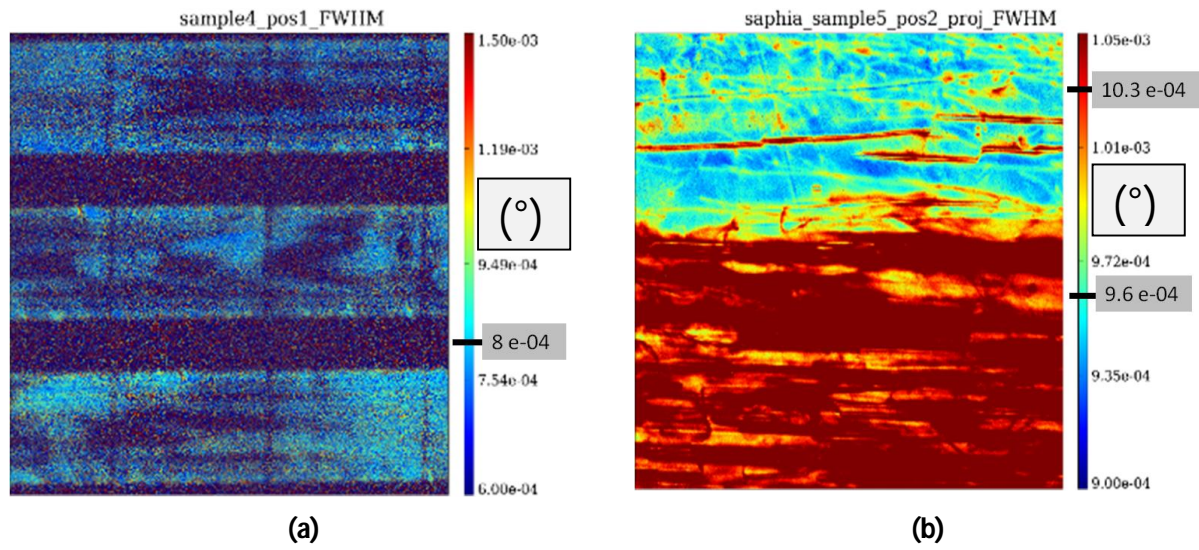


**Figure 4.19:** FWHM plots **(a)** for a region (point 4-MD) with no dislocations (average FWHM value marked in the colour map) and **(b)** for a region (point 5-TD) with the transition between milky (average FWHM value marked in the colour map) and non-milky zone (average FWHM value marked in the colour map).

## 4.5 Stress Analysis

### 4.5.1 Temperature gradient

The finite element software COMSOL Multiphysics was used for modelling the heat transfer and melt convection during the Kyropoulos growth of Ti-doped sapphire crystals as explained in Appendix III.

Figure 4.20 shows the results obtained at the solidification time  $t=30$  h for an ingot growing in a crucible 15 cm in diameter. The growth interface has a conical shape with a large curvature which corresponds to the shape of crystals observed in figure 2.16 in chapter 2. The colour map displayed in this figure shows the temperature field in the solid-liquid sample. Temperature gradients in the solid phase are lower than in the liquid phase, due to the internal radiative effects in the sapphire crystal. The temperature distribution in the melt is strongly influenced by the convection, which is driven by buoyancy and Marangoni effects. One single vortex, with the fluid moving down along the symmetry axis, is obtained (see the right side of the image shown in Figure. 4.20). The isotherms are plotted in blue on the left side of the image. One can see that the temperature distribution in the melt is quite homogeneous, except for the region located near the symmetry axis and in the flow boundary layers at the growth interface, where the density of isotherms increases significantly. The Marangoni convection, which drives the hot fluid from the crucible wall to the crystal, invades the triple solid-liquid-gas point, leading to an increased temperature gradient in this region.



The temperature distribution in the liquid influences the thermal field in the crystal near the growth interface.

Figure 4.20 shows that the density of isotherms in the crystal is higher near the triple point (crystal periphery) than in the region located near the symmetry axis (crystal centre). The temperature gradient in the solid, perpendicular to the solid-liquid interface, has been computed in four reference points located in the crystal near the growth interface. The radial coordinates of these points are:  $r=0.1\text{cm}$ , 1 cm, 2 cm and 3 cm. The plot shown in figure 4.21 indicates that the temperature gradient increases significantly near the triple point region. Therefore, the thermal stresses, which influence the dislocations density, are higher at the crystal periphery than at the centre [Sen, 2016].

The temperature gradient as calculated from the numerical model in figure 4.20 indicates that the values are higher at the triple point and decrease towards the centre of the crystal as depicted in figure 4.21. The plot shown in figure 4.21 indicates that the temperature gradient increases significantly near the triple point region. The temperature gradient in the solid, perpendicular to the solid-liquid interface has been computed in four reference points located in the crystal near the growth interface. The radial coordinates of these points are:  $r=0.1\text{cm}$ , 1 cm, 2 cm and 3 cm. Although the points analysed in figure 4.20 are not at the same axial distance, the increasing temperature gradient with the radial distance is an indicator of higher thermal stress at the periphery of the crystal than at its centre. Further, during the growth evolution, as the crystal radius increases there is an increased influence of the Marangoni convection on the thermal field. This increases the temperature gradient towards the triple point from the interface centre leading to increased thermal stress at the outer region of the growing crystal [Gao, 2015] [Liu, 2015]. Apart from the thermal stress arising in the crystal during the growth process there are also significant stresses acting on the crystal during the cooling process in the crucible, which are more intense on the crystal surface near the crucible walls than in the centre [S. Wang, 2016].

Therefore, the thermal stresses which are an effect of the temperature gradients are higher at the crystal periphery as compared to the centre and influence the dislocation density. Thus the radially increasing dislocation density shown in figure 4.12 can be connected to the radially increasing thermal gradient visualised in figure 4.20.[Sen, 2016]

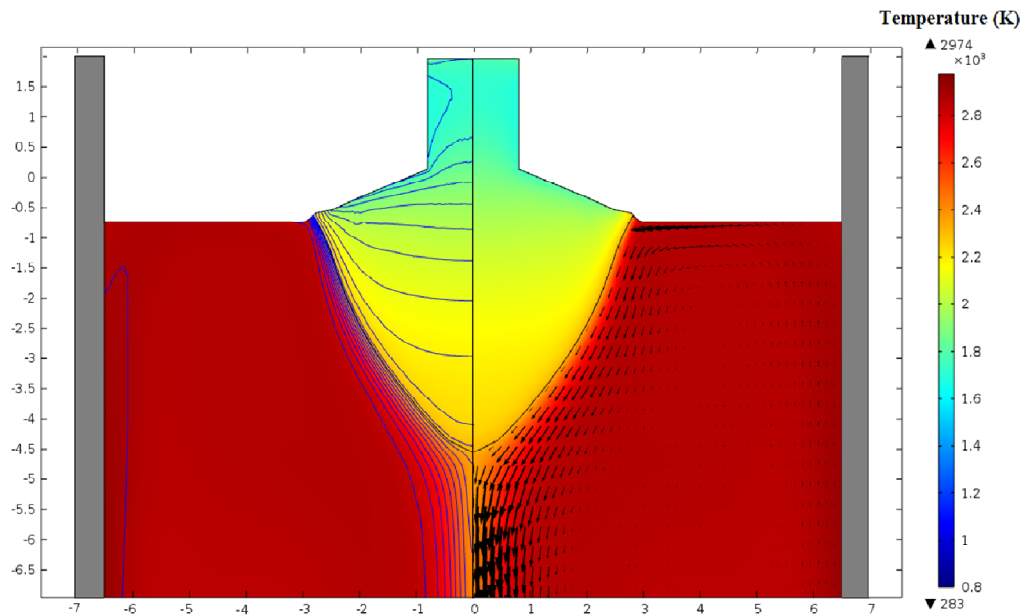


**Figure 4.20:** Numerical results obtained at the solidification time  $t=30$  h: isotherms (left side) and flow velocities (right side). The colour map displays the temperature field in the solid-liquid sample. The maximum flow velocity is  $u_{max}=4$  cm/s.

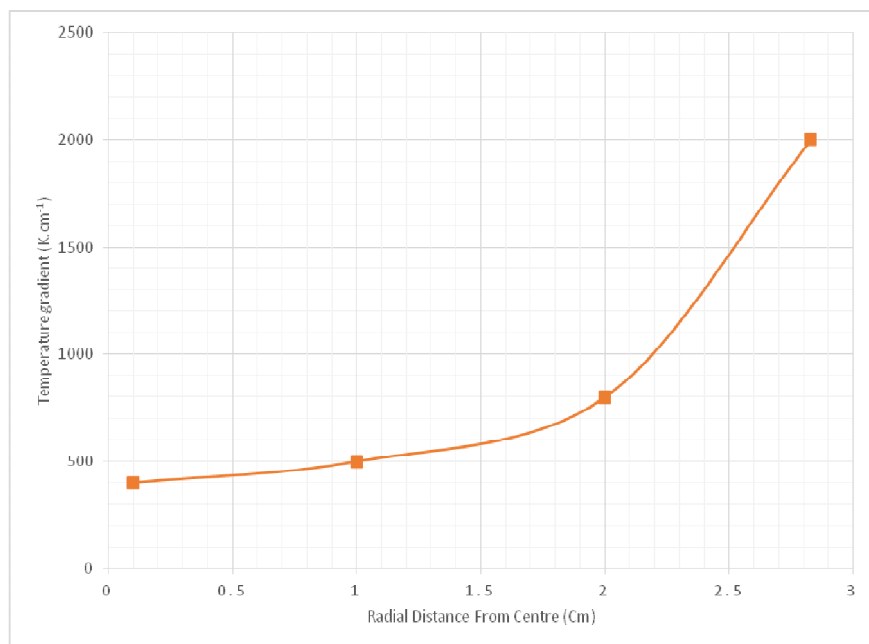


**Figure 4.21:** Plot representing the temperature gradient at various radial positions on the solid-liquid interface. The gradients were calculated in some reference points located in the crystal near the growth interface.

#### 4.5.2 Thermal stress

The software COMSOL Multiphysics has also been used for modelling thermal stresses in the crystal. The thermal stress in the growing crystal during a particular instant of growth has been obtained using 3D-modeling for anisotropic properties and 2D-modelling considering isotropic conditions as explained in Appendix III.

##### 4.5.2.1 *von Mises stress*

Figure 4.22(a) shows the results carried out from 2D-axisymmetric global modeling of the Kyropoulos furnace at the growth time  $t=67$  h. The left side of figure 4.22(a) shows the temperature field and the isotherms, while the right side shows the velocity field in the melt. The plot of isotherms in the crystal reveals low radial temperature gradients in the internal part of the crystal, except for the region around the triple crystal-melt-gas line, where the isotherms density increases significantly.

The computed temperatures are used for 3D simulations of thermal stress in the sapphire crystal grown along the A-axis (Figure 4.22(b)). The simulation domain is limited only to one half part of the crystal, since (x-z) is a symmetry plane in the present system (x-axis is parallel to a-axis, and z-axis is parallel to c-axis of sapphire). The plot of von Mises stress in Figure 4.22(b) shows high values along the triple crystal-melt-gas line.

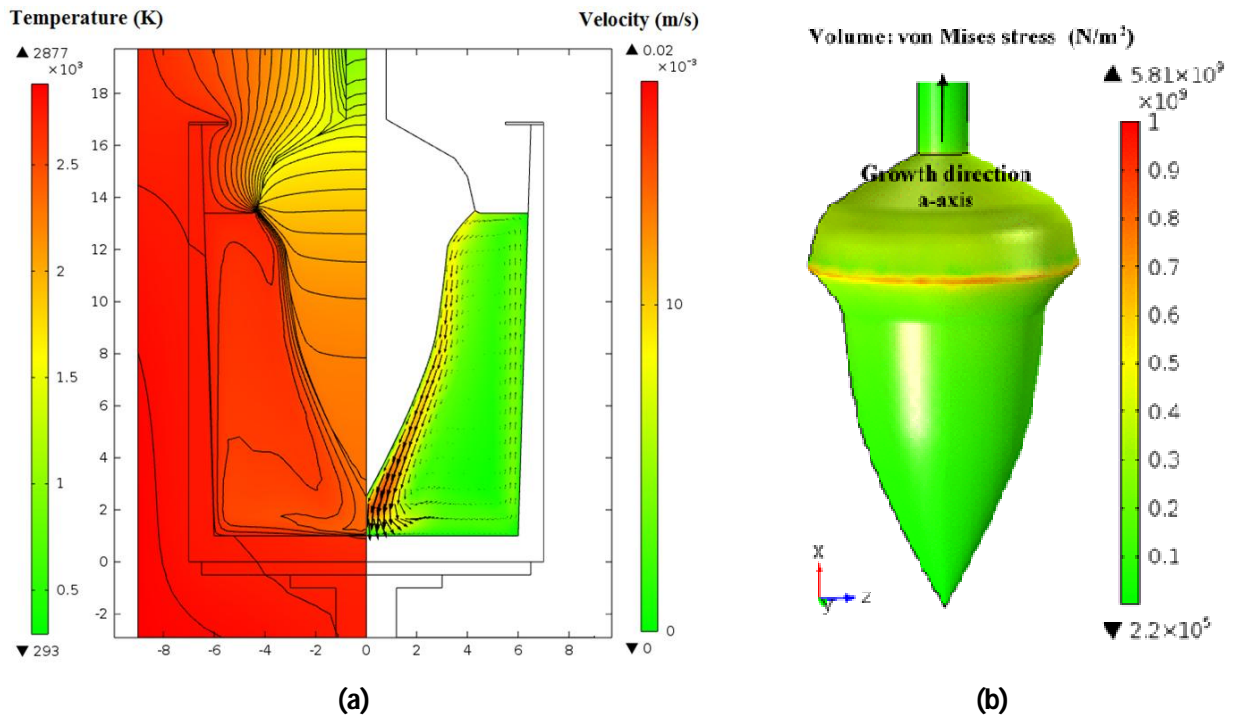


**Figure 4.22:** **(a)** temperature distribution and isotherms (left side), velocity field (right side) carried out from global 2D axisymmetric computation. **(b)** von Mises stress distribution on the crystal outer surface carried out from local 3D computation [Stelian, 2018].

Figure 4.23 shows the von Mises stress distribution in the longitudinal section (x-z plane) and two transversal sections (y-z plane at x=12 cm and x=14 cm) of the sapphire ingot. Results plotted in the longitudinal section show that the high thermal stress is located in a thin region near the outer surface of the crystal, while a much lower stressed region spreads in the internal part of the crystal (Figure 4.23(a)). Values of the von Mises stress are plotted in some points, showing maximum values along the triple crystal-melt-gas line (575 MPa). Almost 90% of the longitudinal section of the crystal exhibits very low thermal stress (values less than 80 MPa). The plot in the transversal section of the crystal reveals differences in thermal stress distribution over the slices cut at x=12 cm and x=14 cm (Figure 4.23(b)).

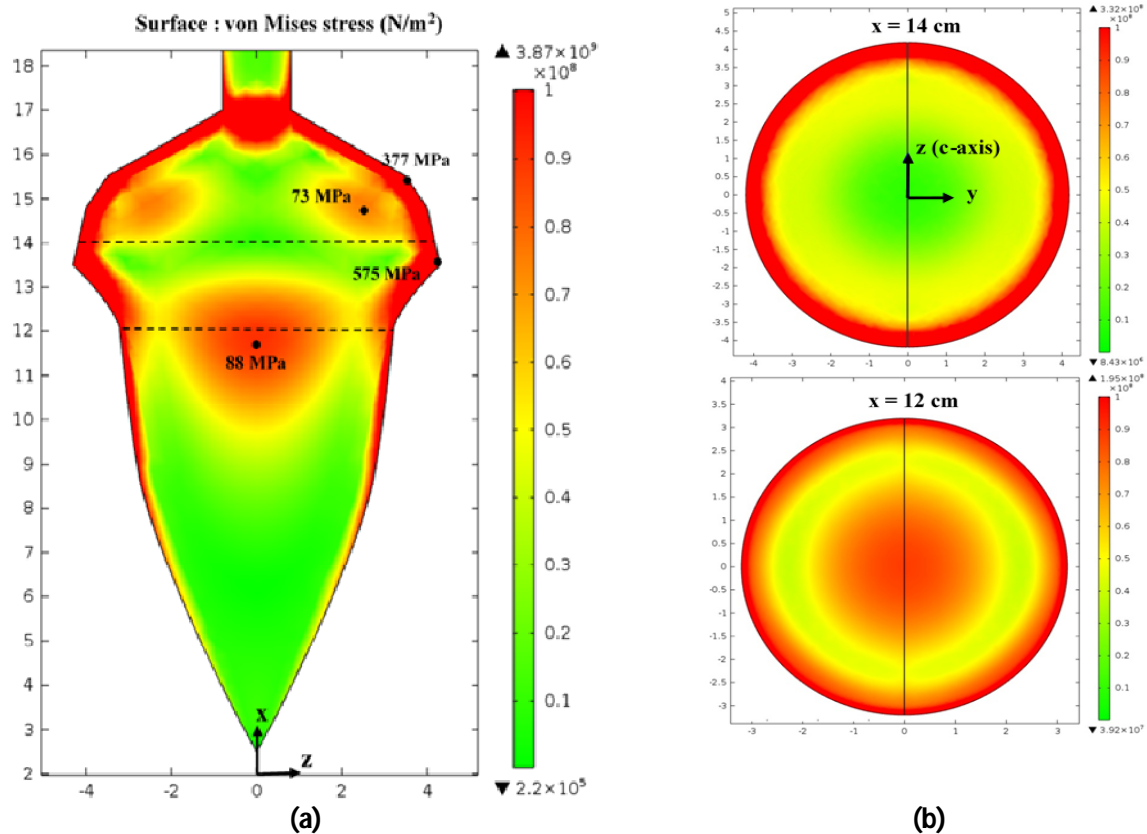


**Figure 4.23:** (a) von Mises stress distribution in the longitudinal ( $x, z$ ) section of the crystal (values in some points are shown on the figure); (b) von Mises stress distribution in two transversal ( $y, z$ ) sections of the crystal ( $x=12$  cm and  $x=14$  cm) [Stelian, 2018].

The transversal section at  $x=12$  cm corresponds to the submerged ingot part, while the section at  $x=14$  cm corresponds to the floated ingot part. The cut at  $x=12$  cm reveals the stress distribution, with a maximum region in the center, then a minimum and a maximum at the crystal periphery. It is very interesting to notice that the distribution profile is not completely axisymmetric and there is a short bridge of high stress band between the outer and inner maximum stress regions along the C-axis passing through the centre. The non axisymmetric distribution is further asserted from figure 4.24 where the von Mises stress distribution in the longitudinal section of the crystal along the C-plane and C-axis is provided side by side and the stress regions at  $x=12$  cm are not symmetrical.

The stress distribution in the transversal section at  $x=14$  cm is with a minimum in the centre and a maximum at the crystal outer surface. It should be pointed that the radial temperature profiles are completely different in these two sections, exhibiting increasing temperatures from the centre to the

crystal periphery at  $x=12$  cm and decreasing temperatures to the crystal periphery for the section at  $x=14$  cm.

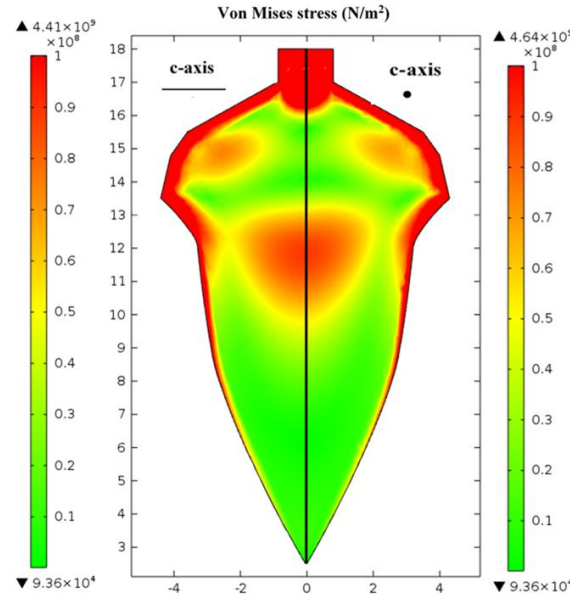


**Figure 4.24:** von Mises stress distribution in the longitudinal ( $x, z$ ) section of the crystal. (Left)- section along the C-axis, (Right)- section along the C-plane [Stelian, 2018].

Numerical analysis were carried out for the comparison between 3D modelling and 2D axisymmetric computations. There were some variations between the two results, but the stress variation with radial distance show the same trend and hence the 2D axisymmetric calculations can be reliably used for the analysis of regions with peculiar stress values in our crystals [Stelian, 2018].

#### 4.5.2.2 Stress component for Basal slip

For sapphire crystal the basal slip has the lowest critical resolved shear stress at elevated temperatures, making it the easiest slip system to activate. A schematic of the basal slip mechanism is shown in figure 4.25(a). The critical resolved shear stress at the high-strain yield point is shown in figure 4.25(b) as a function of temperature, based on data obtained from deformation experiments at elevated temperatures [Lagerlof, 1994].

As evident from the study of dislocations in the earlier sections a low dislocation density in the milky defect zone is observed and the measured value of Burgers vector also corresponds to dislocations moving in the basal slip system [Snow, 1973]. This suggests that the low dislocation density regions in the milky defect zone would consist of dislocations predominantly due to basal slip. Thus it is important to calculate the

stress components responsible for the basal slip system and check if the low dislocation density region corresponds to the low stress component region for the basal slip system.

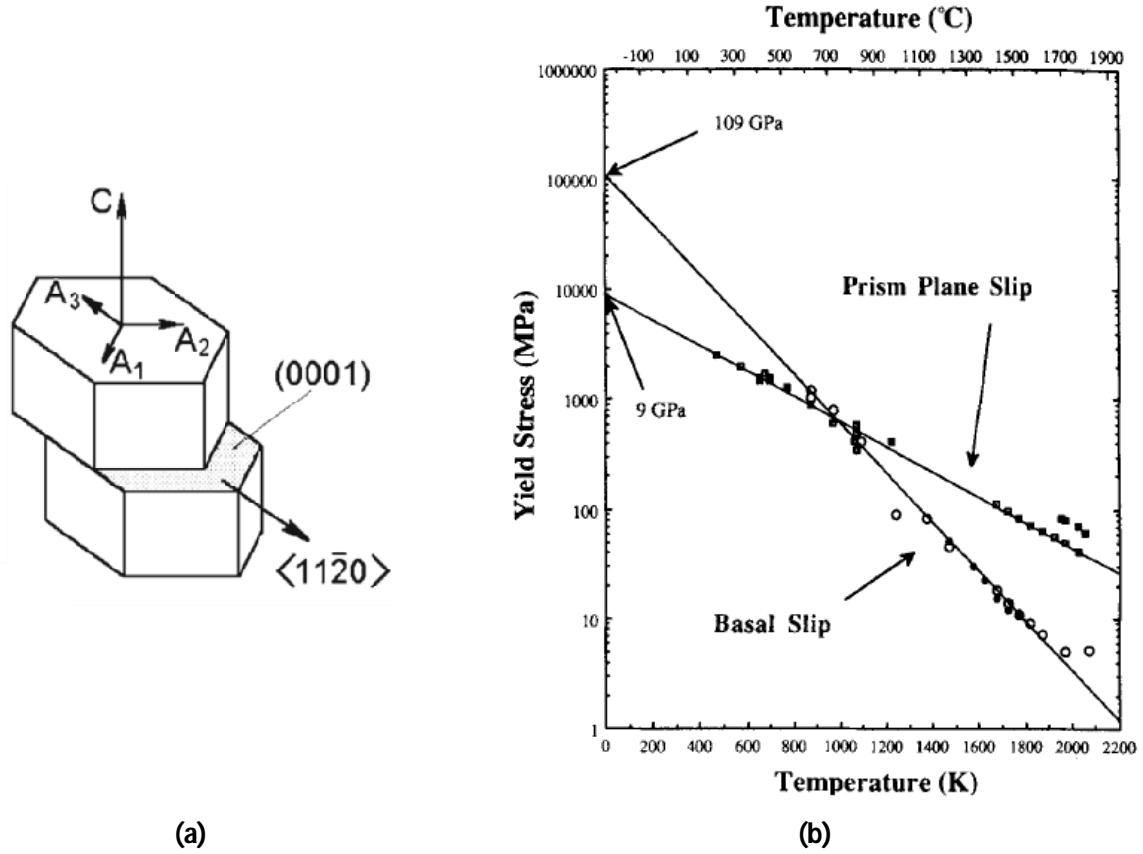


**Figure 4.25: (a)** Schematic diagram of Basal slip system in sapphire **(b)** Plot of  $\tau_{crss}$  versus temperature( $T$ ) for basal slip and prism plane slip [Lagerlof, 1994].

The von Mises stress computed in the 2D axisymmetric system is presented for the longitudinal section of the crystal in figure 4.26(a) and a plot of the radial distribution of the stress in two transversal section,  $x=12$  cm and  $x=14$  cm in figure 4.26(b).

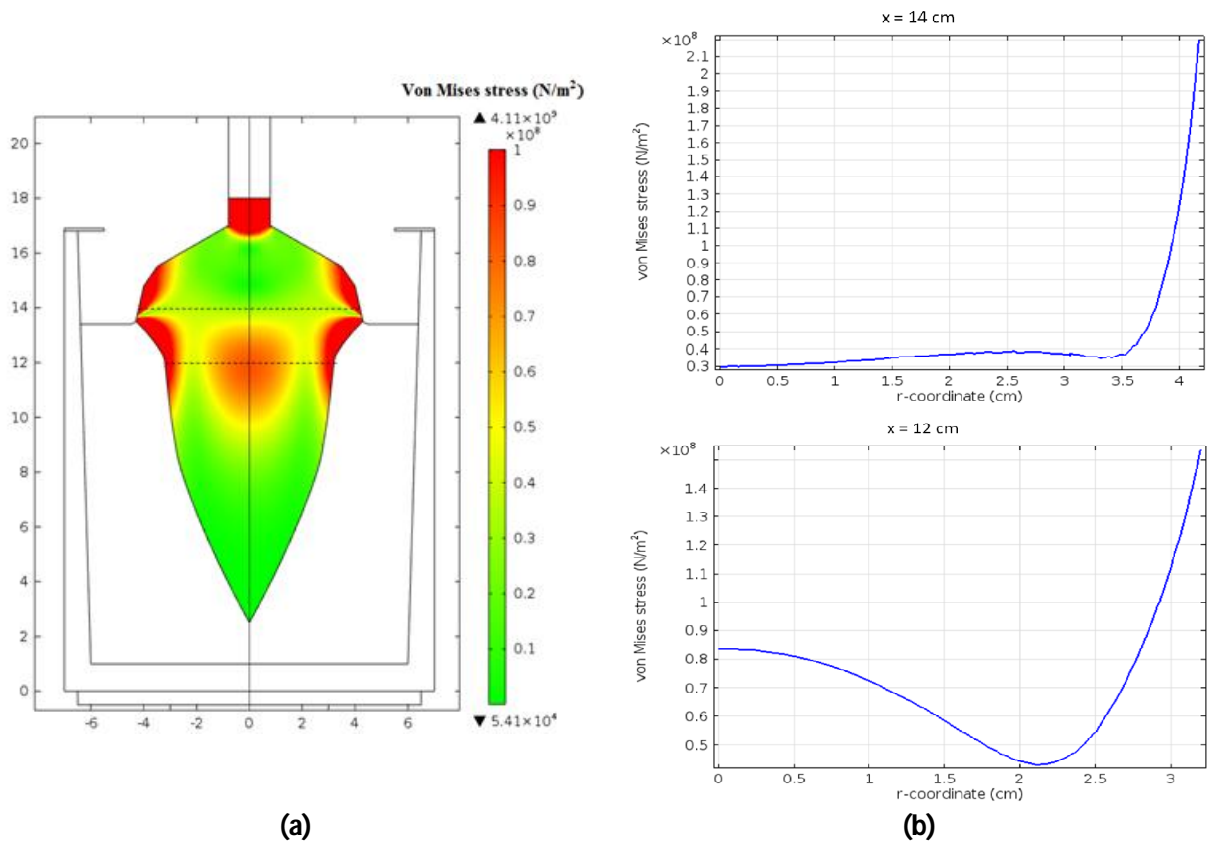


**Figure 4.26: (a)** von Mises stress distribution in the longitudinal ( $x, z$ ) section of the crystal in 2D axisymmetric system; **(b)** Radial distribution of von Mises stress in two transversal ( $y, z$ ) sections of the crystal ( $x=12$  cm and  $x=14$  cm) [Stelian, 2018].

In an axisymmetric approximation, the stress components are: the normal stress in the radial direction( $\sigma_r$ ), the normal stress in the azimuthal direction( $\sigma_\phi$ ), the normal stress in the axial direction( $\sigma_z$ ) and the shear stress( $\sigma_{rz}$ ). Out of these four components the shear stress has a very small component on the C-plane and hence does not contribute to the basal slip. Thus it is important to study the other three normal stress components and calculate their projection on the C-plane along the A-axis which constitutes the basal slip system. The stress components are visualised on the longitudinal section and the transversal section as shown in figure 4.27.



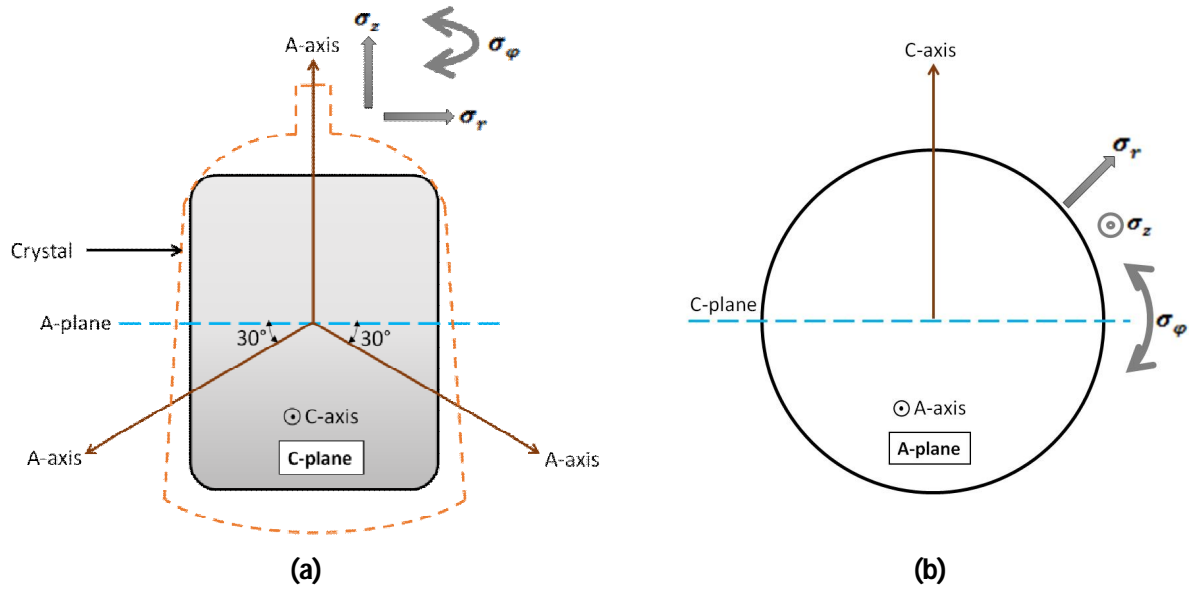


**Figure 4.27:** The normal stress components  $\sigma_r$ ,  $\sigma_\phi$  and  $\sigma_z$  shown on **(a)** the longitudinal crystal section and **(b)** transversal crystal section.

In the following sections the components of the three normal stresses are projected on the C-plane along the A-axis direction for two transversal sections of the crystal at  $x=12$  cm and  $x=14$  cm. The axisymmetric radial distribution of the stress values are obtained from the 2D axisymmetric thermal stress modelling. Based on these results their components are calculated for the A-axis direction in the C-plane for varying radial distance and radial direction. All stress values displayed on the transversal sections are in MPa.

#### 4.5.2.3 Azimuthal normal stress component ( $\sigma_\phi$ )

From figure 4.28 we realise that the azimuthal normal stress component,  $\sigma_\phi$  has the highest magnitude and it acts very heavily in the direction of C-axis. While it's component on the central C-plane is zero. The values are much higher for the section at  $x=14$  cm reaching upto 191 MPa than for  $x=12$  cm where it reaches a maximum value of 65 MPa.

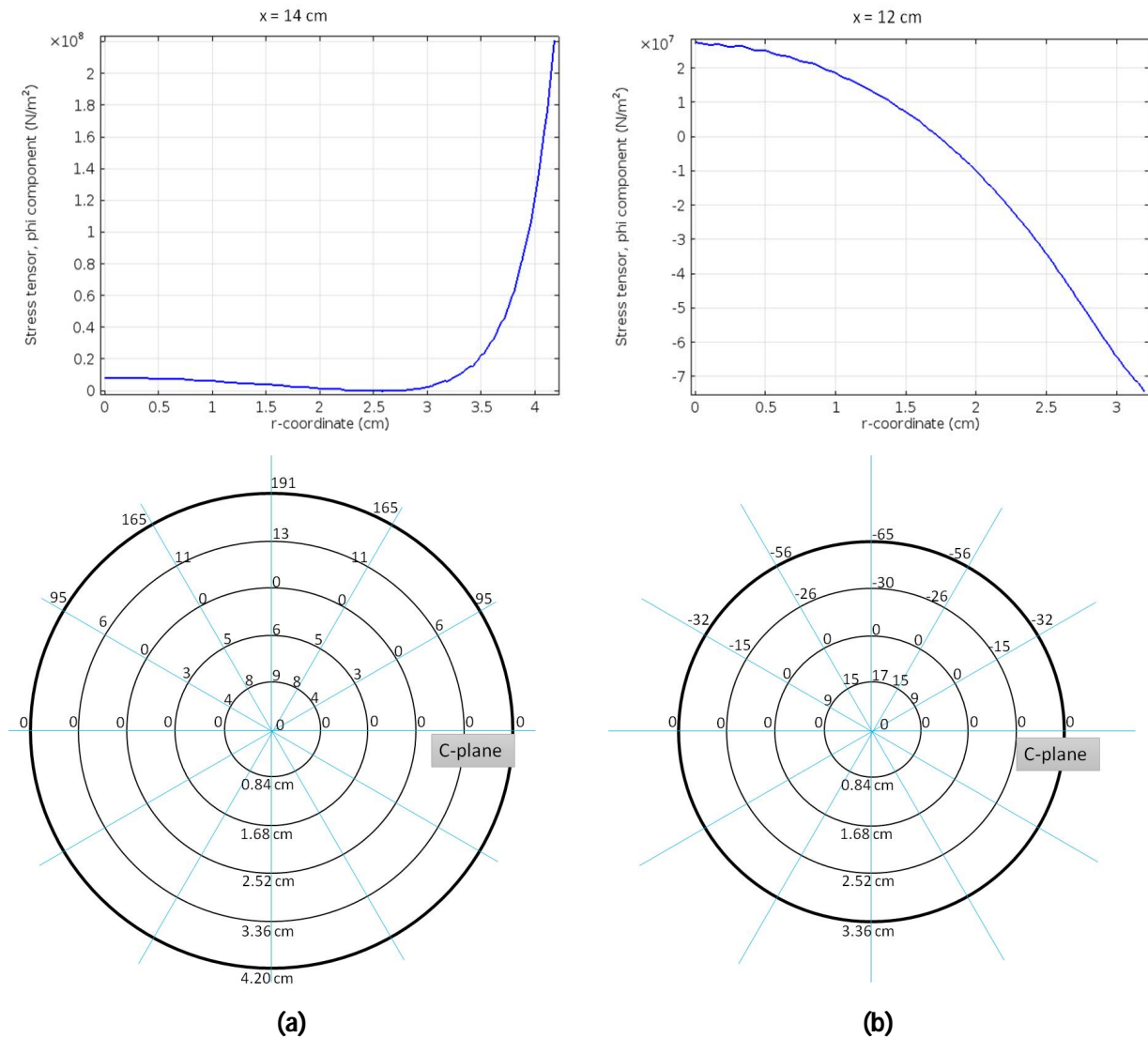


**Figure 4.28:** Radial distribution of  $\sigma_\phi$  (top) and its component responsible for basal slip (bottom) for **(a)**  $x=14$  cm and **(b)**  $x=12$  cm.

#### 4.5.2.4 Radial normal stress component ( $\sigma_r$ )

From figure 4.29 it is realised that the radial normal stress component,  $\sigma_r$  has much lower magnitude than  $\sigma_\phi$  and  $\sigma_z$ . Thus it is not a big contributor for basal slip. The radial stress acts on the direction parallel to the central C-plane while its component on the C-axis direction is zero. The values are much higher for the section at  $x=12$  cm reaching upto 23 MPa than for  $x=14$  cm where it reaches a maximum value of 7 MPa.

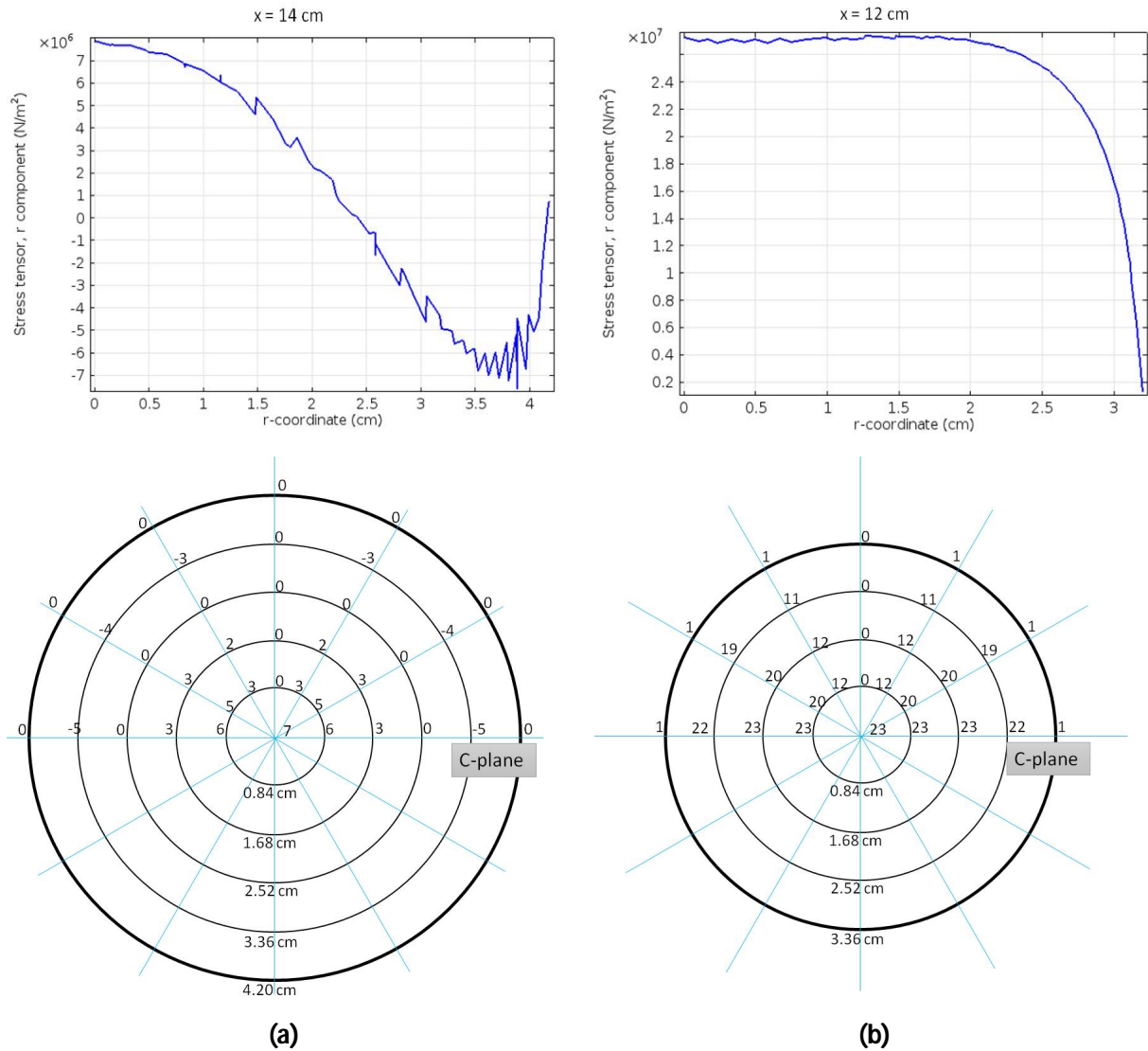


**Figure 4.29:** Radial distribution of  $\sigma_r$  (top) and its component responsible for basal slip (bottom) for (a)  $x=14$  cm and (b)  $x=12$  cm.

#### 4.5.2.5 Axial normal stress component ( $\sigma_z$ )

From figure 4.30 it is realised that the axial normal stress component,  $\sigma_z$  is axisymmetrical. The values are much higher for the section at  $x=12$  cm reaching upto 50 MPa than for  $x=14$  cm where it reaches a maximum value of 9 MPa. For the section at  $x=12$  cm the values are comparable to those for  $\sigma_\phi$ , while for the section  $x=14$  cm the values are comparable to those for  $\sigma_r$  but much lower than that of  $\sigma_\phi$ .

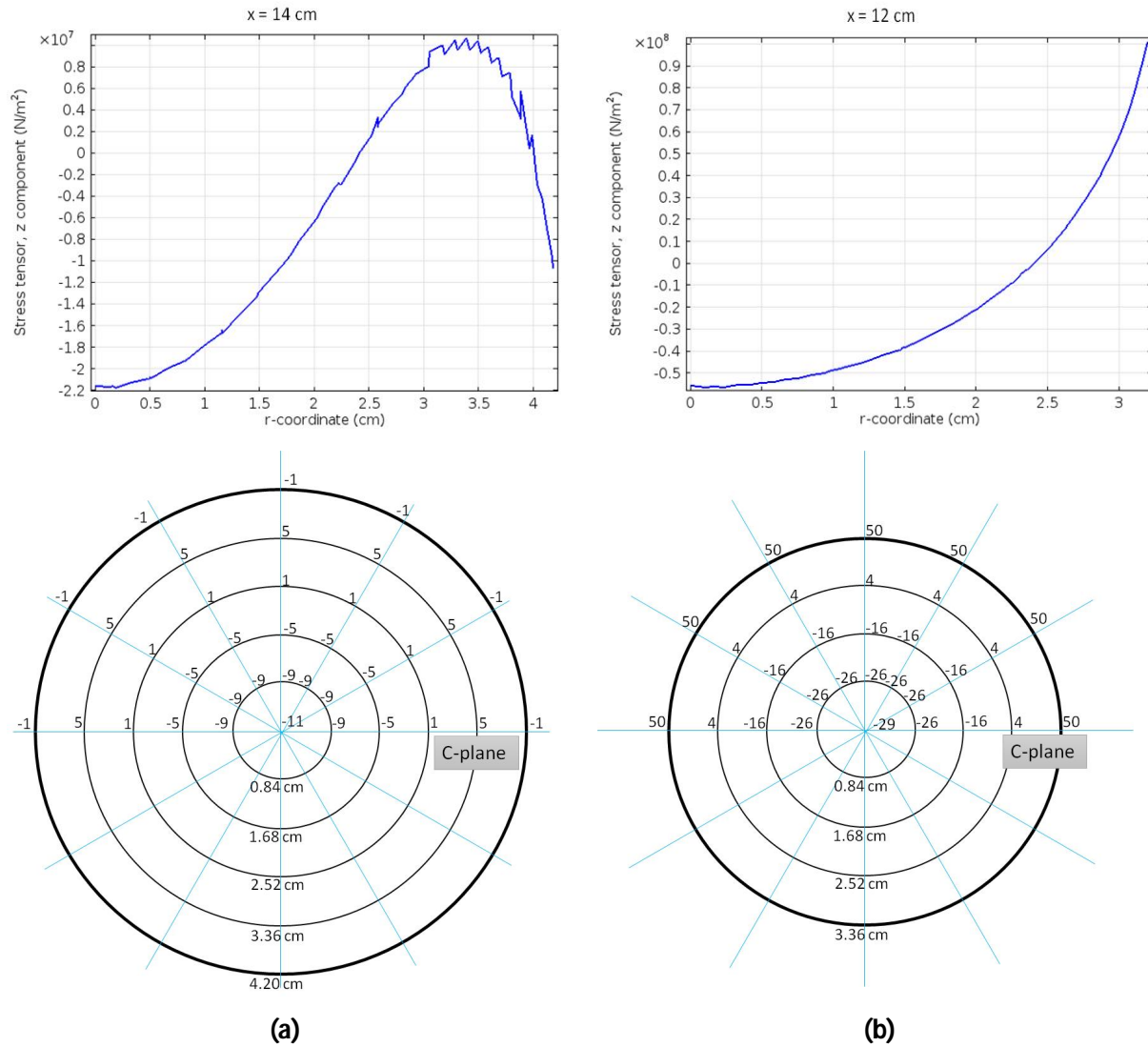


**Figure 4.30:** Radial distribution of  $\sigma_z$  (up) and its component responsible for basal slip (down) for **(a)**  $x=14$  cm and **(b)**  $x=12$  cm.

#### 4.5.2.6 Resultant stress component for basal slip

From the stress distribution values, we can see that the stress responsible for the basal slip and hence the dislocations are definitely not axisymmetrical. The maximum stress values on the region along the central C-axis are much higher than the values on the region around the central C-plane. This could possibly lead to greater extent of basal slip in the regions along the C-axis radial direction and decreasing towards the regions in the C-plane radial direction. The dislocation multiplication is activated only in places where the stress is higher than the critical resolved shear stress. Théodore, in a study on dislocation multiplication during the EFG sapphire growth, estimated the critical stress to be 28 MPa [Théodore, PhD Thesis]. Where the stress is below this value, dislocation multiplication does not occur. Hence, suggesting a mechanism

which could lead to a lower dislocation density along the central C-plane region corresponding to the milky defect zone as observed in the earlier sections.

It is to be noted that the stress calculations for the basal slip mechanism were carried out here only for the two transversal section at  $x=12$  cm and  $x=14$  cm. Also, all calculations are for a particular instant during the crystal growth,  $t=67$  h. To have completely reliable data, it is necessary to have the maximum stress component values for basal slip for the whole growth process and throughout the crystal volume. If these calculations reveal a low stress region along the C-plane corresponding to the milky defect zone, it would confirm the hypothesis of the dislocations being the ones due to basal slip.

## 4.6 Characterisation of Point defects (Vacancies)

### 4.6.1 Thermoluminescence (TSL)

#### 4.6.1.1 Experimental set-up

Normalised thermoluminescence (TSL) curves were recorded from 2 disc samples prepared from the milky and non-milky zones with dimensions of 10 mm in diameter and 1 mm in thickness.

The TSL studies of irradiated samples were performed in a Janis VPF-800 cryostat. An X-ray tube (W anode, 40 kV, 10 mA) was used for sample irradiation at room temperature for 5 minutes providing a dose rate of approximately  $20 \text{ Gy/s/cm}^2$ . TSL curves were recorded using a Hamamatsu H8259 photon counting head in the temperature interval of 295-700 K at a heating rate of 10 K/min. The TSL spectrum was repeatedly measured for 60 s using an ARC SpectraPro 300i grating monochromator equipped with a CCD detector with a spectral sensitivity in the range of 190–1100 nm. Considering the given heating rate, each emission spectrum was measured within a temperature interval of 10 K. This allowed measuring several spectra in the temperature range of each TSL peak.

#### 4.6.1.2 TSL glow curves

Figure 4.31 show normalised TSL curves recorded from the two samples. For both samples a prominent TSL peak at 415 K is registered. Its half-width (FWHM) is 34 K, and according to the accepted classification, it is a narrow one [Kortov, 2017]. A small high temperature peak is also observed at 515 K for both samples. High-temperature TSL peaks in the range of 500 K – 850 K appear after high-dose irradiation, when the luminescence yield of the main peak is saturated and charge carriers undergo efficient trapping by deep traps in alumina. The most striking feature is that for the milky defect sample the peak intensity at 415 K is 2.5 times higher than that for the non-milky sample.

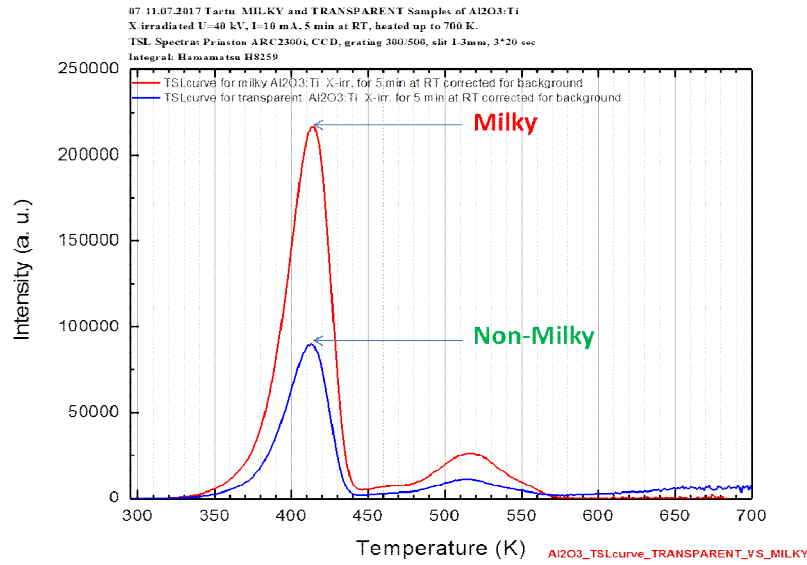
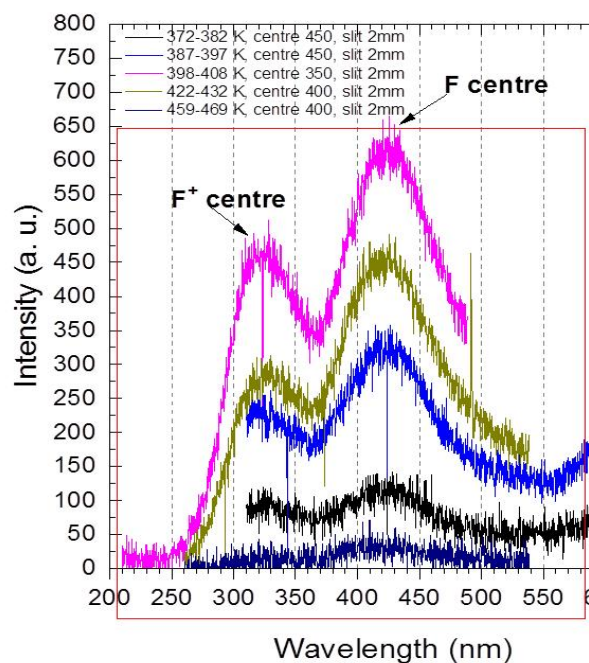


**Figure 4.31:** Normalised TSL curves obtained from milky and non-milky zone sample.

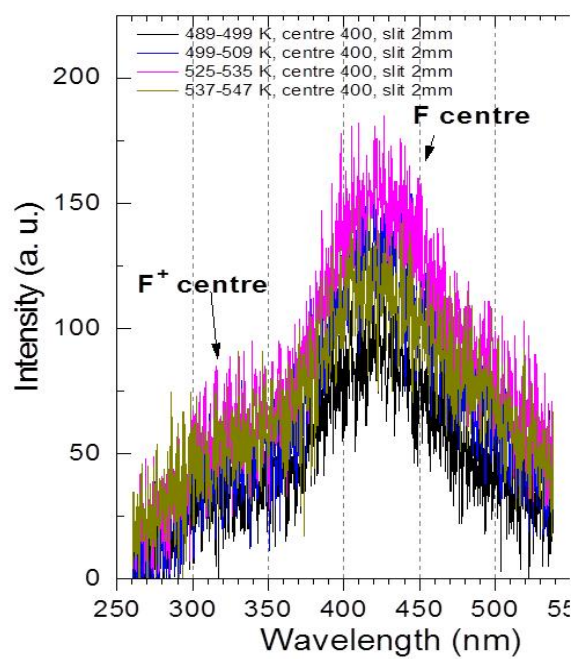
#### 4.6.1.3 Emission spectra in the main TSL peak

For both milky and non-milky samples, various emission spectra were measured during the sample heating from 357 K to 547 K. The spectra at higher temperatures are not significant due to an increased contribution from the thermal background of the heater and the sample holder plate. The emission spectra observed from the temperature range of the maximum of the TSL peak (415 K) features two bands peaking at 330 nm and 430 nm as shown in figure 4.32 and figure 4.33. The emission peak at 330 nm is related to the  $F^+$  centres and the peak at 430 nm is associated with the emission of F centres [Kortov, 2017]. The F and  $F^+$  centres are oxygen vacancies with two and one trapped electron respectively [Moroño, 1997].



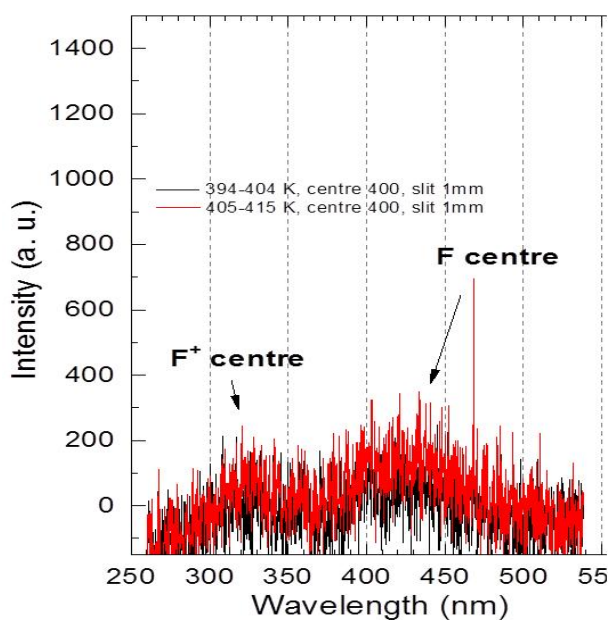


(a)

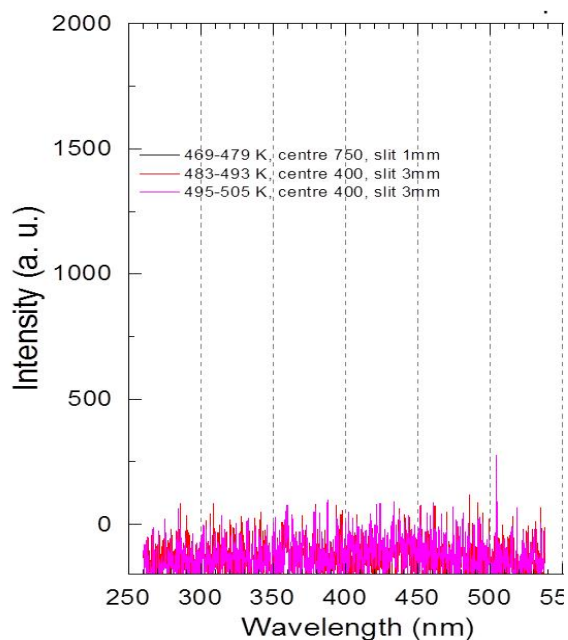


(b)

**Figure 4.32:** Emission spectra for different temperature intervals of the main TSL peak from (a) 372 K to 470 K and (b) 490 K to 547 K in 10 K interval width for the milky sample.



(a)



(b)

**Figure 4.33:** Emission spectra for different temperature intervals of the main TSL peak from (a) 394 K to 415 K and (b) 470 K to 505 K in 10 K interval width for the non-milky sample.

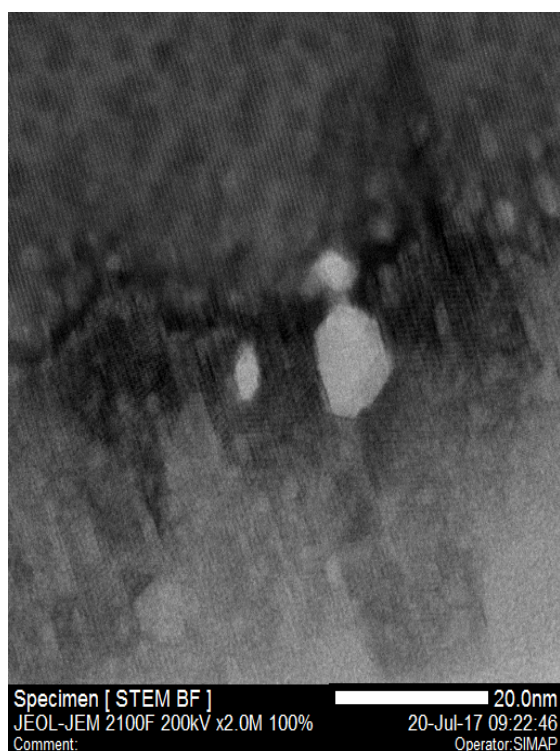
Thus it can be derived from the results of the TSL glow curve and the contributing emission spectra that the peaks observed at 415 K in figure 4.31 are due to the presence of oxygen vacancies. The higher peak intensity for the milky sample shows that there is the presence of a higher concentration of oxygen vacancies in the milky defect zone than in the non-milky zone.

#### 4.6.2 TEM analysis

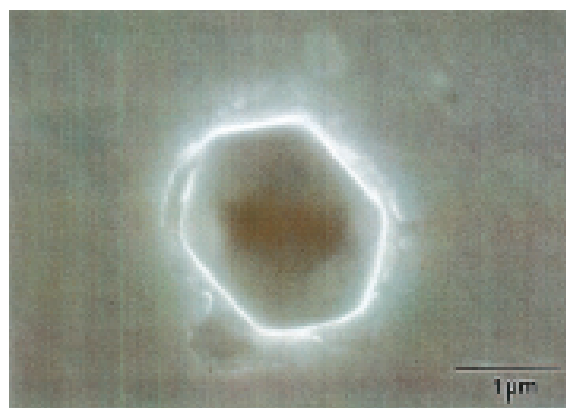
TEM microscopy analysis was carried out on 3 samples prepared by FIB polishing. Two samples were prepared from the milky defect zone and one sample from the non-defect zone. Many small pits like features in the range of 1nm to 5 nm were observed in samples from both the zones. But the nature of these features could not be determined and did not show any special features in the milky defect sample. One interesting observation was a faceted shape feature in one of the milky defect samples as shown in figure 4.34(a). It is comparable in feature with respect to the distinct hexagonal faceted shape of a pore along the A-plane in an annealed sapphire sample as shown in figure 4.34(b) [Kitayama, 2004] and to the vacancy void formation as shown in figure 1.22 in chapter 1. But it is to be noted that the scale of dimensions of the feature we observed are in nm while those in figure 4.34(b) is in  $\mu\text{m}$ .

Thus we could possibly explore the possibility of formation of voids in the milky defect region in the range of few nm, but the TEM images do not sufficiently support this hypothesis, since we see only one such feature in one of the defect samples. It is to be noted that the image width with TEM analysis is only around  $100\text{nm} \times 100\text{nm}$  and hence it is possible we do not come across more such features in our limited analysed images.





(a)



(b)

**Figure 4.34:** (a) TEM microscopy image showing a faceted feature in the milky defect sample, and (b) SEM image of  $2\mu\text{m} \times 2\mu\text{m} \times 0.37\mu\text{m}$  pore exposed parallel to the  $a$ -plane undoped sapphire after 80 h at  $1800^\circ\text{C}$  [Kitayama, 2004].

#### 4.6.3 SAXS

Small-Angle X-ray Scattering is an experimental technique that allows measuring some characteristics of the fluctuations of the scattering factor due to fluctuations of atomic number. Thus it is used to extract information on the size and volume fraction of precipitates in the sample.

A preliminary examination was carried out on a sample from the milky defect zone 30 microns in thickness and with a diameter of 2 mm. The plot of scattering intensity against the scattering vector is presented in figure 4.35. A first approximation from this plot after applying various fits and estimates gives a rough approximation of the dimensions of precipitates expected inside the sample [De Geuser, 2012].

The observation of a small angle scattering signal demonstrates the presence of heterogeneities of electron density. For small scattering vector, the intensity follows a  $1/q^4$  behaviour which is known as the Porod law [Glatter, 1982]. It is characteristic of the contribution of objects which are larger than the maximal observable features in this configuration, i.e.  $\sim 10\text{nm}$ . In addition, there is a comparatively weak

contribution of objects in the 1.5nm range, which give rise to a deviation from the low q behaviour for q higher than  $0.1\text{\AA}^{-1}$ .

To have a more reliable analysis, it will be needed to have a mapping over a greater area of sample and see for differences in signals within the milky defect zone and outside it.

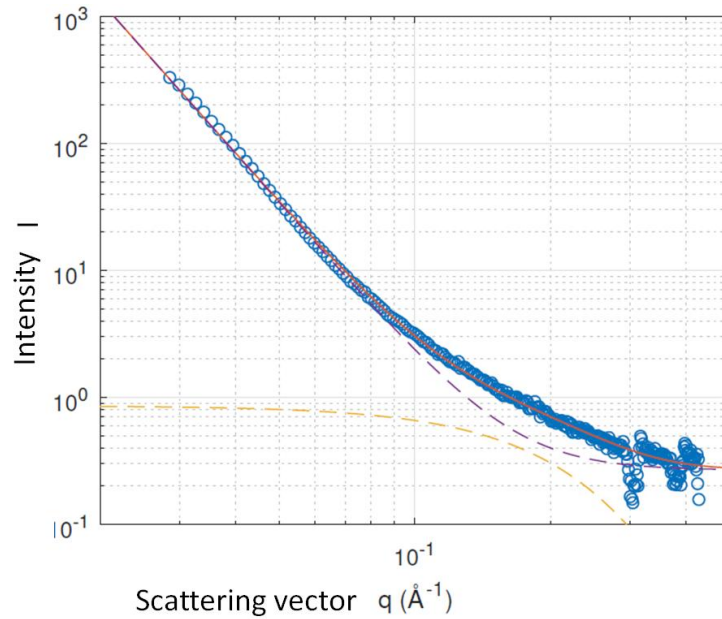
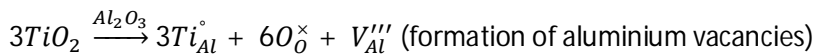
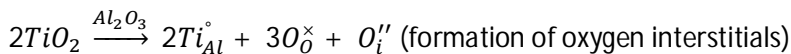
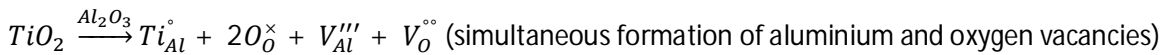


**Figure 4.35:** SAXS plot for a sample from the milky defect zone.

#### 4.6.4 Point defects formation

High-temperature growth of sapphire crystals in a crystallisation chamber composed of graphite and molybdenum elements takes place in a reducing atmosphere. This leads to the surface reduction of sapphire by carbon oxides and hence gives rise to the generation of oxygen vacancies [Borodin, 1990]. Additionally, in the case of Ti-doped sapphire with low concentration of  $\text{Ti}^{4+}$  there is simultaneous formation of both aluminium and oxygen vacancies [Rasmussen, 1970].

When alumina is doped with  $\text{TiO}_2$ , Ti ions can be incorporated into the lattice according to either of the following reactions [Reddy, 1982] [Lagerlof, 1989] [Rasmussen, 1970]:



Point defects in oxides have a strong columbic binding, due to their generally large charge. Hence, there is the possibility of formation of clusters and complexes of point defects in  $\text{Al}_2\text{O}_3$  [Mitchell, 1979].

#### 4.6.5 Interaction between point defects and dislocations

A dislocation is generally subjected to a climbing force normal to its slip plane when the point defect concentration in the immediate vicinity of the dislocation is not in local equilibrium with the defect sources and sinks on the dislocation. Point defects (vacancies or interstitials) may be absorbed at a dislocation, and the dislocation climbs in an attempt to establish local equilibrium by absorbing the point defect [Thomson, 1962].

In a simple climb process of a pure edge dislocation as shown in the figure 4.36, the dislocation core can be represented by the edge of an extra edge where point defect (vacancy) may be incorporated. In the climb process, the point defect move toward the dislocation from the lattice under the effect of the elastic lattice deformation around the dislocation, diffuse along the core, and are finally absorbed there.

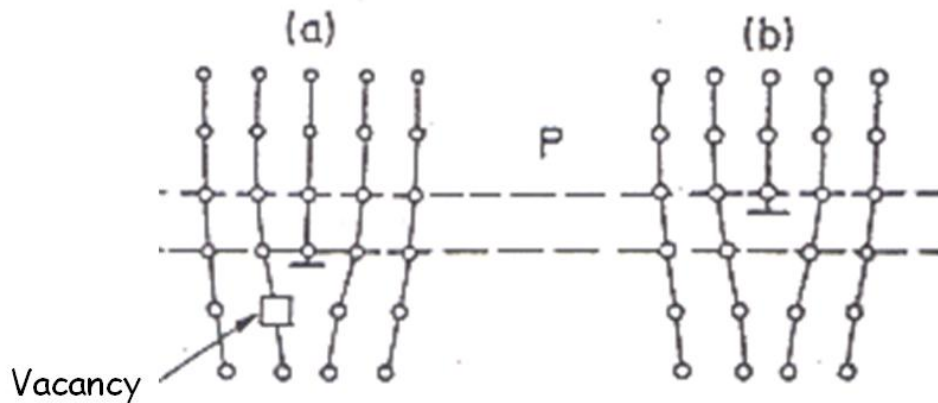


**Figure 4.36:** (a) Vacancy site in a crystal lattice next to a pure edge dislocation and (b) climb of the dislocation by migration and annihilation of the vacancy site [Thierry Duffar, Grenoble-INP course lecture].

In  $\text{Al}_2\text{O}_3$ , it has been established that oxygen vacancies diffuse 1000 times slower than the aluminium vacancies in the high-temperature range [Lagerlof, 1989] [Mitchell, 1979] [Pletka, 1977]. In the case of titanium doped  $\text{Al}_2\text{O}_3$ , it has been noticed that the oxygen vacancy diffusion decreases further [Lagerlof, 1989] [Haneda, 1989] [Reddy, 1982]. Thus, it can be assumed that aluminium vacancies diffuse much more easily than oxygen vacancies towards dislocations and get dissipated leaving a surplus of oxygen vacancies compared to aluminium vacancy in the lattice. In the case of a region with low dislocation density as observed in our samples with milky defect zone, where there are not many sinks available for diffusion of the slower diffusing oxygen vacancies they can bind together and form aggregates.

The phenomenon of aggregation of point defects like oxygen vacancies can be explained with the help of the image presented in figure 4.37. If a system is considered with 'N' number of vacancies of volume 'V<sub>vac</sub>', with the formation energy of each vacancy being 'E<sub>vac</sub>' distributed homogenously as shown in figure 4.37(a) the total energy of the vacancies in the system is N.E<sub>vac</sub>. But if vacancy concentration in the system increases beyond a critical value, N<sub>critical</sub>, it can be demonstrated that the total energy of the system is reduced by aggregation of the vacancies into a sphere thus favouring formation of a void as shown in figure 4.37(b).

The critical value for the vacancy concentration for aggregation into a micro-void is given by:

$$N_{critical} = \left(\frac{\sigma_{sv}}{E_{vac}}\right)^3 36\pi(V_{vac})^2$$

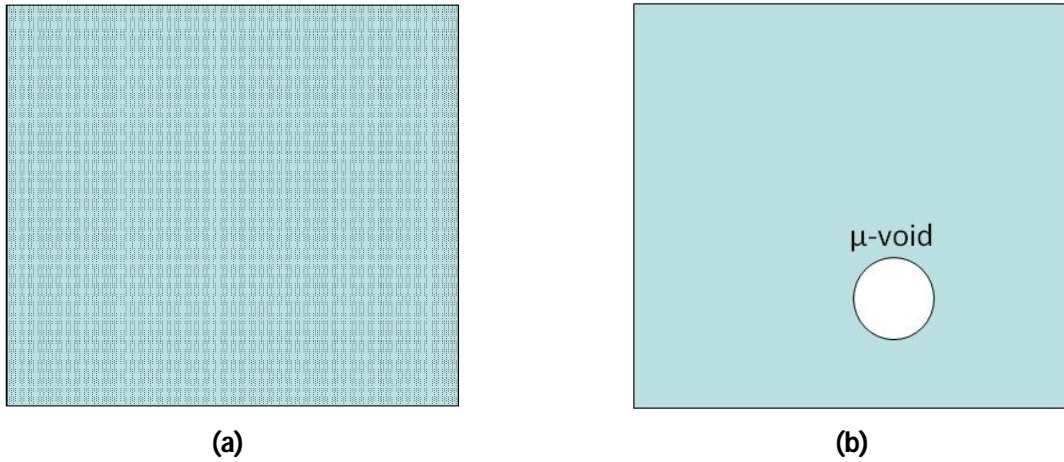


**Figure 4.37:** (a) System with 'N' number of vacancies uniformly distributed. (b) System with aggregation of 'N' number of vacancies to form a single micro-void [Thierry Duffar, Grenoble-INP course lecture].

## 4.7 Discussion

Herein, we summarise the results of all the characterisation efforts on the samples and try to link together a series of hypotheses to explain the nature of the milky defect zone and its origin.

### 4.7.1 Observations

1. The milky defect-zone is always oriented along the C-plane and passes through the centre.
2. There is a directional diffusion of laser light in this milky defect.
3. The dislocation density in this milky defect zone is much lower than the rest of the non-defect zone and there is a sharp transition between the two regions.
4. The dislocations in the milky defect zone are due to the basal slip of the C-plane.

5. Stress calculations suggest a low stress zone along the C-plane corresponding to the milky defect zone for basal slip occurrence (to be confirmed further).
6. The milky-defect zone has a higher concentration of oxygen vacancies than the non-defect zone.
7. There could be the formation of nanometric voids in the milky defect zone (to be confirmed further).

#### 4.7.2 Bibliographic references

Evidence for sub-micrometer inclusions in titanium doped sapphire crystals grown by Czochralski technique along the A-axis has been reported earlier and they have been found to form colonies oriented along the C-plane as shown in figure 4.37(a) [I. V. Kryvonosov, 2012] [Vyshnevskiy, 2006]. Interestingly, evidence for faceted voids in the range of 20 nm – 30 nm arranged along the C-plane has also been reported for undoped sapphire crystals grown by the EFG technique as shown in figure 4.38(b) [Borodin, 1990]. In both these cases, the voids have been determined to be formed due to high concentration of oxygen vacancies generated by the reducing atmosphere in the furnace formed of carbon containing elements.

In the case of undoped sapphire crystals grown by the HEM technique there are interferogram images for the A-plane discs which show a linear band of perturbed wave transmission not observed in the C-plane or M-plane discs as shown in figure 4.39(a) [Smith, 1999]. Interferogram for the titanium doped sapphire samples prepared during this project also show a similar band of perturbed wave transmission as shown in figure 4.39(b). Although the orientation of the this linear perturbed band is not mentioned in Smith's paper, in these two analyses it passes exactly through the centre and it is possible that it is oriented along the C-plane and is an effect of a milky defect as observed in our samples.

Another interesting case which is similar to the milky defect in our case has been reported as 'Haze' for undoped sapphire crystals grown by the SAPMAC method as shown in figure 4.40. The haze appears in the central region of the crystal between the top shoulder and the bottom base and seems to be oriented along a central plane. In this case the haze has been reported to be constituted by CO<sub>2</sub> bubbles in the range of 10-100 µm, but no explanation has been provided for the evident alignment of this haze structure [Zhang, 2011-b]. This suggests that the milky defect zone occurrence may not be exclusive to just titanium doped sapphire crystals.

Thus even though there is not a very conclusive evidence yet for the presence of voids from the TEM analysis or the SAXS analysis, the results along with reported references allows to raise the hypothesis for the presence of colonies of faceted voids with dimensions of few nanometers along the C-plane giving rise to the milky-defect zone. Since similar phenomenon has also been observed in undoped sapphire crystals,

it can be deduced that titanium doping is not a factor for this defect regime. But it is possible that titanium doping enhances the mechanism of oxygen vacancy generation and void formation and also the red colour it imparts to the crystal just enhances the visibility of this defect. In figure 4.5 the demonstration of the phenomenon that the diffusion of the laser light observed in the milky defect zone is sensitive to the sample orientation can be explained by the phenomenon of Tyndall scattering of light from these sub-micrometer size inclusions which are non-spherical in shape [Vyshnevskiy, 2006].

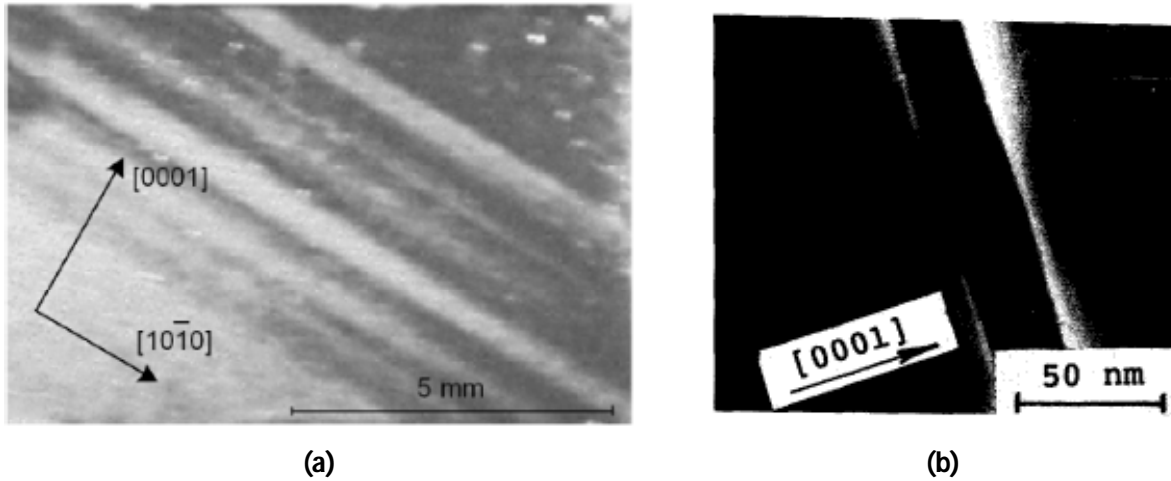


**Figure 4.38:** (a) Striate-like distribution of sub-micron inclusions in Ti-sapphire [Vyshnevskiy, 2006], (b) SEM micrograph of the transverse section of vacancy void in undoped sapphire.

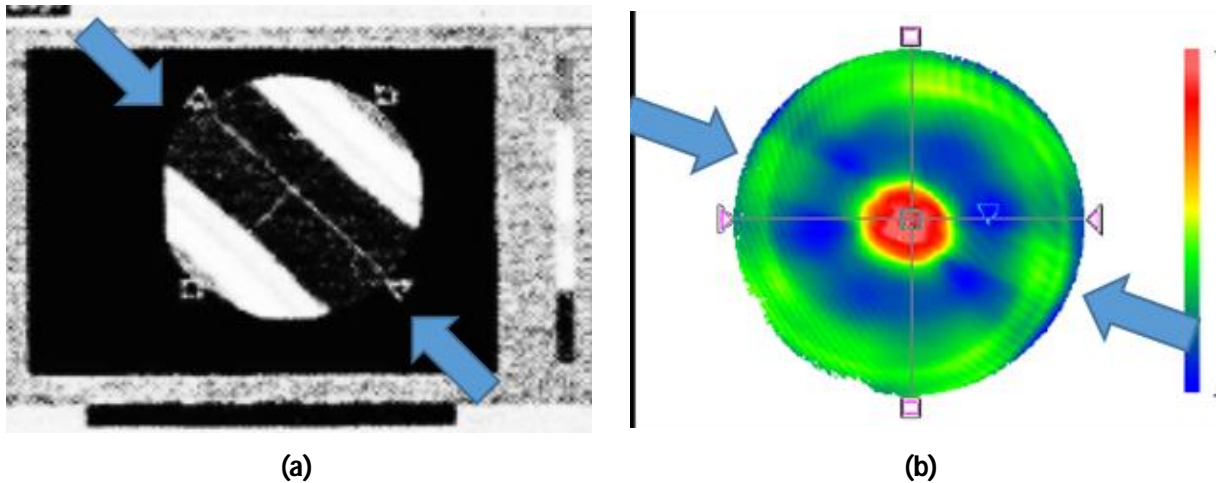


**Figure 4.39:** (a) Interferogram of an A-plane disc sample cut and polished from an undoped A-axis grown sapphire crystal by HEM method. [Smith, 1999] (b) Interferogram showing the wave front propagation after passing through the bulk of the sample for an A-axis oriented sample from Ti-sapphire crystal.





**Figure 4.40: (a) (b):** Distribution of haze in sapphire crystals grown by SAPMAC method [Zhang, 2011-b].

#### 4.7.3 Best-fit hypothesis

Thus taking into account all the available data from the characterisation efforts, the thermal stress simulation and the available literature the following hypotheses for the mechanism of formation of this milky defect can be proposed:

1. The crystal grows at very high temperature in a furnace composed of many carbon-containing structures.
2. This creates a reducing atmosphere in the furnace and hence leads to formation of oxygen vacancies throughout the growing crystal. Ti doping may enhance this production.
3. During the growth of crystal there is thermal stress acting on the crystal which can give rise to dislocations.
4. The thermal stresses responsible for dislocation generation are lower in a band along the C-plane passing through the centre than in the rest of the sample.
5. The critical resolved shear stress required for basal slip is not reached in this region along the C-plane and hence there are very few dislocations in this region compared to the rest of the crystal.
6. The dislocations acts as sinks for the point defects and hence attract most of the oxygen vacancies in the crystal.
7. But, since there are very few dislocations in the region along the central C-plane there are not enough sinks for the oxygen vacancies in this region.
8. The oxygen vacancies in this region start to bind together and aggregate to form voids.
9. Thus, the concentration of these voids is inversely proportional to the dislocation density and hence to the stress.

10. These voids take the shape of the negative crystal and get faceted and oriented.
11. Tyndall scattering of light from these voids oriented along the central C-plane gives the milky-defect.

A schematic representation of the proposed hypothesis for the milky-defect formation is presented in figure 4.41.

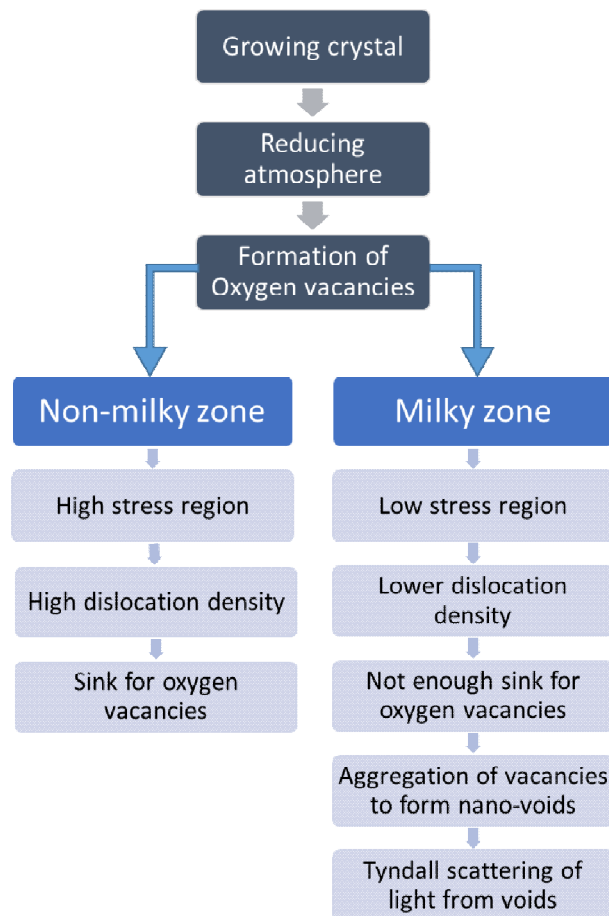


**Figure 4.41:** Scheme to describe the mechanism for formation of the milky-defect zone.

## 4.8 Conclusion

At the moment, the succession of the phenomena described is the best fit hypothesis for the explanation of the milky defect as it aggregates and satisfies most of the observations. However, it is not ascertained at all and cannot be taken to be the theoretical explanation for the defect formation. Hence there is a need for further characterisation and analysis for the samples.



It is required to do a quantitative analysis of the laser light diffusion by the milky defect for the phenomenon described in figure 4.5. From these measurements, it would be possible to calculate the dimensions of the features responsible for the diffusion of light and understand their shape factor with respect to the principle of Tyndall scattering [Vyshnevskiy, 2006]. It is also desired to study the dislocation structure in a single 3D frame possibly by chemical etching techniques to better understand their peculiarities in the milky defect and non-defect zone.

It is important to simulate numerically the thermal stress evolution during the complete crystal growth process and then check for zones with lower than critical resolved shear stress corresponding to the milky defect zone. To confirm the presence of possible voids in the milky defect zone a much more detailed SAXS measurement and mapping around the transition zone between the defect and non-defect zone is required. Also, quantitative data for the  $\text{Ti}^{4+}$  concentration will be important to check for its contribution to the vacancy formation mechanism.

It should also be noted that Carmen Stelian has proposed a different explanation for the formation of this milky defect that is presented in Appendix II. It is based on the variation of refractive index with the Ti concentration, birefringence and polarization phenomena. While it is not always consistent with the evident volume phenomenon observed in the light diffusion experiments, and is not applicable to undoped samples, it is reasonable to believe that such birefringence and polarization effects could be introduced in the explanation of the milky defect, which is observed much better in Ti doped sapphire samples.

# Conclusion

## Summary

Due to the increasing demand for  $\text{Ti:Al}_2\text{O}_3$  crystals for high power laser applications the project TITANSaphir was conceived to supply discs with dimensions of more than 20 cm in diameter. A detailed study of all the growth processes suitable for bulk crystal growth with their advantages and disadvantages was carried out and it was evident that the Kyropoulos growth was the most suitable for growth of crystals with large dimensions and low defect concentration.

As a part of this project, for this thesis, research work was carried out to make improvements in the growth process and understand the defects affecting the optical quality of the crystals.

At the company RSA le Rubis the Kyropoulos growth system was already established for the growth of crystals weighing up to 30 kg, but the quality of crystals obtained was not acceptable as the one shown in figure 5.1 (a). The crystals did not grow with a constant diameter and there were severe deformities which led to many defects such as bubbles and cavities. So for these crystals, a detailed study for the evolution of the growth parameters during the whole growth process was carried out and a relation between the crystal morphology and the growth parameters was established. An ideal set of growth parameters which would allow growth of crystals with desired shape was suggested. Crystals were grown by following these ideal parameters and there was an evident improvement in the shape and quality of the crystals as shown in figure 5.1 (b).



(a)



(b)

**Figure 5.1:** (a) Crystal with severe deformities and (b) crystal with desired shape.

Discs cut from the grown crystals were checked for optical homogeneity and a radially increasing titanium concentration from the centre to the edges was revealed using luminescence and absorption profiles. Experiments were conducted in which crystals were extracted during the early growth stages. This revealed the conical shape of the solid-liquid growth interface and hence it explains the radial profile of titanium concentration due to chemical segregation.

The Kyropoulos growth process is very slow and it takes up to 30 days to grow a crystal weighing 30 kg. In spite of the already existing control system, it requires regular operator supervision to monitor its growth and detect any variation from desired growth conditions. Up to now there has been no system which can allow the operator to visualise the growing crystal's shape during the growth process and hence an attempt was made to address this problem. A detailed study of all the forces acting on the growing crystal during its growth which contribute to the measured weight was done and a relation between the crystal radius and the measured parameters was established. This required the system to have the capability of measuring an additional parameter, which to our idea, could be the melt height during the crystal growth, which is not currently available. A mathematical demonstration was presented for a simulated crystal shape which showed that by knowing the measured parameters including the liquid melt height it is possible to estimate the crystal radius at the solid-liquid-gas triple point at each time step and hence reconstruct the crystal shape. This opens up the interesting possibility of building a system which would allow accurate monitoring of the growing crystal shape and hence automation of the Kyropoulos growth system. However it was shown that realistic application would be restricted to the cylindrical growth at full crystal diameter.

The discs prepared from crystals of good quality present a defect passing diametrically through the centre, called the 'milky defect'. This defect zone diffuses light and affects the laser efficiency in the otherwise acceptable samples. Thus, it is of great interest to understand the nature and origin of this defect zone. Samples were prepared which were representative of this defect zone and the non-defect region, and a series of characterisation measurements were done on these samples starting with white beam topography and rocking curve imaging at the European Synchrotron Radiation Facility (ESRF). These analyses revealed a low dislocation density in all the samples suggesting good crystalline quality, but interestingly at the defect zone there was a very sharp drop in the dislocation density compared to the non-defect zone around. Thermo-mechanical simulations of the Kyropoulos furnace configuration suggested a low stress region along the C-plane passing through the centre which corresponds to the defect zone and hence could explain the low dislocation density in this defect. Thermo luminescence analysis showed an increased number of oxygen vacancies for the defect zone, and a preliminary Small Angle X-ray Scattering experiment revealed the presence of some features with dimensions of around 2 nm in the defect zone. TEM images

from one of the defect zone samples detected a faceted void measuring about 5nm. These results from the characterisation analyses led to a hypothesis which explains the relation between the low stress region in the milky zone and formation of nanometric voids by aggregation of oxygen vacancies which leads to the scattering of the light leading to the visible milky defect. This is just a preliminary guess for the mechanism of the defect formation and more studies have to be carried out in order to completely justify this hypothesis.

## Perspectives

The Kyropoulos growth process at RSA le Rubis company is well established and has been demonstrated to be capable of the growth of crystals with dimensions greater than 20 cm. But the phenomenon of segregation of titanium coupled with the conical interface of the growing crystal leads to a radially varying profile of the titanium concentration in the discs prepared for laser applications. But, for laser applications a constant concentration of titanium concentration is desired in the prepared discs.

Up to now, the discs have been cut from the crystal perpendicular to the A-axis which corresponds to the pulling direction. One solution to improve the Ti segregation profile in the discs would be to cut discs perpendicular to the two other available A-axis directions as shown in figure 5.2 (b), since, the growing crystal interface approximately corresponds to the normal direction of these A-axes as shown in figure 5.2 (a). This would change the segregation profile from a radial one as shown in figure 5.2 (c) to the one as shown in figure 5.2 (d). This proposed solution is yet to be tested, but it could prove to be a very cost-effective method of improving the Ti segregation problem although it does not completely eliminate it.

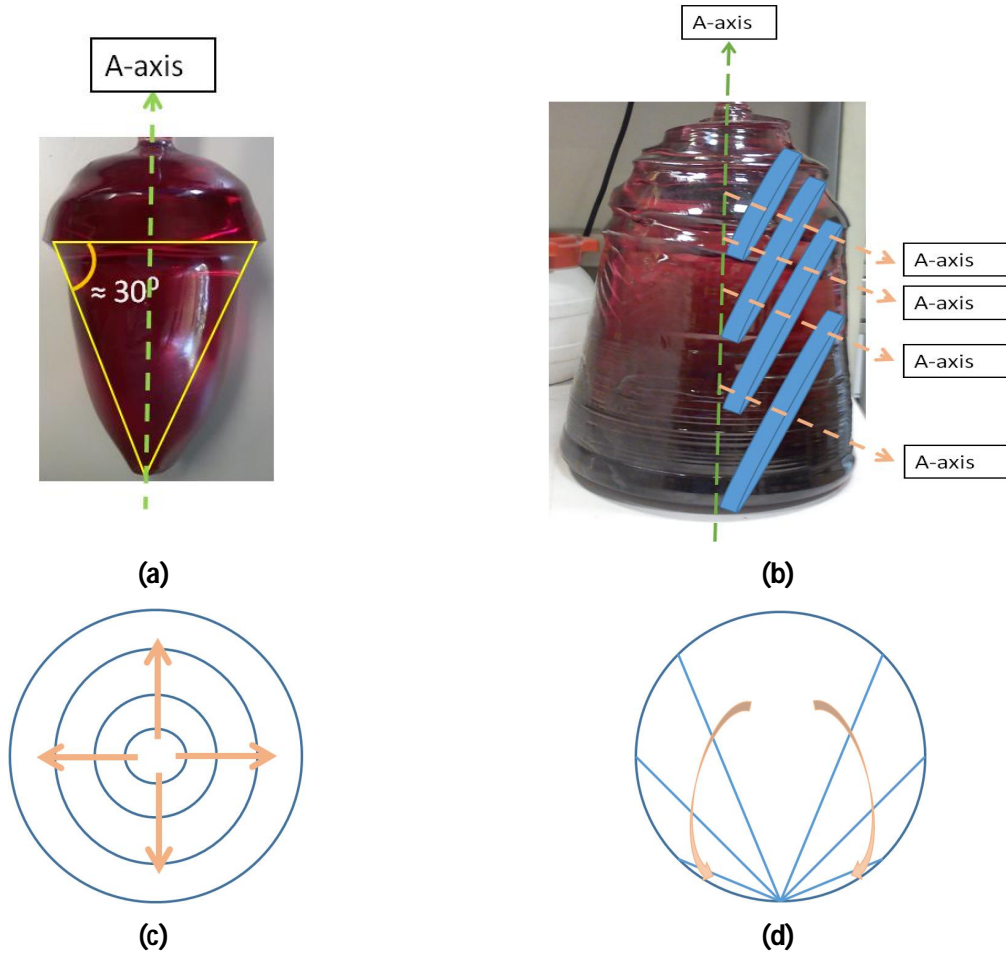


**Figure 5.2:** **(a)** Crystal growth interface during initial growth stages. **(b)** Proposed idea to cut discs normal to A-axis other than along the pulling direction. **(c)** Radial segregation profile of Ti in discs cut perpendicular to the pulling direction. **(d)** Expected segregation profile of Ti in discs cut along the A-axis as proposed in figure 5.2 (b). **(c), (d)** Arrows point to the trend of increasing Ti concentration.

Also, it is very interesting to understand the quantitative values of the titanium ions in its  $\text{Ti}^{3+}$  and  $\text{Ti}^{4+}$  oxidised states in the crystal, because  $\text{Ti}^{4+}$  ions are detrimental to the laser performance. We currently have a qualitative estimate of the distribution profile for them from absorption profiles [Guillaume Alombert-Goget, 2017], but the possibilities of EPR techniques and SQUID magnetometry could be explored to find a quantitative estimate for  $\text{Ti}^{3+}$  and  $\text{Ti}^{4+}$  in the samples [Benmessai, 2013] [Farr, 2013]. These values in turn could be used to calibrate the absorption profiles and use them for quantitative estimates in the future.

A mathematical system has been developed and presented in Chapter 3 which would help us to reconstruct the shape of the growing crystal. But this method is not restricted to crystals and can be applied to any system consisting of a solid body submerged in a liquid. Hence, it would be very interesting to build a

working experiment which would help validate this mathematical model. It would consist of a weighing balance from which an axisymmetric body with known geometry is submerged in a liquid and a tool capable of measuring the liquid level which feeds the required input parameters to the mathematical model. The mathematical model can then give the output for the calculated radius at the melt interface and it can be compared to the known geometry, thus validating the model as shown in figure 5.3. The simplest solid-melt system for such an experiment would be water and some equivalent density polymer like PVC or PMMA which can be fabricated easily. The physical properties for such materials like density, contact angle etc are easily available and hence can be substituted for the sapphire properties in the mathematical model already developed. The next step would be to take this configuration inside an existing Kyropoulos furnace by just retrofitting the melt level measurement tool and checking the mechanism at ambient temperature conditions. Finally, when the system is proved to be reliable, it could be adapted for service during the actual crystal growth under high temperature conditions.

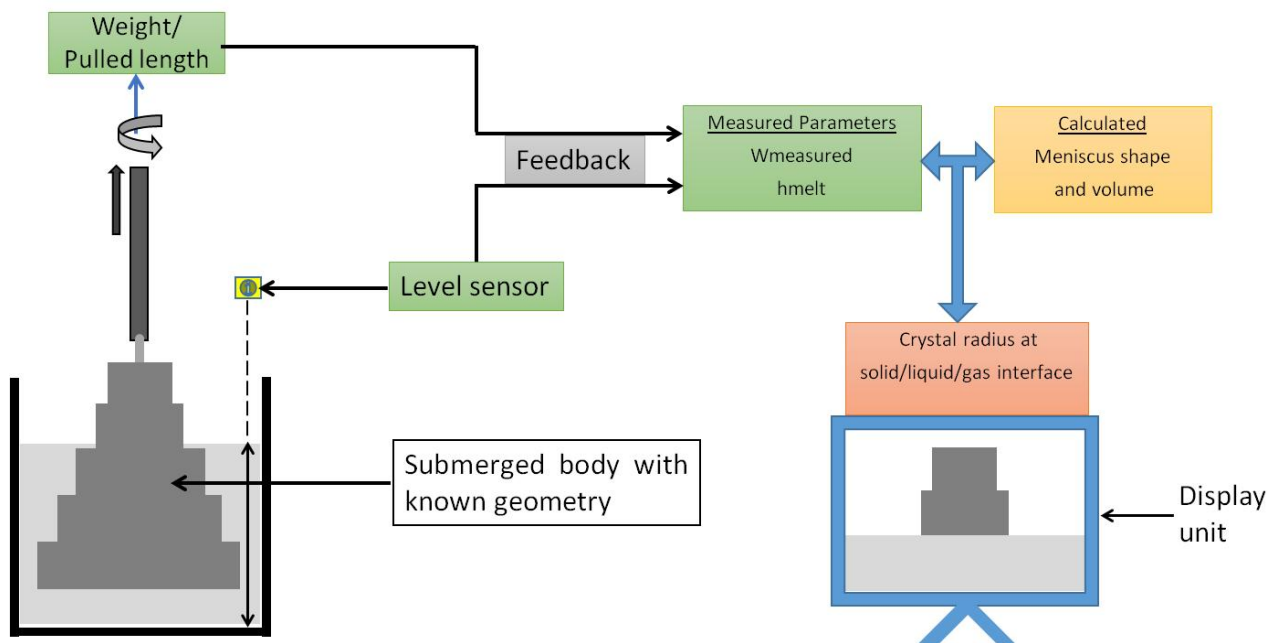


**Figure 5.3:** A system to validate the mathematical model of reconstruction of an axisymmetric submerged body.

The milky defect has been studied in great detail by performing various characterisation techniques on the samples and comparing with available literature. But to better understand the nature of the defect zone, some of the characterisation techniques have to be carried out again on more samples and much more extensively to be sure that the results are representative of the actual phenomenon and not some aberrations that we came across. X-ray white beam topography and Rocking curve imaging have been used

to study the dislocation patterns in our crystals, which help in obtaining a lot of quantitative data for comparison. But mostly these allow for a representation of the features corresponding to a few particular crystallographic planes at once and hence it is difficult to realise the 3D structure and the interacting features. To get over this problem, it could be possible to carry out chemical etching for the samples using various combinations of orthophosphoric acid ( $\text{H}_3\text{PO}_4$ ) [Alford, 1963] [Scheuplin, 1960], sulphuric acid ( $\text{H}_2\text{SO}_4$ ) [Marasina, 1982], hydrochloric acid (HCl) and nitric acid ( $\text{HNO}_3$ ) [Xiao, 2004] and study them under optical and SEM microscopes which would reveal the dislocation structures on the whole crystal cross section at once. Similarly, detailed SAXS mapping could be carried out on the samples to look for any sharp variation at the transition between the milky defect and non-defect zone which would suggest the presence of nanometric voids. Finally, stress calculations using the simulation model have to be carried out in time-dependant mode during the whole growth process and for various locations to ascertain the presence of a low stress zone which would lead to low dislocation density corresponding to the milky defect regions. All these results together would help prove or improve the proposed hypothesis for the mechanism of formation of this milky defect.

# Appendix I: Crystal morphology analysis

Herein, we present a detailed analysis for the morphology of all the crystals grown in the configuration no.4 at RSA. The crystals described here have been referenced in Chapter 2.



K04-04-14

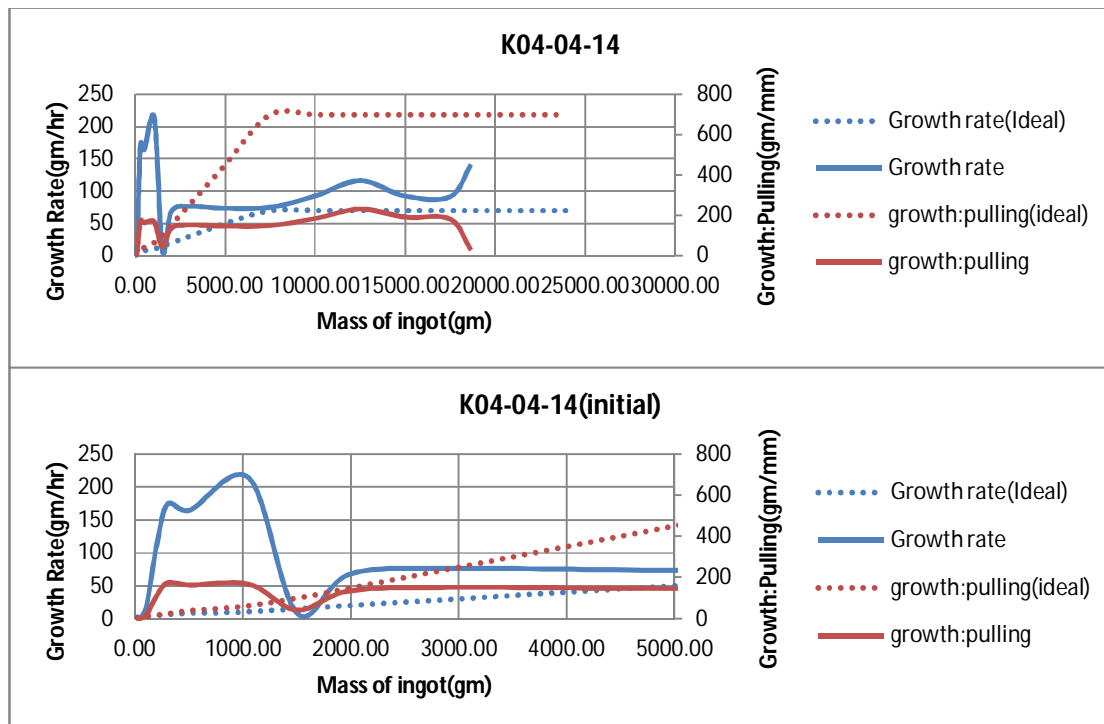


Figure I.1: Top view and side view of crystal K04-04-14 weighing 18.6 kg.

### Crystal Morphology

- 1) Conical head formation till 15 mm. [1] [4] [7]
- 2) Small diameter flat plate. [2] [5] [6] [8]
- 3) Plate without milky layer beneath. [2] [5] [6] [8]
- 4) Big Cavity below plate at 50mm from seed. [3] [9]
- 5) Overall uneven crystal shape with changes in diameter throughout the height. [2] [5] [8] [10]

k04-04-14																	
time	mass	time diff	Growth rate	raz crist	(nSeed posi	posn diff	pulling rate	températi	Temp diff	temp rate	puissance	power dif	power rate	temp. pow	growth.pl	Growth:T: growth.ps	growth:ps
hr	gm	hr	gm/hr	mm	mm	mm	mm/hr	°C	°C	°C/hr	%	%	%/hr	C/power%	gm/mm	gm/°C	gm/power%
0.02	13.40			-52.38	0.00			2080.00			38.00						
22.44	20.00	22.43	0.29	-42.73	9.65	9.65	0.43	2081.00	-1.00	-0.04	37.64	0.36	0.0161	-2.78	0.68	-6.60	18.33
34.06	50.10	11.61	2.59	-31.57	20.81	11.16	0.96	2081.00	0.00	0.00	37.46	0.18	0.0155	0.00	2.70	#DIV/0!	167.22
36.98	100.60	2.92	17.30	-28.65	23.73	2.92	1.00	2081.00	0.00	0.00	37.42	0.04	0.0137	0.00	17.29	#DIV/0!	1262.50
37.85	202.50	0.88	115.91	-27.77	24.61	0.88	1.00	2084.00	-3.00	-3.41	37.41	0.01	0.0114	-300.00	115.80	-33.97	10190.00
38.42	300.70	0.56	174.06	-27.21	25.17	0.56	0.99	2086.00	-2.00	-3.55	37.40	0.01	0.0177	-200.00	175.36	-49.10	9820.00
39.65	502.40	1.23	164.32	-25.98	26.40	1.23	1.00	2089.00	-3.00	-2.44	37.38	0.02	0.0163	-150.00	163.98	-67.23	10085.00
42.25	1055.80	2.60	212.48	-22.67	29.71	3.31	1.27	2090.00	-1.00	-0.38	37.40	-0.02	-0.0077	50.00	167.19	-553.40	-27670.00
97.39	1500.70	55.14	8.07	-12.18	40.20	10.49	0.19	2083.00	7.00	0.13	37.34	0.06	0.0011	116.67	42.41	63.56	7415.00
104.71	2000.40	7.32	68.31	-8.52	43.86	3.66	0.50	2082.00	1.00	0.14	37.26	0.08	0.0109	12.50	136.53	499.70	6246.25
117.79	3000.00	13.09	76.37	-1.97	50.41	6.55	0.50	2080.00	2.00	0.15	37.13	0.13	0.0099	15.38	152.61	499.80	7689.23
145.05	5000.30	27.26	73.39	11.66	64.04	13.63	0.50	2074.00	6.00	0.22	36.82	0.31	0.0114	19.35	146.76	333.38	6452.58
178.46	7500.80	33.41	74.84	28.37	80.75	16.71	0.50	2065.00	9.00	0.27	36.32	0.50	0.0150	18.00	149.64	277.83	5001.00
205.50	10000.20	27.04	92.44	41.90	94.28	13.53	0.50	2051.00	14.00	0.52	35.82	0.50	0.0185	28.00	184.73	178.53	4998.80
227.05	12501.10	21.55	116.06	52.68	105.06	10.78	0.50	2036.00	15.00	0.70	35.40	0.42	0.0195	35.71	231.99	166.73	5954.52
254.16	15000.60	27.11	92.20	65.75	118.13	13.07	0.48	2020.00	16.00	0.59	35.00	0.40	0.0148	40.00	191.24	156.22	6248.75
281.60	17500.20	27.44	91.10	79.48	131.86	13.73	0.50	2002.00	18.00	0.66	34.59	0.41	0.0149	43.90	182.05	138.87	6096.59
289.78	18653.60	8.18	140.97	121.50	173.88	42.02	5.14	2002.00	0.00	0.00	34.42	0.17	0.0208	0.00	27.45	#DIV/0!	6784.71



### *Growth Features*

#### **Growth Rate:**

Low initial growth rate values. (0g – 50g) [1]

High growth rate of crystal mass in the later stages of the growth process. (200g – 1000g) [2]

Sudden abnormal decrease in growth rate. (1500g) [3]

#### **Pulling Rate:**

Initial higher rates of pulling for seed. (0g – 50g) [4]

Too high pulling speed of seed for later stages. (300g – 17500g) [5]

#### **Temp:Power:**

High negative values. (0g – 500g) [6]

#### **Growth:Pulling:**

Low initial values. (0g – 50g) [7]

Higher values. (200g – 1000g) [8]

Sudden abnormal decrease. (1500g) [9]

Low values for later stages of growth process. (5000g – 2000g) [10]

K08-04-14

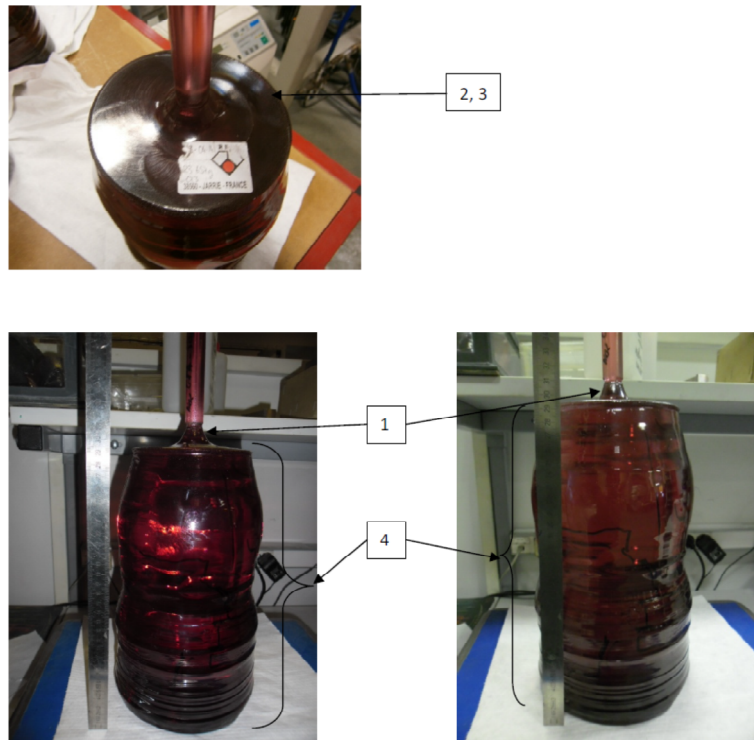
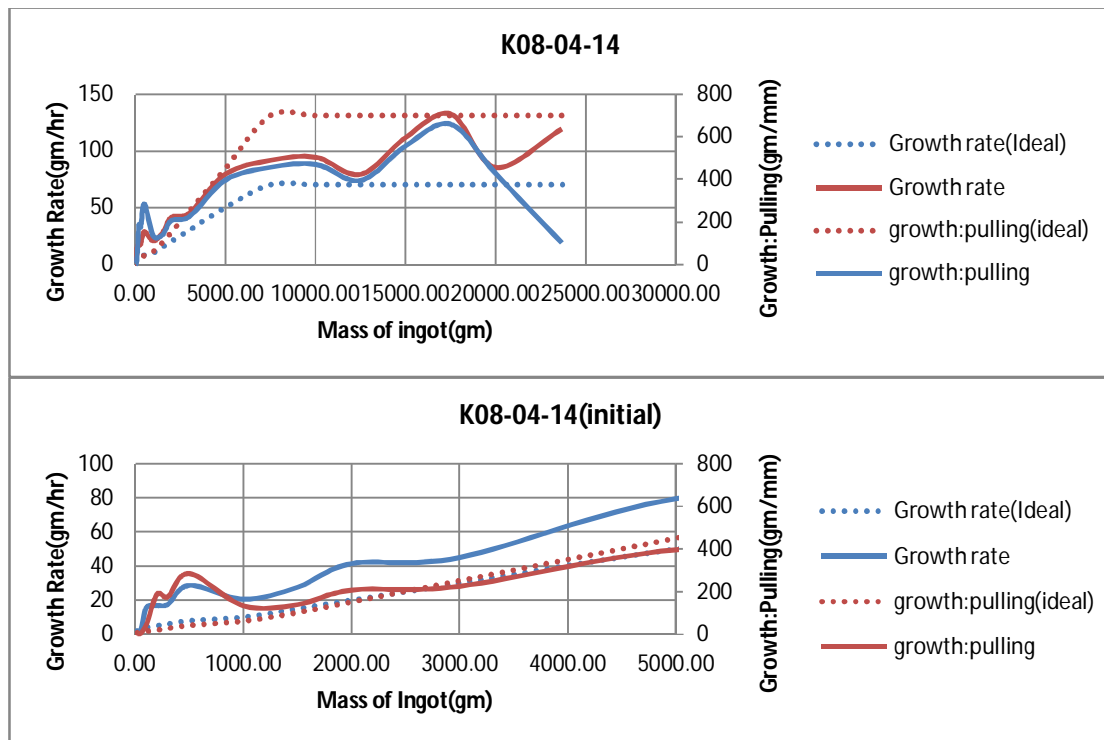


Figure I.2: Top view and side view of crystal K08-04-14 weighing 23.7 kg.

### Crystal Morphology

- 1) Conical head formation till 20 mm. [1] [4] [8]
- 2) Small diameter flat plate. [2] [5] [7] [9]
- 3) Plate without milky layer beneath. [2] [5] [7] [9]
- 4) Overall even crystal shape with uniform diameter throughout the height. [3] [6] [10]

k08-04-14																	
time	mass	time diff	Growth rate	crystal (r)	Seed posn	posn diff	pulling rate	températi	Temp diff	temp rate	puissance	power dif	power rat	temp.pov	growth:pi	Growth.T	growth:pi
hr	gm	hr	gm/hr	mm	mm	mm	mm/hr	°C	°C	°C/hr	%	%	%/hr	C/power%	gm/mm	gm/°C	m/power%
0.02	7.50			-10.05	0.00			2081.00			36.90						
18.25	20.00	18.23	0.69	-2.96	7.09	7.09	0.39	2077.00	4.00	0.22	36.76	0.14	0.0077	28.57	1.76	3.13	89.29
31.60	50.00	13.35	2.25	3.71	13.76	6.67	0.50	2074.00	3.00	0.22	36.63	0.13	0.0097	23.08	4.50	10.00	230.77
34.84	100.20	3.24	15.52	4.88	14.93	1.17	0.36	2076.00	-2.00	-0.62	36.67	-0.04	-0.0124	50.00	42.91	-25.10	-1255.00
40.73	200.10	5.89	16.96	5.41	15.46	0.53	0.09	2079.00	-3.00	-0.51	36.65	0.02	0.0034	-150.00	188.49	-33.30	4995.00
46.43	300.40	5.71	17.58	5.98	16.03	0.57	0.10	2079.00	0.00	0.00	36.61	0.04	0.0070	0.00	175.96	#DIV/0!	2507.50
53.37	500.00	6.93	28.79	6.68	16.73	0.70	0.10	2079.00	0.00	0.00	36.56	0.05	0.0072	0.00	285.14	#DIV/0!	3992.00
77.55	1000.00	24.19	20.67	10.42	20.47	3.74	0.15	2078.00	1.00	0.04	36.26	0.30	0.0124	3.33	133.69	500.00	1666.67
95.67	1500.40	18.12	27.62	14.02	24.07	3.60	0.20	2074.00	4.00	0.22	36.01	0.25	0.0138	16.00	139.00	125.10	2001.60
107.71	2000.60	12.04	41.53	16.43	26.48	2.41	0.20	2070.00	4.00	0.33	35.84	0.17	0.0141	23.53	207.55	125.05	2942.35
129.86	3000.50	22.15	45.15	20.86	30.91	4.43	0.20	2065.00	5.00	0.23	35.52	0.32	0.0144	15.63	225.71	199.98	3124.69
154.97	5001.20	25.12	79.66	25.89	35.94	5.03	0.20	2055.00	10.00	0.40	35.19	0.33	0.0131	30.30	397.75	200.07	6062.73
182.25	7500.10	27.27	91.62	31.35	41.40	5.46	0.20	2045.00	10.00	0.37	34.87	0.32	0.0117	31.25	457.67	249.89	7809.06
208.74	10001.80	26.49	94.43	36.66	46.71	5.31	0.20	2033.00	12.00	0.45	34.55	0.32	0.0121	37.50	471.13	208.48	7817.81
240.26	12501.30	31.52	79.30	42.98	53.03	6.32	0.20	2020.00	13.00	0.41	34.13	0.42	0.0133	30.95	395.49	192.27	5951.19
262.62	15002.00	22.36	111.82	47.46	57.51	4.48	0.20	2001.00	19.00	0.85	33.84	0.29	0.0130	65.52	558.19	131.62	8623.10
281.50	17502.10	18.88	132.42	51.25	61.30	3.79	0.20	1988.00	13.00	0.69	33.62	0.22	0.0117	59.09	659.66	192.32	11364.09
310.78	20001.30	29.28	85.35	57.11	67.16	5.86	0.20	1976.00	12.00	0.41	33.27	0.35	0.0120	34.29	426.48	208.27	7140.57
341.45	23664.80	30.67	119.46	93.29	103.34	36.18	1.18	1969.00	7.00	0.23	32.90	0.37	0.0121	18.92	101.26	523.36	9901.35



### Growth Features

#### Growth Rate:

Low initial growth rate values. (0g – 50g) [1]

High growth rate of crystal mass. (100g – 500g) [2]

Good values of growth rate for later stages of growth process. (1000g – 12500g) [3]

#### Pulling Rate:

Initial higher rates of pulling for seed. (0g – 100g) [4]

Too low pulling speed of seed for later stages. (200g – 500g) [5]

Low values of growth rate for later stages of growth process. [6]

#### Temp:Power:

Slight negative values. (200g – 500g) [7]

#### Growth:Pulling:

Low initial values. (0g – 50g) [8]

High values for later stages of growth process. (100g – 500g) [9]

Good values for later stages of growth process. (1500 – 17500) [10]

K09-04-14

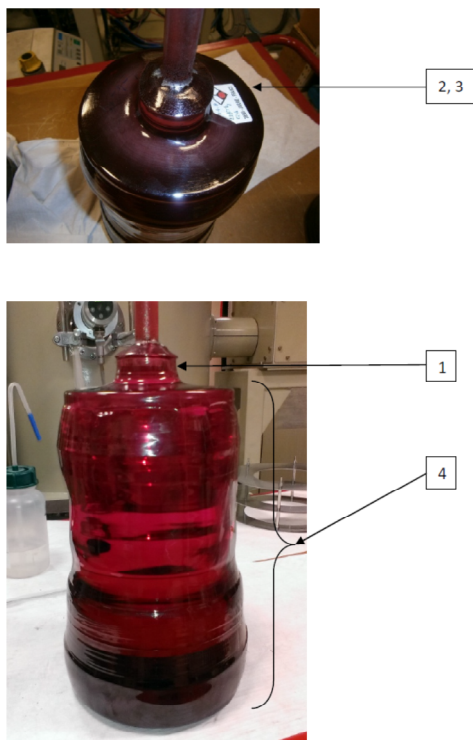
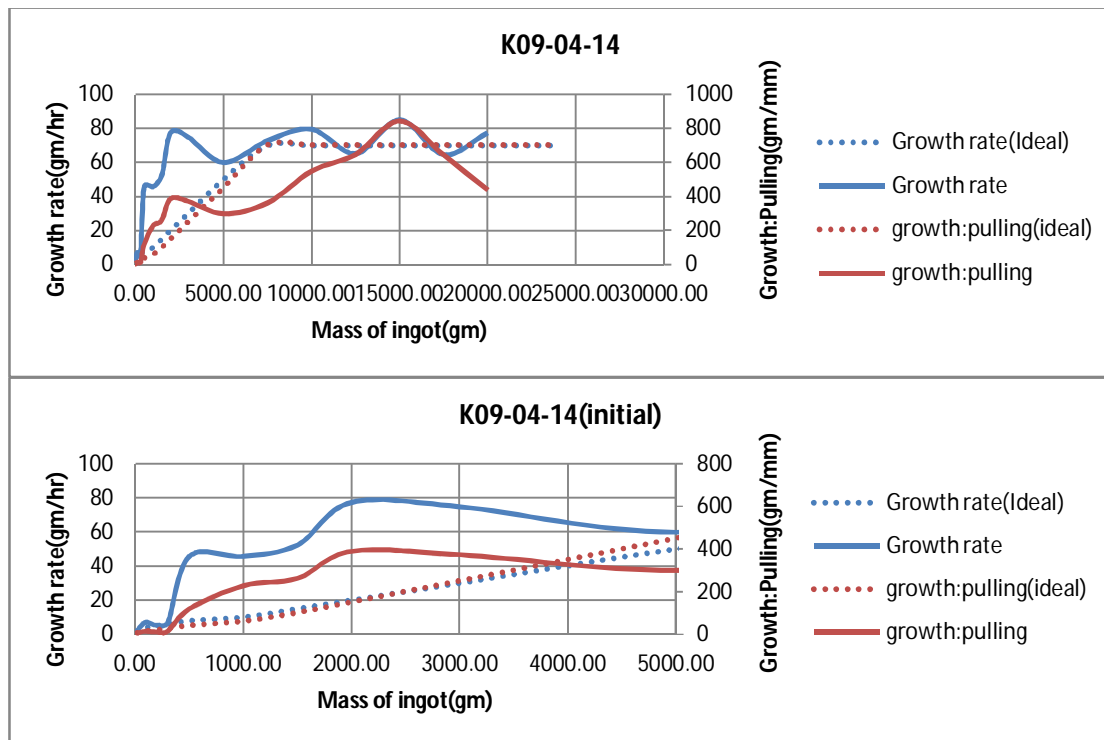


Figure I.3: Top view and side view of crystal K09-04-14 weighing 23.3 kg.

### Crystal Morphology

- 1) Conical head formation till 40 mm. [1] [4] [7]
- 2) Small diameter flat plate. [2] [6] [8]
- 3) Plate with milky layer beneath. [2] [6] [8]
- 4) Overall even crystal shape with uniform diameter throughout the height. [3] [5] [9]

k09-04-14																
time	mass	time diff	Growth	raz cristal	(nSeed posi	posn diff	pulling rat	températi	Temp diff	temp rate	puissance	power dif	power rat	temp pow growth	px Growth	Ti growth po
hr	gm	hr	gm/hr	mm	mm	mm	mm/hr	°C	°C	°C/hr	%	%	%/hr	C/power%	gm/mm	gm/°C
0.02	6.70			-13.47	0.00			2080.00			35.75					
6.93	20.00	6.92	1.92	-11.09	2.38	2.38	0.34	2076.00	4.00	0.58	35.70	0.05	0.0072	80.00	5.59	3.33
13.47	50.00	6.54	4.59	-7.83	5.64	3.26	0.50	2077.00	-1.00	-0.15	35.67	0.03	0.0046	-33.33	9.20	-30.00
20.74	100.00	7.27	6.88	-4.19	9.28	3.64	0.50	2078.00	-1.00	-0.14	35.63	0.04	0.0055	-25.00	13.74	-50.00
40.72	200.10	19.99	5.01	5.80	19.27	9.99	0.50	2072.00	6.00	0.30	35.41	0.22	0.0110	27.27	10.02	16.68
55.79	300.00	15.06	6.63	13.03	26.50	7.23	0.48	2069.00	3.00	0.20	35.17	0.24	0.0159	12.50	13.82	33.30
60.17	500.20	4.38	45.72	14.72	28.19	1.69	0.39	2073.00	-4.00	-0.91	35.10	0.07	0.0160	-57.14	118.46	-50.05
71.15	1000.60	10.98	45.57	16.92	30.39	2.20	0.20	2070.00	3.00	0.27	34.94	0.16	0.0146	18.75	227.45	166.80
80.69	1500.10	9.54	52.37	18.83	32.30	1.91	0.20	2067.00	3.00	0.31	34.79	0.15	0.0157	20.00	261.52	166.50
87.15	2000.50	6.47	77.35	20.12	33.59	1.29	0.20	2064.00	3.00	0.46	34.69	0.10	0.0155	30.00	387.91	166.80
100.54	3001.30	13.39	74.76	22.81	36.28	2.69	0.20	2060.00	4.00	0.30	34.50	0.19	0.0142	21.05	372.04	250.20
133.97	5000.10	33.43	59.80	29.50	42.97	6.69	0.20	2056.00	4.00	0.12	34.16	0.34	0.0102	11.76	298.77	499.70
168.41	7501.80	34.44	72.64	36.39	49.86	6.89	0.20	2044.00	12.00	0.35	33.82	0.34	0.0099	35.29	363.09	208.48
199.91	10001.30	31.50	79.35	40.93	54.40	4.54	0.14	2031.00	13.00	0.41	33.49	0.33	0.0105	39.39	550.55	192.27
238.36	12501.20	38.45	65.01	44.78	58.25	3.85	0.10	2016.00	15.00	0.39	33.03	0.46	0.0120	32.61	649.32	166.66
267.79	15001.20	29.43	84.95	47.74	61.21	2.96	0.10	1996.00	20.00	0.68	32.72	0.31	0.0105	64.52	844.59	125.00
306.55	17500.30	38.77	64.47	51.62	65.09	3.88	0.10	1981.00	15.00	0.39	32.38	0.34	0.0088	44.12	644.10	166.61
338.87	20000.30	32.31	77.37	57.31	70.78	5.69	0.18	1970.00	11.00	0.34	31.98	0.40	0.0124	27.50	439.37	227.27
339.96	23309.30	1.10	3021.15	107.90	121.37	50.59	46.19	1971.00	-1.00	-0.91	31.97	0.01	0.0091	-100.00	65.41	-3309.00



### *Growth Features*

#### **Growth Rate:**

Low initial growth rate values. (0g – 300g) [1]

High growth rate of crystal mass. (500g – 3000g) [2]

Good values of growth rate for later stages of growth process. (5000g – 20000g) [3]

#### **Pulling Rate:**

Initial higher rates of pulling for seed. (0g – 300g) [4]

Low values of growth rate for later stages of growth process. (3000g – 17500g) [5]

#### **Temp:Power:**

Slight negative values. (50g – 100g, 500g) [6]

#### **Growth:Pulling:**

Low initial values. (0g – 300g) [7]

High values for later stages of growth process. (500g – 2000g) [8]

Good values for later stages of growth process. (5000g – 17500g) [9]

K11-04-14

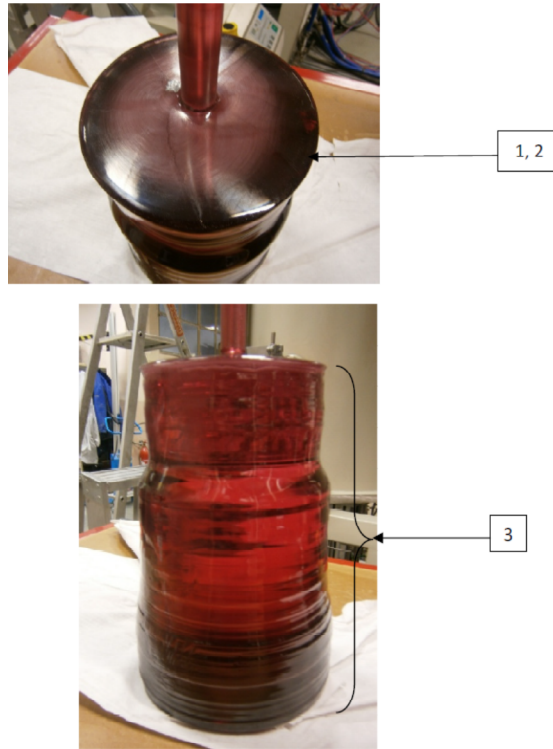


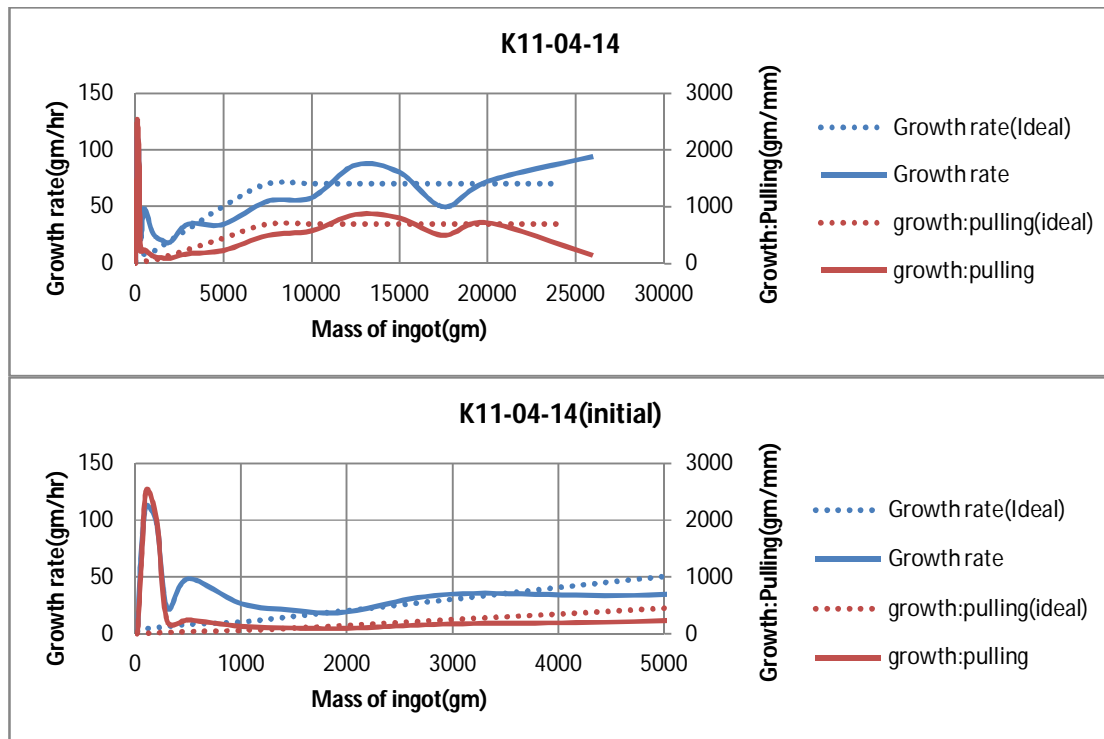
Figure I.4: Top view and side view of crystal K11-04-14 weighing 26 kg.

### Crystal Morphology

- 1) Big Diameter flat plate. [1] [3] [5] [6]
- 2) Plate with milky layer beneath. [1] [3] [5] [6]
- 3) Overall even crystal shape with uniform diameter throughout the height. [2] [4] [7]

k11-04-14																			
time	mass	time diff	Growth rate	z cristal	(n Seed)	posi	posn	diff	pulling rate	temp	rate	puissance	power diff	power rate	temp	pow	growth	ps	Growth
hr	gms	hr	gm/hr	mm	mm	mm	mm	mm/hr	°C	°C	°C/hr	%	%	%/hr	°C/power	gm/mm	gm/°C	gm/power	gm/°C
0.02	6.20			-28.19	0.00				2026.20			36.00							
86.03	20.10	86.01	0.16	-26.61	1.58	1.58	0.02	0.02	2024.30	1.90	0.02	35.81	0.19	0.0022	10.00	8.80	7.32	73.16	
86.50	50.70	0.46	65.89	-26.58	1.61	0.03	0.06	0.06	2026.30	-2.00	-4.31	35.81	0.00	0.0000	#DIV/0!	1020.00	-15.30	#DIV/0!	
86.94	101.10	0.45	112.49	-26.56	1.63	0.02	0.04	0.04	2028.70	-2.40	-5.36	35.81	0.00	0.0000	#DIV/0!	2520.00	-21.00	#DIV/0!	
87.97	200.60	1.03	96.73	-26.51	1.68	0.05	0.05	0.05	2032.00	-3.30	-3.21	35.81	0.00	0.0000	#DIV/0!	1990.00	-30.15	#DIV/0!	
92.44	300.70	4.46	22.43	-26.06	2.13	0.45	0.10	0.10	2030.10	1.90	0.43	35.81	0.00	0.0000	#DIV/0!	222.44	52.68	#DIV/0!	
96.57	500.20	4.13	48.30	-25.24	2.95	0.82	0.20	0.20	2029.00	1.10	0.27	35.79	0.02	0.0048	55.00	243.29	181.36	9975.00	
115.58	1000.30	19.01	26.31	-21.44	6.75	3.80	0.20	0.20	2029.40	-0.40	-0.02	35.71	0.08	0.0042	-5.00	131.61	-1250.25	6251.25	
139.99	1500.60	24.42	20.49	-16.55	11.64	4.89	0.20	0.20	2028.50	0.90	0.04	35.60	0.11	0.0045	8.18	102.31	555.89	4548.18	
166.50	2000.00	26.51	18.84	-11.25	16.94	5.30	0.20	0.20	2027.00	1.50	0.06	35.41	0.19	0.0072	7.89	94.23	332.93	2628.42	
195.32	3000.00	28.82	34.70	-5.48	22.71	5.77	0.20	0.20	2022.50	4.50	0.16	35.21	0.20	0.0069	22.50	173.31	222.22	5000.00	
253.40	5000.00	58.08	34.43	3.20	31.39	8.68	0.15	0.15	2014.60	7.90	0.14	34.70	0.51	0.0088	15.49	230.41	253.16	3921.57	
299.01	7500.60	45.60	54.83	8.25	36.44	5.05	0.11	0.11	1999.80	14.80	0.32	34.14	0.56	0.0123	26.43	495.17	168.96	4465.36	
342.15	10000.60	43.15	57.94	12.57	40.76	4.32	0.10	0.10	1990.60	9.20	0.21	33.72	0.42	0.0097	21.90	578.70	271.74	5952.38	
370.94	12500.40	28.78	86.85	15.46	43.65	2.89	0.10	0.10	1978.90	11.70	0.41	33.46	0.26	0.0090	45.00	864.98	213.66	9614.62	
402.08	15000.20	31.14	80.28	18.58	46.77	3.12	0.10	0.10	1964.50	14.40	0.46	33.23	0.23	0.0074	62.61	801.22	173.60	10868.70	
452.21	17500.10	50.13	49.86	23.60	51.79	5.02	0.10	0.10	1951.60	12.90	0.26	32.83	0.40	0.0080	32.25	497.99	193.79	6249.75	
486.73	20000.40	34.52	72.42	27.07	55.26	3.47	0.10	0.10	1939.70	11.90	0.34	32.50	0.33	0.0096	36.06	720.55	210.11	7576.67	
550.10	25985.30	63.36	94.46	68.54	96.73	41.47	0.65	0.65	1927.00	12.70	0.20	31.93	0.57	0.0090	22.28	144.32	471.25	10499.82	





### *Growth Features*

#### **Growth Rate:**

High growth rate of crystal mass in the growth process. (50g – 1000g) [1]

Good values of growth rate for later stages of growth process. (2000g – 20000g) [2]

#### **Pulling Rate:**

Low initial rates of pulling for seed. (0g – 300g) [3]

Low values of growth rate for later stages of growth process. (5000g – 20000g) [4]

#### **Temp:Power:**

Negative values. (50g – 300g, 1000g) [5]

#### **Growth:Pulling:**

Very High initial values. (50g – 1000g) [6]

Good values for later stages of growth process. (3000g – 10000g) [7]



K01-04-15

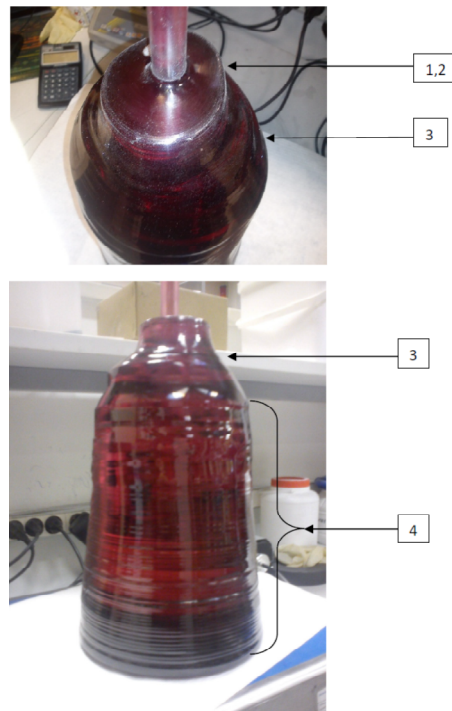
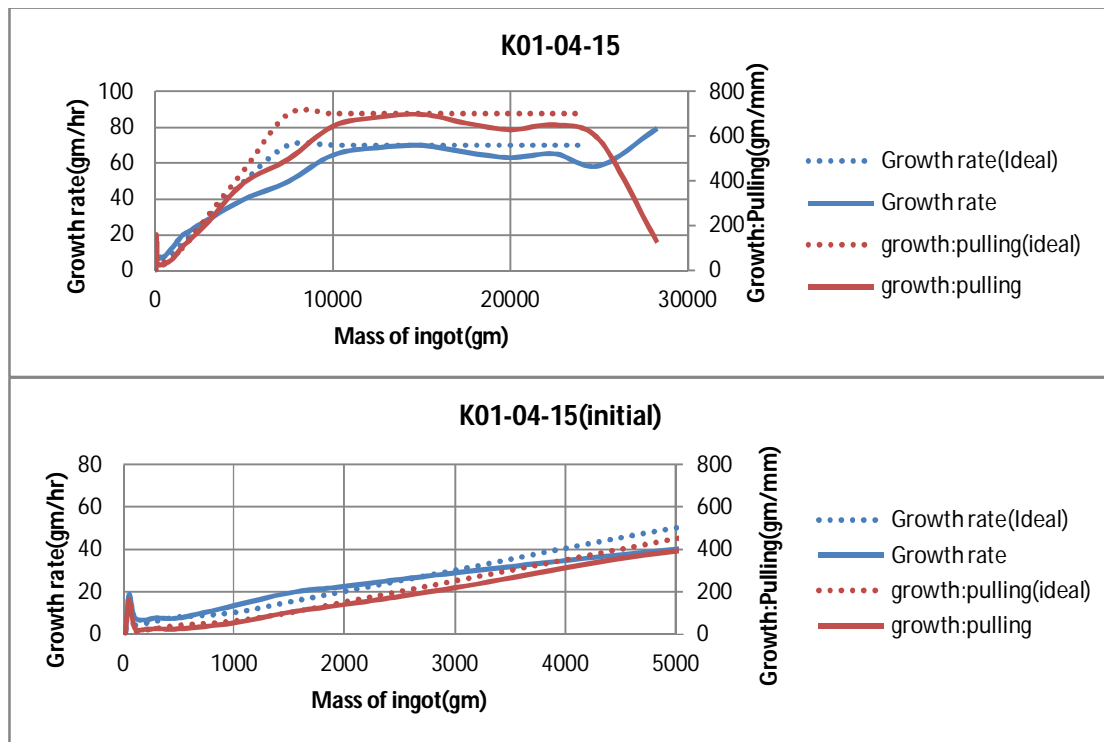


Figure I.5: Top view and side view of crystal K01-04-15 weighing 28.3 kg.

### Crystal Morphology

- 1) Small diameter flat plate. [1] [3] [5]
- 2) Plate without milky layer beneath. [2] [4] [6]
- 3) Conical head formation. [2] [4] [6]
- 4) Overall even crystal shape with uniform diameter throughout the height. [2] [4] [6]

k01-04-15																			
time	mass	time diff	Growth rate	z cristal	(nSeed)	posi	posn	diff	pulling rate	températi	Temp diff	temp rate	puissance	power diff	power rate	temp pos	growth pi	Growth To growth pi	
hr	gm	hr	gm/hr	mm	mm	mm	mm/hr			°C	°C	°C/hr	%	%	%/hr	C/power%	gm/mm	gm/°C	m/power%
0.05	5.00			-15.06	0.00					2030.20			36.450						
24.06	20.00	24.01	0.62	-14.24	0.82	0.82	0.03			2025.30	4.90	0.20	36.270	0.18	0.0075	27.22	18.29	3.06	83.33
25.70	50.40	1.64	18.51	-14.05	1.01	0.19	0.12			2026.90	-1.60	-0.97	36.440	-0.17	-0.1035	9.41	160.00	-19.00	-178.82
32.03	100.00	6.34	7.83	-12.42	2.64	1.63	0.26			2030.50	-3.60	-0.57	36.440	0.00	0.0000	#DIV/0!	30.43	-13.78	#DIV/0!
47.23	200.00	15.20	6.58	-7.87	7.19	4.55	0.30			2032.30	-1.80	-0.12	36.480	-0.04	-0.0026	45.00	21.98	-55.56	-2500.00
60.50	300.00	13.27	7.54	-3.89	11.17	3.98	0.30			2030.30	2.00	0.15	36.460	0.02	0.0015	100.00	25.13	50.00	5000.00
87.24	500.00	26.74	7.48	4.14	19.20	8.03	0.30			2028.30	2.00	0.07	36.240	0.22	0.0082	9.09	24.91	100.00	909.09
124.97	1000.20	37.72	13.26	13.66	28.72	9.52	0.25			2022.90	5.40	0.14	35.970	0.27	0.0072	20.00	52.54	92.63	1852.59
150.91	1500.10	25.95	19.27	18.51	33.57	4.85	0.19			2021.00	1.90	0.07	35.720	0.25	0.0096	7.60	103.07	263.11	1999.60
173.23	2000.30	22.31	22.42	22.10	37.16	3.59	0.16			2018.40	2.60	0.12	35.430	0.29	0.0130	8.97	139.33	192.38	1724.83
208.10	3000.50	34.87	28.68	26.68	41.74	4.58	0.13			2013.90	4.50	0.13	35.210	0.22	0.0063	20.45	218.38	222.27	4546.36
258.28	5001.00	50.18	39.86	31.78	46.84	5.10	0.10			2006.00	7.90	0.16	35.000	0.21	0.0042	37.62	392.25	253.23	9526.19
308.38	7500.60	50.10	49.89	36.80	51.86	5.02	0.10			1997.90	8.10	0.16	34.490	0.51	0.0102	15.88	497.93	308.59	4901.18
347.01	10000.10	38.64	64.69	40.67	55.73	3.87	0.10			1990.20	7.70	0.20	34.220	0.27	0.0070	28.52	645.87	324.61	9257.41
383.39	12500.10	36.38	68.72	44.32	59.38	3.65	0.10			1982.80	7.40	0.20	33.960	0.26	0.0071	28.46	684.93	337.84	9615.38
419.11	15001.10	35.72	70.02	47.90	62.96	3.58	0.10			1971.00	11.80	0.33	33.750	0.21	0.0059	56.19	698.60	211.95	11909.52
456.88	17500.20	37.77	66.16	51.69	66.75	3.79	0.10			1954.60	16.40	0.43	33.470	0.28	0.0074	58.57	659.39	152.38	8925.36
496.47	20000.60	39.58	63.17	55.66	70.72	3.97	0.10			1942.40	12.20	0.31	33.120	0.35	0.0088	34.86	629.82	204.95	7144.00
534.75	22500.20	38.29	65.28	59.50	74.56	3.84	0.10			1932.80	9.60	0.25	32.940	0.18	0.0047	53.33	650.94	260.37	13886.67
577.46	25000.00	42.70	58.54	63.78	78.84	4.28	0.10			1923.60	9.20	0.22	32.520	0.42	0.0098	21.90	584.07	271.72	5951.90
618.42	28260.90	40.96	79.60	90.04	105.10	26.26	0.64			1917.00	6.60	0.16	32.280	0.24	0.0059	27.50	124.18	494.08	13587.08



### Growth Features

#### Growth Rate:

High growth rate of crystal mass. (50g) [1]

Good values of growth rate for later stages of growth process. (200g – 25000g) [2]

#### Pulling Rate:

Too low initial rates of pulling for seed. (0g – 50g) [3]

Low values of growth rate for later stages of growth process. (200g – 25000g) [4]

#### Growth:Pulling:

Initial high values for initial stages of growth process. (0g – 100g) [5]

Good values for later stages of growth process. (300g – 25000g) [6]

K02-04-15

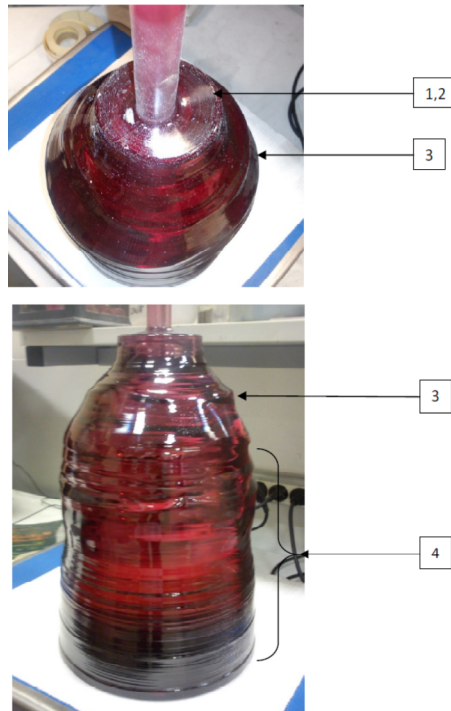
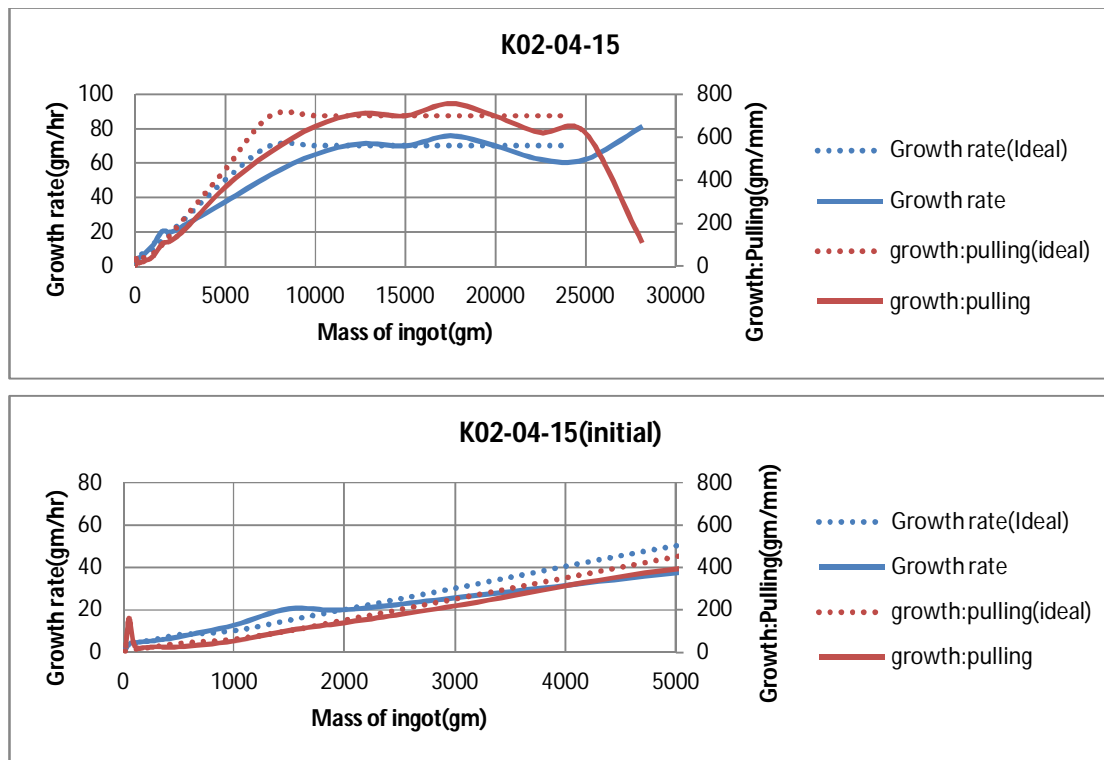


Figure I.6: Top view and side view of crystal K02-04-15 weighing 28.2 kg.

### Crystal Morphology

- 1) Small diameter flat plate. [2] [4] [5]
- 2) Plate without milky layer beneath. [1] [3]
- 3) Conical head formation. [1] [3]
- 4) Overall even crystal shape with uniform diameter throughout the height. [1] [3] [6]

k02-04-15																	
time	mass	time diff	Growth	raz cristal	(nSeed	posn	posn diff	pulling rat	températu	Temp diff	temp rate	puissance	power dif	power rat	temp: pow	growth: p	Growth: T
hr	gm	hr	gm/hr	mm	mm	mm	mm/hr	°C	°C	°C/hr	%	%	%/hr	°C/power%	gm/mm	gm/°C	°m/power%
0.02	6.20			-16.93	0.00			2029.90				36.600					
11.43	20.00	11.41	1.21	-16.08	0.85	0.85	0.07	2029.40	0.50	0.04	36.580	0.02	0.0018	25.00	16.24	27.60	690.00
19.46	50.00	8.03	3.74	-15.28	1.65	0.80	0.10	2029.80	-0.40	-0.05	36.620	-0.04	-0.0050	10.00	37.50	-75.00	-750.00
30.84	100.00	11.38	4.39	-13.00	3.93	2.28	0.20	2032.20	-2.40	-0.21	36.590	0.03	0.0026	-80.00	21.93	-20.83	1666.67
51.01	200.00	20.17	4.96	-6.95	9.98	6.05	0.30	2032.20	0.00	0.00	36.560	0.03	0.0015	0.00	16.53	#DIV/0!	3333.33
69.39	300.00	18.38	5.44	-1.44	15.49	5.51	0.30	2030.20	2.00	0.11	36.460	0.10	0.0054	20.00	18.15	50.00	1000.00
97.45	500.20	28.06	7.13	6.98	23.91	8.42	0.30	2027.20	3.00	0.11	36.270	0.19	0.0068	15.79	23.78	66.73	1053.68
136.98	1000.20	39.53	12.65	17.43	34.36	10.45	0.26	2027.30	-0.10	0.00	36.160	0.11	0.0028	-0.91	47.85	-5000.00	4545.45
161.45	1500.30	24.47	20.44	22.13	39.06	4.70	0.19	2026.40	0.90	0.04	36.180	-0.02	-0.0008	-45.00	106.40	555.67	-25005.00
186.53	2000.20	25.08	19.93	26.28	43.21	4.15	0.17	2024.40	2.00	0.08	36.030	0.15	0.0060	13.33	120.46	249.95	3332.67
225.65	3000.20	39.12	25.56	31.45	48.38	5.17	0.13	2020.60	3.80	0.10	35.750	0.28	0.0072	13.57	193.42	263.16	3571.43
279.03	5000.00	53.38	37.46	36.86	53.79	5.41	0.10	2014.00	6.60	0.12	35.450	0.30	0.0056	22.00	369.65	303.00	6666.00
326.03	7500.80	47.00	53.21	41.57	58.50	4.71	0.10	2006.10	7.90	0.17	35.120	0.33	0.0070	23.94	530.96	316.56	7578.18
364.37	10000.30	38.34	65.19	45.41	62.34	3.84	0.10	1998.90	7.20	0.19	34.870	0.25	0.0065	28.80	650.91	347.15	9998.00
399.43	12501.50	35.06	71.34	48.93	65.86	3.52	0.10	1991.40	7.50	0.21	34.590	0.28	0.0080	26.79	710.57	333.49	8932.86
435.08	15001.30	35.65	70.12	52.50	69.43	3.57	0.10	1979.70	11.70	0.33	34.200	0.39	0.0109	30.00	700.22	213.66	6409.74
467.98	17500.00	32.90	75.95	55.80	72.73	3.30	0.10	1962.40	17.30	0.53	34.040	0.16	0.0049	108.12	757.18	144.43	15616.87
503.63	20000.10	35.65	70.13	59.38	76.31	3.58	0.10	1950.60	11.80	0.33	33.730	0.31	0.0087	38.06	698.35	211.87	8064.84
543.81	22500.20	40.18	62.22	63.40	80.33	4.02	0.10	1942.50	8.10	0.20	33.350	0.38	0.0095	21.32	621.92	308.65	6579.21
584.02	25001.60	40.21	62.21	67.43	84.36	4.03	0.10	1933.90	8.60	0.21	33.150	0.20	0.0050	43.00	620.69	290.86	12507.00
622.81	28158.20	38.79	81.38	96.45	113.38	29.02	0.75	1929.50	4.40	0.11	32.820	0.33	0.0085	13.33	108.77	717.41	9565.45



### *Growth Features*

#### **Growth Rate:**

Good values of growth rate throughout the growth process. [1]

#### **Pulling Rate:**

Too low initial rates of pulling for seed. (0g – 100g) [2]

Low values of growth rate for later stages of growth process. (1500g – 25000g) [3]

#### **Temp:Power**

Slight negative Values. (100g, 1000-1500g) [4]

#### **Growth:Pulling:**

High values for initial stages of growth process. (0g – 100g) [5]

Good values for later stages of growth process. (10000g – 25000g) [6]

## Appendix II: Milky defect explained as an optical effect by Carmen Stelian

Milky defect is observed in Ti-doped sapphire crystals which display a light region of 1-1.5 cm width, perpendicular to the c-axis (see Fig. II.1). The diffused light in this region could be explained as an optical effect, which involves three factors:

### Birefringence of the sapphire crystal

Ti-doped sapphire crystal is a uniaxial negative medium having the optic axis parallel to the c-axis of the crystal. The values of the ordinary and extraordinary refractive indices are  $n_o = 1.768$  and  $n_E = 1.760$ .

### Variation of the extraordinary refractive index as function of Ti concentration

Qualitative measurements of  $Ti^{3+}$  ion concentration in several slices cut perpendicular to the growth direction, performed by microluminescence and transmittance analysis, have shown that the concentration is higher at the periphery of the crystal as compared to the central part of the ingot. Figure II.2 shows the measured absorption coefficient on the radial direction in a sample of 10 cm in diameter. The values of the absorption coefficient, which is proportional to Ti concentration in the crystal, indicate large radial variation in Ti composition, especially for the slices cut from the middle part of the Kyropoulos ingot. This significant compositional inhomogeneity was numerically explained by accounting large curvatures of the growth interface.

The non-uniformity in the radial titanium distribution in the crystal determines variations of the refractive index. "TROPEL" measurements of the extraordinary refractive index performed by scanning the surface of a slice cut perpendicular to the growth direction, shows that  $n_E$  is directly dependent on Ti concentration (Fig. II.3). The plot of  $n_E$  versus the radial coordinate in Fig. II.3b exhibits the same U-shaped profile as the Ti distribution shown in Fig. II.2.

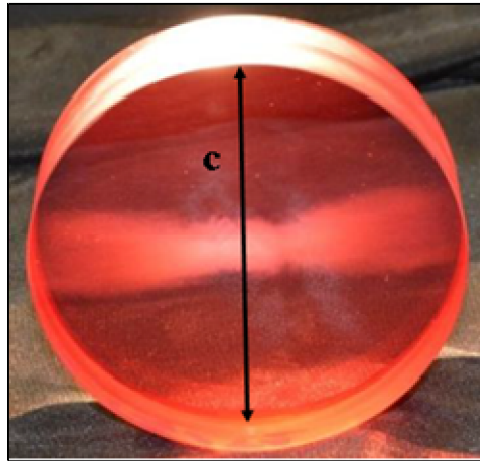


**Fig. II.1** Milky defect observed in Ti-doped sample of 10 cm in diameter cut perpendicular to the growth direction.

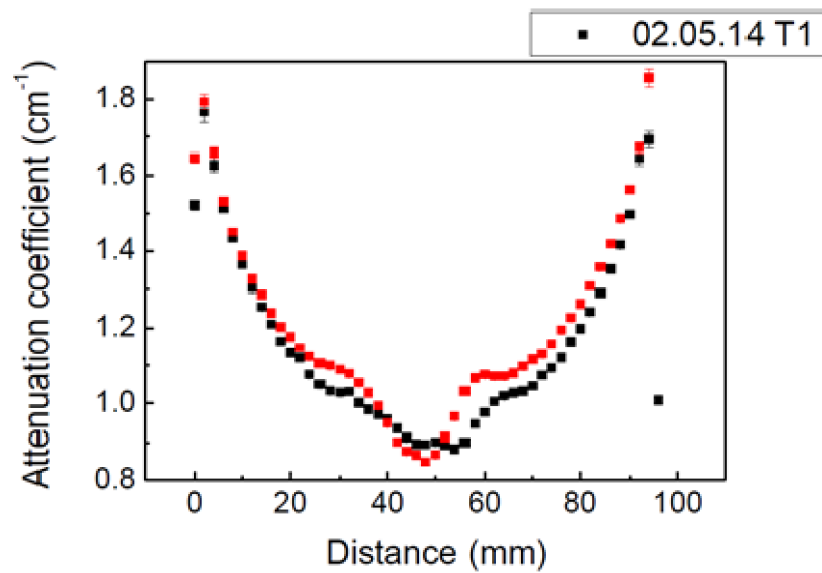


**Fig. II.2** Absorption coefficient recorded in a slice of 10 cm in diameter along the direction parallel to c-axis (black squares) and perpendicular to c-axis (red squares).

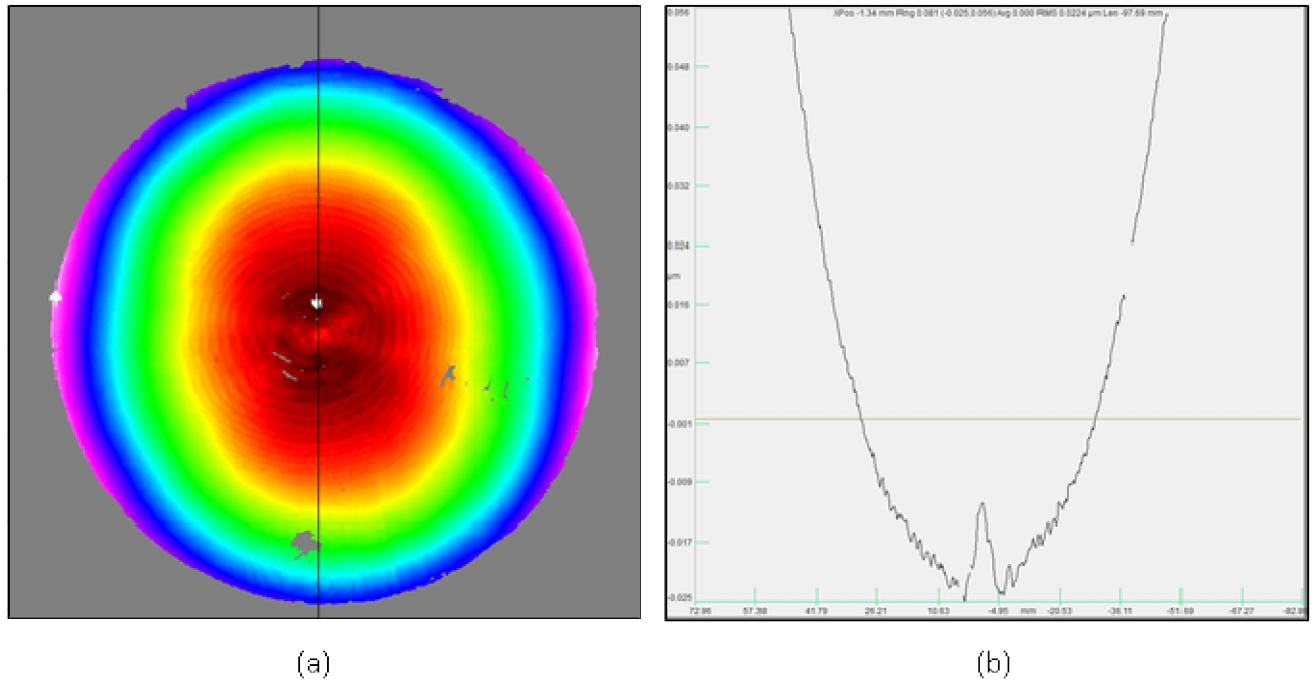


**Fig. II.3** “TROPEL” measurements of the extraordinary refractive index: (a) Color map of obtained by scanning the surface of a slice cut perpendicular to growth direction; (b) Radial profile of in the sample. The quantitative measurements are doubtful since the maximum variation of the refractive index is very small Measurements uncertainties within this technique are also very improbable.

The measurements of the ordinary and extraordinary refractive indices performed by using M-lines spectroscopy in different regions of the sample (exhibiting or not the milky defect), have shown much significant variations of the extraordinary refractive index (maximum ), while the ordinary refractive index is almost unchanged (see Tab. II.1).

		Echantillon			
longueur d'onde	Zone	2		3	
		Indice ordinaire	Indice extraordinaire	Indice ordinaire	Indice extraordinaire
à 543.5 nm	Non perturbée	1,7730	1,7655	1,7730	1,7652
	Perturbée	1,7728	1,7665	1,7731	1,7666
à 594 nm	Non perturbée	1,7700	1,7623	1,7702	1,7620
	Perturbée	1,7700	1,7638	1,7700	1,7634
à 632.8 nm	Non perturbée	1,7680	1,7607	1,7680	1,7601
	Perturbée	1,7680	1,7620	1,7679	1,7618

**Table II.1:** Measurements of the ordinary and extraordinary refractive indices performed by using M-lines spectroscopy in different regions of the sample, exhibiting or not the milky defect.

In conclusion, the measurements of the refractive index show that the extraordinary refractive index increases to the crystal periphery following the increasing Ti concentration profile, while the ordinary refractive index is much less sensitive to the radial chemical inhomogeneity of the crystal.

## Reflection and refraction of polarized light described by the Fresnel equations

When light moves between media of different refractive indices ( $n_1$  and  $n_2$ ), both reflection and refraction of the light may occur. The Fresnel equations describe what fraction of the incident light is reflected, and, respectively refracted (transmitted). The fraction of the incident power which is reflected is given by the reflectance (R), and the fraction which is transmitted is given by the transmittance (T). The behavior depends on the polarization of the incident ray:

The reflectance of the polarized light with its electric field perpendicular to the plane of incidence is given by:

$$R_{\perp} = \left( \frac{n_1 \cos \theta_i - n_2 \cos \theta_t}{n_1 \cos \theta_i + n_2 \cos \theta_t} \right)^2 \quad (1)$$



The reflectance of the polarized light with its electric field parallel to the plane of incidence is given by:

$$R_{\parallel} = \left( \frac{n_1 \cos \theta_t - n_2 \cos \theta_i}{n_1 \cos \theta_t + n_2 \cos \theta_i} \right)^2 \quad (2)$$

In the above equations  $\theta_i$  and  $\theta_t$  are the angles that the incident and the transmitted rays make with the normal of the interface between the two media.

### Huygens' construction

The light propagation in a cylindrical Ti-doped sapphire sample is analyzed by applying the principle of wavelets developed by Huygens (Huygens' construction). In Fig. II.4, a cone of unpolarized light strikes the top surface of the sample. Every incident ray splits in two rays which are linearly polarized in planes orthogonal to each other: the ordinary (RO) and, respectively the extraordinary (RE) ray. The light propagation in the crystal will be analyzed in two preferential planes of incidence: A) plane of incidence perpendicular to the c-axis of the crystal; B) plane of incidence parallel to the c-axis of the crystal.

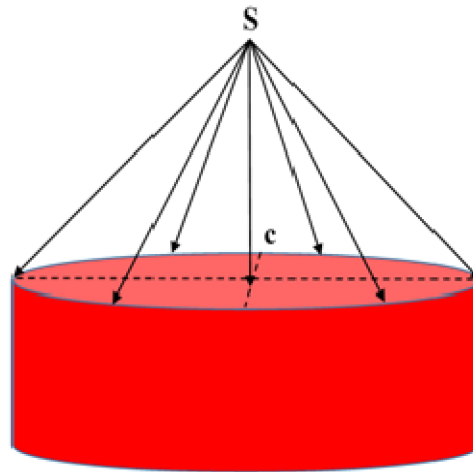


**Fig. II.4** Cone of unpolarized light which strikes the top surface of the crystal.

#### 4.8.1 Huygens' construction in the case of the optic axis perpendicular to plane of incidence

The wavefront propagation in anisotropic media is constructed by applying the Huygens' principle of wavelets. In uniaxial crystals, the wavelets associated with the ordinary ray have the same velocity in all directions (spherical wavelets). The wavelets associated with the extraordinary ray are ellipsoids of revolution which coincide with the spherical wavelets along the optic axis. When the optic axis is perpendicular to the plane of incidence (Fig. II.5a), the sections of both ordinary and extraordinary

wavelets are circles. Since  $n_E < n_o$ , the velocity of the extraordinary wavelets is greater than the velocity of the ordinary wavelets. Two cases are investigated in Fig. II.5

The case of small incidence angle, when the incident ray reaches the top surface of the sample in the central region is shown in Fig. II.5b. The extraordinary ray is more deviated from the normal compared to the ordinary ray. When reaching the bottom surface of the crystal, the extraordinary ray, which is polarized perpendicular to the plane of incidence, will be essentially reflected ( $R_{\perp} = 0.12$ ), while the ordinary ray, which is polarized parallel to the plane of incidence, will be essentially transmitted ( $R_{\parallel} = 0.039$ ). The values of the reflectance were estimated by using the Fresnel equations Eq. (1-2). The incidence angle at the bottom surface of the crystal  $\theta_i = 20^\circ$  corresponds to an incidence angle of the light at the top surface of the crystal of  $\cong 37^\circ$ . Since only the extraordinary refractive index depends on the titanium distribution in the crystal, the extraordinary light will be diffused at the bottom surface of the crystal, as will be explained on the Fig. II.5c.

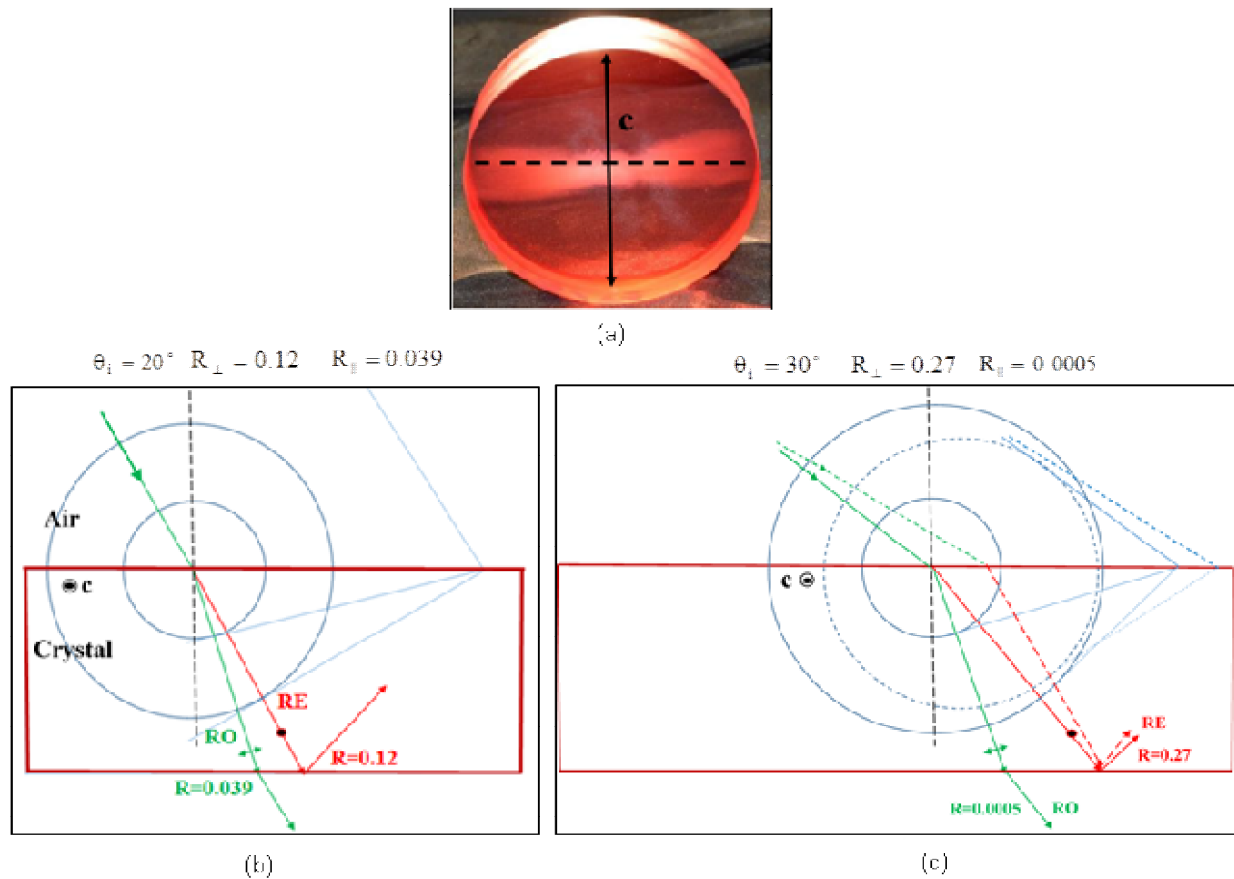


**Fig. II.5** Huygens' construction in the case of the optic axis perpendicular to plane of incidence: (a) Sample of 10 cm diameter featuring diffused light in the central plane perpendicular to c-axis; (b) Case of small

*incidence angle at the bottom surface of the crystal  $\theta_i = 20^\circ$ ; (c) Case of increased incidence angle at the bottom surface of the crystal  $\theta_i = 30^\circ$ .*

The case of increased incidence angle, when the incoming ray reaches the top surface of the sample near the crystal periphery is shown in Fig. II.5c. The values of the reflectance estimated for an incidence angle at the bottom surface of the crystal  $\theta_i = 30^\circ$ . are:  $R_{\perp} = 0.27$  and  $R_{\parallel} = 0.0005$ . It is found that the fraction of the incident light reflected at the bottom surface of the crystal increases significantly with increasing incidence angle. The trajectory of a second ray (dashed green line) reaching the top surface of the crystal at an incidence angle slightly greater than the first ray is drawn on Fig. II.5c. Only the extraordinary wavelet and the extraordinary refracted ray are shown for the second incident ray. Since the Ti concentration increases to the crystal periphery, the extraordinary refractive index increases also, so the rayon of the second extraordinary wavelet will be smaller (dashed blue circle). The graphical construction shows that both the refracted extraordinary rays arrive at the same incidence point on the bottom surface of the crystal, and are reflected upon different angles (since the incidence angles are different). Therefore, an incident conical beam, centered by the first ray, will be focalized in the same point at the bottom surface of the sample then diffused in the crystal. The effect is amplified near the crystal periphery, since the reflectance of the extraordinary light increases with increasing incidence angle. That could explain the diffused light in the transversal region of the crystal, which is perpendicular to the c-axis. It is also found that the diffused light is polarized with vibrations parallel to the c-axis.

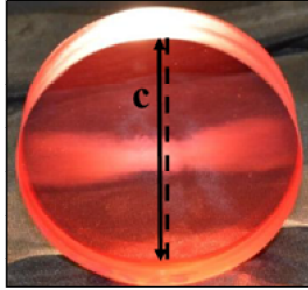
#### **Huygens' construction in the case of the optic axis parallel to plane of incidence**

The propagation of the incoming light with the incidence plane parallel to the optic axis is investigated in Fig.II. 6. In this case the section of the ordinary and extraordinary wavelets gives a circle, and, respectively, an ellipse. Two cases, at small and increased incidence angle are shown on the figure:

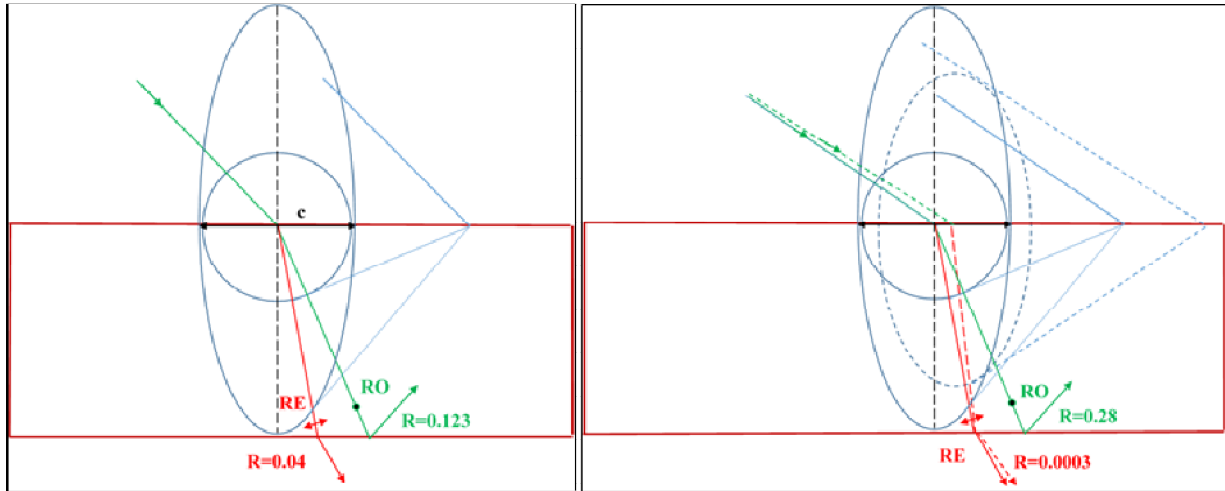
The case of small incidence angle ( $\theta_i = 20^\circ$  at the bottom face of the crystal) is shown in Fig.II.6b. The extraordinary ray is less deviated from the normal compared to the ordinary ray. When reaching the bottom surface of the crystal, the extraordinary ray, which is polarized parallel to the plane of incidence, will be essentially transmitted ( $R_{\parallel} = 0.04$ ), while the ordinary ray, which is polarized perpendicular to the plane of incidence, will be essentially reflected ( $R_{\perp} = 0.123$ ). Therefore, less diffused light is observed in the centre of the crystal, along the direction parallel to c-axis.

The case of increased incidence angle ( $\theta_i = 30^\circ$  at the bottom face of the crystal) is shown in Fig. II.6c. The estimated values of the reflectance are:  $R_{\perp} = 0.28$  and  $R_{\parallel} = 0.0003$ . In this case, the incident conical beam,

centered by the first ray, will be focalized in the same point at the bottom surface of the sample, then refracted. Therefore, the light is no more diffused near the crystal periphery along the direction parallel to c-axis.



(a)



(b)

(c)

**Fig. II.6** Huygens' construction in the case of the optic axis parallel to plane of incidence: (a) Sample of 10 cm diameter featuring no diffused light near the crystal periphery along the direction parallel to c-axis; (b) Case of small incidence angle at the bottom surface of the crystal  $\theta_i = 20^\circ$ ; (c) Case of increased incidence angle at the bottom surface of the crystal  $\theta_i = 30^\circ$ .

## Conclusion

In conclusion, the milky defect could be explained as an optical effect caused by the crystal birefringence and the non-homogeneous distribution of titanium in Kyropoulos ingots. This hypothesis is validated by the experimental observations such as:

- Milky defect was not observed in white sapphire grown by the Kyropoulos technique.

- Milky defect is not so obvious in samples cut from the top part of the ingot, where the radial variation of Ti concentration is very small.
- The diffused light is polarized with vibrations parallel to c-axis, as observed in experiments.

# Appendix III: Numerical modelling of the Kyropoulos growth process (model by Carmen Stelian)

## Heat transfer and melt convection

The finite element software COMSOL Multiphysics is used for modelling the heat transfer and melt convection during the Kyropoulos growth of Ti-doped sapphire crystal. The simulation is performed in two steps. First, global modelling is applied to compute the temperature field in the furnace, as well as the velocity field in the liquid sample. Then, the temperatures carried from the global computations are used as boundary conditions for an axisymmetric local model which includes the crystal, melt, crucible and the surrounding gas.

The governing equations of heat transfer and melt convection are:

$$\rho C_p \left( \frac{\delta T}{\delta t} + \vec{u} \cdot \nabla T \right) = \lambda_T \nabla^2 T + Q_R \quad \text{Equation III.1}$$

$$\rho \left( \frac{\delta \vec{u}}{\delta t} + (\vec{u} \cdot \nabla) \vec{u} \right) = -\nabla p + \eta \nabla^2 \vec{u} - \rho \vec{g} (\beta_T (T - T_0)) \quad \text{Equation III.2}$$

The internal radiative heat transfer in the sapphire crystal is simulated by accounting the radiative heat source  $Q_R$  in Equation III.4. The P1 approximation model, which relies on the hypothesis that the participating medium is optically thick, is applied in the present case. The optical thickness varies between 2.4 and 40 as function of the dimension of growing sapphire ingot. The melt has been considered opaque in the present computations. The radiative heat source in Equation III.4 is given by:

$$Q_R = \alpha (G - 4n^2 \sigma_{st} T^4) \quad \text{Equation III.3}$$

The incident radiation  $G$  is computed by solving the following equation:

$$-\nabla(D_{P1} \nabla G) = \alpha (G - 4n^2 \sigma_{st} T^4) \quad \text{Equation III.4}$$

where  $D_{P1}$  is P1 diffusion coefficient defined as

$$D_{P1} = \frac{1}{3k+b(3-l_1)} \quad \text{Equation III.5}$$

In the above equation,  $l_1$  is the linear Legendre coefficient of the scattering phase function and  $b$  is the scattering coefficient (the scattering effect is not considered in the present simulation).

The radiative heat flux at the solid boundaries of the crystal, which are considered opaque, is given by

$$\phi_R = \frac{\varepsilon}{2(2-\varepsilon)} (4n^2\sigma_{st}T^4 - G) \quad \text{Equation III.6}$$

The crystal-melt interface has been considered to be a black wall ( $\varepsilon = 1$ ).

The release of the latent heat at the crystal-melt interface is given by the following equation:

$$(\lambda_{T(s)} \nabla T_{(s)} - \lambda_{T(l)} \nabla T_{(l)}) \vec{n} = \rho_s \cdot h_f \cdot V \quad \text{Equation III.7}$$

where (s) and (l) denotes the solid and the liquid phases.

For the global simulation model, we impose the ambient temperature value of 300 K at the furnace outer walls.

The melt convection is driven by buoyancy and Marangoni effects. The Marangoni flow occurs at the free surface of the melt, due to the dependence of the interface tension on the temperature. This effect has been modelled by introducing the following boundary condition at the free surface of the melt:

$$\eta \frac{\delta u_s}{\delta n} = \gamma_T \frac{\delta T}{\delta s} \quad \text{Equation III.8}$$

where,  $\gamma_T = \frac{\delta \gamma_{lv}}{\delta T}$  is the derivative of the surface tension as function of the temperature

$$\gamma_T = -3.5 \cdot 10^{-5} \frac{N}{m.K} [\text{C.-H. Chen, 2011}] [\text{Tandjaoui, 2016}]$$

The boundary conditions used for the flow computations are: (a) No slip condition for the liquid melt in contact with the crucible inner walls, ( $\vec{u} = 0$ ) and (b) Slip conditions at the liquid melt free surface; ( $u_s \neq 0$ ,  $u_n = 0$ )

The transient modelling of the solidification process is performed by using the deformed mesh technique. There are three moving interfaces in the present model: the crystal-melt interface which takes the shape of the solidification isotherm, the crystal-gas interface which gives the external shape of the crystal, and the melt-gas interface which is moving down during the crystallization process. The mesh used for the local

simulation has 10,000 triangular elements. The maximum time step in the transient simulations is 0.5 s. [Stelian, 2016] [Stelian, 2017-a]

## Thermal stress

### 3D calculation

The software COMSOL Multiphysics has also been used for modelling thermal stresses in the crystal [Stelian, 2018]. The 2D global simulation is performed at a given stage of the growth process. The power in the heater is adjusted until the temperature in the triple crystal-melt-gas point reaches the melting point. The temperatures carried out from the global modeling are used for three dimensional modeling of thermal stress in the crystal. The stress-strain relation is given by the generalized law of Hooke:

$$\sigma_{ij} = C_{ijkl} (\varepsilon_{kl} - \beta_{kl}(T - T_{ref})) \quad \text{Equation III.9}$$

The elastic constant matrix for sapphire, which has a trigonal structure, is given by:

$$C_{ij} = \begin{bmatrix} C_{11} & C_{12} & C_{13} & C_{14} & 0 & 0 \\ C_{12} & C_{11} & C_{13} & -C_{14} & 0 & 0 \\ C_{13} & C_{13} & C_{33} & 0 & 0 & 0 \\ C_{14} & -C_{14} & 0 & C_{44} & 0 & 0 \\ 0 & 0 & 0 & 0 & C_{44} & C_{14} \\ 0 & 0 & 0 & 0 & C_{14} & \frac{1}{2}(C_{11} - C_{12}) \end{bmatrix}$$

The elastic constants  $C_{ij}$  determined in the coordinate system xyz (where x-axis is parallel to a-axis, and z-axis is parallel to c-axis of sapphire) are given by:  $C_{11}=497$  GPa,  $C_{12}=162.66$  GPa,  $C_{13}=117.26$  GPa,  $C_{14}=22.96$  GPa,  $C_{33}=501.8$  GPa,  $C_{44}=147.2$  GPa [Winey, 2001]. The thermal expansion coefficient is considered constant in the present computations  $\beta_T = 5 \cdot 10^{-6} K^{-1}$  [Demina, 2008].

The von Mises stress in the crystal is given by:

$$\sigma_{Mises} = \sqrt{\frac{(\sigma_{xx} - \sigma_{yy})^2 + (\sigma_{yy} - \sigma_{zz})^2 + (\sigma_{zz} - \sigma_{xx})^2 + 6(\sigma_{xy}^2 + \sigma_{yz}^2 + \sigma_{xz}^2)}{2}}$$

To calculate the thermal stress, free boundary conditions are applied to all crystal boundaries except for the top surface of the seed rod, which is considered fixed.



## 2D calculation

The axisymmetric thermal strain–stress equations for sapphire are calculated in cylindrical coordinate. The thermal elastic stress–strain relation is based on Hooke's law. [Fang, 2013-b] [Jin, 2014][Fainberg, 1996]

The isotropic elastic constant matrix is given by:

$$C_{ij} = \frac{E}{(1 + \nu)(1 - 2\nu)} \begin{bmatrix} (1 - \nu) & \nu & \nu & 0 \\ \nu & (1 - \nu) & \nu & 0 \\ \nu & \nu & (1 - \nu) & 0 \\ 0 & 0 & 0 & (1 - \nu) \end{bmatrix}$$

To calculate stress distribution, the following equations are solved:

$$\frac{\delta \sigma_r}{\delta r} + \frac{\delta \sigma_{rz}}{\delta z} + \frac{\sigma_r - \sigma_\theta}{r} = 0$$

$$\frac{\delta \sigma_{rz}}{\delta r} + \frac{\delta \sigma_z}{\delta z} + \frac{\sigma_{rz}}{r} = 0$$

The von Mises stress is calculated by:

$$\sigma_{Mises} = \sqrt{\frac{(\sigma_r - \sigma_z)^2 + (\sigma_\theta - \sigma_r)^2 + (\sigma_\theta - \sigma_z)^2 + 6\sigma_{rz}^2}{2}}$$

In this case, the elastic properties of sapphire are considered isotropic. The values of the Young modulus and Poisson ratio used in these computations are:  $E = 400 \text{ GPa}$  and  $\nu = 0.28$ .

## Appendix IV: Chemical Analysis

Since, we are growing titanium doped sapphire crystal for laser applications, it is really important to understand the Ti content and its distribution in our crystals. To this effect 1 cm x 1cm samples were prepared from the rectangular and circular sample presented in figure 4.6. The location of these samples in the circular and rectangular sample are shown in figure IV.1

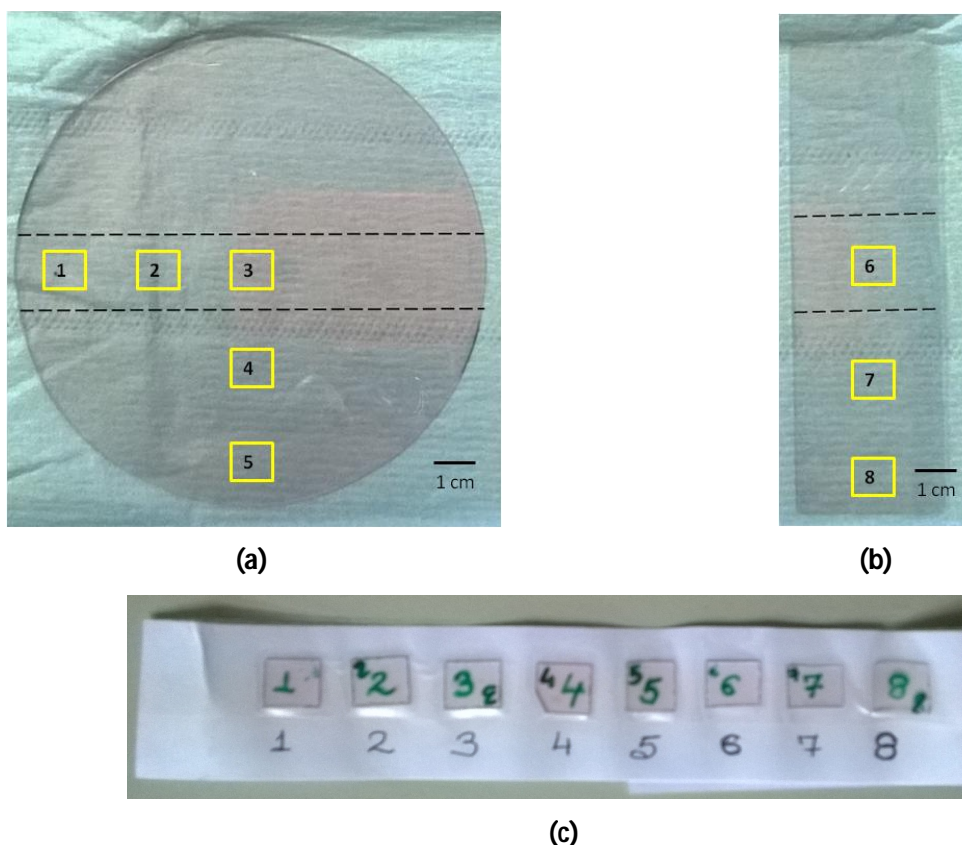


**Figure IV.1:** Samples prepared for chemical analysis from (a) Circular sample, (b) Rectangular sample and (c) the samples laid out individually.

These samples were sent to Institute of Analytical Sciences in Lyon for chemical quantitative analysis.

The chemical analysis was carried out using Inductively coupled plasma mass spectrometry (ICP-MS), which is a type of mass spectrometry which is capable of detecting metals and several non-metals at concentrations as low as one part in  $10^{15}$  (part per quadrillion, ppq) on non-interfered low-background isotopes. This is achieved by ionizing the sample with inductively coupled plasma and then using a mass spectrometer to separate and quantify those ions.

The chemical measurements were carried out for other elements to check for impurity concentrations along with Ti. The values of concentrations in ppm for the elements analysed are provided in Table IV.1.

From the table it is evident that Ti is the highest constituent as expected due to the doping. But, large traces of Si are also observed which can be due to the extensive use of silica in the polishing process which could lead to the contamination of the prepared samples.

The analysis technique has a minimum threshold for some elements below which it cannot resolve the variations in concentration.

<b>Element</b>	<b>1</b>	<b>2</b>	<b>3</b>	<b>4</b>	<b>5</b>	<b>6</b>	<b>7</b>	<b>8</b>
<b>Ti</b>	398	290	315.5	419	307	317	275	396.5
<b>Mo</b>	<10	<10	<10	<10	<10	<10	<10	<10
<b>Mg</b>	15	<10	11.5	<10	211	<10	11	<10
<b>Y</b>	<20	<20	<20	<20	<20	<20	<20	<20
<b>Na</b>	92	93	68.5	<50	216	<50	<50	55
<b>S</b>	<500	<500	<500	<500	<500	<500	<500	<500
<b>Ca</b>	<100	<100	184	<100	161	<100	117	<100
<b>P</b>	<200	<200	<200	<200	240	<200	<200	<200
<b>K</b>	<50	<50	56.5	<50	77	<50	<50	<50
<b>Cl</b>	<15	<15	<15	<15	<15	<15	<15	<15
<b>Si</b>	371	111	292.5	<50	81	81	<50	488

**Table IV.1:** Elemental concentrations in ppm.



# Bibliography

Akselrod, M. S., & Bruni, F. J. (2012). Modern trends in crystal growth and new applications of sapphire. *Journal of Crystal Growth*, 360(1), 134–145. <https://doi.org/10.1016/j.jcrysgro.2011.12.038>

Alford, W. J., & Stephens, D. L. (1963). Chemical Polishing and Etching Techniques for Al<sub>2</sub>O<sub>3</sub> Single Crystals. *Journal of the American Ceramic Society*, 46(4), 193–194. <https://doi.org/10.1111/j.1151-2916.1963.tb11715.x>

Alombert-Goget, G., Lebbou, K., Barthalay, N., Legal, H., & Chériaux, G. (2014). Large Ti-doped sapphire bulk crystal for high power laser applications. *Optical Materials*, 36(12), 2004–2006. <https://doi.org/10.1016/j.optmat.2014.01.011>

Alombert-Goget, G., Li, H., Faria, J., Labor, S., Guignier, D., & Lebbou, K. (2016). Titanium distribution in Ti-sapphire single crystals grown by Czochralski and Verneuil technique. *Optical Materials*, 51, 1–4. <https://doi.org/10.1016/j.optmat.2015.11.016>

Alombert-Goget, G., Li, H., Guyot, Y., Brenier, A., & Lebbou, K. (2016). Luminescence and coloration of undoped and Ti-doped sapphire crystals grown by Czochralski technique. *Journal of Luminescence*, 169, 516–519. <https://doi.org/10.1016/j.jlumin.2015.02.001>

Alombert-Goget, G., Sen, G., Pezzani, C., Barthalay, N., Duffar, T., & Lebbou, K. (2016). Large Ti-doped sapphire single crystals grown by the kyropoulos technique for petawatt power laser application. *Optical Materials*, 61, 21–24. <https://doi.org/10.1016/j.optmat.2016.04.025>

Alombert-Goget, G., Trichard, F., Li, H., Pezzani, C., Silvestre, M., Barthalay, N., ... Lebbou, K. (2017). Titanium distribution profiles obtained by luminescence and LIBS measurements on Ti: Al<sub>2</sub>O<sub>3</sub> grown by Czochralski and Kyropoulos techniques. *Optical Materials*, 65, 28–32. <https://doi.org/10.1016/j.optmat.2016.09.049>

Asadchikov, V. E., Butashin, A. V., Buzmakov, A. V., Deryabin, A. N., Kanevsky, V. M., Prokhorov, I. A., ... Hermann, R. P. (2016). Single-crystal sapphire microstructure for high-resolution synchrotron X-ray monochromators. *Crystal Research and Technology*, 51(4), 290–298. <https://doi.org/10.1002/crat.201500343>

Authier, A. (2003). *Dynamical Theory of X-Ray Diffraction*. Oxford University Press. <https://doi.org/10.1093/acprof:oso/9780198528920.001.0001>

- Bagdasarov, K. S. (1988). The problems of high-temperature crystallization. *Progress in Crystal Growth and Characterization*, 16(C), 59–80. [https://doi.org/10.1016/0146-3535\(88\)90015-9](https://doi.org/10.1016/0146-3535(88)90015-9)
- Bagdasarov, K. S. (2002). Fundamentals of High-Temperature Crystallization. *Crystallography Reports*, 47, S27–S34.
- Barthalay, N. (2013). *Présentation du Projet TITANSaphir*.
- Benmessai, K., Farr, W. G., Creedon, D. L., Reshitnyk, Y., Le Floch, J. M., Duty, T., & Tobar, M. E. (2013). Hybrid electron spin resonance and whispering gallery mode resonance spectroscopy of Fe<sup>3+</sup> in sapphire. *Physical Review B - Condensed Matter and Materials Physics*, 87(9), 1–9. <https://doi.org/10.1103/PhysRevB.87.094412>
- Biderman, S., Ben-Amax, G., Einav, Y., Horowitz, A., Laor, U., Weiss, M., & Stern, A. (1987). Crystal Growth of optical materials By The Gradient Solidification Method. *SPIE*, 157–164. <https://doi.org/10.1117/12.941813>
- Biderman, S., Horowitz, A., Einav, Y., Gazit, D., Stern, A., & Weiss, M. (1991). Production of sapphire domes by the growth of near net shape single crystals. *SPIE*, 1535, 27–34.
- Borodin, V. A., Ionov, A. M., & Yalovets, T. N. (1990). Void formation upon annealing of shaped sapphire crystals. *Journal of Crystal Growth*, 104(1), 157–164. [https://doi.org/10.1016/0022-0248\(90\)90326-G](https://doi.org/10.1016/0022-0248(90)90326-G)
- Boulon, G. (2012). Fifty years of advances in solid-state laser materials. *Optical Materials*, 34(3), 499–512. <https://doi.org/10.1016/j.optmat.2011.04.018>
- Bruni, F. J. (2015). Crystal growth of sapphire for substrates for high-brightness, light emitting diodes. *Crystal Research and Technology*, 50(1), 133–142. <https://doi.org/10.1002/crat.201400230>
- Bruni, F. J., Liu, C.-M., & Stone-Sundberg, J. (2013). Will Czochralski Growth of Sapphire Once Again Prevail? *Acta Physica Polonica A*, 124(2), 213–218. <https://doi.org/10.12693/APhysPolA.124.213>
- Bunoiu, O., Defoort, F., Santailler, J. L., Duffar, T., & Nicoara, I. (2005). Thermodynamic analyses of gases formed during the EFG sapphire growth process. *Journal of Crystal Growth*, 275(1–2). <https://doi.org/10.1016/j.jcrysgro.2004.11.249>
- Calamiotou, M., Chrysanthakopoulos, N., Papaioannou, G., & Baruchel, J. (2007). Dynamics of photodeformations and space charge field in photorefractive Fe:LiNbO<sub>3</sub> studied with synchrotron

- area diffractometry. *Journal of Applied Physics*, 102(8). <https://doi.org/10.1063/1.2798636>
- Carroz, L., & Duffar, T. (2015). Working point of the EFG process. *Crystal Research and Technology*, 50(6), 473–481. <https://doi.org/10.1002/crat.201500021>
- Chen, C.-H., Chen, J.-C., Lu, C.-W., & Liu, C.-M. (2012). Effect of power arrangement on the crystal shape during the Kyropoulos sapphire crystal growth process. *Journal of Crystal Growth*, 352(1), 9–15. <https://doi.org/10.1016/j.jcrysgro.2012.01.017>
- Chen, C.-H., Chen, J.-C., Lu, C.-W., Liu, C.-M., Chena, C.-H., Chen, J.-C., ... Liu, C.-M. (2011). Numerical simulation of heat and fluid flows for sapphire single crystal growth by the Kyropoulos method. *Journal of Crystal Growth*, 318(1), 162–167. <https://doi.org/10.1016/j.jcrysgro.2010.10.121>
- Chen, C., Chen, H. J., Yan, W. B., Min, C. H., Yu, H. Q., Wang, Y. M., ... Liu, C. C. (2014). Effect of crucible shape on heat transport and melt–crystal interface during the Kyropoulos sapphire crystal growth. *Journal of Crystal Growth*, 388, 29–34. <https://doi.org/10.1016/j.jcrysgro.2013.11.002>
- Chen, W., Tang, H., Wang, J., Yuan, Q., Jiang, D., Qian, X., & Xu, J. (2014). Research on the multi-crystalline structure in sapphire grown by Kyropoulos technique. *Crystal Research and Technology*, 49(7), 507–513. <https://doi.org/10.1002/crat.201400098>
- Chenghai, X., Songhe, M., Mingfu, Z., Hongbo, Z., & Guigen, W. (2007). Thermal stresses and cracks during the growth of large-sized sapphire with SAPMAC method. *Chinese Journal of Aeronautics*, 20(5), 475–480. [https://doi.org/10.1016/S1000-9361\(07\)60070-3](https://doi.org/10.1016/S1000-9361(07)60070-3)
- Chernov, A. A. (1984). *Modern Crystallography III. Modern Crystallography III* (Vol. 36). Berlin, Heidelberg: Springer Berlin Heidelberg. <https://doi.org/10.1007/978-3-642-81835-6>
- De Geuser, F., & Deschamps, A. (2012). Precipitate characterisation in metallic systems by small-angle X-ray or neutron scattering. *Comptes Rendus Physique*, 13(3), 246–256. <https://doi.org/10.1016/j.crhy.2011.12.008>
- Demina, S. E., Bystrova, E. N., Postolov, V. S., Eskov, E. V., Nikolenko, M. V., Marshanin, D. A., ... Kalaev, V. V. (2008). Use of numerical simulation for growing high-quality sapphire crystals by the Kyropoulos method. *Journal of Crystal Growth*, 310(7–9), 1443–1447. <https://doi.org/10.1016/j.jcrysgro.2007.11.083>
- Dienes, G. J., Welch, D. O., Fischer, C. R., Hatcher, R. D., Lazareth, O., & Samberg, M. (1975). Shell-model

- calculation of some point-defect properties in  $\alpha$ -Al<sub>2</sub>O<sub>3</sub>. *Physical Review B*, 11(8), 3060–3070.  
<https://doi.org/10.1103/PhysRevB.11.3060>
- Duffar, T. (2010). *Crystal Growth Processes Based on Capillarity*. (T. Duffar, Ed.). Wiley.
- Fainberg, J., & Leister, H. J. (1996). Finite volume multigrid solver for thermo-elastic stress analysis in anisotropic materials. *Computer Methods in Applied Mechanics and Engineering*, 137(2), 167–174.  
[https://doi.org/10.1016/S0045-7825\(96\)01063-8](https://doi.org/10.1016/S0045-7825(96)01063-8)
- Fang, H. S., Jin, Z. L., Zhang, M. J., Zhang, Z., & Zhao, C. J. (2013). Role of internal radiation at the different growth stages of sapphire by Kyropoulos method. *International Journal of Heat and Mass Transfer*, 67, 967–973. <https://doi.org/10.1016/j.ijheatmasstransfer.2013.08.074>
- Fang, H. S., Pan, Y. Y., Zheng, L. L., Zhang, Q. J., Wang, S., & Jin, Z. L. (2013). To investigate interface shape and thermal stress during sapphire single crystal growth by the Cz method. *Journal of Crystal Growth*, 363, 25–32. <https://doi.org/10.1016/j.jcrysgro.2012.09.050>
- Farr, W. G., Creedon, D. L., Goryachev, M., Benmessai, K., & Tobar, M. E. (2013). Ultrasensitive microwave spectroscopy of paramagnetic impurities in sapphire crystals at millikelvin temperatures. *Physical Review B - Condensed Matter and Materials Physics*, 88(22), 1–8.  
<https://doi.org/10.1103/PhysRevB.88.224426>
- Furlong, D. N., & Hartland, S. (1979). Wall effect in the determination of surface tension using a wilhelmy plate. *Journal of Colloid And Interface Science*, 71(2), 301–315. [https://doi.org/10.1016/0021-9797\(79\)90241-8](https://doi.org/10.1016/0021-9797(79)90241-8)
- Gao, Y., Guo, X., & Lu, J. (2015). Analysis of cracking at the bottom during the last stage of Kyropoulos sapphire crystal growth. *International Journal of Science*, 2(8), 146–153.
- Gay, P., Hirsch, P. ., & Kelly, A. (1953). The estimation of dislocation densities in metals from X-ray data. *Acta Metallurgica*, 1(3), 315–319. [https://doi.org/10.1016/0001-6160\(53\)90106-0](https://doi.org/10.1016/0001-6160(53)90106-0)
- Ghezal, E. A., Li, H., Nehari, A., Brenier, A., Lebbou, K., Joubert, M. F., & Soltani, M. T. (2012). Effect of Pulling Rate on Bubbles Distribution in Sapphire Crystals Grown by the Micropulling Down ( $\mu$ -PD) Technique. *Crystal Growth and Design*, 4098–4103. <https://doi.org/dx.doi.org/10.1021/cg300589h>
- Glatter, V. O., & Kratky, O. (1982). *Small Angle X-ray Scattering*. *Small Angle X-ray Scattering*. London: Academic Press Inc. Ltd.



- Haneda, H., & Monty, C. (1989). Oxygen self-diffusion in magnesium-or titanium-doped alumina single crystals. *Journal of the American Ceramic Society*, 72(7), 1153–1157. <https://doi.org/10.1111/j.1151-2916.1989.tb09728.x>
- Harris, D. C. (2004). A Century of Sapphire Crystal Growth. In *Proceedings of the 10th DoD Electromagnetic Windows Symposium Norfolk, Virginia, May 2004*.
- Harris, D. C. (2009). Evolution of the sapphire industry: Rubicon Technology and Gavish. In R. W. Tustison (Ed.), *SPIE* (Vol. 7302, p. 730202). <https://doi.org/10.1117/12.816843>
- Hartland, S., & Hartley, R. W. (1976). *Axisymmetric fluid-liquid interfaces*. Zurich: Elsevier.
- Horowitz, A., Biderman, S., Amar, G. B., Laor, U., Weiss, M., & Stern, A. (1987). The growth of single crystals of optical materials via the gradient solidification method. *Journal of Crystal Growth*, 85(1–2), 215–222. [https://doi.org/10.1016/0022-0248\(87\)90225-9](https://doi.org/10.1016/0022-0248(87)90225-9)
- Horowitz, A., Biderman, S., Gazit, D., Einav, Y., Ben-Amar, G., & Weiss, M. (1993). The growth of dome-shaped sapphire crystals by the gradient solidification method (GSM). *Journal of Crystal Growth*, 128(1–4 PART 2), 824–828. [https://doi.org/10.1016/S0022-0248\(07\)80052-2](https://doi.org/10.1016/S0022-0248(07)80052-2)
- Hoszowska, J., Freund, A. K., Boller, E., Sellschop, J. P. F., Level, G., Rtwig, J., ... Baruchel, J. (2001). Characterization of synthetic diamond crystals by spatially resolved rocking curve measurements. *Journal of Physics D: Applied Physics*, 34(10A), A47–A51. <https://doi.org/10.1088/0022-3727/34/10A/311>
- Jayaraman, A. (2000). A brief overview of gem materials: Natural and synthetic. *Current Science*, 79(11), 1555–1565.
- Jianwei, X., Yongzong, Z., Guoqing, Z., & Peizhen, D. (1998). Growth of large-sized sapphire boules by temperature gradient technique (TGT). *Journal of Crystal Growth*, 193(1–2), 123–126. [https://doi.org/10.1016/S0022-0248\(98\)00462-X](https://doi.org/10.1016/S0022-0248(98)00462-X)
- Jin, Z. L., Fang, H. S., Yang, N., Zhang, Z., Wang, S., & Xu, J. F. (2014). Influence of temperature-dependent thermophysical properties of sapphire on the modeling of Kyropoulos cooling process. *Journal of Crystal Growth*, 405, 52–58. <https://doi.org/10.1016/j.jcrysgro.2014.07.049>
- Johansen, T. H. (1987). Analysis of the crystal weighing method applied to liquid encapsulated Czochralski growth. *Journal of Crystal Growth*, 84, 609–620.

- Joyce, D. B., & Schmid, F. (2010). Progress in the growth of large scale Ti:sapphire crystals by the heat exchanger method (HEM) for petawatt class lasers. *Journal of Crystal Growth*, 312(8), 1138–1141. <https://doi.org/10.1016/j.jcrysgro.2009.11.002>
- Khattak, C. P., Filgate, J., Shetty, R., Schwerdtfeger, C. R., & Ullal, S. (2015). 20-inch diameter CHES® sapphire boules. *SPIE*, 9453(603), 945305. <https://doi.org/10.1117/12.2180647>
- Khattak, C. P., Shetty, R., Schwerdtfeger, C. R., & Ullal, S. (2016). World's largest sapphire for many applications. *Journal of Crystal Growth*, 452, 44–48. <https://doi.org/10.1016/j.jcrysgro.2015.11.026>
- Kitayama, M., & Glaeser, A. M. (2004). The Wulff Shape of Alumina: III, Undoped Alumina. *Journal of the American Ceramic Society*, 85(3), 611–622. <https://doi.org/10.1111/j.1151-2916.2002.tb00140.x>
- Kluender, R. T., Philip, A., Meyssonier, J., & Baruchel, J. (2011). Three-dimensional distortion measurements by section rocking curve imaging: Application to ice crystals. *Physica Status Solidi (A) Applications and Materials Science*, 208(11), 2505–2510. <https://doi.org/10.1002/pssa.201184265>
- Kortov, V., Lushchik, A., Nagirnyi, V., Ananchenko, D., & Romet, I. (2017). Spectrally resolved thermally stimulated luminescence of irradiated anion-defective alumina single crystals. *Journal of Luminescence*, 186(February), 189–193. <https://doi.org/10.1016/j.jlumin.2017.02.023>
- Kryvonosov, I. V., & Lytvynov, L. A. (2016). Analysis of dynamic parameters of the KY-crystallization process. *Functional Materials*, 23(2), 300–306. <https://doi.org/10.15407/fm23.02.300>
- Kryvonosov, I. V., & Lytvynov, L. A. (2017). Optimization of KY-crystallization process. *Functional Materials*, 24(1), 138–142. <https://doi.org/10.15407/fm24.01.138>
- Kryvonosov, I. V., & Lytvynov, L. A. (2012). Properties of Ti-sapphire as laser material. *Crystallography Reports*, 57(7), 967–973. <https://doi.org/10.1134/S1063774512070139>
- Kurz, W., & D.J.Fisher. (1998). *Fundamentals of Solidification*. Trans Tech Publications Ltd, Switzerland (Fourth Rev). Brindrain, Switzerland: Trans Tech Publications Ltd. Retrieved from <http://doi.wiley.com/10.1002/crat.2170210909>
- Kyropoulos, S. (1926). Ein Verfahren zur Herstellung großer Kristalle. *Zeitschrift Für Anorganische Und Allgemeine Chemie*, 154(1), 308–313. <https://doi.org/10.1002/zaac.19261540129>
- Lagerlof, K. P. D., Heuer, A. H., Castaing, J., Riviere, J. P., & Mitchell, T. E. (1994). Slip and Twinning in

- Sapphire ( $\alpha$ -Al<sub>2</sub>O<sub>3</sub>). *Journal of the American Ceramic Society*, 77(2), 385–397.  
<https://doi.org/10.1111/j.1151-2916.1994.tb07006.x>
- Lagerlof, K. P. D., Mitchell, T. E., & Heuer, A. H. (1989). Lattice Diffusion Kinetics in Undoped and Impurity-Doped Sapphire ( $\alpha$ -Al<sub>2</sub>O<sub>3</sub>): A Dislocation Loop Annealing Study. *Journal of the American Ceramic Society*, 72(11), 2159–2171. <https://doi.org/10.1111/j.1151-2916.1989.tb06049.x>
- Lee, W. J., Lee, Y. C., Jo, H. H., Park, Y. H., & Sapphire, B. (2011). Effect of crucible geometry on melt convection and interface shape during Kyropoulos growth of sapphire single crystal. *Journal of Crystal Growth*, 324(1), 248–254. <https://doi.org/10.1016/j.jcrysgro.2011.03.032>
- Li, H., Ghezal, E. A., Nehari, A., Alombert-Goget, G., Brenier, A., & Lebbou, K. (2013). Bubbles defects distribution in sapphire bulk crystals grown by Czochralski technique. *Optical Materials*, 35(5), 1071–1076. <https://doi.org/10.1016/j.optmat.2012.12.022>
- Liu, W., Lu, J., Chen, H., Yan, W., Min, C., Lian, Q., ... Xu, Y. (2015). Study on crystal-melt interface shape of sapphire crystal growth by the KY method. *Journal of Crystal Growth*, 431, 15–23.  
<https://doi.org/10.1016/j.jcrysgro.2015.08.018>
- Lübbert, D., Baumbach, T., Härtwig, J., Boller, E., & Pernot, E. (2000).  $\mu$ m-resolved high resolution X-ray diffraction imaging for semiconductor quality control. *Nuclear Instruments and Methods in Physics Research Section B: Beam Interactions with Materials and Atoms*, 160(4), 521–527.  
[https://doi.org/10.1016/S0168-583X\(99\)00619-9](https://doi.org/10.1016/S0168-583X(99)00619-9)
- Lübbert, D., Ferrari, C., Mikulík, P., Pernot, P., Helfen, L., Verdi, N., ... Baumbach, T. (2005). Distribution and Burgers vectors of dislocations in semiconductor wafers investigated by rocking-curve imaging. *Journal of Applied Crystallography*, 38(1), 91–96. <https://doi.org/10.1107/S0021889804028195>
- Macfarlane, R. M., J.Y.Wong, & M.D.Sturge. (1968). Dynamic Jahn-Teller Effect in Octahedrally Coordinated d<sup>1</sup> Impurity Systems. *Physical Review*, 166(2), 250–258.
- Maiman, T. H. (1960). Stimulated Optical Radiation in Ruby. *Nature*, 187(4736), 493–494.  
<https://doi.org/10.1038/187493a0>
- Marasina, L. A., Malinovsky, V. V., Pichugin, I. G., & Prentky, P. (1982). Chemical etching of sapphire. *Crystal Research and Technology*, 17(3), 365–371. <https://doi.org/10.1002/crat.2170170320>
- McCallum, J. C., Morpeth, L. D., & Norman, M. J. (2002). Characterisation of Ti:sapphire layers synthesized

- energy ion implantation. In *Conference on Optoelectronic and Microelectronic Materials and Devices*. (pp. 555–558). IEEE. <https://doi.org/10.1109/COMMAD.2002.1237312>
- Mitchell, T. E., Hobbs, L. W., Heuer, A. H., Castaing, J., Cadoz, J., & Philibert, J. (1979). Interaction between point defects and dislocations in oxides. *Acta Metallurgica*, 27, 1677–1691.
- Miyagawa, C., Kobayashi, T., Taishi, T., & Hoshikawa, K. (2013). Demonstration of crack-free c-axis sapphire crystal growth using the vertical Bridgman method. *Journal of Crystal Growth*, 372, 95–99. <https://doi.org/10.1016/j.jcrysgro.2013.03.006>
- Moroño, A., & Hodgson, E. R. (1997). On the origin of the F+ centre radioluminescence in sapphire. *Journal of Nuclear Materials*, 249(2–3), 128–132. [https://doi.org/10.1016/S0022-3115\(97\)00227-4](https://doi.org/10.1016/S0022-3115(97)00227-4)
- Moulton, P. F. (1982). Ti-doped sapphire: tunable solid-state laser. *Optics News*, 8(December), 9.
- Moulton, P. F. (1986). Spectroscopic and laser characteristics of Ti:Al<sub>2</sub>O<sub>3</sub>. *Journal of the Optical Society of America B*, 3(1), 125. <https://doi.org/10.1364/JOSAB.3.000125>
- Moulton, P. F. (1987). Titanium-Doped Sapphire Laser Research and Design Study. *NASA-National Aeronautics and Space Administration, NASA CR-40*(September), 1–44.
- Musatov, M. I. (2009). The creation of a method of growing large crystals of optical synthetic sapphire at the S I Vavilov State Optical Institute. *Journal of Optical Technology*, 76(2), 107. <https://doi.org/10.1364/JOT.76.000107>
- Musatov, M. I. (2010). Mikhail Ivanovich Musatov (On the eightieth anniversary of his birth). *J Opt Technol Eng Tr*, 77(11), 737.
- Nassau, K. (1972). DR. A. V. L. VERNEUIL: The man and the method. *Journal of Crystal Growth*, 13(1 972), 12–18.
- Nehari, A., Brenier, A., Panzer, G., Lebbou, K., Godfroy, J., Labor, S., ... Moncorgé, R. (2011). Ti-doped sapphire (Al<sub>2</sub>O<sub>3</sub>) single crystals grown by the kyropoulos technique and optical characterizations. *Crystal Growth and Design*, 11(2), 445–448. <https://doi.org/10.1021/cg101190q>
- Nehari, A., Duffar, T., Ghezal, E. A., & Lebbou, K. (2014). Chemical segregation of titanium in sapphire single crystals grown by micro-pulling-down technique: Analytical model and experiments. *Crystal Growth and Design*, 14(12), 6492–6496. <https://doi.org/10.1021/cg5013582>

- Nicoara, I., Bunoiu, O. M., & Vizman, D. (2006). Voids engulfment in shaped sapphire crystals. *Journal of Crystal Growth*, 287(2), 291–295. <https://doi.org/10.1016/j.jcrysgro.2005.11.032>
- Ostrogorsky, A. G., & Glicksman, M. E. (2015). Segregation and Component Distribution. In *Handbook of Crystal Growth* (Second Edi, Vol. 2, pp. 995–1047). Elsevier. <https://doi.org/10.1016/B978-0-444-63303-3.00025-0>
- Paladino, A. E., & Roiter, B. D. (1964). Czochralski Growth of Sapphire. *Journal of the American Ceramic Society*, 47(9), 465–465. <https://doi.org/10.1111/j.1151-2916.1964.tb14437.x>
- Pamplin, B. R. (1977). The evolution of crystal growth techniques. *Progress in Crystal Growth and Characterization*, 1(1), 5–22. [https://doi.org/10.1016/0146-3535\(77\)90003-X](https://doi.org/10.1016/0146-3535(77)90003-X)
- Perner, B., Kvapil, J., V, S., & Kvapil, J. (1979). Growth of Sapphire by the Kyropoulus Method. *Kristall Und Technik*, 14(6), 661–664.
- Pernot, J., Volpe, P. N., Omnès, F., Muret, P., Mortet, V., Haenen, K., & Teraji, T. (2010). Hall hole mobility in boron-doped homoepitaxial diamond. *Physical Review B - Condensed Matter and Materials Physics*, 81(20), 1–7. <https://doi.org/10.1103/PhysRevB.81.205203>
- Pishchik, V., Lytvynov, L. A., & Dobrovinskaya, E. R. (2009). *Sapphire*. Boston, MA: Springer US. <https://doi.org/10.1007/978-0-387-85695-7>
- Pletka, B. J., Heuer, A. H., & Mitchell, T. E. (1977). Work-hardening in sapphire ( $\alpha$ -Al<sub>2</sub>O<sub>3</sub>). *Acta Metallurgica*, 25(1), 25–33. [https://doi.org/10.1016/0001-6160\(77\)90242-5](https://doi.org/10.1016/0001-6160(77)90242-5)
- Rasmussen, J. ., & Kingery, W. D. (1970). Effect of Dopants on the Defect Structure of Single-Crystal Aluminum Oxide. *Journal of the American Ceramic Society*, 53(8), 436–440. <https://doi.org/10.1111/j.1151-2916.1970.tb12672.x>
- Reddy, K. P. R., & Cooper, A. R. (1982). Oxygen Diffusion in Sapphire. *Journal of the American Ceramic Society*, 65(12), 634–638. <https://doi.org/10.1111/j.1151-2916.1982.tb09944.x>
- Richard Schwerdtfeger, C., Ullal, S., Shetty, R., Filgate, J., & Dhanaraj, G. (2014). Latest developments of large-diameter c-axis sapphire grown by CHES method. *Journal of Crystal Growth*, 393, 123–128. <https://doi.org/10.1016/j.jcrysgro.2013.10.056>
- Schaffer, P. S. (1965). Vapor-Phase Growth of Alpha Alumina Single Crystals. *Journal of the American*

- Ceramic Society*, 48(10), 508–511. <https://doi.org/10.1111/j.1151-2916.1965.tb14650.x>
- Scheuplin, R., & Gibbs, P. (1960). Surface Structure in Corundum: I, Etching of Dislocations. *Journal of the American Ceramic Society*, 43(9), 458–472. <https://doi.org/10.1111/j.1151-2916.1960.tb13698.x>
- Schmid, F., Khattak, C. P., Rogers, H. H., Felt, D. M., Askinazi, J., & Wientzen, R. V. (1999). Current status of very large sapphire crystal growth for optical applications. *SPIE*, 3705(April 1999), 70–76.
- Schmid, F., & Viechnicki, D. (1970). Growth of Sapphire Disks from the Melt by a Gradient Furnace Technique. *Journal of the American Ceramic Society*, 53(9), 528–529. <https://doi.org/10.1111/j.1151-2916.1970.tb16009.x>
- Sen, G., Tran Caliste, T. N., Stelian, C., Baruchel, J., Barthalay, N., & Duffar, T. (2016). Synchrotron X-ray diffraction imaging studies of dislocations in Kyropoulos grown Ti doped sapphire crystal. *Journal of Crystal Growth*, 468(xxxx), 477–483. <https://doi.org/10.1016/j.jcrysgro.2016.12.079>
- Singh, G., Ghosh, B., & Deshpande, R. Y. (1981). On the Shape of Crystals Grown by Kyropoulos Technique. *Crystal Research and Technology*, 1239–1245.
- Smith, M., Schmid, K., Schmid, F., Khattak, C. P., & Lambropoulos, J. (1999). Correlation of crystallographic orientation with processing of sapphire optics. *SPIE*, 3705(April), 85–92.
- Snow, J. D., & Heuer, A. H. (1973). Slip system in Al<sub>2</sub>O<sub>3</sub>. *Journal of the American Ceramic Society*, 56(3), 153–157. <https://doi.org/10.1111/j.1151-2916.1973.tb15432.x>
- Song, D. W., Kim, K. S., & Kim, H. (2015). A conical shape-evolution model for the control of sapphire crystal growth in Kyropoulos (KY) method. *Korean Journal of Chemical Engineering*, 32(3), 486–493. <https://doi.org/10.1007/s11814-014-0226-9>
- Stelian, C., Alombert-Goget, G., Sen, G., Barthalay, N., Lebbou, K., & Duffar, T. (2017). Interface effect on titanium distribution during Ti-doped sapphire crystals grown by the Kyropoulos method. *Optical Materials*, 69, 73–80. <https://doi.org/10.1016/j.optmat.2017.04.020>
- Stelian, C., Barthalay, N., & Duffar, T. (2017). Numerical investigation of factors affecting the shape of the crystal-melt interface in edge-defined film-fed growth of sapphire crystals. *Journal of Crystal Growth*, 470, 159–167. <https://doi.org/10.1016/j.jcrysgro.2017.05.001>
- Stelian, C., Sen, G., Barthalay, N., & Duffar, T. (2016). Comparison between numerical modeling and

- experimental measurements of the interface shape in Kyropoulos growth of Ti-doped sapphire crystals. *Journal of Crystal Growth*, 453, 90–98. <https://doi.org/10.1016/j.jcrysgro.2016.08.001>
- Stelian, C., Sen, G., Caliste, T. N. T., Baruchel, J., & Duffar, T. (2018). Comparison of thermal stress computations in Czochralski and Kyropoulos growth of sapphire crystals. *Submitted to CrystEngComm*.
- Suzuki, T., Shiotsuki, K., Taishi, T., & Hoshikawa, K. (2014). Contact angle of sapphire melt and bubble generation on crucible material. *Journal of Crystal Growth*, 401, 508–510. <https://doi.org/10.1016/j.jcrysgro.2013.11.090>
- Tandjaoui, A., Cherif, M., Carroz, L., Sanchez, J., Reboud, R., Garnier, C., & Duffar, T. (2016). Investigation of liquid oxide interactions with refractory substrates via sessile drop method. *Journal of Materials Science*, 51(4), 1701–1712. <https://doi.org/10.1007/s10853-015-9504-0>
- Tatartchenko, V. A. (2005). Sapphire Crystal Growth and Applications. In P. Capper (Ed.), *Bulk Crystal Growth of Electronic, Optical & Optoelectronic Materials* (pp. 300–338). Chichester, UK: John Wiley & Sons, Ltd. <https://doi.org/10.1002/9780470012086>
- Thomson, R. M., & Balluffi, R. W. (1962). Kinetic theory of dislocation climb. I. General models for edge and screw dislocations. *Journal of Applied Physics*, 33(3), 803–816. <https://doi.org/10.1063/1.1777171>
- Timofeev, V. V., Kalaev, V. V., & Ivanov, V. G. (2015). 3D melt convection in sapphire crystal growth: Evaluation of physical properties. *International Journal of Heat and Mass Transfer*, 87, 42–48. <https://doi.org/10.1016/j.ijheatmasstransfer.2015.03.058>
- Tran Thi, T. N., Morse, J., Caliste, D., Fernandez, B., Eon, D., Härtwig, J., ... Baruchel, J. (2017). Synchrotron Bragg diffraction imaging characterization of synthetic diamond crystals for optical and electronic power device applications. *Journal of Applied Crystallography*, 50(2), 561–569. <https://doi.org/10.1107/S1600576717003831>
- Tsoutsouva, M. G., Oliveira, V. a., Baruchel, J., Camel, D., Marie, B., & Lafford, T. a. (2015). Characterization of defects in mono-like silicon for photovoltaic applications using X-ray Bragg diffraction imaging. *Journal of Applied Crystallography*, 48, 645–654. <https://doi.org/10.1107/S1600576715004926>
- Vyshnevskiy, S. ., Kryvonosov, Y. V., & Lytvynov, L. A. (2006). Foreign phase inclusions in Ti-sapphire grown in a carbon-containing medium. *Functional Materials*, 13(2), 238–244.
- Wall, K. F., & Sanchez, A. (1990). Titanium Sapphire lasers. *The Lincoln Laboratory Journal*, 3(3), 447–462.

<https://doi.org/10.2184/ljsj.21.73>

- Wang, B., Bliss, D. F., & Callahan, M. J. (2009). Hydrothermal growth of Ti:sapphire ( $\text{Ti}^{3+}$ :  $\text{Al}_2\text{O}_3$ ) laser crystals. *Journal of Crystal Growth*, 311(3), 443–447. <https://doi.org/10.1016/j.jcrysgro.2008.09.052>
- Wang, G. G., Zhang, M. F., Wu, Q. B., Zhang, H. Y., Zuo, H. B., Han, J. C., ... Huang, W. X. (2010). Synchrotron X-ray diffraction studies of large sapphire crystal grown by Kyropoulos-like method. *Physica Status Solidi (A) Applications and Materials Science*, 207(1), 92–96. <https://doi.org/10.1002/pssa.200925150>
- Wang, S., & Fang, H. (2016). Dependence of thermal stress evolution on power allocation during Kyropoulos sapphire cooling process. *Applied Thermal Engineering*, 95, 150–156. <https://doi.org/10.1016/j.applthermaleng.2015.11.003>
- Wie, C. R. (1994). High resolution X-ray diffraction characterization of semiconductor structures. *Materials Science and Engineering R13*, 1–56.
- Winey, J. M., Gupta, Y. M., & Hare, D. E. (2001). R-Axis Sound Speed and Elastic Properties of Sapphire Single Crystals. *Journal of Applied Physics*, 90(6), 3109–3111. <https://doi.org/10.1063/1.1391420>
- Xiao, J., Yin, S., Shao, M., & Zhang, X. (2004). Observation of dislocation etch pits in a sapphire crystal grown by Cz method using environmental SEM. *Journal of Crystal Growth*, 266(4), 519–522. <https://doi.org/10.1016/j.jcrysgro.2004.03.021>
- Xu, C. H., Zhang, M. F., Meng, S. H., Han, J. C., Wang, G. G., & Zuo, H. B. (2007). Temperature field design, process analysis and control of SAPMAC method for the growth of large size sapphire crystals. *Crystal Research and Technology*, 42(8), 751–757. <https://doi.org/10.1002/crat.200710902>
- Zhang, L., Zuo, H., Cao, F., Xing, D., Sun, J., Wang, X., & Han, J. (2012). Process design for the shape control of crystals grown by Kyropoulos or SAPMAC method. *Crystal Research and Technology*, 47(2), 175–182. <https://doi.org/10.1002/crat.201100480>
- Zhang, L., Zuo, H., Sun, J., Wang, X., Han, J., & Xing, D. (2011). Theoretical analysis of the shape evolution of crystals grown by pulling. *Crystal Research and Technology*, 46(10), 1019–1026. <https://doi.org/10.1002/crat.201100147>
- Zhang, L., Zuo, H., Zhou, J., Sun, J., Xing, D., & Han, J. (2011). Haze in sapphire crystals grown by SAPMAC method. *Crystal Research and Technology*, 46(7), 669–675. <https://doi.org/10.1002/crat.201100122>



- Zharikov, E. V. (2012). Problems and recent advances in melt crystal growth technology. *Journal of Crystal Growth*, 360(1), 146–154. <https://doi.org/10.1016/j.jcrysgro.2011.11.049>
- Zhou, D., Xia, C., Guyot, Y., Zhong, J., Xu, X., Feng, S., ... Lebbou, K. (2015). Growth and spectroscopic properties of Ti-doped sapphire single-crystal fibers. *Optical Materials*, 47(October), 495–500. <https://doi.org/10.1016/j.optmat.2015.06.027>
- Zhou, G., Dong, Y., Xu, J., Li, H., Si, J., Qian, X., & Li, X. (2006).  $\Phi$ 140 Mm Sapphire Crystal Growth By Temperature Gradient Techniques and Its Color Centers. *Materials Letters*, 60(7), 901–904. <https://doi.org/10.1016/j.matlet.2005.10.092>
- Zhou, Y., Xia, H., Huang, Z., Lu, M., Deng, P., Qiao, J., ... Hu, B. (1992). Growth of large-size Ti:Al<sub>2</sub>O<sub>3</sub> tunable laser crystal (Poster Paper). In G. J. Quarles (Ed.), *SPIE* (p. 230). <https://doi.org/10.1117/12.60165>

